Impact of data density and endmember definitions on long-term trends in ground cover fractions across European grasslands

Katarzyna Ewa Lewińska [1,2], Akpona Okujeni [3,1], Katja Kowalski [4,1], Fabian Lehmann [5],

Volker C. Radeloff [2], Ulf Leser [5], Patrick Hostert [1,6]

[1] Geography Department, Humboldt-Universität zu Berlin, Unter den Linden 6, 10099 Berlin, Germany.

[2] SILVIS Lab, Department of Forest and Wildlife Ecology, University of Wisconsin-Madison, 1630 Linden Drive, Madison WI 53706, USA.

[3] Helmholtz Center Potsdam, GFZ German Research Center for Geosciences, Telegrafenberg, 14473 Potsdam, Germany

[4] Earth Observation for Ecosystem Management, School of Life Sciences, Technical University of Munich, 11 Hans-Carl-v.-Carlowitz-Platz 2, 85354 Freising, Germany

[5] Department of Computer Science, Humboldt-Universität zu Berlin, Unter den Linden 6, 10099 Berlin, Germany

[6] Integrative Research Institute on Transformations of Human-Environment Systems (IRI THESys), Humboldt-Universität zu Berlin, Unter den Linden 6, 10099 Berlin, Germany

*corresponding author: Katarzyna Ewa Lewińska (Lewinska@hu-berlin.de)

This is a non-peer reviewed preprint submitted to EarthArXiv and is currently under review in Remote Sensing of Environment

Abstract

Long-term monitoring of grasslands is pivotal for ensuring continuity of many environmental services and for supporting food security and environmental modelling. Remote sensing provides an irreplaceable source of information for studying changes in grasslands. Specifically, Spectral Mixture Analysis (SMA) allows for quantification of physically meaningful ground cover fractions of grassland ecosystems (i.e., green vegetation, non-photosynthetic vegetation, and soil), which is crucial for our understanding of change processes and their drivers. However, although popular due to straightforward implementation and low computational cost, 'classical' SMA relies on a single endmember definition for each targeted ground cover component, thus offering limited suitability and generalization capability for heterogeneous landscapes. Furthermore, the impact of irregular data density on SMA-based long-term trends in grassland ground cover has also not yet been critically addressed.

We conducted a systematic assessment of i) the impact of data density on long-term trends in ground cover fractions in grasslands; and ii) the effect of endmember definition used in 'classical' SMA on pixel- and map-level trends of grassland ground cover fractions. We performed our study for 13 sites across European grasslands and derived the trends based on the Cumulative Endmember Fractions calculated from monthly composites. We compared three different data density scenarios, i.e., complete Landsat data record as is, Landsat data record with the monthly probability of data after 2014 adjusted to the pre-2014 levels, and the combined Landsat and Sentinel-2 datasets. For each site we ran SMA using a selection of site-specific and generalized endmembers, and compared the pixel- and map-level trends. Our results indicated no significant impact of varying data density on the long-term trends from Cumulative Endmember Fractions in European grasslands. Conversely, the use of different

endmember definitions led in some regions to significantly different pixel- and map-level long-term trends confirming questionable suitability of the 'classical' SMA for complex landscapes and big areas. Therefore, we caution against using the 'classical' SMA for remote-sensing-based applications across broader scales or in heterogenous landscapes, particularly for trend analyses, as the results may lead to erroneous conclusions.

1. Introduction

Time series of satellite data are an invaluable source of information for studying Earth's systems (Roy et al., 2014; Wulder et al., 2022). Consistent inter- and intra-annual observations allow for identification and thorough analyses of change patterns with long-term time series of data enabling tracking even subtle gradual changes or spurious deviations from 'normal' conditions (Woodcock et al., 2020). Historical observations provide valuable insight into the past, enhancing our understanding of the monitored processes, which is desirable for apt predictions of future conditions under diverse climatic scenarios (Duveiller et al., 2018; Lenton et al., 2024).

Monitoring long-term changes in grassland ecosystems is important due to grasslands' significant role in soil carbon-storing and sequestration capacities (Dangal et al., 2020; Lorenz and Lal, 2018) as well as numerous other ecosystem services (Bengtsson et al., 2019). European grasslands alone are a critical asset at local to global scales (Chaplin-Kramer et al., 2022) supporting food security, biodiversity, and cultural values (Bengtsson et al., 2019; Habel et al., 2013; Pellaton et al., 2022; Wilson et al., 2012). Concomitantly, grassland ecosystems in Europe experience different dynamics and development arising from diverse management strategies (Pazúr et al., 2024; Schils et al., 2022) and changes in meteorological conditions (Spinoni et al., 2020). Long-term analyses across European grassland ecosystems highlight shifts in water-use-efficiency (Poppe Terán et al., 2023), phenology (Bellini et al., 2022), biomass production (Choler et al., 2021; Munier et al., 2018), livestock carrying capacity (Piipponen et al., 2022), and species composition (Frantz et al., 2022; Suess et al., 2018) often signifying degradation (Bardgett et al., 2021) and decrease in capacity to support ecosystem services (Schils et al., 2022). Consequently, comprehensive long-term monitoring of grasslands is essential to better understand ongoing changes and to attain grasslands' environmental and economic roles (Ali et al., 2016; Dara et al., 2020; Lewińska et al., 2021; Schils et al., 2022; Yin et al., 2020).

Although the recent years offer an abundance of satellite observations at a variety of spatial and spectral resolutions, the Landsat data archive provides the only consistent source of optical medium-resolution acquisitions spanning already more than 40 years. With its 30-m spatial resolution, between 16- and 8-day equatorial revisit time when one or two satellites are in operation, respectively, Landsat provides an unparalleled source of information for land use and land cover applications (Potapov et al., 2020; Radeloff et al., 2024; Roy et al., 2014; Wulder et al., 2022). This exceptionally long data record enables long-term analyses, many of which explore long-term trends in vegetation cover, productivity and composition (Frantz et al., 2022; Hermosilla et al., 2019; Kowalski et al., 2024; Lewińska et al., 2021) enhancing our understanding of environmental responses at the field-level (Wulder et al., 2022; Zhu et al., 2020). However, the availability of Landsat data is highly variable across time and space, with significantly more acquisitions available since 2014 (Zhang et al., 2022), which poses challenges for consistent analyses, especially when including the early years of the Landsat record (Lewińska et al., 2024b, 2024a).

The abundancy of 'Landsat-like' satellite data in recent years presents an opportunity for densifying Landsat time series via sensor constellations (Wulder et al., 2015). The Sentinel-2 mission of the European Commission's Copernicus programme (Phiri et al., 2020) is a particularly prominent source of such data since the end of 2015. The 10-20-m resolution (Drusch et al., 2012), maximum 5-day equatorial revisit time and a 'free, full and open data policy' (European Commission, 2011), propel synergetic use of Landsat and Sentinel-2 data, which is further enabled through various harmonization workflows and harmonized analysis ready datasets (Claverie et al., 2018; Frantz, 2019; Saunier et al., 2022). The added value of higher temporal data availability arising from changes in the Landsat operational scheme as well as combining Landsat and Sentinel-2 data is clear for applications, such as mowing detection (Griffiths et al., 2020; Schwieder et al., 2022), land cover classification (Griffiths et al., 2019), and crop-type identification (Blickensdörfer et al., 2022; Johnson and Mueller, 2021). Concurrently, low data density may impact land cover and land use change (LCLUC) results (Frantz et al., 2023, 2022). However, despite great variability in data availability across the past 40 years, the impact of temporal density of observations on long-term trends is rarely questioned not only for Landsat data alone (Kolecka, 2021; Lewińska et al., 2024b), but also when combining Landsat and Sentinel-2 archives (Kowalski et al., 2024; Runge and Grosse, 2020). Yet, phenology-oriented studies suggest a clear relation between satellite-derived phenology metrics and data density (Mas and Soares De Araújo, 2021) and the overestimation of trends in phenological metrics due to greater data availability after 2014 (Bayle et al., 2024).

Long-term monitoring of agricultural lands commonly relies on vegetation indices derived based on active optical data (White et al., 2022; Zhang et al., 2017; Zhu et al., 2016). This approach enables a 'compression' of several bands into a proxy suitable for monitoring selected land cover features, reducing the computational strain and simplifying the results. Because vegetation indices correlate with green biomass, they are frequently used to approximate vegetation health. Furthermore, aggregation of equidistantly distributed index values over one year or a vegetation season approximates vegetation primary production and allows for a straightforward comparison among the years (Reed et al., 1994). However, interpretation of the index-based results is often problematic due to their lack of physical meaning, which limits a direct link to the underlying processes. Conversely, Spectral Mixture Analysis (SMA; Adams et al., 1986) quantifies abundances of selected ground cover components while relying on all available spectral bands, providing easily interpretable physically based information. These advantages led to the increasing use of SMA in LCLUC trend-based analyses (Chen et al., 2021; Hill and Guerschman, 2022; Sun et al., 2024) especially in regions with complex and occasionally sparse vegetation cover, such as grasslands (Frantz et al., 2022; Lewińska et al., 2023, 2021).

Since the 'classical' SMA only considers linear combinations of *n* ground cover fractions (represented by, so-called, endmembers), where *n* is smaller than the number of input bands, the method has limited suitability for complex landscapes encompassing different surfaces and vegetation types. Consequently, multiple new variants and enhancements of SMA have been developed to allow for accurate unmixing of images comprising many ground covers and materials. For example, multiple endmember SMA (MESMA; Dennison and Roberts, 2003; Roberts et al., 1998) select for each pixel the number and definition of endmembers to optimize SMA results, whereas regression-based approaches leverage machine learning algorithms trained on quantitative information, among others generated through synthetically mixing a wide selection of endmembers (Okujeni et al., 2013; Senf et al., 2020; Stanimirova et al., 2022). Yet, the 'classical' linear SMA is still frequently used in broad-scale analyses (Frantz et al., 2022; Hill and Guerschman, 2022, 2020; Lewińska et al., 2023, 2021) due to its straightforward implementation and lower computational costs as well as widespread accessibility on cloud-based geospatial analysis platforms. In such cases, a single set of 'generalized' endmembers is identified to analyze an entire area of interest (Guerschman et al., 2015; Guerschman and Hill, 2018). Although SMA is less accurate for regions located farther from where the image endmembers were sampled or parametrized (Guerschman et al., 2015) and shows seasonal variability reflecting phenological changes (Dudley et al., 2015; Okujeni et al., 2021), alike for vegetation indices, pixel-level aggregation of equidistantly distributed fraction values for one year or vegetation season (i.e., Cumulative Endmember Fractions - CEF; Lewińska et al., 2021, 2020) normalizes these intra-seasonal variabilities and allows for straightforward comparison among the years, and for green vegetation approximates vegetation primary production (Hobi et al., 2017; Reed et al., 1994).

The overarching goal of this study was to analyze how data density and definitions of endmembers affect long-term trends in grassland-specific ground cover fractions identified with the 'classical' SMA. Answering these questions is critical to verify the credibility of trends derived using time series comprising years with high and low availability of satellite data, and to raise awareness for the aptness of the 'classical' SMA for monitoring trends across vast and complex regions. With individual studies relying typically on a single set of endmembers, we lack insight into how the pixel-level and map-level trends diverge for different endmember sets, potentially leading to alternative conclusions. We conducted our analyses for green vegetation, non-photosynthetic vegetation, and soil ground cover fractions in European grasslands using CEF from Landsat and Sentinel-2 data. Specifically, our research objectives (RO) were to:

i) investigate whether greater density of Landsat acquisitions after 2014 impacts the 1984-2021 long-term pixel- and map-level trends in grasslands' ground cover CEFs;
ii) assess whether combining Landsat and Sentinel-2 data archives alters the long-term 1984-2021 trends in grasslands ground cover CEFs, as compared to the Landsat-only trends;
iii) evaluate pixel-level and map-level differences in long-term trends in CEFs in grasslands arising from endmember definitions used to derive ground cover fractions through SMA.

2. Methods

2.1. Study area

We performed our analyses on 13 test sites located across Europe (Figure 1). We selected the test sites to cover a wide range of environmental conditions expressed in biogeographical regions (EEA, 2016), dominant soil types (FAO, 2003), soil biomass productivity (Tóth et al., 2013), distribution and share of grasslands (Copernicus, 2018), and probability of clear sky observations (based on Sentinel-2 cloud probability) (Table SA1). Concomitantly, we targeted all five grassland management intensity clusters identified by Estel et al. (2018). Each test site comprised between 900 km² and 3,600 km² with the mean grassland coverage ranging between 14% (SE) and 68% (IE), and mean altitude ranging between -0.1 m b.s.l. (BX) and 434 m a.s.l. (SA) (Table SA1).

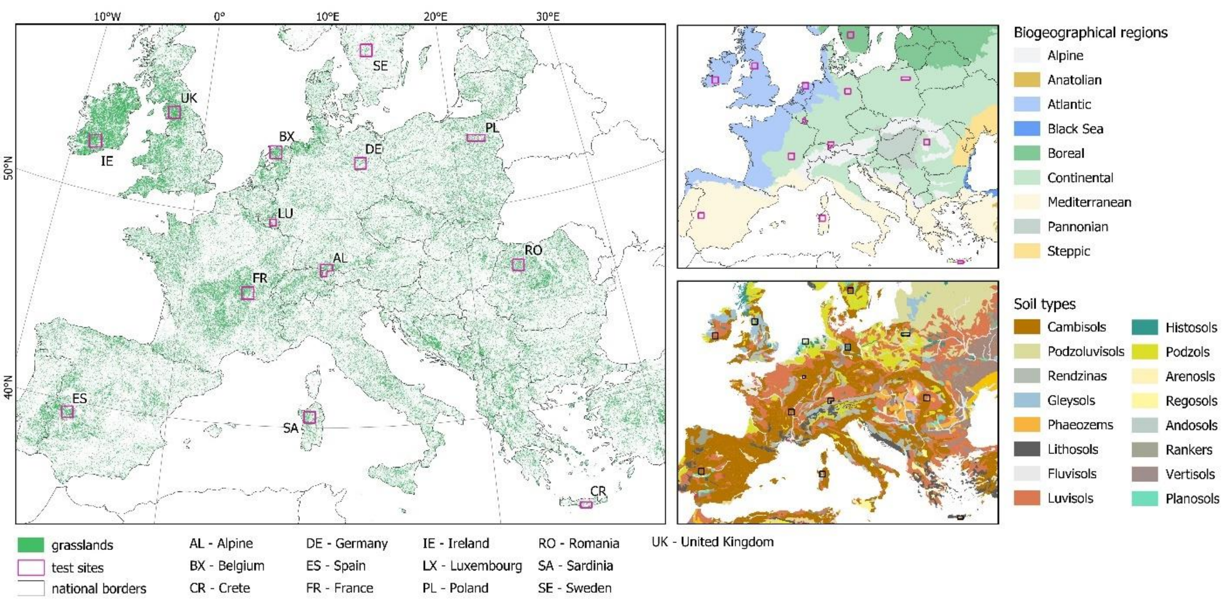

Figure 1 Location and an overview of selected characteristics of test sits. Environmental conditions at each site in Table SA1.

2.2. Landsat and Sentinel-2 time series

We based our analyses on Landsat and Sentinel-2 surface reflectance data. We downloaded all Tier 1 (Collection 2) Landsat scenes available for 1984 through 2021 from USGS/EROS, and Sentinel-2 TOA Level-1C (pre-Collection) for 2015 through 2021 from the Google Cloud Storage (data accessed in January 2023). For both time series we used only scenes with cloud cover of less than 70%. We excluded all ETM+ scenes acquired after 31 December 2020 due to the Landsat 7's orbit drift (Qiu et al., 2021). We used the Framework for Operational Radiometric Correction for Environmental monitoring (FORCE; Frantz, 2019) processing engine to derive surface reflectance, which involved atmospheric (Doxani et al., 2018), topographic (Buchner et al., 2020) and BRDF corrections (Li et al., 2019; Roy et al., 2016), detection and masking of clouds, cloud shadows, and low-quality pixels (Baetens et al., 2019; Zekoll et al., 2021; Zhu et al., 2015), and co-registration of Sentinel-2 scenes to the Landsat NIR base-map (Rufin et al., 2020).

Following findings of Okujeni et al. (2024) we cross-normalized all data to ETM+ feature space. We derived the normalization coefficients using the linear regression type 2 with reduced major axis based on 45,144 points distributed over all 13 sites in a regular 10-km grid and pairing scenes acquired maximum ± one day apart. We selected ETM+ as the cross-normalization baseline due to the coincidence of its timeline with all other used scanners, as well as the fact that ETM+ scenes alone accounted for 32% of our data archive. For Sentinel-2 datasets we normalized only bands matching ETM+ (i.e., B2, B3, B4, B8, B11, and B12; normalization coefficients in Table SA2).

2.3. Ancillary data

To conduct our analysis, we used a selection of ancillary data. We performed topographic correction of Landsat and Sentinel-2 data using Copernicus GLO-30 Digital

Elevation Model at 30m resolution (ESA, 2020). We applied the Copernicus HR 10m grassland 2018 mask (Copernicus, 2018) to determine grassland and pasture areas for our analysis, and assumed land cover invariant for the complete period of the analysis. To exclude isolated pixels and increase compactness of the mask we applied sequential morphology filtering of erosion (3x3), grow (5x5), and erosion (3x3). We characterized environmental conditions at each site using the dominant major soil types from the Digital Soil Map of the World (FAO, 2003). Finally, we used the Land Use/Cover Area frame statistical Survey (LUCAS) from 2018 (Eurostat, 2018) and the LUCAS Topsoil Survey (Fernández-Ugalde et al., 2020) to revise in-situ information on exact land cover and soil spectra across our test sites (both accessed in March 2023).

2.4. Landsat baseline - time series with consistent probability of monthly observations

To analyze how data availability affects long-term trends for each test site we constructed an additional Landsat time series (herein Landsat-baseline), characterized by consistent probability of usable monthly observations across the complete time series. To achieve this, we selectively masked out 2015-2021 data to match respective pixel level 1984-2014 monthly probabilities of usable observations ($P_{m\_84\text{-}14}$ where m represents each month). When $P_{m\_84\text{-}14}$ was smaller than $P_{m\_15\text{-}21}$ (probability of usable data in month m for 2015-2021) we randomly masked the appropriate number observations in month m in the 2015-2021 time series to match the $P_{m\_84\text{-}14}$. Due to the different length of both time periods (32 vs. 7 years), probability of a single event in $P_{m\_84\text{-}14}$ and $P_{m\_15\text{-}21}$ differs (1/32 vs. 1/7), limiting the precision of the comparison to 0.143 (1/7).

2.5. Endmember identification

For each site we independently identified endmembers characterizing grassland ground cover i.e., green vegetation, non-photosynthetic vegetation (i.e., dry leaves, shrub twigs), soil (or rock), and shade (i.e., vegetation micro-shadowing and topographic effect). We did so based on the triangular feature space between NDVI and the ratio of SWIR bands (Guerschman et al., 2009; Kowalski et al., 2022) where pure endmembers for green vegetation (*gv*), non-photosynthetic vegetation (*npv*) and *soil* mark the vertices of the triangle. The approach has been successfully implemented for endmembers selection across diverse grassland ecosystems from savannas (Hill et al., 2017; Zhou et al., 2016), prairies (Smith et al., 2015) to temperate grasslands (Kowalski et al., 2023, 2022).

We performed the endmember selection in a semi-automatic manner. Using the location of LUCAS plots we sampled image spectra across the cross-normalized 1984-2021 time series. We used only points with cropland, grassland, and bare soil land cover, and for all sites outside the Mediterranean region we excluded the winter months (i.e., November through February) to eliminate snow-related spectral impurities. For each site we identified the green vegetation endmember as the spectra with the lowest divergence from the mean spectrum calculated from 10 spectra with the highest NDVI and the lowest SWIR ratio values. We ensured to use only *gv* spectra with the plausible physical meaning. We relied on soil spectral library from the LUCAS Topsoil Survey to identify the *soil* image endmember. From the site-specific pool of pixels with soil spectra available in the LUCAS spectral library we choose the *soil* image spectrum with the lowest RMSE from the corresponding library spectrum. We used the image endmembers over the laboratory-measured spectra to keep consistency among the SMA inputs. Finally, we selected the *npv* endmember for each site by first identifying a pool of candidates located near the npv-related vertex of point cloud in the NDVI~SWIR ratio feature space (Guerschman et al., 2009), which we approximated as an intersection between normal to the *gv-soil* line and the convex-hull of the point cloud excluding outliers (α=0.1; Kandanaarachchi and Hyndman, 2022) providing the maximum distance from the *gv-soil* line. Next, we selected the final *npv* endmember ensuring the lowest collinearity with the previously identified *gv* and *soil* endmembers (Van der Meer and Jia, 2012; results and feature spaces in Figure SA1 and Table SA3). Finally, we approximated the shade endmember with close to 0 reflectance in all spectral bands (Lewińska et al., 2021; Sonnenschein et al., 2011).

Based on the identified site-specific endmembers (Figure 2, Table SA3), we determined generalized sets of regional endmembers, specific for each biogeographical region. We did so, by selecting from all site-specific endmembers identified for each biogeographical region a set of final endmembers that ensured the lowest collinearity (Van der Meer and Jia, 2012). Since the Boreal region was represented only by the SE site, we used it as representative for the region (Table SA3). We used the generalized sets to mimic SMA analyses where endmembers are adopted from other studies or sites that share different levels of spectral similarity to the target area.

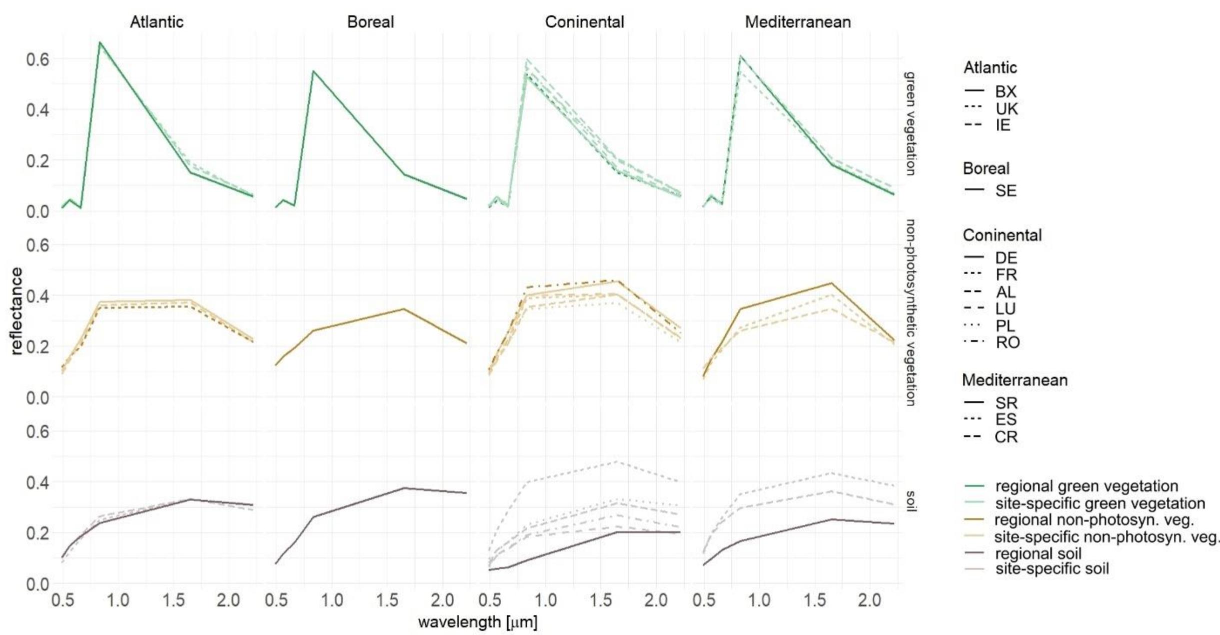

Figure 2 Spectra of green vegetation, non-photosynthetic vegetation, and soil endmembers identified across all the test sites and grouped by biogeographical regions. Line types legends are region-specific.

2.6. *Cumulative Endmember Fractions*

We based our analyses on CEFs – i.e., growing-season sums of green vegetation, non-photosynthetic vegetation, and soil ground cover fractions (Lewińska et al., 2021, 2020). In line with our objectives, we derived CEF time series for each site by running SMA using the site-specific set of endmembers and all generic sets representing regions (five SMA runs for each site, except SA and SE where site-specific and regional sets were identical hence only four SMA runs sufficed). We evaluated the SMA results derived using site-specific and regional endmembers following the commonly used protocol of comparing them against pixel-level abundances of ground cover fractions derived through a visually interpreted very-high-resolution data available in Google Earth Pro (data accessed February-July 2024) (Kowalski et al., 2022; Lobert et al., 2024; Okujeni et al., 2024; Schug et al., 2024). We allowed for no more than two days of temporal differences between the Landsat and Sentinel-2 acquisitions used in SMA and the very-high-resolution datasets used for evaluation (Table SA4). To ensure representation of the complete 0-100% cover range for *gv*, *npv*, and *soil* ground cover fractions, we used stratified random sampling with mutually inclusive 10%-wide fractional cover strata, resulting in between 25 and 49 validation points for each site. The visual interpretation was performed by four independent interpreters, with one operator evaluating all the points and three remaining experts cross-evaluating four points across the selected site (Figures SA2-14).

Each resulting time series of endmembers was next interpolated using Radial Basis Function (RBF; Schwieder et al., 2016) parametrized for 16-day interpolation steps and independently executed for two sets of recursive gaussians with width of 8, 16, and 32 days, and 16, 48, and 96 days, respectively. For runs combining Landsat and Sentinel-2 time series we downscaled needed Sentinel-2 bands to 30 m using point spread function. We carried out the aforementioned processing in the Higher-Level Processing System of FORCE (Figure 3).

For each site, each endmember set, and each considered time series variant we derived respective endmember-specific time series of monthly composites. The monthly compositing window provided a good tradeoff between spatio-temporal data availability (Figures SB1-13) and desired temporal resolution (Lewińska et al., 2024b). We used RBF-interpolated time series to sequentially fill in data gaps, giving priority to the results derived with narrow filter's width. Whenever possible, we used the original unmixing values to derive monthly composites, and when more than one observation was available, we used the set of endmembers with the lowest unmixing RMSE (Figure 3).

To determine the per-pixel growing season period required for the CEFs, for each site we ran the Polynomial Spline Models (Mader, 2012) on the *gv* time series derived using the site-specific set of endmembers. To account for inter-annual and systematic changes for each pixel, we identified the overall start and end of the season dates as the 25th and 75th percentile of their specific 1984-2021 date distribution, respectively. Finally, we re-casted the start and end of season dates to monthly intervals, including a month into the growing season only when it comprised at least 15 days of the growing season (14 for February). We next masked the time series of monthly endmembers accordingly and summed up the growing season observations to derive CEFs time series (Figure 3). For better interpretability, we rescaled the CEF values from 0 to 100, preserving the constrain on the sum of CEFs for all ground cover fractions in each year to total to 100.

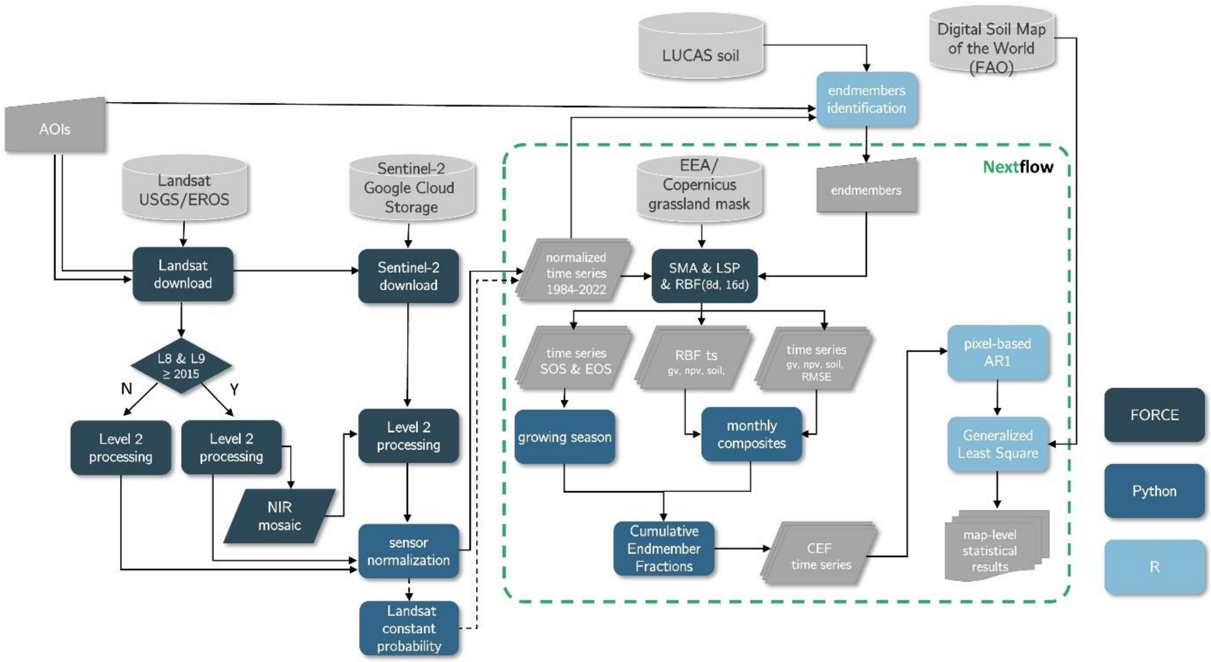

Figure 3 Analysis workflow.

2.7. *Long-term trend analyses*

To derive per-pixel time trends in CEFs we used autoregressive (AR(1)) trend model implemented in the R package remotePARTS (Morrow and Ives, 2023) which accounts for temporal autocorrelation in the time series (Ives et al., 2022, 2021). We evaluated map-level significance of respective trends with Generalized Least square Regression (GLS) while accounting for spatial autocorrelation (Ives et al., 2022, 2021), which we estimated independently for each site and each endmember in all datasets. Furthermore, we tested for the relation of soil type on trends at the map-level (Figure 3). To mitigate for reduced statistical power arising from high correlation between adjacent pixels (Ives et al., 2021) and speed up the computations, we ran our GLS analyses on a subsampled datasets, taking only every 10th pixel in the x and y direction of each map (Lewińska et al., 2023). Due to the CEFs' rescaling, the trend slope results indicate the percentage point change for one year.

2.8. Analyses design

To address our research questions, we broke down the analysis into two parts. In the first part we examined how data density (RO i) and joint use of Landsat and Sentinel-2 data archives (RO ii) affect 1984-2021 trends in grassland ground cover fractions (i.e., *gv*, *npv*, and *soil*). Accordingly, we evaluated 1984-2021 AR(1) trends derived from Landsat, Landsat-baseline, and combined Landsat and Sentinel-2 time series for each test site using only site-specific sets of endmembers. We compared pixel-level trend maps, density distribution of trend slopes (Kolmogorov-Smirnov test), and map-level trends.

In the second part of the analysis, we evaluated the impact of endmember definitions on long-term trends (RO iii). Here, we used only the Landsat time series, and for each site we compared results derived using local- and regional sets of endmembers. Specifically, we compared pixel-level trends, distribution of trend slopes (Kolmogorov-Smirnov test), and the overall map-level trends, as well as map-level effect of soil types on trends. We selected the soil-related covariate because soil had the greatest spectral variability across our study region.

To orchestrate execution of post-processing- and analysis-related parts of our workflow (Figure 3) we used the scientific workflow management system Nextflow (Di Tommaso et al., 2017). Nextflow allows to seamlessly integrate all the steps implemented in different processing environments and scripting languages into a single workflow, represented by a directed acyclic graph. This made our workflow easy to reuse and considerably enhanced reproducibility of the analyses, which was advantageous given the repetitive character of the comparison-based design.

3. Results

3.1. Landsat-baseline

Across all the sites, the probability of deriving a usable Landsat-based monthly composite was greater in 2015-2021 than in 1984-2014 (Figure 4). Our Landsat-baseline time series mitigated this disparity ensuring comparable probabilities of monthly composites before and after 2015 (Figure SB14). As expected, during both examined periods probabilities of usable monthly composites varied among the sites and months. The overall data availability at the three Mediterranean sites was high with lower chances of successful monthly composites during the winter months coinciding with local peaks in green vegetation due to higher precipitation and thus also higher cloud cover. The probability of successful monthly composites at the IE and UK sites was moderate. Interestingly, the IE site showed the lowest data availability in December-January and in summer. For the remaining sites probability of successful monthly composites followed a typical phenological cycle, with low data probability during winter and high data probability in summer. At the BX, FR, LX, and RO sites we noted small decreases in data availability during spring. Overall, across the 13 sites, high and low data availability coincided with different phenological phases and ground cover development (Figure 4).

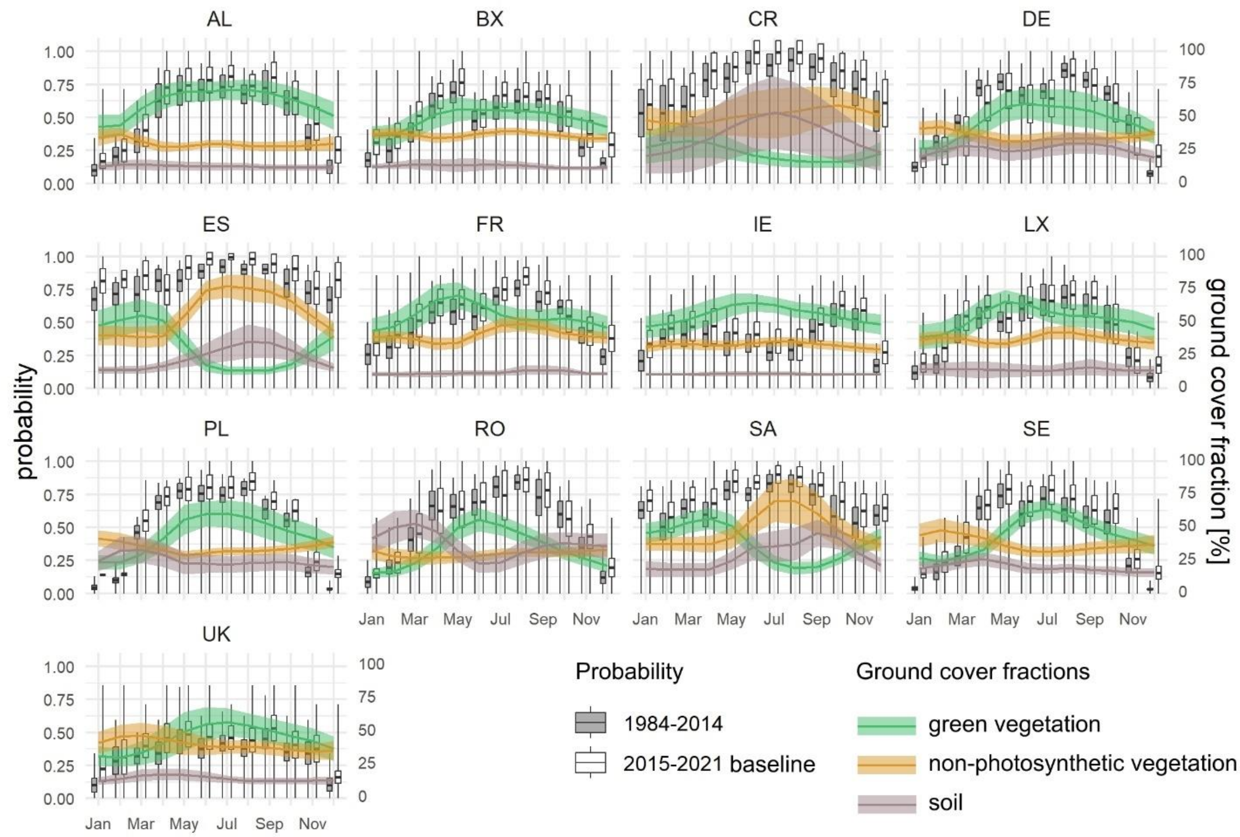

Figure 4 Monthly mean probabilities (± standard deviation) of usable Landsat observations for the 1984-2014 and 2015-2021 time periods on a backdrop of mean (± standard deviation) monthly green vegetation, non-photosynthetic vegetation, and soil fractions. Site codes correspond to Figure 1. Probabilities for Landsat-baseline time series in Figure SB14.

3.2. Impact of time series density on trends

The density of the time series had limited impact on the long-term trends in grassland ground cover CEFs at the 13 test sites (Table 1). The maps of pixel-level trends derived based on Landsat-baseline, Landsat, and combined Landsat and Sentinel-2 time series were visually undistinguishable (Figure 5, Figures SC1-12) with small but mostly significant absolute differences in the density distribution of slope across all test sites and ground cover fractions (Table SC1). Furthermore, the range of spatial autocorrelation derived for each ground cover fraction using Landsat-baseline, Landsat, and combined Landsat and Sentinel-2 time series was also very similar across all the sites (Table SC2).

For the majority of sites, the map-level trends in ground cover fractions were, again, remarkably similar across all three analyzed time series (Table 1) with comparable trend slopes, slope standard errors, and p-values. However, we noted a few exceptions. For example, combining Landsat and Sentinel-2 data resulted in a significant negative trend in *npv* at the SA site. Moreover, Landsat-baseline time series produced map-level trends opposing the results derived for the Landsat and combined Landsat and Sentinel-2 datasets for *gv* at the AL and RO sites, with, respectively, insignificant and significant and positive trends. We noted the greatest differences in map-level trends for the LX site (Table 1), where using only Landsat acquisitions resulted in a negative significant trend in *gv*, while combining Landsat and Sentinel-2 led to negative significant trends in *npv* and *soil* ground cover fractions. These disparities were even visible in the pixel-level maps (Figure 5).

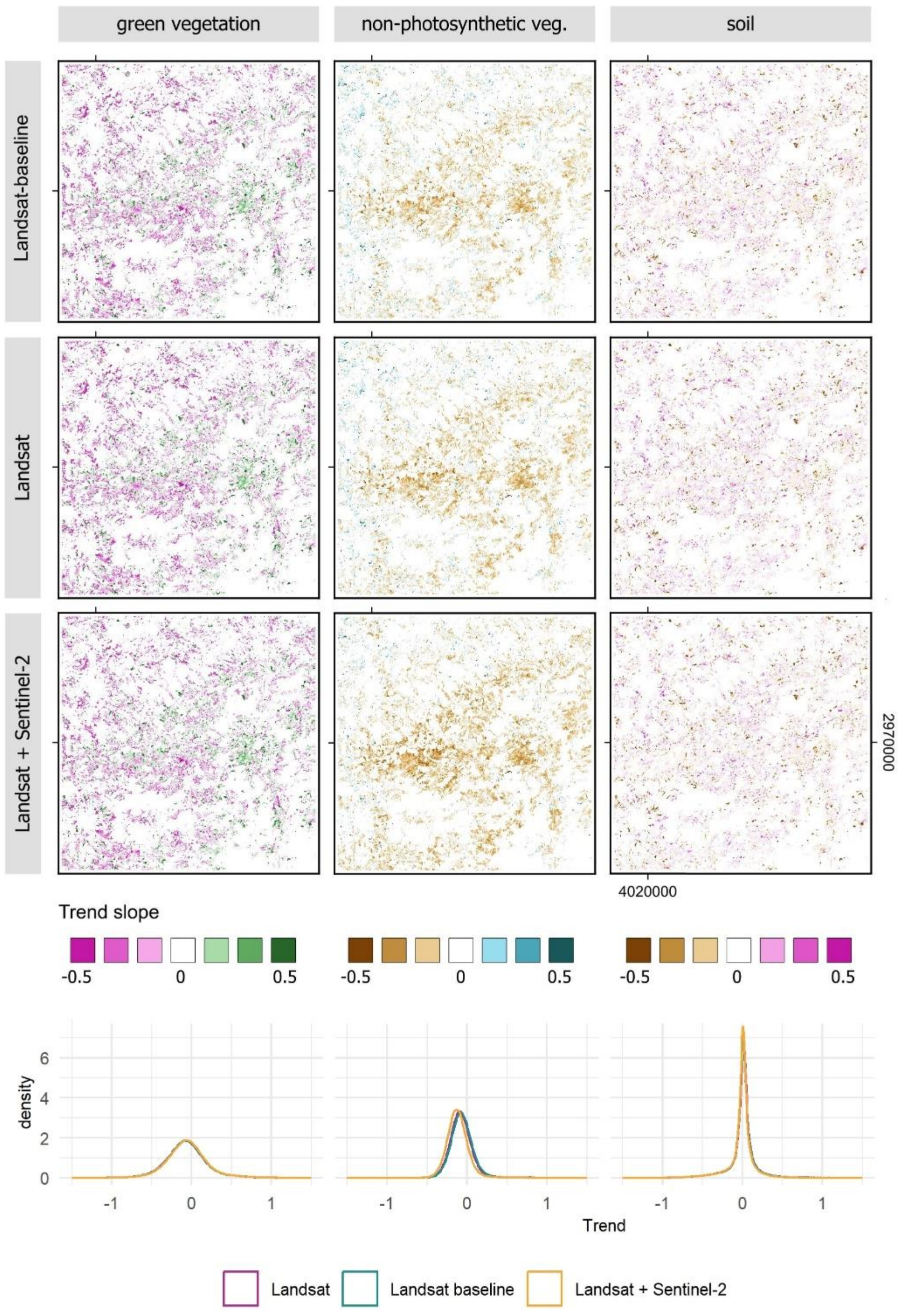

Figure 5 Slope (in percentage point) of long-term trends in green vegetation, non-photosynthetic vegetation, and soil ground covers derived for the LX test site using 1984-2021 time series of Landsat-baseline, Landsat, and combined Landsat and Sentinel-2. Density distribution of respective trend slope values below the maps. Other test sites in Figures SC1-12. Comparison among density distribution of slopes based on the Kolmogorov-Smirnov test in Table SC1.

3.3. *Impact of endmember definitions on trends*

Endmember definitions of grassland ground covers had a substantial impact on the pixel- and map-level (Table 2) trends in Landsat-based CEFs across all the test sites, with the *gv* being the most robust. Already the maps of pixel-level trends revealed great differences among trends in *npv* and *soil* ground covers obtained using different endmembers sets (Figure 6, Figures SC13-24), which was further supported by formal comparison among the density distributions of trend slopes (Table SC3). In many cases, the differences were limited to the steepness of the trend slope (e.g., AL, BX, FR, IE, PL, SE), but in some areas different sets of endmembers produced trends with contrasting directions (e.g., CR, DE, ES, LX, RO, SA, UK). The long-term trends in *npv* and *soil* CEFs were most prone to change direction depending on the endmembers used for the unmixing. Trends calculated for *gv* ground cover fractions showed, typically, limited, yet statistically significant, variability related to the endmembers' definition (Table SC3).

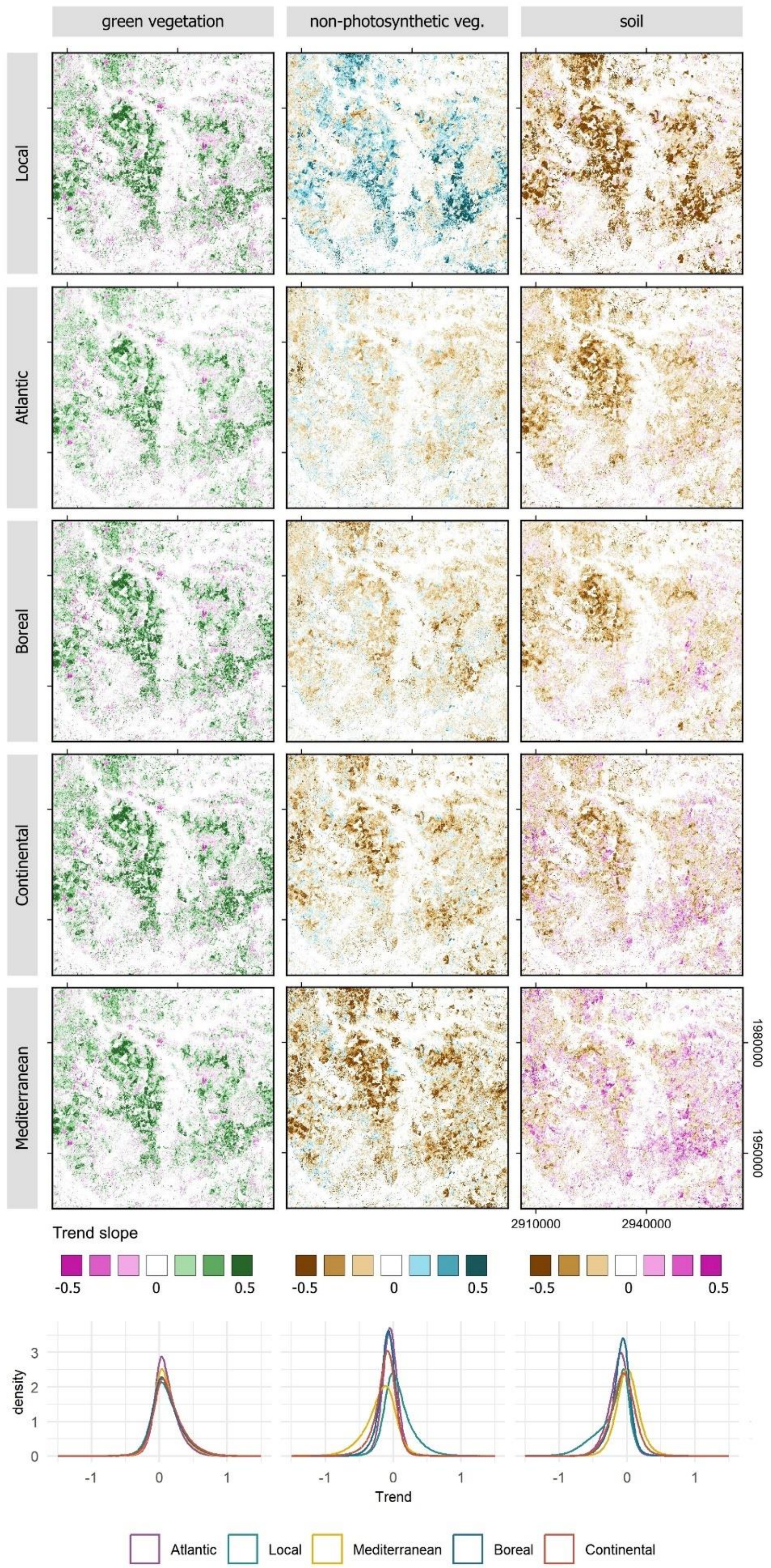
green vegetation
non-photosynthetic veg.
soil
Local
Atlantic
Boreal
Continental
Mediterranean
1980000
1950000
2910000
2940000
Trend slope
-0.5
0
0.5
-0.5
0
0.5
-0.5
0
0.5
density
3
2
1
0
-1
0
1
Trend
Atlantic
Local
Mediterranean
Boreal
Continental

Figure 6 Slope (in percentage point) of long-term trends in green vegetation, non-photosynthetic vegetation, and soil ground cover fractions derived for the ES test site using 1984-2021 time series of Landsat data using different sets of endmembers. Endmembers' definitions in Figure 2. Comparison among density distribution of slopes based on the Kolmogorov Smirnov test in Table SC3.

The relation between the range of spatial autocorrelation in the time series of CEFs and the endmember definitions was limited (Table SC4). For *gv* the range of spatial autocorrelation at each site was almost identical across the different endmember sets, with only the ES site fostering a bit wider range (between 45 and 53 km). Site-specific ranges of spatial autocorrelation in *soil* time series were more disperse but mostly diverged by no more than 10 km. The greatest disparity occurred, again, at the ES site where the *soil*-specific autocorrelation range was ~25 km for the local set of endmembers, whereas all the other sets indicated ranges between 60 and 73 km (Table SC4). We detected the greatest differences in ranges of spatial autocorrelation for the *npv*. For the majority of sites, i.e., AL, BX, CR, IE, LX, PL, RO, SA, and UK the absolute divergence in the detected ranges were below 5 km, whereas for DE, ES, FR, and SE sites, the range varied by up to 13 km.

The use of different endmember definitions led to divergences in the map-level trends derived for each test site. We observed discrepancies in the direction of trends (i.e., negative vs. positive), significance level, and the combination of both (Table 2). Long-term trends in *gv* were mostly unsusceptible to the respective endmember definitions. We noted divergences between results derived using different endmembers only at the CR and SA sites. While at the CR site the Local, Mediterranean, and Boreal endmember sets yielded negative insignificant trends, Atlantic and Temperate sets suggested insignificant increase in *gv*. At the SA site, all sets but Temperate indicated negative map-level change in *gv*, though all these trends were insignificant (Table 2).

The map-level trends detected for *npv* revealed slightly higher on-site diversity among different endmembers sets (Table 2). At the ES site, using Boreal and Temperate endmembers led to significant negative map-level changes, while Atlantic and Mediterranean endmember sets produced insignificant negative trends. Application of the Local ES set of endmembers resulted in a positive but insignificant map-level trend. Similarly, at the LX site, the Local set of endmembers yielded negative but insignificant map-level changes, which contrasted with the negative significant trends obtained for all the remaining endmembers sets. Simultaneously, at the SE site use of the Atlantic- and Temperate-specific endmembers led to significant map-level increase in *npv*, while Mediterranean and Local/Boreal endmembers resulted in insignificant and marginally positive and negative trends, respectively. Across the remaining sites our analyses revealed significant decreasing map-level trends in *npv*. Only the CR site was characterized by a significant increase in *npv*, whereas trends in PL were also positive but insignificant.

Differences in the endmember sets affected the most map-level trends in the *soil* ground cover fraction (Table 2). Significant map-level positive and negative long-term trends were present at CR, DE, IE, and UK sites, however only at the DE and IE sites significant results were obtained for the Local endmembers sets. For the AL, BX, FR, LX, and RO sites we detected at least one map-level significant trend indicating increase in presence of the *soil* ground cover fraction, although only for the AL sites the results were uniformly significant across all endmember sets. For the ES and PL sites different endmember sets led to positive and negative changes though the map-level trends were always insignificant. Finally, only at the SA and SE sites we detected significant negative map-level trends, with all trends at the SE site uniformly significant, yet showing different slope values.

The effect of soil type on trends in ground cover fractions was limited. The map-level trends in *gv* identified for 13 dominant soil types across all the test sites were mostly positive and significant, and comparable for each soil type among all five endmember sets (Table SC5). The effect of soil type on trends in *gv* was significant for the results derived using all regional endmember sets. The map-level trends in *npv* were predominantly negative and significant, and like for *gv* the specific soil types fostered analogous values across different endmember sets (Table SC6). Again, all the results derived using different regional endmember sets fostered a significant effect of soil type on map-level trends (Table SC6). Map-level trends in *soil* had the greatest variability among different endmember sets we tested (Table SC7). Soil type had a significant effect on map-level trends in *soil* fraction only for the Mediterranean, Boreal, and site-specific endmember sets. However, while for the local endmembers, the trends derived for each soil type were mostly insignificant, the application of the Mediterranean or Boreal sets resulted in mostly positive significant trends.

4. Discussion

Analyses of long-term changes in Earth's land cover are central for multiple applications and allow us to identify the causes and directions of future developments through statistical modeling. Yet, the impact of irregular data density on time trend analyses is still not fully explored. Similarly, the impact of endmember definitions used in SMA-based large-area studies of long-term trends in ground cover fractions is also uncharted. Both could obscure true changes detected through unmixing-based long-term analyses, potentially leading to erroneous conclusions about the ongoing processes. Our analysis evaluated both of the aforementioned aspects. We based our study on annual CEFs calculated from monthly composites facilitated with RBF filtering, which adheres to data processing approaches used in vegetation-related studies and trend analysis (Frantz et al., 2022; Gong et al., 2015; Hobi et al., 2017; Kong et al., 2019; Lewińska et al., 2023). Our results indicate that the data density of the underlying time series has a limited impact on the pixel- or map-level trends when using cumulated fractions. Conversely, the use of different endmember definitions for the 'classical' SMA leads in some regions to significantly different pixel- and map-level long-term trends. Consequently, our results raise awareness and concern for aptness of large-scale analyses employing a single set of endmembers for the 'classical' SMA, showing that the results are dependent on the used definitions of endmembers.

4.1. Impact of time series density on trends

Our results demonstrated that the long-term trends in the ground cover fractions in grasslands were rather consistent under all three data density scenarios. Neither the more frequent Landsat data record after 2014 coinciding with the operational phase of Landsat 8, nor enhancing the Landsat data record with Sentinel-2 acquisitions after 2016 significantly altered the results. Overall, despite often statistically significant differences among the distribution of trend slope values obtained for three considered time series, the pixel-level trends agreed on the direction and magnitude of the changes and the map-level trends revealed largely similar values at comparable significance levels. Among the few exceptions most of the differences in map-level trends were limited to the preserved change direction but with the divergent significance levels (i.e., trends in *gv* at AL, LX, and RO sites, in *npv* at the LX site, in *soil* at the SA site).

The average revisit period of <5 days when considering Landsat and Sentinel-2 satellites together (Jia et al., 2024), increases the probability of usable acquisitions during the typically more cloudy months (Lewińska et al., 2024b). Consequently, while before 2014 the satellite observations for these time windows were often missing and thus needed to be augmented using the RBF filter, the respective monthly composites after 2014 were more likely to include actual satellite acquisitions. This explains marginally greater *gv* pixel-level trends at CR and SA sites and lower pixel-level *gv* trend values at the AL, BX, DE, PL, RO, SE, and UK sites. On the one hand, for the Mediterranean sites, the green peak coincides with the wet season thus lowering the probability of clear-sky observations. Any actual data acquisition during this period is likely to reveal abundant green vegetation fraction, consequently driving the *gv* CEF up. On the other hand, lower than predicted with RBF *gv* values observed during the vegetation onset and senescence time at the selected Atlantic and Continental sites lead to a decrease in the *gv* CEF, leading to marginally lower trends. An analogous, explanation can be applied to *npv*, which for the combined time series of Landsat and Sentinel-2 data revealed slightly greater pixel-level trend values at CR, ES, and SE sites and marginally lower pixel-level *npv* trends at BX, FR, IE, LX, PL, and SA sites.

Our results showed limited differences in pixel- and map-level trends derived based on time series with different data densities. The study thus confirms a lack of systematic bias and lends credibility to trend analyses based on annual or seasonal aggregates calculated from monthly composites derived using Landsat and combined Landsat and Sentinel-2 data archives. However, the validity of this conclusion is conditional on certain conditions. Importantly, the density of the satellite observations must be sufficient and data augmentation needs to be apt but not over-extensive. Due to sometimes far-reaching spatial and temporal variability in availability of the usable satellite observations, trend analyses over some regions and based on selected compositing periods are susceptible to being heavily conditioned by the data interpolation, putting into question the credibility of the results. For Europe, monthly composites ensure, overall, a good tradeoff between 1984-2021 data availability and temporal resolution suitable for vegetation phenology-related analyses (Lewińska et al., 2024b).

Furthermore, the RBF-based data augmentation approach also ensures reliable data interpolation, which is in essence comparable to other frequently used data interpolation methods such as the Savitzky-Golay filter (Chen et al., 2004), which has a long-standing history of use in enhancing time series of remotely sensed data.

Arguably, the relative coarseness of the monthly composites we used for CEFs combined with the aggregative character of the CEFs might obscure some of the short-term variability in ground covers, and 'stabilize' the time series. Generalization is a common feature in long-term trend analyses based on temporally equidistant composites but also concerns algorithms that rely on all available observations and mathematically deconstruct a time series into a seasonal, trend, and residual components, thus neglecting more subtle changes (e.g., BFAST: Verbesselt et al., 2010, BEAST: Zhao et al., 2019, DRMAT: Li et al., 2024). However, approaches based on temporal aggregation and decomposition provide much more comprehensive insight into vegetation conditions than trend analyses based on annual (Chen et al., 2019; Cortés et al., 2021; Zhang et al., 2017) or seasonal (Eisfelder et al., 2023) means, seasonal maxima (Bayle et al., 2024; Sulla-Menashe et al., 2016) or single numerical measures (Yan et al., 2022). Importantly, trends captured with each of above-mentioned methods reflect on different vegetation characteristics and may lead to different results.

To inspect the impact of compositing window on CEFs we compared CEFs calculated based on monthly and 10-day composites. Because monthly composites are the shortest time window feasible for pan-European analyses based on the complete Landsat data archive (Lewińska et al., 2024b) we restricted our comparison to 2016-2021. Results derived for the CR and DE sites confirmed very strong agreement between both measures (Supplement D), though the impact of respective endmember definition should not be neglected. We are hence confident our CEFs based on monthly composites processed with PARTS are robust and at the same time sensitive to monthly variability in the observed ground cover fractions, and thus suitable for long-term trend analyses.

Finally, although the period characterized by the increased data availability is relatively short (i.e., six years - 2015-2021), it is long enough to alter long-term trends if such an underlying effect occurs. Even when using the autoregressive trend analyses that account for temporal autocorrelation in the time series, the change in the CEF arising from the systematic change in the underlying data availability would have an abrupt character but persist after the breakpoint thus having a limited autocorrelation component (Ives et al., 2021). However, although our analyses indicate that data density has no significant effect on trends in grassland ground cover fractions across Europe, we do not exclude the possibility that such effects exist and are significant for other geographies and other land cover measures.

4.2. Impact of endmember definitions on trends

The definition of endmembers had an important impact on pixel- and map-level trends in ground cover fractions across European grasslands. Although the pixel-level trends in *gv* showed limited variability among the different endmember sets, trends in *npv* and *soil* were much more sensitive to the changes in endmember definition. Importantly, the differences were pronounced not only when we used generalized regional endmember sets representing biogeographical regions not native to a specific site (e.g., DE, IE, LX, and RO sites), but also when we used generalized endmember sets comprising endmembers identified within the same biogeographical region but outside the specific area of interest (e.g., CR, DE, ES, FR, PL, SA, and UK). The limited transferability of spectra is not surprising (Schug et al., 2024), especially concerning the wide variability of soil spectra identified across the test sites (Figure 2) fostered by soil type and vegetation variability (Figure 1).

The pixel-level differences in trends translated further into map-level statistics. While the application of different endmember sets for *gv* and *npv* did not change the direction of the significant map-level trends, we noted that at the CR, DE, IE, RO, SA, and UK sites, long-term significant map-level trends in *soil* were either positive or negative depending on the respective endmember set used. Although in some cases it is feasible to exclude the potentially spurious results based on the independent SMA evaluation following commonly used protocols (Kowalski et al., 2022; Okujeni et al., 2024; Schug et al., 2024; e.g., Figures SA4 and 11), in other instances evaluation can be ambiguous (e.g., Figure SA5, 8, 12, and 14), which is a common dispute in complex environments (Lobert et al., 2024). Furthermore, even if the direction of trends across all ground cover fractions remained constant across different endmember sets, the magnitude and significance levels often varied. Consequently, these findings challenge the validity of long-term trends in ground cover fractions derived over heterogeneous regions using the 'classical' SMA approach, especially where endmembers were adopted from different studies or regions.

Two aspects play a critical role in the aptness of the 'classical' SMA for consistent quantification of ground cover fractions: i) how well do the chosen endmembers compare against the spectral variability within the target ground cover fractions (here *gv*, *npv*, and *soil*) across the area of interest; and ii) how good is the spectral separability of endmembers representing each target ground cover fraction. Our analyses demonstrated expected considerable spectral variability of the *soil* endmembers across Europe, which aligns well with previous studies (Broeg et al., 2024; Fernández-García et al., 2021; Kowalski et al., 2023; Lobert et al., 2024; Safanelli et al., 2020). Furthermore, *npv* and *soil* spectra, as depicted by Landsat and Sentinel-2 spectral bands, have, in general, high collinearity arising predominantly from the omission of the lignocellulose absorption maxima in the SWIR bands (Dennison et al., 2023;

Hively et al., 2021; Verrelst et al., 2023). This lack of distinctive spectral features can hamper clear separation between both ground cover fractions when relying on multispectral scanners (Asner and Heidebrecht, 2002; Verrelst et al., 2023). Although in some studies and geographies affinity between *soil* and *npv* spectra is less pronounced and allows for successful separation (Guerschman and Hill, 2018; Hively et al., 2021; Zheng et al., 2019) and even intra-annual variability of soil properties does not necessarily affect the results (Guerschman et al., 2015), it is not the case in the broad-scale, European context.

To overcome limitations of the 'classical' SMA, other variants, enhancements, and approaches offer important improvements for addressing high spectral intra-class variability and limited spectral separability of the ground cover fractions. For example, Multiple Endmember Spectral Mixture Analysis (MESMA; Roberts et al., 1998) enables multiple spectra to represent each targeted ground cover to ensure better identification of local conditions (Converse et al., 2021; Fernández-García et al., 2021). Concomitantly, approaches based on synthetic mixing of endmembers representing the spectral variability of each target ground cover into extensive training data sets that feed into a regression model (Okujeni et al., 2013) allow for extensive generalization, fostering robustness even in complex and heterogeneous landscapes (Okujeni et al., 2021, 2017; Senf et al., 2020; Suess et al., 2018). Moreover, the synthetic mixing-based approach ensures temporal stability of ground cover estimates (Okujeni et al., 2024) sufficient for trend analyses (Stanimirova et al., 2022). Further improvement in the accuracy of unmixing results can be achieved by regional stratification of data according to soil spectral behavior (Lobert et al., 2024). Such soil-specific unmixing enables pixel-specific signatures not only accounting for spectral variability within a studied region, but also guarantees the use of appropriate endmembers and thus creates more accurate results. Overall, these alternative approaches for estimating ground cover fractions offer much greater adaptability and stability than the 'classical' SMA, which is desired in complex landscapes. However, these alternative approaches have considerably higher entry barriers arising from their methodical complexity, demands of spectral databases, greater costs in computation power, and lower algorithm availability in established cloud environments, which might be difficult to overcome for inexperienced users. Consequently, the straightforwardness of the 'classical' SMA combined with its easy implementation explain why the method is still used.

Excitingly, some of the new and upcoming environmental satellite missions have been designed to ensure better separability between soil and non-photosynthetic vegetation. For example, current hyperspectral satellite missions, such as PRISMA (Cogliati et al., 2021) and EnMAP (Chabrillat et al., 2024; Guanter et al., 2015; Storch et al., 2023) offer unprecedented ability to identify and distinguish between different materials and ground cover fractions thanks to a wide range of narrow spectral bands. However, today's limited spatial and temporal coverage inhibit operational applications. Future operational hyperspectral satellite mission like CHIME (Buschkamp et al., 2023; Nieke and Rast, 2018) and SBG (Cawse-Nicholson et al., 2021) are currently in development and aim to overcome these limitations. Importantly, also forthcoming Landsat Next will incorporate new bands specifically designed to monitor non-photosynthetic vegetation (Hively et al., 2021) allowing for wall-to-wall coverage. Similarly, the ongoing consultations on Sentinel-2 NG also foresee additional SWIR bands. Although the future of spectral unmixing looks exciting, the long-term analyses of ground cover fractions will remain challenging due to the limitations inherited from the historical missions.

5. Conclusions

Our analyses clarified two important questions related to long-term trend analyses of ground cover fractions derived based on the 'classical' SMA. Firstly, when using CEFs we demonstrated the absence of a systematic bias in trends arising from variable data density across the complete 1984-2021 Landsat data record and from the surplus of acquisitions after 2016 when the Landsat and Sentinel-2 data are processed jointly. This finding, valid at the pixel- and map-level and in the context of Europe-specific data availability, lends credibility to the analogously processed long-term change analyses based on Landsat and Sentinel-2 composites. Moreover, validity of these results extends to all annual aggregates based on equidistant composites. Secondly, we showed that due to inherent limited spectra separation and generalization capabilities, the 'classical' SMA can produce suboptimal and even erroneous pixel- and map-level trend results across heterogeneous landscapes. Although *gv* trends demonstrated robustness against changes in endmember definition, trends in *npv* and *soil* were very sensitive to the changes. Therefore, we acknowledge great utility of the 'classical' SMA, its clear design and accessibility, but consider this approach being suboptimal for many remote-sensing-based applications across broader scales or in heterogenous landscapes. Consequently, we caution users against using SMA in analyses addressing large areas and regions characterized by considerable variability of ground cover fractions. Instead, we recommend using unmixing approaches with greater spatial and spectral generalization capabilities, preferably further enhanced with spatial stratification and pixel-specific endmember signatures.

Acknowledgements

The research presented in this paper was funded by the Deutsche Forschungsgemeinschaft (DFG, German Research Foundation) – Project-ID 414984028 – SFB 1404 FONDA. This research contributed to the Landsat Science Team 2018–2023.

Table 1 Overall map-level trends in green vegetation (gv), non-photosynthetic vegetation (npv), and soil CEFs derived based on Landsat and Sentinel-2 data. Respective ranges of autocorrelation in Table SC2.

Test site	Time series	gv				npv				soil			
		Slope	Slope SE	t-val	p-val	Slope	Slope SE	t-val	p-val	Slope	Slope SE	t-val	p-val
AL	Landsat	-0.037	0.012	-3.223	0.001	-0.077	0.008	-9.741	0.000	0.034	0.002	18.184	0.000
	Landsat-baseline	-0.012	0.010	-1.165	0.244	-0.079	0.007	-11.069	0.000	0.033	0.002	18.467	0.000
	Landsat + Sentinel-2	-0.066	0.011	-6.056	0.000	-0.077	0.009	-8.937	0.000	0.039	0.002	23.036	0.000
BX	Landsat	0.066	0.014	4.676	0.000	-0.195	0.014	-14.085	0.000	-0.004	0.007	-0.525	0.599
	Landsat-baseline	0.085	0.012	6.827	0.000	-0.182	0.013	-13.985	0.000	-0.001	0.007	-0.180	0.857
	Landsat + Sentinel-2	0.054	0.013	4.284	0.000	-0.235	0.012	-20.141	0.000	-0.007	0.006	-1.123	0.261
CR	Landsat	-0.025	0.077	-0.330	0.741	0.057	0.008	7.162	0.000	-0.043	0.026	-1.641	0.101
	Landsat-baseline	-0.020	0.046	-0.428	0.668	0.074	0.010	7.382	0.000	-0.024	0.035	-0.671	0.502
	Landsat + Sentinel-2	-0.018	0.072	-0.244	0.807	0.083	0.011	7.576	0.000	-0.083	0.052	-1.593	0.111
DE	Landsat	0.124	0.064	1.944	0.052	-0.214	0.035	-6.164	0.000	0.094	0.034	2.798	0.005
	Landsat-baseline	0.084	0.054	1.563	0.118	-0.263	0.020	-13.344	0.000	0.092	0.033	2.827	0.005
	Landsat + Sentinel-2	0.095	0.068	1.403	0.161	-0.231	0.035	-6.564	0.000	0.092	0.028	3.239	0.001
ES	Landsat	0.087	0.184	0.472	0.637	0.043	0.104	0.411	0.681	-0.184	0.108	-1.707	0.088
	Landsat-baseline	0.080	0.171	0.467	0.640	0.047	0.103	0.460	0.646	-0.177	0.106	-1.663	0.096
	Landsat + Sentinel-2	0.067	0.154	0.431	0.666	0.078	0.082	0.946	0.344	-0.187	0.115	-1.623	0.105
FR	Landsat	-0.031	0.035	-0.886	0.376	-0.089	0.014	-6.539	0.000	-0.013	0.013	-0.970	0.332
	Landsat-baseline	-0.028	0.036	-0.770	0.441	-0.073	0.014	-5.345	0.000	-0.011	0.013	-0.835	0.404
	Landsat + Sentinel-2	-0.026	0.032	-0.796	0.426	-0.115	0.014	-8.205	0.000	-0.020	0.015	-1.379	0.168
IE	Landsat	0.151	0.012	12.606	0.000	-0.159	0.008	-19.794	0.000	-0.011	0.001	-12.157	0.000
	Landsat-baseline	0.153	0.011	13.708	0.000	-0.152	0.008	-18.915	0.000	-0.012	0.001	-12.414	0.000
	Landsat + Sentinel-2	0.143	0.012	11.709	0.000	-0.170	0.010	-17.822	0.000	-0.012	0.001	-14.137	0.000
LX	Landsat	-0.097	0.049	-1.963	0.050	-0.032	0.043	-0.753	0.452	0.002	0.006	0.290	0.772
	Landsat-baseline	-0.090	0.047	-1.906	0.057	-0.019	0.042	-0.454	0.650	0.000	0.005	0.013	0.990
	Landsat + Sentinel-2	-0.077	0.046	-1.687	0.092	-0.075	0.037	-2.011	0.044	-0.013	0.004	-2.979	0.003
PL	Landsat	0.380	0.097	3.924	0.000	0.005	0.117	0.045	0.964	0.044	0.075	0.589	0.556
	Landsat-baseline	0.411	0.105	3.905	0.000	-0.007	0.109	-0.066	0.947	0.039	0.072	0.538	0.591
	Landsat + Sentinel-2	0.361	0.115	3.155	0.002	-0.003	0.115	-0.028	0.978	0.040	0.067	0.601	0.548
RO	Landsat	0.072	0.039	1.847	0.065	-0.138	0.017	-8.265	0.000	-0.020	0.049	-0.411	0.681
	Landsat-baseline	0.101	0.038	2.676	0.007	-0.141	0.017	-8.381	0.000	-0.026	0.049	-0.527	0.598
	Landsat + Sentinel-2	0.045	0.034	1.309	0.190	-0.142	0.015	-9.195	0.000	-0.033	0.051	-0.653	0.514
SA	Landsat	-0.005	0.026	-0.211	0.833	-0.143	0.035	-4.142	0.000	-0.016	0.018	-0.868	0.385
	Landsat-baseline	-0.014	0.024	-0.573	0.567	-0.136	0.032	-4.186	0.000	-0.002	0.017	-0.106	0.916
	Landsat + Sentinel-2	0.018	0.027	0.674	0.500	-0.166	0.042	-3.951	0.000	-0.069	0.023	-2.989	0.003
SE	Landsat	0.103	0.020	5.142	0.000	-0.002	0.018	-0.092	0.927	-0.064	0.012	-5.485	0.000
	Landsat-baseline	0.134	0.018	7.583	0.000	-0.013	0.018	-0.697	0.486	-0.051	0.011	-4.474	0.000
	Landsat + Sentinel-2	0.058	0.019	3.003	0.003	0.001	0.015	0.081	0.936	-0.089	0.011	-8.201	0.000
UK	Landsat	0.195	0.021	9.288	0.000	-0.227	0.018	-12.500	0.000	0.026	0.019	1.361	0.174
	Landsat-baseline	0.211	0.017	12.530	0.000	-0.234	0.015	-15.485	0.000	0.028	0.020	1.415	0.157
	Landsat + Sentinel-2	0.186	0.020	9.106	0.000	-0.244	0.015	-15.894	0.000	0.004	0.018	0.208	0.836

Table 2 Overall map-level trends in green vegetation (gv), non-photosynthetical vegetation (npv), and soil ground cover fractions derived for Landsat 1984-2021 time series using different set of endmembers. Slope – slope of the trend; slope SE, slope standard error; t-val., t-test value; p-val. Respective ranges of autocorrelation in Table SC4.

Test site	Endmembers set	gv				npv				soil			
		Slope	Slope SE	t-val	p-val	Slope	Slope SE	t-val	p-val	Slope	Slope SE	t-val	p-val
AL	Local	-0.037	0.012	-3.223	0.001	-0.077	0.008	-9.741	0.000	0.034	0.002	18.184	0.000
	Atlantic	-0.034	0.011	-3.170	0.002	-0.103	0.007	-14.119	0.000	0.026	0.002	16.788	0.000
	Mediterranean	-0.047	0.011	-4.249	0.000	-0.134	0.010	-13.612	0.000	0.097	0.007	13.299	0.000
	Boreal	-0.055	0.011	-5.032	0.000	-0.119	0.010	-11.824	0.000	0.065	0.004	14.669	0.000
	Continental	-0.039	0.012	-3.188	0.001	-0.092	0.006	-16.467	0.000	0.066	0.004	15.179	0.000
BX	Atlantic	0.069	0.015	4.456	0.000	-0.203	0.015	-13.135	0.000	-0.009	0.006	-1.501	0.133
	Local	0.066	0.014	4.676	0.000	-0.195	0.014	-14.085	0.000	-0.004	0.007	-0.525	0.599
	Mediterranean	0.043	0.014	3.148	0.002	-0.238	0.018	-13.545	0.000	0.038	0.011	3.513	0.000
	Boreal	0.052	0.015	3.411	0.001	-0.228	0.019	-12.018	0.000	0.029	0.008	3.840	0.000
	Continental	0.079	0.018	4.405	0.000	-0.167	0.011	-15.270	0.000	-0.001	0.012	-0.056	0.955
CR	Atlantic	0.002	0.004	0.582	0.561	0.197	0.004	54.789	0.000	-1.141	0.099	-11.534	0.000
	Local	-0.025	0.077	-0.330	0.741	0.057	0.008	7.162	0.000	-0.043	0.026	-1.641	0.101
	Mediterranean	-0.018	0.034	-0.535	0.593	0.444	0.011	42.171	0.000	0.201	0.021	9.648	0.000
	Boreal	-0.018	0.064	-0.278	0.781	0.201	0.030	6.638	0.000	-0.152	0.046	-3.317	0.001
	Continental	0.021	0.037	0.555	0.579	0.300	0.017	17.490	0.000	-0.077	0.010	-7.933	0.000
DE	Atlantic	0.058	0.046	1.269	0.205	-0.110	0.019	-5.761	0.000	-0.097	0.039	-2.506	0.012
	Local	0.124	0.064	1.944	0.052	-0.214	0.035	-6.164	0.000	0.094	0.034	2.798	0.005
	Mediterranean	0.076	0.048	1.607	0.108	-0.249	0.028	-8.754	0.000	0.058	0.029	2.007	0.045
	Boreal	0.082	0.059	1.396	0.163	-0.242	0.027	-9.118	0.000	0.027	0.034	0.798	0.425
	Continental	0.090	0.050	1.818	0.069	-0.128	0.011	-11.373	0.000	-0.079	0.058	-1.370	0.171
ES	Atlantic	0.076	0.126	0.605	0.545	-0.059	0.044	-1.342	0.180	-0.140	0.139	-1.006	0.314
	Local	0.087	0.184	0.472	0.637	0.043	0.104	0.411	0.681	-0.184	0.108	-1.707	0.088
	Mediterranean	0.087	0.172	0.502	0.616	-0.193	0.100	-1.920	0.055	0.010	0.061	0.168	0.867
	Boreal	0.089	0.188	0.473	0.636	-0.092	0.030	-3.015	0.003	-0.097	0.165	-0.587	0.557
	Continental	0.102	0.158	0.648	0.517	-0.120	0.059	-2.028	0.043	-0.071	0.085	-0.835	0.404
FR	Atlantic	-0.030	0.026	-1.146	0.252	-0.148	0.005	-31.073	0.000	0.031	0.029	1.055	0.291
	Local	-0.031	0.035	-0.886	0.376	-0.089	0.014	-6.539	0.000	-0.013	0.013	-0.970	0.332
	Mediterranean	-0.047	0.029	-1.658	0.097	-0.170	0.018	-9.684	0.000	0.091	0.017	5.426	0.000
	Boreal	-0.049	0.033	-1.450	0.147	-0.144	0.016	-9.109	0.000	0.055	0.025	2.165	0.030
	Continental	-0.036	0.032	-1.137	0.256	-0.136	0.005	-27.727	0.000	0.078	0.035	2.219	0.026
IE	Atlantic	0.136	0.011	12.139	0.000	-0.158	0.009	-18.463	0.000	-0.002	0.001	-2.421	0.015
	Local	0.151	0.012	12.606	0.000	-0.159	0.008	-19.794	0.000	-0.011	0.001	-12.157	0.000
	Mediterranean	0.140	0.014	10.316	0.000	-0.194	0.009	-22.228	0.000	0.041	0.007	5.499	0.000
	Boreal	0.147	0.013	11.386	0.000	-0.187	0.011	-17.414	0.000	0.036	0.005	7.774	0.000
	Continental	0.168	0.013	12.778	0.000	-0.137	0.006	-22.735	0.000	0.001	0.003	0.290	0.772

Table 2 continuation

Test site	Endmembers set	gv				npv				soil			
		Est	Slope SE	t-val	p-val	Est	Slope SE	t-val	p-val	Est	Slope SE	t-val	p-val
LX	Atlantic	-0.080	0.037	-2.196	0.028	-0.107	0.032	-3.373	0.001	0.053	0.012	4.387	0.000
	Local	-0.097	0.049	-1.963	0.050	-0.032	0.043	-0.753	0.452	0.002	0.006	0.290	0.772
	Mediterranean	-0.097	0.040	-2.433	0.015	-0.161	0.030	-5.452	0.000	0.164	0.021	7.944	0.000
	Boreal	-0.093	0.037	-2.485	0.013	-0.130	0.025	-5.210	0.000	0.092	0.017	5.506	0.000
	Continental	-0.089	0.041	-2.186	0.029	-0.119	0.022	-5.521	0.000	0.130	0.023	5.604	0.000
PL	Atlantic	0.255	0.079	3.235	0.001	0.255	0.177	1.443	0.149	-0.041	0.055	-0.752	0.452
	Local	0.380	0.097	3.924	0.000	0.005	0.117	0.045	0.964	0.044	0.075	0.589	0.556
	Mediterranean	0.316	0.105	3.020	0.003	0.043	0.135	0.317	0.751	0.071	0.085	0.837	0.403
	Boreal	0.331	0.123	2.692	0.007	0.123	0.207	0.594	0.553	0.071	0.057	1.240	0.215
	Continental	0.329	0.106	3.118	0.002	0.116	0.094	1.235	0.217	-0.012	0.074	-0.168	0.867
RO	Atlantic	0.028	0.028	1.012	0.312	-0.091	0.024	-3.782	0.000	-0.069	0.029	-2.395	0.017
	Local	0.072	0.039	1.847	0.065	-0.138	0.017	-8.265	0.000	-0.020	0.049	-0.411	0.681
	Mediterranean	0.040	0.033	1.220	0.223	-0.212	0.023	-9.123	0.000	0.060	0.037	1.640	0.101
	Boreal	0.038	0.036	1.039	0.299	-0.220	0.023	-9.648	0.000	0.057	0.028	2.053	0.040
	Continental	0.046	0.037	1.231	0.218	-0.092	0.017	-5.274	0.000	-0.073	0.047	-1.529	0.126
SA	Atlantic	-0.003	0.026	-0.102	0.919	-0.102	0.026	-3.944	0.000	-0.071	0.023	-3.092	0.002
	Local/Mediterr.	-0.005	0.026	-0.211	0.833	-0.143	0.035	-4.142	0.000	-0.016	0.018	-0.868	0.385
	Boreal	-0.006	0.027	-0.209	0.834	-0.091	0.016	-5.631	0.000	-0.065	0.021	-3.073	0.002
	Continental	0.007	0.031	0.235	0.814	-0.113	0.027	-4.119	0.000	-0.050	0.026	-1.889	0.059
SE	Atlantic	0.071	0.015	4.577	0.000	0.067	0.014	4.934	0.000	-0.144	0.018	-8.059	0.000
	Mediterranean	0.100	0.019	5.354	0.000	0.007	0.017	0.389	0.697	-0.114	0.015	-7.586	0.000
	Local/Boreal	0.103	0.020	5.142	0.000	-0.002	0.018	-0.092	0.927	-0.064	0.012	-5.485	0.000
	Continental	0.107	0.021	5.025	0.000	0.041	0.010	3.960	0.000	-0.162	0.020	-8.206	0.000
UK	Atlantic	0.167	0.018	9.142	0.000	-0.159	0.016	-9.978	0.000	-0.035	0.012	-2.975	0.003
	Mediterranean	0.167	0.017	9.836	0.000	-0.218	0.019	-11.358	0.000	0.031	0.026	1.184	0.236
	Boreal	0.180	0.019	9.539	0.000	-0.240	0.019	-12.618	0.000	0.057	0.016	3.555	0.000
	Continental	0.202	0.021	9.616	0.000	-0.124	0.012	-10.573	0.000	-0.052	0.022	-2.373	0.018
	Local	0.195	0.021	9.288	0.000	-0.227	0.018	-12.500	0.000	0.026	0.019	1.361	0.174

References

Adams, J.B., Smith, M.O., Johnson, P.E., 1986. Spectral mixture modeling: A new analysis of rock and soil types at the Viking Lander 1 Site. J. Geophys. Res. 91, 8098. https://doi.org/10.1029/JB091iB08p08098

Ali, I., Cawkwell, F., Dwyer, E., Barrett, B., Green, S., 2016. Satellite remote sensing of grasslands: from observation to management. JPECOL 9, 649–671. https://doi.org/10.1093/jpe/rtw005

Asner, G.P., Heidebrecht, K.B., 2002. Spectral unmixing of vegetation, soil and dry carbon cover in arid regions: Comparing multispectral and hyperspectral observations. International Journal of Remote Sensing 23, 3939–3958. https://doi.org/10.1080/01431160110115960

Baetens, L., Desjardins, C., Hagolle, O., 2019. Validation of Copernicus Sentinel-2 Cloud Masks Obtained from MAJA, Sen2Cor, and FMask Processors Using Reference Cloud Masks Generated with a Supervised Active Learning Procedure. Remote Sensing 11, 433. https://doi.org/10.3390/rs11040433

Bardgett, R.D., Bullock, J.M., Lavorel, S., Manning, P., Schaffner, U., Ostle, N., Chomel, M., Durigan, G., L. Fry, E., Johnson, D., Lavallee, J.M., Le Provost, G., Luo, S., Png, K., Sankaran, M., Hou, X., Zhou, H., Ma, L., Ren, W., Li, X., Ding, Y., Li, Y., Shi, H., 2021. Combatting global grassland degradation. Nat Rev Earth Environ 2, 720–735. https://doi.org/10.1038/s43017-021-00207-2

Bayle, A., Gascoin, S., Berner, L.T., Choler, P., 2024. Landsat-based greening trends in alpine ecosystems are inflated by multidecadal increases in summer observations. Ecography e07394. https://doi.org/10.1111/ecog.07394

Bellini, E., Moriondo, M., Dibari, C., Leolini, L., Staglianò, N., Stendardi, L., Filippa, G., Galvagno, M., Argenti, G., 2022. Impacts of Climate Change on European Grassland Phenology: A 20-Year Analysis of MODIS Satellite Data. Remote Sensing 15, 218. https://doi.org/10.3390/rs15010218

Bengtsson, J., Bullock, J.M., Egoh, B., Everson, C., Everson, T., O'Connor, T., O'Farrell, P.J., Smith, H.G., Lindborg, R., 2019. Grasslands—more important for ecosystem services than you might think. Ecosphere 10, e02582. https://doi.org/10.1002/ecs2.2582

Blickensdörfer, L., Schwieder, M., Pflugmacher, D., Nendel, C., Erasmi, S., Hostert, P., 2022. Mapping of crop types and crop sequences with combined time series of Sentinel-1, Sentinel-2 and Landsat 8 data for Germany. Remote Sensing of Environment 269, 112831. https://doi.org/10.1016/j.rse.2021.112831

Broeg, T., Don, A., Gocht, A., Scholten, T., Taghizadeh-Mehrjardi, R., Erasmi, S., 2024. Using local ensemble models and Landsat bare soil composites for large-scale soil organic carbon maps in cropland. Geoderma 444, 116850. https://doi.org/10.1016/j.geoderma.2024.116850

Buchner, J., Yin, H., Frantz, D., Kuemmerle, T., Askerov, E., Bakuradze, T., Bleyhl, B., Elizbarashvili, N., Komarova, A., Lewińska, K.E., Rizayeva, A., Sayadyan, H., Tan, B., Tepanosyan, G., Zazanashvili, N., Radeloff, V.C., 2020. Land-cover change in the Caucasus Mountains since 1987 based on the topographic correction of multi-temporal Landsat composites. Remote Sensing of Environment 248, 111967. https://doi.org/10.1016/j.rse.2020.111967

Buschkamp, P., Hofmann, J., Rio-Fernandes, D., Haberler, P., Gerstmeier, M., Bartscher, C., Bianchi, S., Delpet, P., Weber, H., Strese, H., Nieke, J., 2023. CHIME's Hyperspectral

Imager (HSI): status of instrument design and performance at PDR, in: Minoglou, K., Karafolas, N., Cugny, B. (Eds.), International Conference on Space Optics — ICSO 2022. Presented at the International Conference on Space Optics — ICSO 2022, SPIE, Dubrovnik, Croatia, p. 115. https://doi.org/10.1117/12.2690341
Cawse-Nicholson, K., Townsend, P.A., Schimel, D., Assiri, A.M., Blake, P.L., Buongiorno, M.F., Campbell, P., Carmon, N., Casey, K.A., Correa-Pabón, R.E., Dahlin, K.M., Dashti, H., Dennison, P.E., Dierssen, H., Erickson, A., Fisher, J.B., Frouin, R., Gatebe, C.K., Gholizadeh, H., Gierach, M., Glenn, N.F., Goodman, J.A., Griffith, D.M., Guild, L., Hakkenberg, C.R., Hochberg, E.J., Holmes, T.R.H., Hu, C., Hulley, G., Huemmrich, K.F., Kudela, R.M., Kokaly, R.F., Lee, C.M., Martin, R., Miller, C.E., Moses, W.J., Muller-Karger, F.E., Ortiz, J.D., Otis, D.B., Pahlevan, N., Painter, T.H., Pavlick, R., Poulter, B., Qi, Y., Realmuto, V.J., Roberts, D., Schaepman, M.E., Schneider, F.D., Schwandner, F.M., Serbin, S.P., Shiklomanov, A.N., Stavros, E.N., Thompson, D.R., Torres-Perez, J.L., Turpie, K.R., Tzortziou, M., Ustin, S., Yu, Q., Yusup, Y., Zhang, Q., 2021. NASA's surface biology and geology designated observable: A perspective on surface imaging algorithms. Remote Sensing of Environment 257, 112349. https://doi.org/10.1016/j.rse.2021.112349
Chabrillat, S., Foerster, S., Segl, K., Beamish, A., Brell, M., Asadzadeh, S., Milewski, R., Ward, K.J., Brosinsky, A., Koch, K., Scheffler, D., Guillaso, S., Kokhanovsky, A., Roessner, S., Guanter, L., Kaufmann, H., Pinnel, N., Carmona, E., Storch, T., Hank, T., Berger, K., Wocher, M., Hostert, P., Van Der Linden, S., Okujeni, A., Janz, A., Jakimow, B., Bracher, A., Soppa, M.A., Alvarado, L.M.A., Buddenbaum, H., Heim, B., Heiden, U., Moreno, J., Ong, C., Bohn, N., Green, R.O., Bachmann, M., Kokaly, R., Schodlok, M., Painter, T.H., Gascon, F., Buongiorno, F., Mottus, M., Brando, V.E., Feilhauer, H., Betz, M., Baur, S., Feckl, R., Schickling, A., Krieger, V., Bock, M., La Porta, L., Fischer, S., 2024. The EnMAP spaceborne imaging spectroscopy mission: Initial scientific results two years after launch. Remote Sensing of Environment 315, 114379. https://doi.org/10.1016/j.rse.2024.114379
Chaplin-Kramer, R., Neugarten, R.A., Sharp, R.P., Collins, P.M., Polasky, S., Hole, D., Schuster, R., Strimas-Mackey, M., Mulligan, M., Brandon, C., Diaz, S., Fluet-Chouinard, E., Gorenflo, L.J., Johnson, J.A., Kennedy, C.M., Keys, P.W., Longley-Wood, K., McIntyre, P.B., Noon, M., Pascual, U., Reidy Liermann, C., Roehrdanz, P.R., Schmidt-Traub, G., Shaw, M.R., Spalding, M., Turner, W.R., van Soesbergen, A., Watson, R.A., 2022. Mapping the planet's critical natural assets. Nat Ecol Evol 7, 51–61. https://doi.org/10.1038/s41559-022-01934-5
Chen, C., Park, T., Wang, X., Piao, S., Xu, B., Chaturvedi, R.K., Fuchs, R., Brovkin, V., Ciais, P., Fensholt, R., Tømmervik, H., Bala, G., Zhu, Z., Nemani, R.R., Myneni, R.B., 2019. China and India lead in greening of the world through land-use management. Nat Sustain 2, 122–129. https://doi.org/10.1038/s41893-019-0220-7
Chen, J., Jönsson, Per., Tamura, M., Gu, Z., Matsushita, B., Eklundh, L., 2004. A simple method for reconstructing a high-quality NDVI time-series data set based on the Savitzky–Golay filter. Remote Sensing of Environment 91, 332–344. https://doi.org/10.1016/j.rse.2004.03.014
Chen, S., Woodcock, C.E., Bullock, E.L., Arévalo, P., Torchinava, P., Peng, S., Olofsson, P., 2021. Monitoring temperate forest degradation on Google Earth Engine using Landsat time series analysis. Remote Sensing of Environment 265, 112648. https://doi.org/10.1016/j.rse.2021.112648

Choler, P., Bayle, A., Carlson, B.Z., Randin, C., Filippa, G., Cremonese, E., 2021. The tempo of greening in the European Alps: Spatial variations on a common theme. Global Change Biology 27, 5614–5628. https://doi.org/10.1111/gcb.15820
Claverie, M., Ju, J., Masek, J.G., Dungan, J.L., Vermote, E.F., Roger, J.-C., Skakun, S.V., Justice, C., 2018. The Harmonized Landsat and Sentinel-2 surface reflectance data set. Remote Sensing of Environment 219, 145–161. https://doi.org/10.1016/j.rse.2018.09.002
Cogliati, S., Sarti, F., Chiarantini, L., Cosi, M., Lorusso, R., Lopinto, E., Miglietta, F., Genesio, L., Guanter, L., Damm, A., Pérez-López, S., Scheffler, D., Tagliabue, G., Panigada, C., Rascher, U., Dowling, T.P.F., Giardino, C., Colombo, R., 2021. The PRISMA imaging spectroscopy mission: overview and first performance analysis. Remote Sensing of Environment 262, 112499. https://doi.org/10.1016/j.rse.2021.112499
Converse, R.L., Lippitt, C.D., Lippitt, C.L., 2021. Assessing Drought Vegetation Dynamics in Semiarid Grass- and Shrubland Using MESMA. Remote Sensing 13, 3840. https://doi.org/10.3390/rs13193840
Copernicus, 2018. HRL Grassland 2018.
Cortés, J., Mahecha, M.D., Reichstein, M., Myneni, R.B., Chen, C., Brenning, A., 2021. Where Are Global Vegetation Greening and Browning Trends Significant? Geophysical Research Letters 48, e2020GL091496. https://doi.org/10.1029/2020GL091496
Dangal, S.R.S., Tian, H., Pan, S., Zhang, L., Xu, R., 2020. Greenhouse gas balance in global pasturelands and rangelands. Environ. Res. Lett. 15, 104006. https://doi.org/10.1088/1748-9326/abaa79
Dara, A., Baumann, M., Freitag, M., Hölzel, N., Hostert, P., Kamp, J., Müller, D., Prishchepov, A.V., Kuemmerle, T., 2020. Annual Landsat time series reveal post-Soviet changes in grazing pressure. Remote Sensing of Environment 239, 111667. https://doi.org/10.1016/j.rse.2020.111667
Dennison, P.E., Lamb, B.T., Campbell, M.J., Kokaly, R.F., Hively, W.D., Vermote, E., Dabney, P., Serbin, G., Quemada, M., Daughtry, C.S.T., Masek, J., Wu, Z., 2023. Modeling global indices for estimating non-photosynthetic vegetation cover. Remote Sensing of Environment 295, 113715. https://doi.org/10.1016/j.rse.2023.113715
Dennison, P.E., Roberts, D.A., 2003. Endmember selection for multiple endmember spectral mixture analysis using endmember average RMSE. Remote Sensing of Environment 87, 123–135. https://doi.org/10.1016/S0034-4257(03)00135-4
Di Tommaso, P., Chatzou, M., Floden, E.W., Barja, P.P., Palumbo, E., Notredame, C., 2017. Nextflow enables reproducible computational workflows. Nat Biotechnol 35, 316–319. https://doi.org/10.1038/nbt.3820
Doxani, G., Vermote, E., Roger, J.-C., Gascon, F., Adriaensen, S., Frantz, D., Hagolle, O., Hollstein, A., Kirches, G., Li, F., Louis, J., Mangin, A., Pahlevan, N., Pflug, B., Vanhellemont, Q., 2018. Atmospheric Correction Inter-Comparison Exercise. Remote Sensing 10, 352. https://doi.org/10.3390/rs10020352
Drusch, M., Del Bello, U., Carlier, S., Colin, O., Fernandez, V., Gascon, F., Hoersch, B., Isola, C., Laberinti, P., Martimort, P., Meygret, A., Spoto, F., Sy, O., Marchese, F., Bargellini, P., 2012. Sentinel-2: ESA's Optical High-Resolution Mission for GMES Operational Services. Remote Sensing of Environment 120, 25–36. https://doi.org/10.1016/j.rse.2011.11.026
Dudley, K.L., Dennison, P.E., Roth, K.L., Roberts, D.A., Coates, A.R., 2015. A multi-temporal spectral library approach for mapping vegetation species across spatial and temporal phenological gradients. Remote Sensing of Environment 167, 121–134. https://doi.org/10.1016/j.rse.2015.05.004

Duveiller, G., Hooker, J., Cescatti, A., 2018. A dataset mapping the potential biophysical effects of vegetation cover change. Sci Data 5, 180014. https://doi.org/10.1038/sdata.2018.14
EEA, 2016. Biogeographical regions [WWW Document]. URL https://www.eea.europa.eu/data-and-maps/data/biogeographical-regions-europe-3
Eisfelder, C., Asam, S., Hirner, A., Reiners, P., Holzwarth, S., Bachmann, M., Gessner, U., Dietz, A., Huth, J., Bachofer, F., Kuenzer, C., 2023. Seasonal Vegetation Trends for Europe over 30 Years from a Novel Normalised Difference Vegetation Index (NDVI) Time-Series—The TIMELINE NDVI Product. Remote Sensing 15, 3616. https://doi.org/10.3390/rs15143616
ESA, 2020. GLO-30. https://doi.org/10.5270/ESA-c5d3d65
Estel, S., Mader, S., Levers, C., Verburg, P.H., Baumann, M., Kuemmerle, T., 2018. Combining satellite data and agricultural statistics to map grassland management intensity in Europe. Environ. Res. Lett. 13, 074020. https://doi.org/10.1088/1748-9326/aacc7a
European Commission, 2011. COM (2011) 152 final. European Comission, Brussels.
Eurostat, 2018. LUCAS: Land Use and Coverage Area frame Survey [WWW Document]. URL https://esdac.jrc.ec.europa.eu/projects/lucas
FAO, 2003. The Digital Soil Map of the World.
Fernández-García, V., Marcos, E., Fernández-Guisuraga, J.M., Fernández-Manso, A., Quintano, C., Suárez-Seoane, S., Calvo, L., 2021. Multiple Endmember Spectral Mixture Analysis (MESMA) Applied to the Study of Habitat Diversity in the Fine-Grained Landscapes of the Cantabrian Mountains. Remote Sensing 13, 979. https://doi.org/10.3390/rs13050979
Fernández-Ugalde, O., Jones, A., Meuli, R.G., 2020. Comparison of sampling with a spade and gouge auger for topsoil monitoring at the continental scale. Eur J Soil Sci 71, 137–150. https://doi.org/10.1111/ejss.12862
Frantz, D., 2019. FORCE—Landsat + Sentinel-2 Analysis Ready Data and Beyond. Remote Sensing 11, 1124. https://doi.org/10.3390/rs11091124
Frantz, D., Hostert, P., Rufin, P., Ernst, S., Röder, A., van der Linden, S., 2022. Revisiting the Past: Replicability of a Historic Long-Term Vegetation Dynamics Assessment in the Era of Big Data Analytics. Remote Sensing 14, 597. https://doi.org/10.3390/rs14030597
Frantz, D., Rufin, P., Janz, A., Ernst, S., Pflugmacher, D., Schug, F., Hostert, P., 2023. Understanding the robustness of spectral-temporal metrics across the global Landsat archive from 1984 to 2019 – a quantitative evaluation. Remote Sensing of Environment 298, 113823. https://doi.org/10.1016/j.rse.2023.113823
Gong, Z., Kawamura, K., Ishikawa, N., Goto, M., Wulan, T., Alateng, D., Yin, T., Ito, Y., 2015. MODIS normalized difference vegetation index (NDVI) and vegetation phenology dynamics in the Inner Mongolia grassland. Solid Earth 6, 1185–1194. https://doi.org/10.5194/se-6-1185-2015
Griffiths, P., Nendel, C., Hostert, P., 2019. Intra-annual reflectance composites from Sentinel-2 and Landsat for national-scale crop and land cover mapping. Remote Sensing of Environment 220, 135–151. https://doi.org/10.1016/j.rse.2018.10.031
Griffiths, P., Nendel, C., Pickert, J., Hostert, P., 2020. Towards national-scale characterization of grassland use intensity from integrated Sentinel-2 and Landsat time series. Remote Sensing of Environment 238, 111124. https://doi.org/10.1016/j.rse.2019.03.017
Guanter, L., Kaufmann, H., Segl, K., Foerster, S., Rogass, C., Chabrillat, S., Kuester, T., Hollstein, A., Rossner, G., Chlebek, C., Straif, C., Fischer, S., Schrader, S., Storch, T., Heiden, U., Mueller, A., Bachmann, M., Mühle, H., Müller, R., Habermeyer, M., Ohndorf, A., Hill, J., Buddenbaum, H., Hostert, P., Van Der Linden, S., Leitão, P., Rabe, A., Doerffer, R.,

Krasemann, H., Xi, H., Mauser, W., Hank, T., Locherer, M., Rast, M., Staenz, K., Sang, B., 2015. The EnMAP Spaceborne Imaging Spectroscopy Mission for Earth Observation. Remote Sensing 7, 8830–8857. https://doi.org/10.3390/rs70708830
Guerschman, J.P., Hill, M.J., 2018. Calibration and validation of the Australian fractional cover product for MODIS collection 6. Remote Sensing Letters 9, 696–705. https://doi.org/10.1080/2150704X.2018.1465611
Guerschman, J.P., Hill, M.J., Renzullo, L.J., Barrett, D.J., Marks, A.S., Botha, E.J., 2009. Estimating fractional cover of photosynthetic vegetation, non-photosynthetic vegetation and bare soil in the Australian tropical savanna region upscaling the EO-1 Hyperion and MODIS sensors. Remote Sensing of Environment 113, 928–945. https://doi.org/10.1016/j.rse.2009.01.006
Guerschman, J.P., Scarth, P.F., McVicar, T.R., Renzullo, L.J., Malthus, T.J., Stewart, J.B., Rickards, J.E., Trevithick, R., 2015. Assessing the effects of site heterogeneity and soil properties when unmixing photosynthetic vegetation, non-photosynthetic vegetation and bare soil fractions from Landsat and MODIS data. Remote Sensing of Environment 161, 12–26. https://doi.org/10.1016/j.rse.2015.01.021
Habel, J.C., Dengler, J., Janišová, M., Török, P., Wellstein, C., Wiezik, M., 2013. European grassland ecosystems: threatened hotspots of biodiversity. Biodivers Conserv 22, 2131–2138. https://doi.org/10.1007/s10531-013-0537-x
Hermosilla, T., Wulder, M.A., White, J.C., Coops, N.C., Pickell, P.D., Bolton, D.K., 2019. Impact of time on interpretations of forest fragmentation: Three-decades of fragmentation dynamics over Canada. Remote Sensing of Environment 222, 65–77. https://doi.org/10.1016/j.rse.2018.12.027
Hill, M.J., Guerschman, J.P., 2022. Global trends in vegetation fractional cover: Hotspots for change in bare soil and non-photosynthetic vegetation. Agriculture, Ecosystems & Environment 324, 107719. https://doi.org/10.1016/j.agee.2021.107719
Hill, M.J., Guerschman, J.P., 2020. The MODIS Global Vegetation Fractional Cover Product 2001–2018: Characteristics of Vegetation Fractional Cover in Grasslands and Savanna Woodlands. Remote Sensing 12, 406. https://doi.org/10.3390/rs12030406
Hill, M.J., Zhou, Q., Sun, Q., Schaaf, C.B., Palace, M., 2017. Relationships between vegetation indices, fractional cover retrievals and the structure and composition of Brazilian Cerrado natural vegetation. International Journal of Remote Sensing 38, 874–905. https://doi.org/10.1080/01431161.2016.1271959
Hively, W.D., Lamb, B.T., Daughtry, C.S.T., Serbin, G., Dennison, P., Kokaly, R.F., Wu, Z., Masek, J.G., 2021. Evaluation of SWIR Crop Residue Bands for the Landsat Next Mission. Remote Sensing 13, 3718. https://doi.org/10.3390/rs13183718
Hobi, M.L., Dubinin, M., Graham, C.H., Coops, N.C., Clayton, M.K., Pidgeon, A.M., Radeloff, V.C., 2017. A comparison of Dynamic Habitat Indices derived from different MODIS products as predictors of avian species richness. Remote Sensing of Environment 195, 142–152. https://doi.org/10.1016/j.rse.2017.04.018
Ives, A.R., Zhu, L., Wang, F., Zhu, J., Morrow, C.J., Radeloff, V.C., 2022. Statistical tests for non-independent partitions of large autocorrelated datasets. MethodsX 9, 101660. https://doi.org/10.1016/j.mex.2022.101660
Ives, A.R., Zhu, L., Wang, F., Zhu, J., Morrow, C.J., Radeloff, V.C., 2021. Statistical inference for trends in spatiotemporal data. Remote Sensing of Environment 266, 112678. https://doi.org/10.1016/j.rse.2021.112678

Jia, K., Hasan, U., Jiang, H., Qin, B., Chen, S., Li, D., Wang, C., Deng, Y., Shen, J., 2024. How frequent the Landsat 8/9-Sentinel 2A/B virtual constellation observed the earth for continuous time series monitoring. International Journal of Applied Earth Observation and Geoinformation 130, 103899. https://doi.org/10.1016/j.jag.2024.103899

Johnson, D.M., Mueller, R., 2021. Pre- and within-season crop type classification trained with archival land cover information. Remote Sensing of Environment 264, 112576. https://doi.org/10.1016/j.rse.2021.112576

Kandanaarachchi, S., Hyndman, R.J., 2022. Leave-One-Out Kernel Density Estimates for Outlier Detection. Journal of Computational and Graphical Statistics 31, 586–599. https://doi.org/10.1080/10618600.2021.2000425

Kolecka, N., 2021. Greening trends and their relationship with agricultural land abandonment across Poland. Remote Sensing of Environment 257, 112340. https://doi.org/10.1016/j.rse.2021.112340

Kong, D., Zhang, Y., Gu, X., Wang, D., 2019. A robust method for reconstructing global MODIS EVI time series on the Google Earth Engine. ISPRS Journal of Photogrammetry and Remote Sensing 155, 13–24. https://doi.org/10.1016/j.isprsjprs.2019.06.014

Kowalski, K., Okujeni, A., Brell, M., Hostert, P., 2022. Quantifying drought effects in Central European grasslands through regression-based unmixing of intra-annual Sentinel-2 time series. Remote Sensing of Environment 268, 112781. https://doi.org/10.1016/j.rse.2021.112781

Kowalski, K., Okujeni, A., Hostert, P., 2023. A generalized framework for drought monitoring across Central European grassland gradients with Sentinel-2 time series. Remote Sensing of Environment 286, 113449. https://doi.org/10.1016/j.rse.2022.113449

Kowalski, K., Senf, C., Okujeni, A., Hostert, P., 2024. Large-scale remote sensing analysis reveals an increasing coupling of grassland vitality to atmospheric water demand. Global Change Biology 30, e17315. https://doi.org/10.1111/gcb.17315

Lenton, T.M., Abrams, J.F., Bartsch, A., Bathiany, S., Boulton, C.A., Buxton, J.E., Conversi, A., Cunliffe, A.M., Hebden, S., Lavergne, T., Poulter, B., Shepherd, A., Smith, T., Swingedouw, D., Winkelmann, R., Boers, N., 2024. Remotely sensing potential climate change tipping points across scales. Nat Commun 15, 343. https://doi.org/10.1038/s41467-023-44609-w

Lewińska, K.E., Buchner, J., Bleyhl, B., Hostert, P., Yin, H., Kuemmerle, T., Radeloff, V.C., 2021. Changes in the grasslands of the Caucasus based on Cumulative Endmember Fractions from the full 1987–2019 Landsat record. Science of Remote Sensing 4, 100035. https://doi.org/10.1016/j.srs.2021.100035

Lewińska, K.E., Ernst, S., Frantz, D., Leser, U., Hostert, P., 2024a. Global overview of usable Landsat and Sentinel-2 data for 1982–2023. Data in Brief 111054. https://doi.org/10.1016/j.dib.2024.111054

Lewińska, K.E., Frantz, D., Leser, U., Hostert, P., 2024b. Usable observations over Europe: evaluation of compositing windows for Landsat and Sentinel-2 time series. European Journal of Remote Sensing 57, 2372855. https://doi.org/10.1080/22797254.2024.2372855

Lewińska, K.E., Hostert, P., Buchner, J., Bleyhl, B., Radeloff, V.C., 2020. Short-term vegetation loss versus decadal degradation of grasslands in the Caucasus based on Cumulative Endmember Fractions. Remote Sensing of Environment 248, 111969. https://doi.org/10.1016/j.rse.2020.111969

Lewińska, K.E., Ives, A.R., Morrow, C.J., Rogova, N., Yin, H., Elsen, P.R., de Beurs, K., Hostert, P., Radeloff, V.C., 2023. Beyond “greening” and “browning”: Trends in grassland

ground cover fractions across Eurasia that account for spatial and temporal autocorrelation. Global Change Biology gcb.16800. https://doi.org/10.1111/gcb.16800
Li, Y., Wulder, M.A., Zhu, Z., Verbesselt, J., Masiliūnas, D., Liu, Y., Bohrer, G., Cai, Y., Zhou, Y., Ding, Z., Zhao, K., 2024. DRMAT: A multivariate algorithm for detecting breakpoints in multispectral time series. Remote Sensing of Environment 315, 114402. https://doi.org/10.1016/j.rse.2024.114402
Li, Z., Zhang, H.K., Roy, D.P., 2019. Investigation of Sentinel-2 Bidirectional Reflectance Hot-Spot Sensing Conditions. IEEE Trans. Geosci. Remote Sensing 57, 3591–3598. https://doi.org/10.1109/TGRS.2018.2885967
Lobert, F., Schwieder, M., Alsleben, J., Broeg, T., Kowalski, K., Okujeni, A., Hostert, P., Erasmi, S., 2024. Unveiling Year-Round Cropland Cover by Soil-Specific Spectral Unmixing of Landsat and Sentinel-2 Time Series. https://doi.org/10.31223/X5SD8Q
Lorenz, K., Lal, R., 2018. Carbon Sequestration in Agricultural Ecosystems. Springer International Publishing, Cham. https://doi.org/10.1007/978-3-319-92318-5
Mader, S., 2012. Framework for the Phenological Analysis of Hypertemporal Remote Sensing Data Based on Polynomial Spline Models (Doctoral Thesis). Trier University, Trier, Germany.
Mas, J.-F., Soares De Araújo, F., 2021. Assessing Landsat Images Availability and Its Effects on Phenological Metrics. Forests 12, 574. https://doi.org/10.3390/f12050574
Morrow, C.J., Ives, A.R., 2023. remotePARTS: Spatiotemporal Autoregression Analyses for Large Data Sets.
Munier, S., Carrer, D., Planque, C., Camacho, F., Albergel, C., Calvet, J.-C., 2018. Satellite Leaf Area Index: Global Scale Analysis of the Tendencies Per Vegetation Type Over the Last 17 Years. Remote Sensing 10, 424. https://doi.org/10.3390/rs10030424
Nieke, J., Rast, M., 2018. Towards the Copernicus Hyperspectral Imaging Mission For The Environment (CHIME), in: IGARSS 2018 - 2018 IEEE International Geoscience and Remote Sensing Symposium. Presented at the IGARSS 2018 - 2018 IEEE International Geoscience and Remote Sensing Symposium, IEEE, Valencia, pp. 157–159. https://doi.org/10.1109/IGARSS.2018.8518384
Okujeni, A., Jänicke, C., Cooper, S., Frantz, D., Hostert, P., Clark, M., Segl, K., van der Linden, S., 2021. Multi-season unmixing of vegetation class fractions across diverse Californian ecoregions using simulated spaceborne imaging spectroscopy data. Remote Sensing of Environment 264, 112558. https://doi.org/10.1016/j.rse.2021.112558
Okujeni, A., Kowalski, K., Lewińska, K.E., Schneidereit, S., Hostert, P., 2024. Multidecadal grassland fractional cover time series retrieval for Germany from the Landsat and Sentinel-2 archives. Remote Sensing of Environment 302, 113980. https://doi.org/10.1016/j.rse.2023.113980
Okujeni, A., van der Linden, S., Suess, S., Hostert, P., 2017. Ensemble Learning From Synthetically Mixed Training Data for Quantifying Urban Land Cover With Support Vector Regression. IEEE Journal of Selected Topics in Applied Earth Observations and Remote Sensing 10, 1640–1650. https://doi.org/10.1109/JSTARS.2016.2634859
Okujeni, A., van der Linden, S., Tits, L., Somers, B., Hostert, P., 2013. Support vector regression and synthetically mixed training data for quantifying urban land cover. Remote Sensing of Environment 137, 184–197. https://doi.org/10.1016/j.rse.2013.06.007
Pazúr, R., Nováček, J., Bürgi, M., Kopecká, M., Lieskovský, J., Pazúrová, Z., Feranec, J., 2024. Changes in grassland cover in Europe from 1990 to 2018: trajectories and spatial patterns. Reg Environ Change 24, 51. https://doi.org/10.1007/s10113-024-02197-5

Pellaton, R., Lellei-Kovács, E., Báldi, A., 2022. Cultural ecosystem services in European grasslands: A systematic review of threats. Ambio 51, 2462–2477. https://doi.org/10.1007/s13280-022-01755-7

Phiri, D., Simwanda, M., Salekin, S., Nyirenda, V.R., Murayama, Y., Ranagalage, M., 2020. Sentinel-2 Data for Land Cover/Use Mapping: A Review. REMOTE SENSING 12. https://doi.org/10.3390/rs12142291

Piipponen, J., Jalava, M., De Leeuw, J., Rizayeva, A., Godde, C., Cramer, G., Herrero, M., Kummu, M., 2022. Global trends in grassland carrying capacity and relative stocking density of livestock. Global Change Biology 28, 3902–3919. https://doi.org/10.1111/gcb.16174

Poppe Terán, C., Naz, B.S., Graf, A., Qu, Y., Hendricks Franssen, H.-J., Baatz, R., Ciais, P., Vereecken, H., 2023. Rising water-use efficiency in European grasslands is driven by increased primary production. Commun Earth Environ 4, 95. https://doi.org/10.1038/s43247-023-00757-x

Potapov, P., Hansen, M.C., Kommareddy, I., Kommareddy, A., Turubanova, S., Pickens, A., Adusei, B., Tyukavina, A., Ying, Q., 2020. Landsat Analysis Ready Data for Global Land Cover and Land Cover Change Mapping. Remote Sensing 12, 426. https://doi.org/10.3390/rs12030426

Qiu, S., Zhu, Z., Shang, R., Crawford, C.J., 2021. Can Landsat 7 preserve its science capability with a drifting orbit? Science of Remote Sensing 4, 100026. https://doi.org/10.1016/j.srs.2021.100026

Radeloff, V.C., Roy, D.P., Wulder, M.A., Anderson, M., Cook, B., Crawford, C.J., Friedl, M., Gao, F., Gorelick, N., Hansen, M., Healey, S., Hostert, P., Hulley, G., Huntington, J.L., Johnson, D.M., Neigh, C., Lyapustin, A., Lymburner, L., Pahlevan, N., Pekel, J.-F., Scambos, T.A., Schaaf, C., Strobl, P., Woodcock, C.E., Zhang, H.K., Zhu, Z., 2024. Need and vision for global medium-resolution Landsat and Sentinel-2 data products. Remote Sensing of Environment 300, 113918. https://doi.org/10.1016/j.rse.2023.113918

Reed, B.C., Brown, J.F., VanderZee, D., Loveland, T.R., Merchant, J.W., Ohlen, D.O., 1994. Measuring phenological variability from satellite imagery. J Vegetation Science 5, 703–714. https://doi.org/10.2307/3235884

Roberts, D.A., Gardner, M., Church, R., Ustin, S., Scheer, G., Green, R.O., 1998. Mapping Chaparral in the Santa Monica Mountains Using Multiple Endmember Spectral Mixture Models. Remote Sensing of Environment 65, 267–279. https://doi.org/10.1016/S0034-4257(98)00037-6

Roy, D.P., Wulder, M.A., Loveland, T.R., C.E., W., Allen, R.G., Anderson, M.C., Helder, D., Irons, J.R., Johnson, D.M., Kennedy, R., Scambos, T.A., Schaaf, C.B., Schott, J.R., Sheng, Y., Vermote, E.F., Belward, A.S., Bindschadler, R., Cohen, W.B., Gao, F., Hipple, J.D., Hostert, P., Huntington, J., Justice, C.O., Kilic, A., Kovalskyy, V., Lee, Z.P., Lymburner, L., Masek, J.G., McCorkel, J., Shuai, Y., Trezza, R., Vogelmann, J., Wynne, R.H., Zhu, Z., 2014. Landsat-8: Science and product vision for terrestrial global change research. Remote Sensing of Environment 145, 154–172. https://doi.org/10.1016/j.rse.2014.02.001

Roy, D.P., Zhang, H.K., Ju, J., Gomez-Dans, J.L., Lewis, P.E., Schaaf, C.B., Sun, Q., Li, J., Huang, H., Kovalskyy, V., 2016. A general method to normalize Landsat reflectance data to nadir BRDF adjusted reflectance. Remote Sensing of Environment 176, 255–271. https://doi.org/10.1016/j.rse.2016.01.023

Rufin, P., Frantz, D., Yan, L., Hostert, P., 2020. Operational Coregistration of the Sentinel-2A/B Image Archive Using Multitemporal Landsat Spectral Averages. IEEE Geoscience and Remote Sensing Letters 1–5. https://doi.org/10.1109/LGRS.2020.2982245

Runge, A., Grosse, G., 2020. Mosaicking Landsat and Sentinel-2 Data to Enhance LandTrendr Time Series Analysis in Northern High Latitude Permafrost Regions. Remote Sensing 12, 2471. https://doi.org/10.3390/rs12152471

Safanelli, J.L., Chabrillat, S., Ben-Dor, E., Demattê, J.A.M., 2020. Multispectral Models from Bare Soil Composites for Mapping Topsoil Properties over Europe. Remote Sensing 12, 1369. https://doi.org/10.3390/rs12091369

Saunier, S., Pflug, B., Lobos, I., Franch, B., Louis, J., De Los Reyes, R., Debaecker, V., Cadau, E., Boccia, V., Gascon, F., Kocaman, S., 2022. Sen2Like: Paving the Way towards Harmonization and Fusion of Optical Data. Remote Sensing 14, 3855. https://doi.org/10.3390/rs14163855

Schils, R.L.M., Bufe, C., Rhymer, C.M., Francksen, R.M., Klaus, V.H., Abdalla, M., Milazzo, F., Lellei-Kovács, E., Berge, H. ten, Bertora, C., Chodkiewicz, A., Dămătîrcă, C., Feigenwinter, I., Fernández-Rebollo, P., Ghiasi, S., Hejduk, S., Hiron, M., Janicka, M., Pellaton, R., Smith, K.E., Thorman, R., Vanwalleghem, T., Williams, J., Zavattaro, L., Kampen, J., Derkx, R., Smith, P., Whittingham, M.J., Buchmann, N., Price, J.P.N., 2022. Permanent grasslands in Europe: Land use change and intensification decrease their multifunctionality. Agriculture, Ecosystems & Environment 330, 107891. https://doi.org/10.1016/j.agee.2022.107891

Schug, F., Pfoch, K.A., Pham, V.-D., Van Der Linden, S., Okujeni, A., Frantz, D., Radeloff, V.C., 2024. Land cover fraction mapping across global biomes with Landsat data, spatially generalized regression models and spectral-temporal metrics. Remote Sensing of Environment 311, 114260. https://doi.org/10.1016/j.rse.2024.114260

Schwieder, M., Leitão, P.J., da Cunha Bustamante, M.M., Ferreira, L.G., Rabe, A., Hostert, P., 2016. Mapping Brazilian savanna vegetation gradients with Landsat time series. International Journal of Applied Earth Observation and Geoinformation 52, 361–370. https://doi.org/10.1016/j.jag.2016.06.019

Schwieder, M., Wesemeyer, M., Frantz, D., Pfoch, K., Erasmi, S., Pickert, J., Nendel, C., Hostert, P., 2022. Mapping grassland mowing events across Germany based on combined Sentinel-2 and Landsat 8 time series. Remote Sensing of Environment 269, 112795. https://doi.org/10.1016/j.rse.2021.112795

Senf, C., Laštovička, J., Okujeni, A., Heurich, M., Van Der Linden, S., 2020. A generalized regression-based unmixing model for mapping forest cover fractions throughout three decades of Landsat data. Remote Sensing of Environment 240, 111691. https://doi.org/10.1016/j.rse.2020.111691

Smith, A.M., Hill, M.J., Zhang, Y., 2015. Estimating Ground Cover in the Mixed Prairie Grassland of Southern Alberta Using Vegetation Indices Related to Physiological Function. Canadian Journal of Remote Sensing 41, 51–66. https://doi.org/10.1080/07038992.2015.1042101

Sonnenschein, R., Kuemmerle, T., Udelhoven, T., Stellmes, M., Hostert, P., 2011. Differences in Landsat-based trend analyses in drylands due to the choice of vegetation estimate. Remote Sensing of Environment 115, 1408–1420. https://doi.org/10.1016/j.rse.2011.01.021

Spinoni, J., Barbosa, P., Bucchignani, E., Cassano, J., Cavazos, T., Christensen, J.H., Christensen, O.B., Coppola, E., Evans, J., Geyer, B., Giorgi, F., Hadjinicolaou, P., Jacob, D., Katzfey, J., Koenigk, T., Laprise, R., Lennard, C.J., Kurnaz, M.L., Li, D., Llopart, M., McCormick, N., Naumann, G., Nikulin, G., Ozturk, T., Panitz, H.-J., Porfirio da Rocha, R., Rockel, B., Solman, S.A., Syktus, J., Tangang, F., Teichmann, C., Vautard, R., Vogt, J.V., Winger, K., Zittis, G., Dosio, A., 2020. Future Global Meteorological Drought Hot Spots: A Study Based on CORDEX Data. Journal of Climate 33, 3635–3661. https://doi.org/10.1175/JCLI-D-19-0084.1

Stanimirova, R., Graesser, J., Olofsson, P., Friedl, M.A., 2022. Widespread changes in 21st century vegetation cover in Argentina, Paraguay, and Uruguay. Remote Sensing of Environment 282, 113277. https://doi.org/10.1016/j.rse.2022.113277

Storch, T., Honold, H.-P., Chabrillat, S., Habermeyer, M., Tucker, P., Brell, M., Ohndorf, A., Wirth, K., Betz, M., Kuchler, M., Mühle, H., Carmona, E., Baur, S., Mücke, M., Löw, S., Schulze, D., Zimmermann, S., Lenzen, C., Wiesner, S., Aida, S., Kahle, R., Willburger, P., Hartung, S., Dietrich, D., Plesia, N., Tegler, M., Schork, K., Alonso, K., Marshall, D., Gerasch, B., Schwind, P., Pato, M., Schneider, M., De Los Reyes, R., Langheinrich, M., Wenzel, J., Bachmann, M., Holzwarth, S., Pinnel, N., Guanter, L., Segl, K., Scheffler, D., Foerster, S., Bohn, N., Bracher, A., Soppa, M.A., Gascon, F., Green, R., Kokaly, R., Moreno, J., Ong, C., Sornig, M., Wernitz, R., Bagschik, K., Reintsema, D., La Porta, L., Schickling, A., Fischer, S., 2023. The EnMAP imaging spectroscopy mission towards operations. Remote Sensing of Environment 294, 113632. https://doi.org/10.1016/j.rse.2023.113632

Suess, S., van der Linden, S., Okujeni, A., Griffiths, P., Leitão, P.J., Schwieder, M., Hostert, P., 2018. Characterizing 32 years of shrub cover dynamics in southern Portugal using annual Landsat composites and machine learning regression modeling. Remote Sensing of Environment 219, 353–364. https://doi.org/10.1016/j.rse.2018.10.004

Sulla-Menashe, D., Friedl, M.A., Woodcock, C.E., 2016. Sources of bias and variability in long-term Landsat time series over Canadian boreal forests. Remote Sensing of Environment 177, 206–219. https://doi.org/10.1016/j.rse.2016.02.041

Sun, Q., Zhang, P., Jiao, X., Lin, X., Duan, W., Ma, S., Pan, Q., Chen, L., Zhang, Y., You, S., Liu, S., Hao, J., Li, H., Sun, D., 2024. A global estimate of monthly vegetation and soil fractions from spatiotemporally adaptive spectral mixture analysis during 2001–2022. Earth Syst. Sci. Data 16, 1333–1351. https://doi.org/10.5194/essd-16-1333-2024

Tóth, G., Gardi, C., Bódis, K., Ivits, É., Aksoy, E., Jones, A., Jeffrey, S., Petursdottir, T., Montanarella, L., 2013. Continental-scale assessment of provisioning soil functions in Europe. Ecol Process 2, 32. https://doi.org/10.1186/2192-1709-2-32

Van der Meer, F.D., Jia, X., 2012. Collinearity and orthogonality of endmembers in linear spectral unmixing. International Journal of Applied Earth Observation and Geoinformation 18, 491–503. https://doi.org/10.1016/j.jag.2011.10.004

Verbesselt, J., Hyndman, R., Newnham, G., Culvenor, D., 2010. Detecting trend and seasonal changes in satellite image time series. Remote Sensing of Environment 114, 106–115. https://doi.org/10.1016/j.rse.2009.08.014

Verrelst, J., Halabuk, A., Atzberger, C., Hank, T., Steinhauser, S., Berger, K., 2023. A comprehensive survey on quantifying non-photosynthetic vegetation cover and biomass from imaging spectroscopy. Ecological Indicators 155, 110911. https://doi.org/10.1016/j.ecolind.2023.110911

White, J.C., Hermosilla, T., Wulder, M.A., Coops, N.C., 2022. Mapping, validating, and interpreting spatio-temporal trends in post-disturbance forest recovery. Remote Sensing of Environment 271, 112904. https://doi.org/10.1016/j.rse.2022.112904

Wilson, J.B., Peet, R.K., Dengler, J., Pärtel, M., 2012. Plant species richness: the world records. J Vegetation Science 23, 796–802. https://doi.org/10.1111/j.1654-1103.2012.01400.x
Woodcock, C.E., Loveland, T.R., Herold, M., Bauer, M.E., 2020. Transitioning from change detection to monitoring with remote sensing: A paradigm shift. Remote Sensing of Environment 238, 111558. https://doi.org/10.1016/j.rse.2019.111558
Wulder, M.A., Hilker, T., White, J.C., Coops, N.C., Masek, J.G., Pflugmacher, D., Crevier, Y., 2015. Virtual constellations for global terrestrial monitoring. Remote Sensing of Environment 170, 62–76. https://doi.org/10.1016/j.rse.2015.09.001
Wulder, M.A., Roy, D.P., Radeloff, V.C., Loveland, T.R., Anderson, M.C., Johnson, D.M., Healey, S., Zhu, Z., Scambos, T.A., Pahlevan, N., Hansen, M., Gorelick, N., Crawford, C.J., Masek, J.G., Hermosilla, T., White, J.C., Belward, A.S., Schaaf, C., Woodcock, C.E., Huntington, J.L., Lymburner, L., Hostert, P., Gao, F., Lyapustin, A., Pekel, J.-F., Strobl, P., Cook, B.D., 2022. Fifty years of Landsat science and impacts. Remote Sensing of Environment 280, 113195. https://doi.org/10.1016/j.rse.2022.113195
Yan, J., Zhang, G., Ling, H., Han, F., 2022. Comparison of time-integrated NDVI and annual maximum NDVI for assessing grassland dynamics. Ecological Indicators 136, 108611. https://doi.org/10.1016/j.ecolind.2022.108611
Yin, H., Brandão, A., Buchner, J., Helmers, D., Iuliano, B.G., Kimambo, N.E., Lewińska, K.E., Razenkova, E., Rizayeva, A., Rogova, N., Spawn, S.A., Xie, Y., Radeloff, V.C., 2020. Monitoring cropland abandonment with Landsat time series. Remote Sensing of Environment 246, 111873. https://doi.org/10.1016/j.rse.2020.111873
Zekoll, V., Main-Knorn, M., Louis, J., Frantz, D., Richter, R., Pflug, B., 2021. Comparison of Masking Algorithms for Sentinel-2 Imagery. Remote Sensing 13. https://doi.org/10.3390/rs13010137
Zhang, Y., Song, C., Band, L.E., Sun, G., Li, J., 2017. Reanalysis of global terrestrial vegetation trends from MODIS products: Browning or greening? Remote Sensing of Environment 191, 145–155. https://doi.org/10.1016/j.rse.2016.12.018
Zhang, Y., Woodcock, C.E., Arévalo, P., Olofsson, P., Tang, X., Stanimirova, R., Bullock, E., Tarrio, K.R., Zhu, Z., Friedl, M.A., 2022. A Global Analysis of the Spatial and Temporal Variability of Usable Landsat Observations at the Pixel Scale. Front. Remote Sens. 3, 894618. https://doi.org/10.3389/frsen.2022.894618
Zhao, K., Wulder, M.A., Hu, T., Bright, R., Wu, Q., Qin, H., Li, Y., Toman, E., Mallick, B., Zhang, X., Brown, M., 2019. Detecting change-point, trend, and seasonality in satellite time series data to track abrupt changes and nonlinear dynamics: A Bayesian ensemble algorithm. Remote Sensing of Environment 232, 111181. https://doi.org/10.1016/j.rse.2019.04.034
Zheng, G., Bao, A., Li, X., Jiang, L., Chang, C., Chen, T., Gao, Z., 2019. The Potential of Multispectral Vegetation Indices Feature Space for Quantitatively Estimating the Photosynthetic, Non-Photosynthetic Vegetation and Bare Soil Fractions in Northern China. photogramm eng remote sensing 85, 65–76. https://doi.org/10.14358/PERS.85.1.65
Zhou, Q., Hill, M.J., Sun, Q., Schaaf, C.B., 2016. Retrieving understorey dynamics in the Australian tropical savannah from time series decomposition and linear unmixing of MODIS data. International Journal of Remote Sensing 37, 1445–1475. https://doi.org/10.1080/01431161.2016.1154224
Zhu, Z., Piao, S., Myneni, R.B., Huang, M., Zeng, Z., Canadell, J.G., Ciais, P., Sitch, S., Friedlingstein, P., Arneth, A., Cao, C., Cheng, L., Kato, E., Koven, C., Li, Y., Lian, X., Liu,

Y., Liu, R., Mao, J., Pan, Y., Peng, S., Peñuelas, J., Poulter, B., Pugh, T.A.M., Stocker, B.D., Viovy, N., Wang, X., Wang, Y., Xiao, Z., Yang, H., Zaehle, S., Zeng, N., 2016. Greening of the Earth and its drivers. Nature Clim Change 6, 791–795. https://doi.org/10.1038/nclimate3004

Zhu, Z., Wang, S., Woodcock, C.E., 2015. Improvement and expansion of the Fmask algorithm: cloud, cloud shadow, and snow detection for Landsats 4–7, 8, and Sentinel 2 images. Remote Sensing of Environment 159, 269–277. https://doi.org/10.1016/j.rse.2014.12.014

Zhu, Z., Zhang, J., Yang, Z., Aljaddani, A.H., Cohen, W.B., Qiu, S., Zhou, C., 2020. Continuous monitoring of land disturbance based on Landsat time series. Remote Sensing of Environment 238, 111116. https://doi.org/10.1016/j.rse.2019.03.009

Impact of data density and endmember definitions on long-term trends in ground cover fractions across European grasslands

Supplement A

Katarzyna Ewa Lewińska [1,2], Akpona Okujeni [3,1], Katja Kowalski [4,1], Fabian Lehmann [5], Volker C. Radeloff [2], Ulf Leser [5], Patrick Hostert [1,6]

[1] Geography Department, Humboldt-Universität zu Berlin, Unter den Linden 6, 10099 Berlin, Germany.

[2] SILVIS Lab, Department of Forest and Wildlife Ecology, University of Wisconsin-Madison, 1630 Linden Drive, Madison WI 53706, USA.

[3] Helmholtz Center Potsdam, GFZ German Research Center for Geosciences, Telegrafenberg, 14473 Potsdam, Germany

[4] Earth Observation for Ecosystem Management, School of Life Sciences, Technical University of Munich, 11 Hans-Carl-v.-Carlowitz-Platz 2, 85354 Freising, Germany

[5] Department of Computer Science, Humboldt-Universität zu Berlin, Unter den Linden 6, 10099 Berlin, Germany

[6] Integrative Research Institute on Transformations of Human-Environment Systems (IRI THESys), Humboldt-Universität zu Berlin, Unter den Linden 6, 10099 Berlin, Germany

Table SA1 Summary of environmental conditions across 13 test sites. Biogeographical regions after (EEA, 2016), dominant soil types after (FAO, 2003), soil biomass productivity index after (Tóth et al., 2013), distribution and share of grasslands after (Copernicus, 2018), and clear sky probability according to Sentinel-2 cloud probability product. Test sites codes as in Figure 1.

Test site	Biogeographical region	Dominant soil type	Elevation [m] min	mean	max	Productivity [index]	Grassland cover [%]	Clear sky probability (per month) [%] 1	2	3	4	5	6	7	8	9	10	11	12
AL	Continental/Alpine	Luvisols/Cambisols	372	719	2097	6.25	35.2	34	39	28	55	38	38	46	40	62	40	31	30
BX	Atlantic	Fluvisols/Podzols	-15	-0.1	30	7.30	50.7	17	29	37	49	41	34	37	38	38	33	27	20
CR	Mediterranean	Lithosols/Luvisols	-7	423	2450	4.69	21.6	44	43	63	70	78	90	96	96	90	64	61	48
DE	Continental	Histosols/Cambisols	2	34	111	6.4	26.7	18	32	31	61	44	41	40	33	44	28	18	19
ES	Mediterranean	Cambisols	197	414	1004	4.11	50.9	52	63	64	45	64	76	94	96	70	71	56	48
FR	Continental	Cambisols	149	365	1007	6.30	48.3	14	40	46	55	35	53	58	61	51	34	22	21
IE	Atlantic	Luvisols/Arenosols	-6	132	911	7.56	67.9	22	21	24	28	26	20	19	17	28	26	27	22
LX	Continental	Luvisols/	183	352	553	6.25	27.0	9	28	44	54	34	48	43	37	51	35	20	18
PL	Continental	Podzols/Podzoluvisols	59	122	211	5.49	36.0	17	29	39	59	46	49	41	51	44	34	14	8
RO	Alpine	Luvisols/Phaeozems	176	427	1014	6.18	43.4	22	21	41	50	48	45	58	72	59	52	31	19
SE	Boreal	Cambisols	63	209	369	6.49	14.4	17	28	43	59	43	44	46	30	26	32	19	10
SA	Mediterranean	Andosols/Cambisols	4	434	1262	5.25	40.2	40	54	46	48	55	73	89	84	64	67	39	45
UK	Atlantic	Gleysols	-1	302	945	6.03	65.4	21	33	24	39	31	25	22	15	22	22	16	22

Table SA2 Parameters for band-wise cross normalized between Landsat 7 ETM+ and Landsat 5 TM, Landsat 8/9 OLI, and Sentinel-2 A/B MSI calculated based on paired scenes acquired maximum ± one day apart.

	Landsat 7 ETM+ ~ Landsat 5 TM		Landsat 7 ETM+ ~ Landsat 8/9 OLI		Landsat 7 ETM+ ~ Sentinel-2 A/B MSI	
Band	slope	intercept	slope	intercept	slope	intercept
RED	0.9023	-56.0099	0.9223	32.03327	0.8276	81.58513
Green	0.8570	-3.63653	0.9279	65.84526	0.8578	122.5832
Blue	0.8936	-7.59740	0.9189	82.91101	0.8598	137.3319
NIR	0.9863	-17.1039	0.9410	112.1265	0.9314	171.1741
SWIR1	0.9290	-32.3222	1.0157	54.57690	1.0162	31.26700
SWIR2	0.9526	-3.02198	0.9127	4.745386	0.9172	1.853231

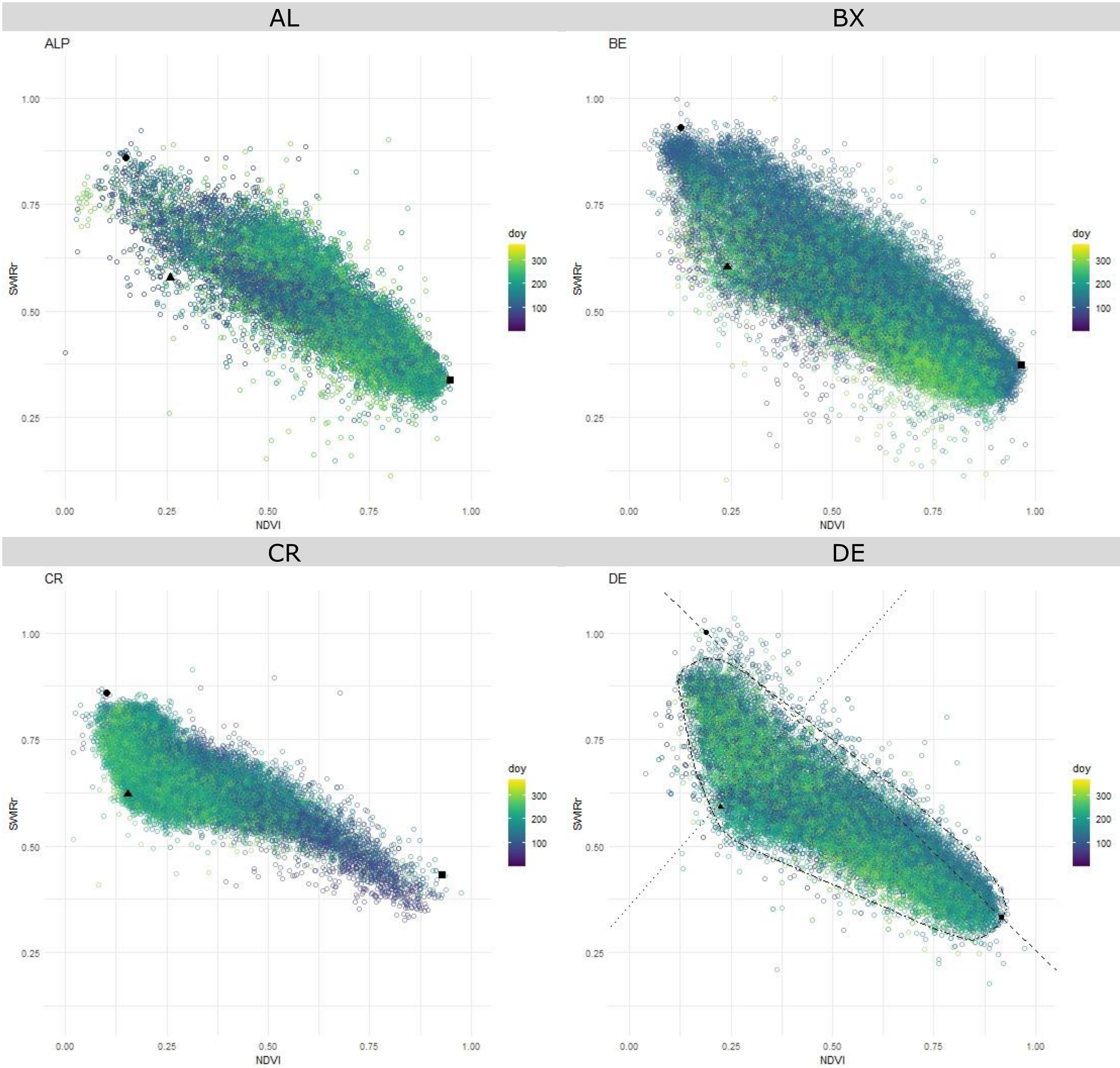

Figure SA1 NDVI~SWIR ratio feature space characterizing each test site with the points representing selected green vegetation, non-photosynthetic vegetation and soil spectra marked with black symbols (square, triangle and circle, respectively). For the DE site *gv-soil* line (dashed) its normal (dotted), and the convex-hull of the point cloud without outliers (α=0.1; Kandanaarachchi and Hyndman, 2022) (dash-dotted) are included. Site abbreviations correspond with Table 1.

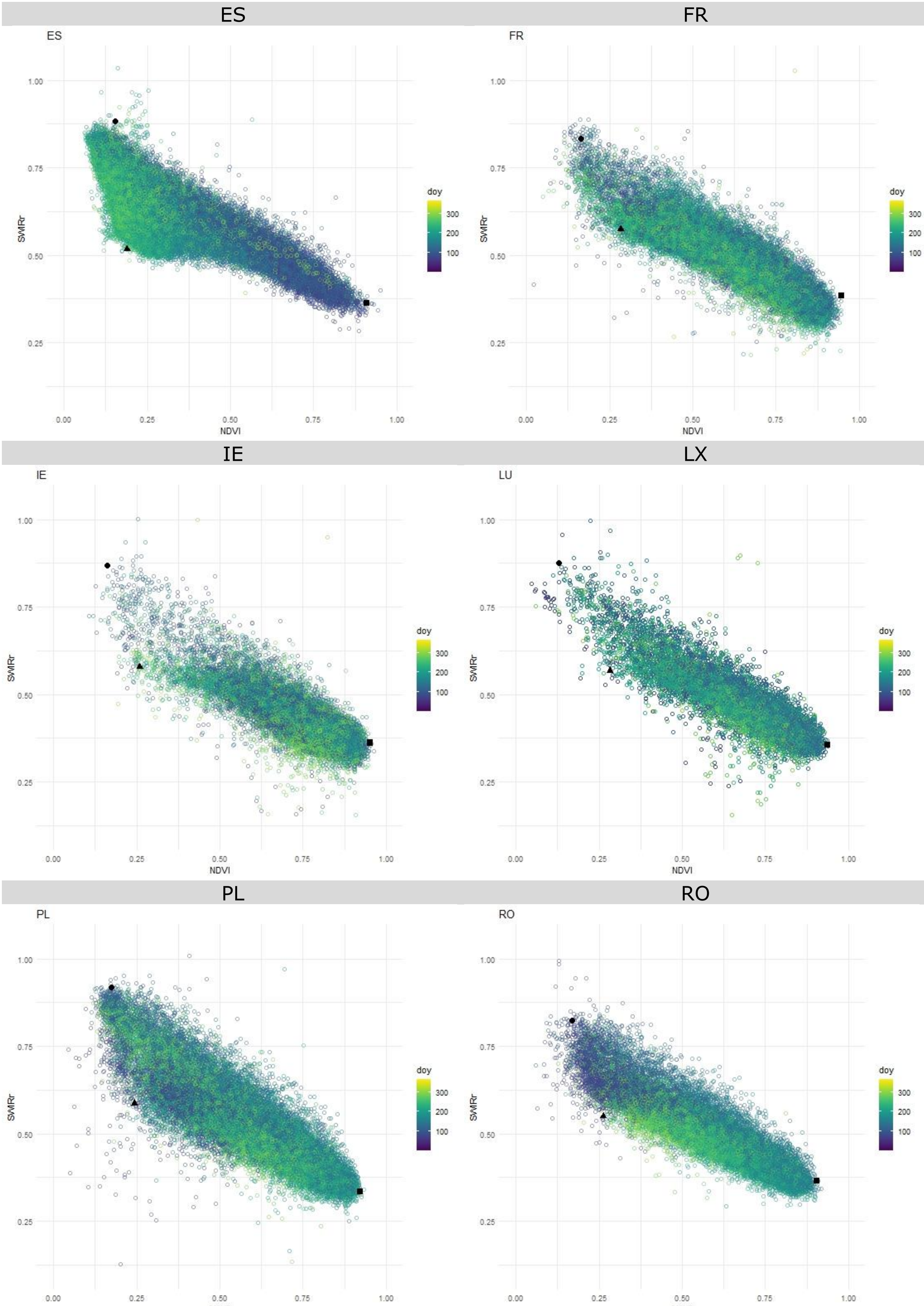

Figure SA1 continuation

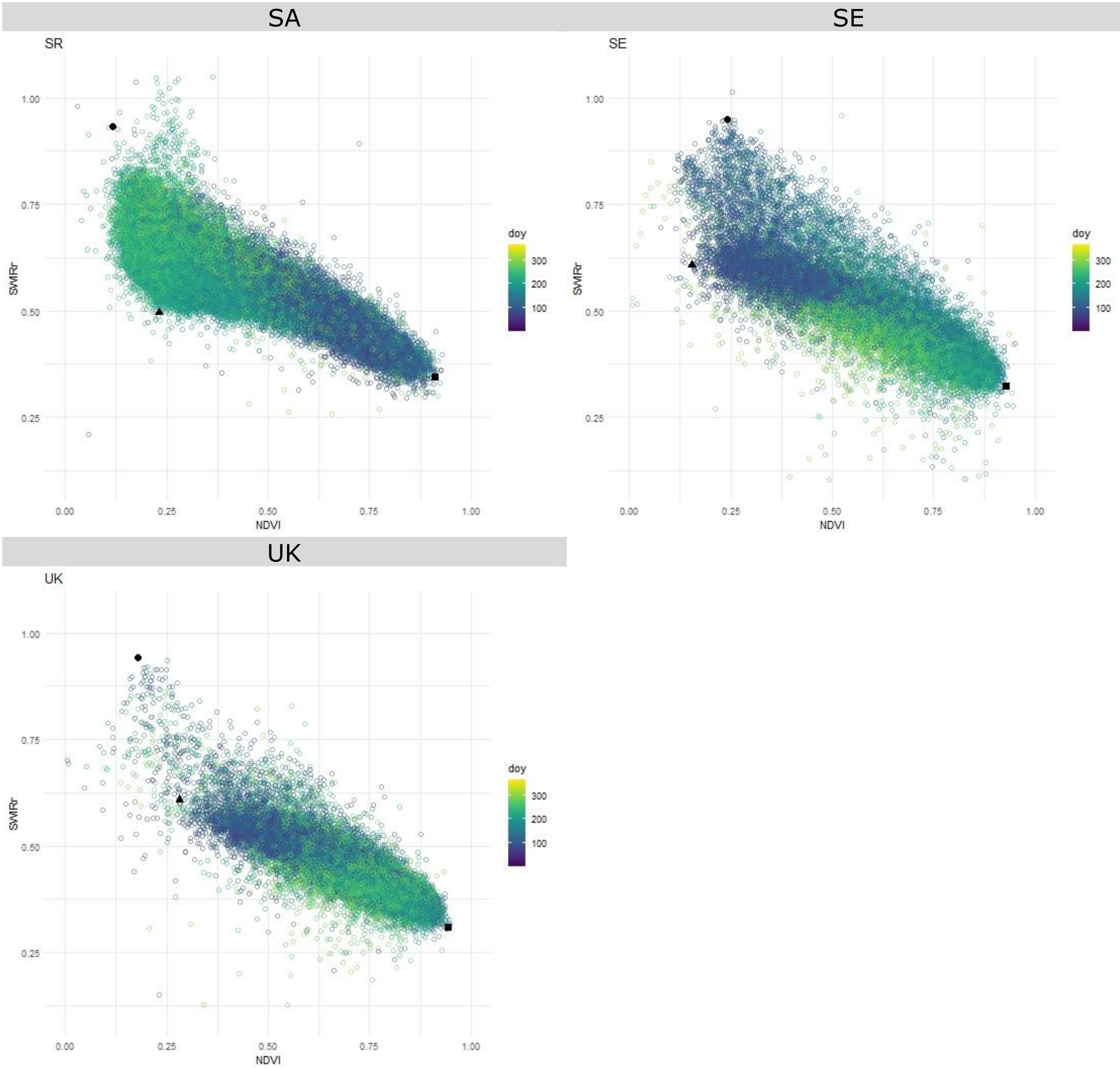

Figure SA1 continuation

Table SA3 Site-specific endmembers. Region-specific endmembers are highlighted with *.

Test site	Biogeographical region	endmember	NDVI	SWIRr	Acquisition date	Reflectance 0.45-0.52 µm	0.52-0.60 µm	0.63-0.69 µm	0.77-0.90 µm	1.55-1.75 µm	2.09-2.35 µm
AL	Continental	soil	0.149	0.860	1999-06-24	0.0824	0.1304	0.1609	0.2173	0.3153	0.2712
AL	Continental	gv	0.950	0.336	2020-07-27	0.0182	0.0515	0.0154	0.5983	0.2053	0.0689
AL	Continental	npv	0.259	0.577	2022-07-25	0.0858	0.1435	0.2089	0.3548	0.4042	0.2334
BX	Atlantic	soil*	0.127	0.930	2010-06-02	0.1036	0.1471	0.1843	0.2378	0.3309	0.3079
BX	Atlantic	gv*	0.968	0.371	2017-04-25	0.01	0.0405	0.0109	0.6649	0.1495	0.0555
BX	Atlantic	npv	0.241	0.602	2021-08-23	0.1033	0.1602	0.229	0.3747	0.3811	0.2294
CR	Mediterranean	soil	0.101	0.859	1986-04-22	0.1213	0.1908	0.2415	0.2959	0.3624	0.3114
CR	Mediterranean	gv	0.929	0.432	2017-05-23	0.0134	0.0628	0.0223	0.607	0.2069	0.0894
CR	Mediterranean	npv	0.154	0.621	2011-10-12	0.1111	0.1527	0.1922	0.2622	0.3477	0.2159
DE	Continental	soil*	0.189	1.000	1999-09-12	0.0519	0.0585	0.0622	0.0911	0.201	0.2011
DE	Continental	gv	0.916	0.332	2014-05-01	0.0237	0.0528	0.023	0.5272	0.1574	0.0522
DE	Continental	npv	0.225	0.592	2018-06-29	0.0929	0.1707	0.2538	0.401	0.456	0.2699
ES	Mediterranean	soil	0.153	0.883	1984-05-28	0.1171	0.195	0.2586	0.352	0.4346	0.3839
ES	Mediterranean	gv	0.910	0.363	2011-04-13	0.017	0.0473	0.0258	0.5486	0.189	0.0687
ES	Mediterranean	npv	0.190	0.517	2021-08-30	0.0696	0.1303	0.1867	0.2741	0.4022	0.2078
FR	Continental	soil	0.163	0.833	2004-05-25	0.1283	0.2086	0.2857	0.3973	0.4795	0.3995
FR	Continental	gv*	0.947	0.384	2015-04-14	0.0141	0.0397	0.0148	0.5396	0.1509	0.058
FR	Continental	npv	0.284	0.573	2003-06-24	0.09	0.1534	0.2176	0.3899	0.4038	0.2315
IE	Atlantic	soil	0.161	0.868	2001-05-08	0.0972	0.144	0.1902	0.263	0.3323	0.2885
IE	Atlantic	gv	0.952	0.361	2015-10-12	0.0188	0.0487	0.016	0.6534	0.176	0.0636
IE	Atlantic	npv	0.260	0.579	2018-07-30	0.0921	0.1443	0.2125	0.3616	0.3728	0.2159
LX	Continental	soil	0.130	0.875	2005-05-12	0.0723	0.1115	0.1414	0.1837	0.2233	0.1953
LX	Continental	gv	0.937	0.356	2008-05-12	0.0179	0.0464	0.0182	0.5636	0.1686	0.0601
LX	Continental	npv	0.283	0.568	2006-07-26	0.1038	0.1683	0.2248	0.4019	0.4048	0.2299
PL	Continental	soil	0.175	0.920	2009-04-23	0.095	0.1293	0.1616	0.2301	0.332	0.3053
PL	Continental	gv	0.922	0.333	2004-07-30	0.0171	0.0562	0.0224	0.5547	0.2005	0.0668
PL	Continental	npv	0.243	0.587	2020-08-18	0.1016	0.1572	0.2119	0.3477	0.3704	0.2174
RO	Continental	soil	0.168	0.823	2021-05-12	0.0657	0.1099	0.135	0.1897	0.2678	0.2205
RO	Continental	gv	0.905	0.365	2020-07-10	0.02	0.0569	0.028	0.5594	0.1974	0.072
RO	Continental	npv*	0.262	0.550	2022-07-20	0.1078	0.1732	0.2522	0.4315	0.4594	0.2525

Table SA3 continuation

Test site	Biogeographical region	endmember	NDVI	SWIRr	Acquisition date	Reflectance					
SE	Boreal	soil*	0.241	0.949	1990-05-05	0.0764	0.116	0.16	0.2617	0.3749	0.3558
SE	Boreal	gv*	0.929	0.322	2016-06-05	0.0133	0.0407	0.0204	0.5505	0.1431	0.0461
SE	Boreal	npv*	0.153	0.607	2003-04-15	0.1245	0.1594	0.1926	0.2623	0.3474	0.211
SA	Mediterranean	soil*	0.117	0.934	2020-08-06	0.0718	0.0956	0.1309	0.1656	0.2518	0.2351
SA	Mediterranean	gv*	0.913	0.343	2018-03-09	0.0158	0.0587	0.0279	0.6102	0.1815	0.0623
SA	Mediterranean	npv*	0.231	0.496	1985-09-14	0.0816	0.1472	0.2171	0.3476	0.4494	0.2231
UK	Atlantic	soil	0.178	0.942	2020-04-21	0.0821	0.1239	0.174	0.2492	0.3289	0.3098
UK	Atlantic	gv	0.945	0.307	2010-06-20	0.0149	0.045	0.0183	0.6467	0.1871	0.0575
UK	Atlantic	npv*	0.282	0.608	1999-09-10	0.1176	0.1587	0.1971	0.3518	0.3567	0.2169

Table SA4 Acquisition dates of very-high resolution images accessed through Google Earth Pro and corresponding Landsat and Sentinel-2 scenes used for visual evaluation of ground cover fractions.

Test site	Date of very-high resolution data	Date of medium resolution data	Medium resolution sensor	Number of validation points
AL	2012-04-02	2012-03-31	Landsat 7/ETM+	46
BE	2020-05-09	2020-05-07	Sentinel-2A/MSI	25
		2020-05-10	Sentinel-2A/MSI	19
CR	2018-09-01	2018-08-31	Sentinel-2B/MSI	22
		2018-09-03	Sentinel-2B/MSI	12
DE	2014-09-05	2014-09-05	Landsat 8/OLI	34
		2014-09-06	Landsat 7/ETM+	6
ES	2019-07-31	2019-08-02	Landsat 7/ETM+	1
	2019-08-02	2019-08-02	Landsat 7/ETM+	24
FR	2020-04-01	2020-04-02	Sentinel-2B/MSI	18
		2020-04-03	Landsat 8/OLI	31
IE	2018-06-28	2018-06-28	Sentinel-2A/MSI	13
		2018-06-30	Landsat 8/OLI	9
		2018-06-30	Sentinel-2B/MSI	10
LU	2021-03-31	2021-03-30	Landsat 8/OLI	18
		2021-04-02	Sentinel-2A/MSI	27
PL	2019-09-01	2019-08-31	Landsat 8/OLI	3
		2019-08-31	Sentinel-2B/MSI	7
		2019-09-01	Landsat 7/ETM+	32
RO	2022-06-08	2022-06-07	Sentinel-2B/MSI	15
		2022-06-10	Sentinel-2B/MSI	17
SA	2017-03-16	2017-03-14	Landsat 8/OLI	8
		2017-03-15	Landsat 7/ETM+	9
		2017-03-15	Sentinel-2A/MSI	17
		2017-03-08	Sentinel-2A/MSI	10
SE	2018-05-31	2018-05-30	Sentinel-2B/MSI	19
		2018-06-01	Sentinel-2A/MSI	14
UK	2018-06-30	2018-06-29	Sentinel-2A/MSI	21
		2018-07-02	Sentinel-2A/MSI	18

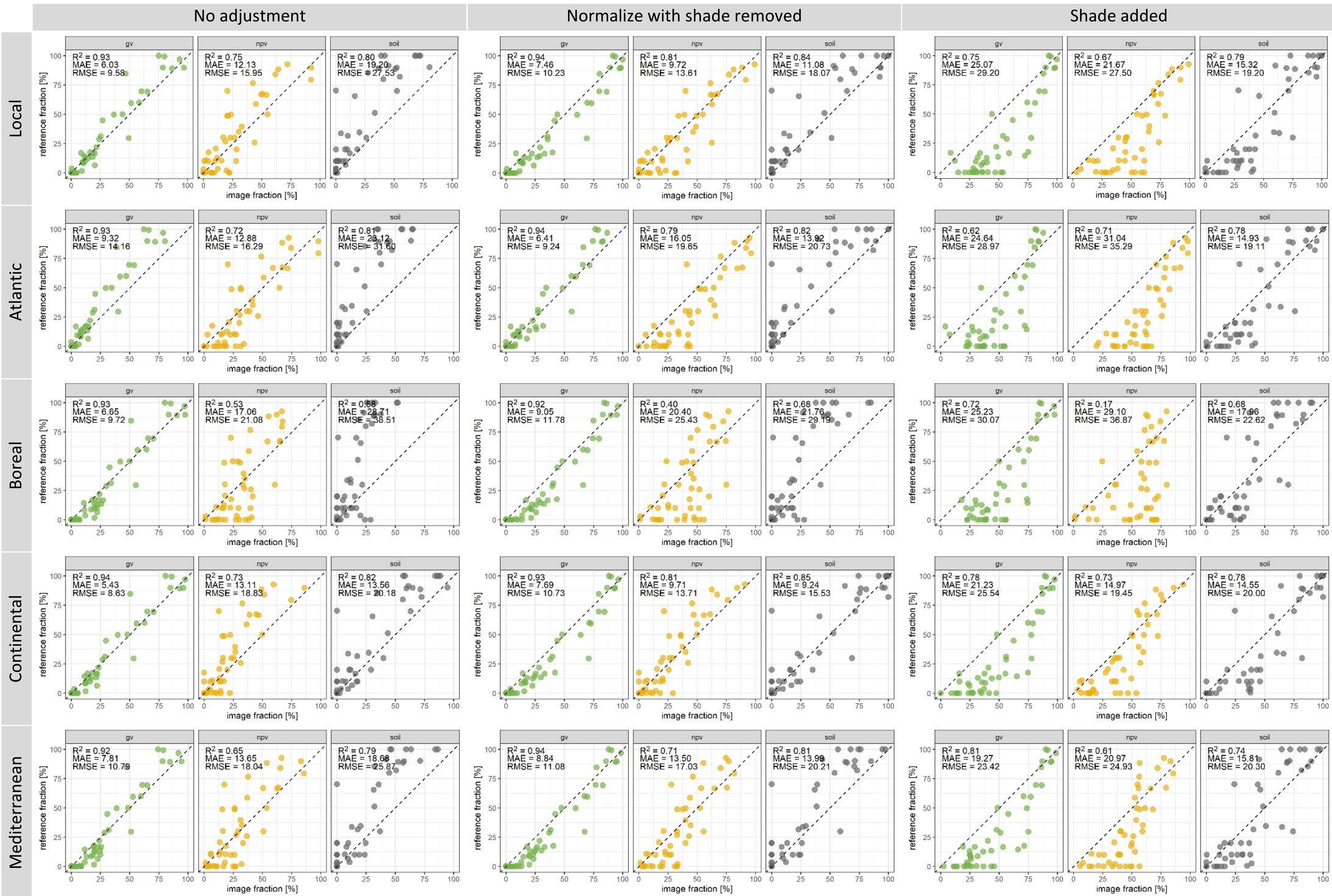

Figure SA2 Validation of the SMA results for the AL site. Results for five different endmember sets and under three different variants of accounting for the shade ground cover fraction.

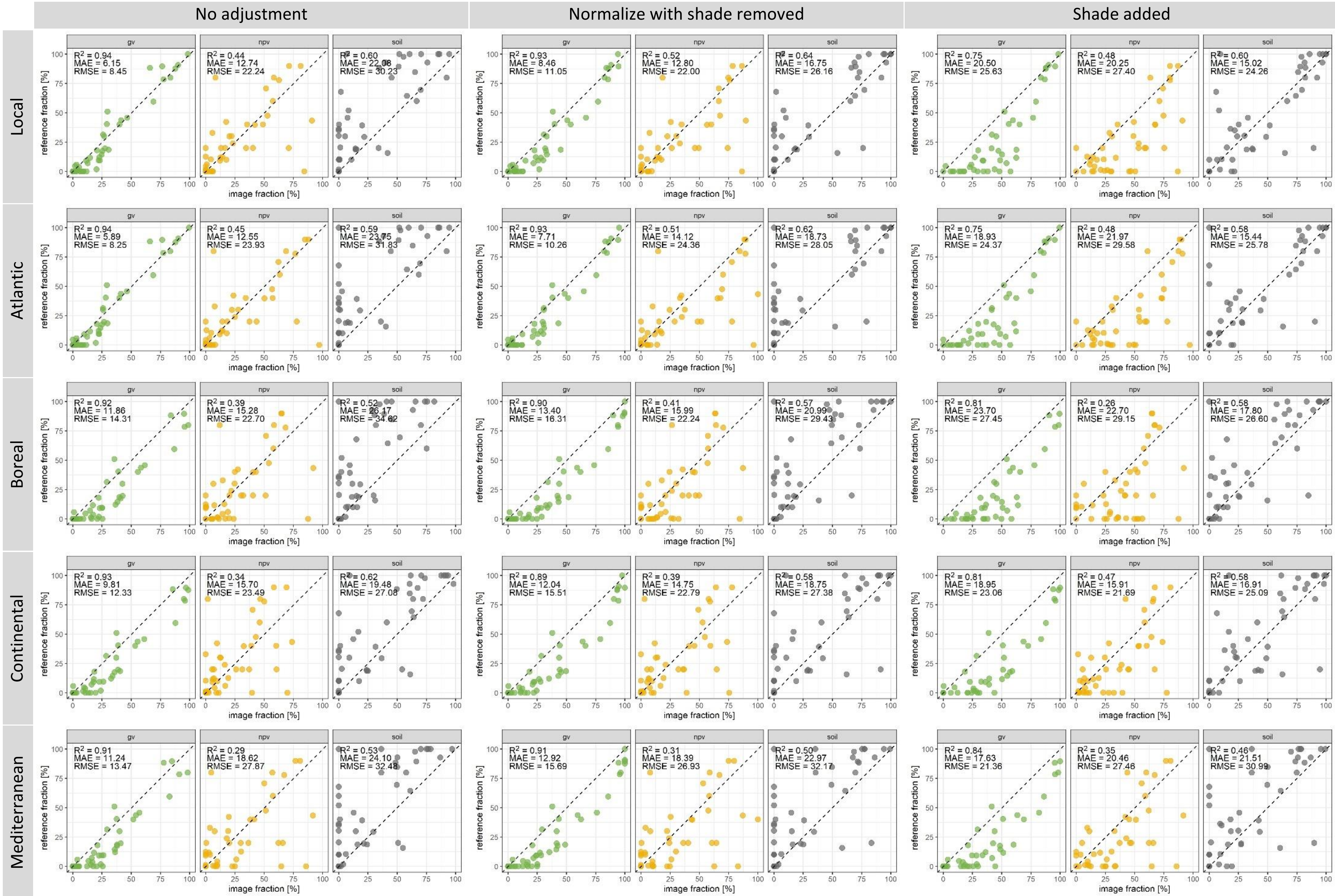

Figure SA3 Validation of the SMA results for the BX site. Results for five different endmember sets and under three different variants of accounting for the shade ground cover fraction.

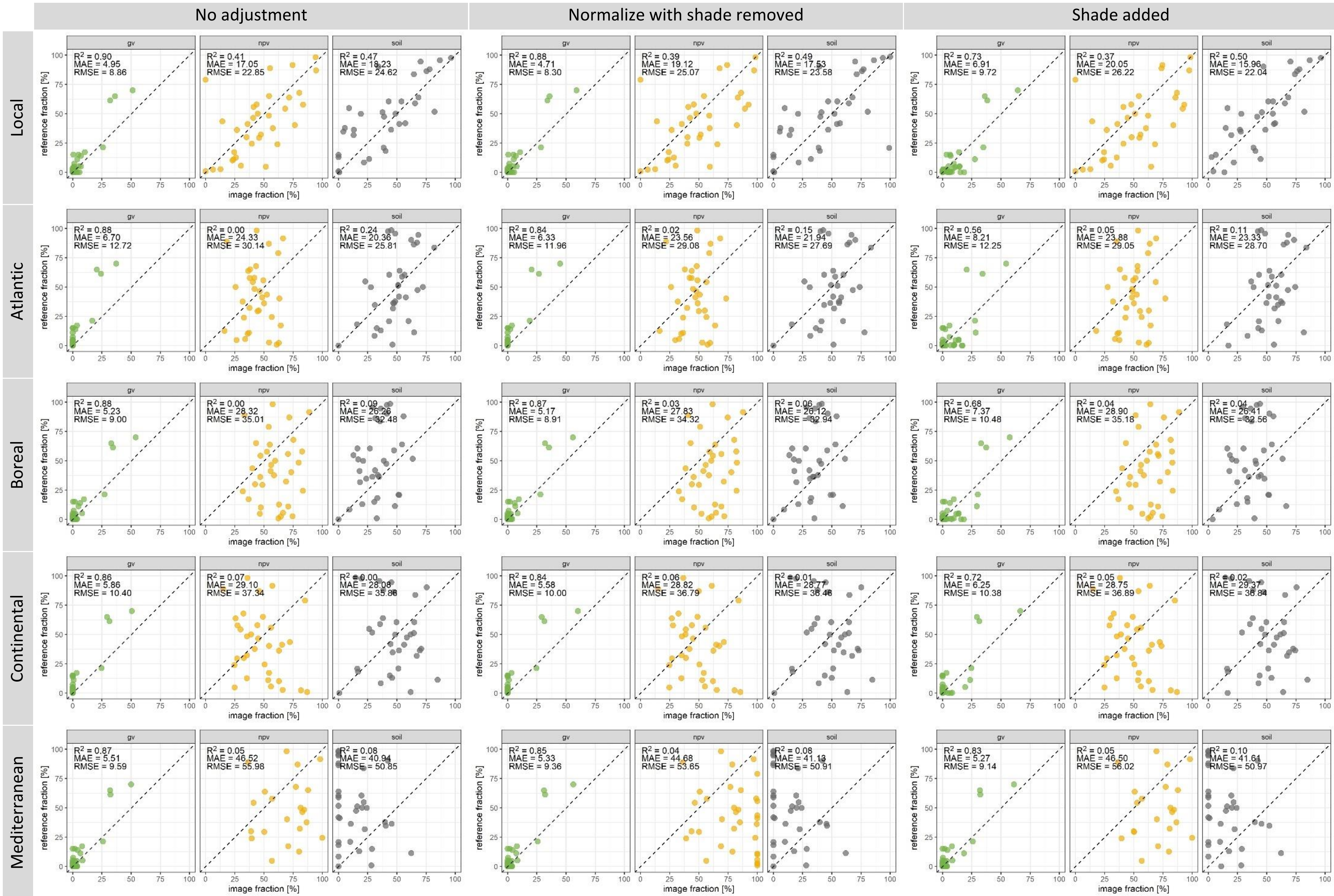

Figure SA4 Validation of the SMA results for the CR site. Results for five different endmember sets and under three different variants of accounting for the shade ground cover fraction.

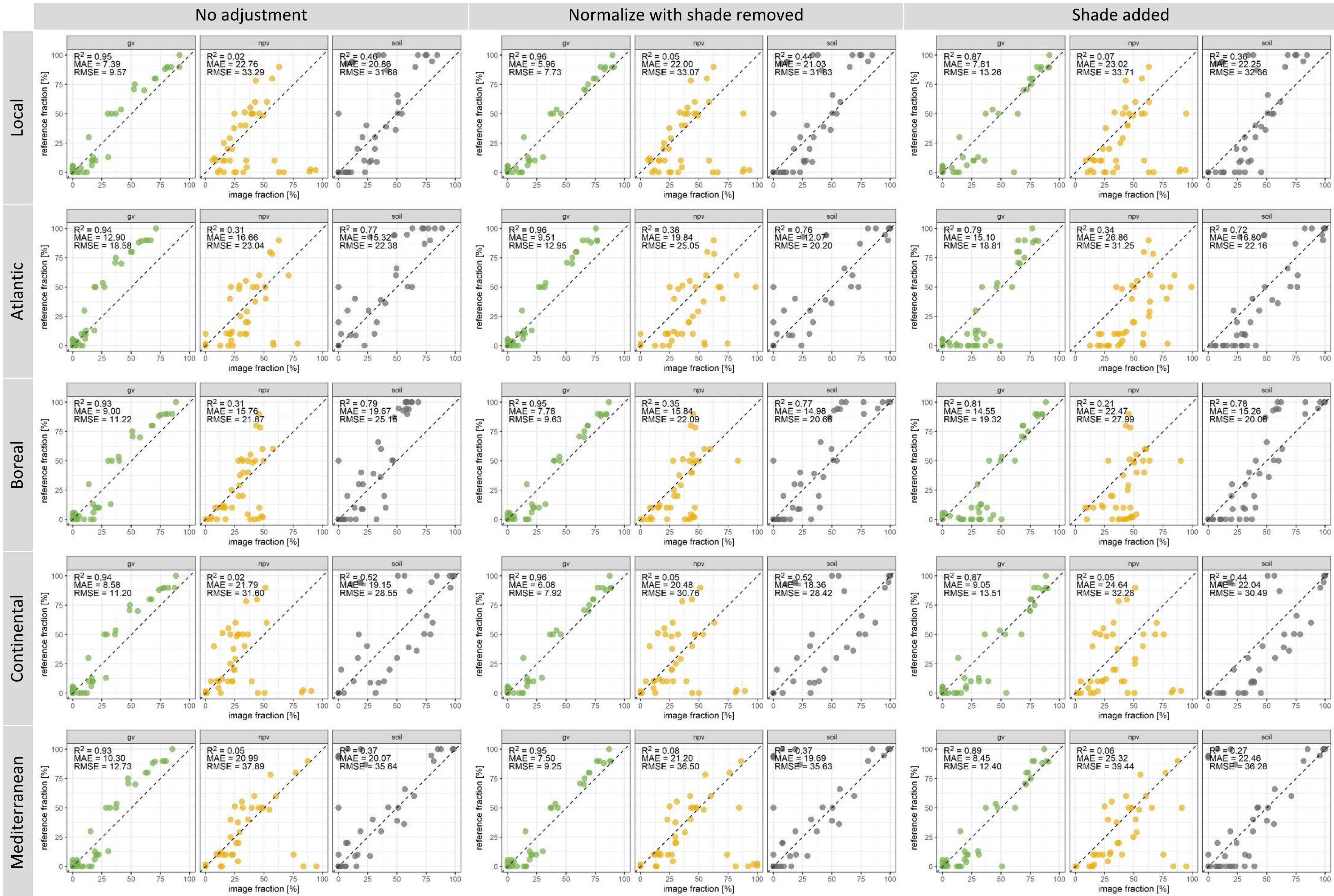

Figure SA5 Validation of the SMA results for the DE site. Results for five different endmember sets and under three different variants of accounting for the shade ground cover fraction.

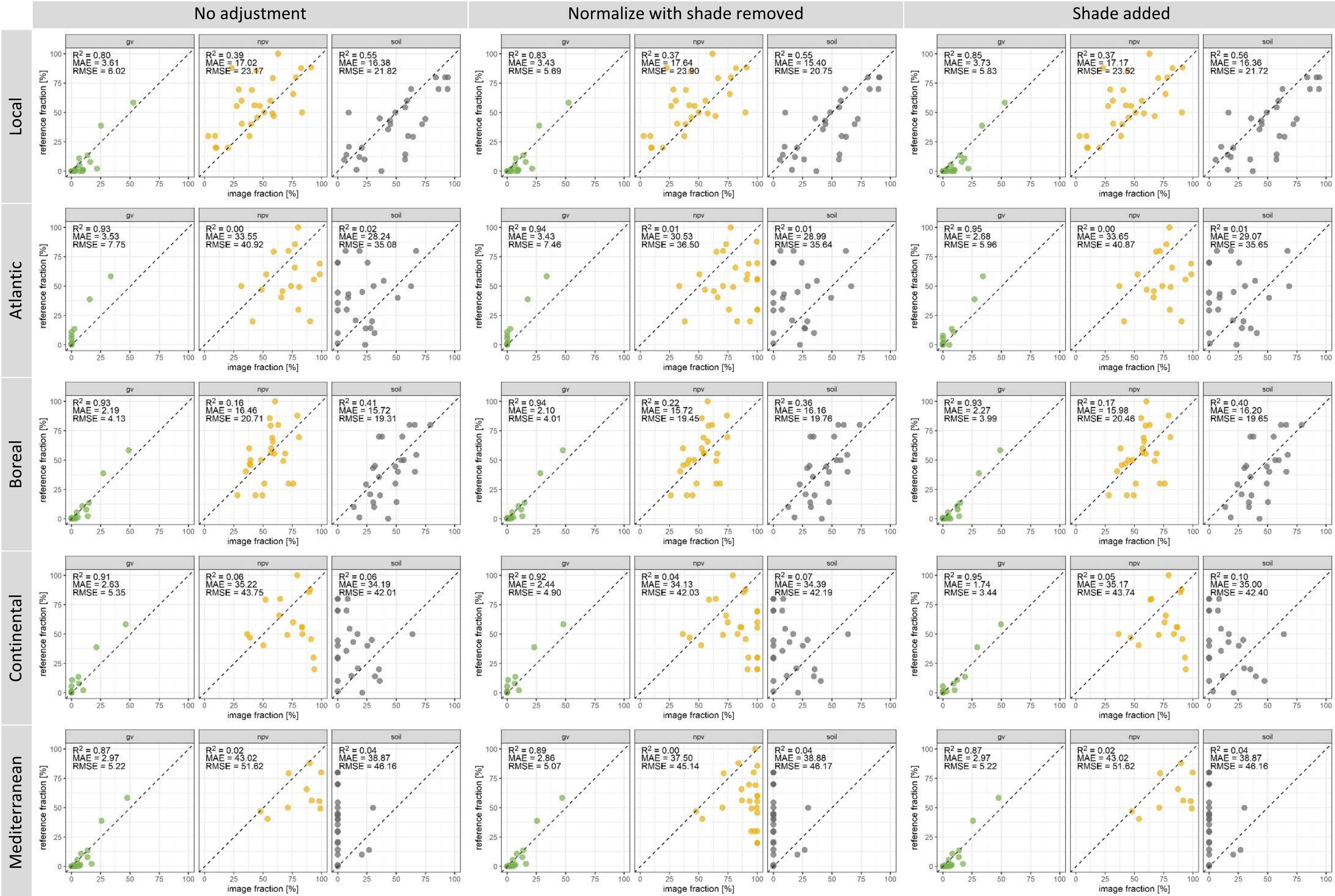

Figure SA6 Validation of the SMA results for the ES site. Results for five different endmember sets and under three different variants of accounting for the shade ground cover fraction.

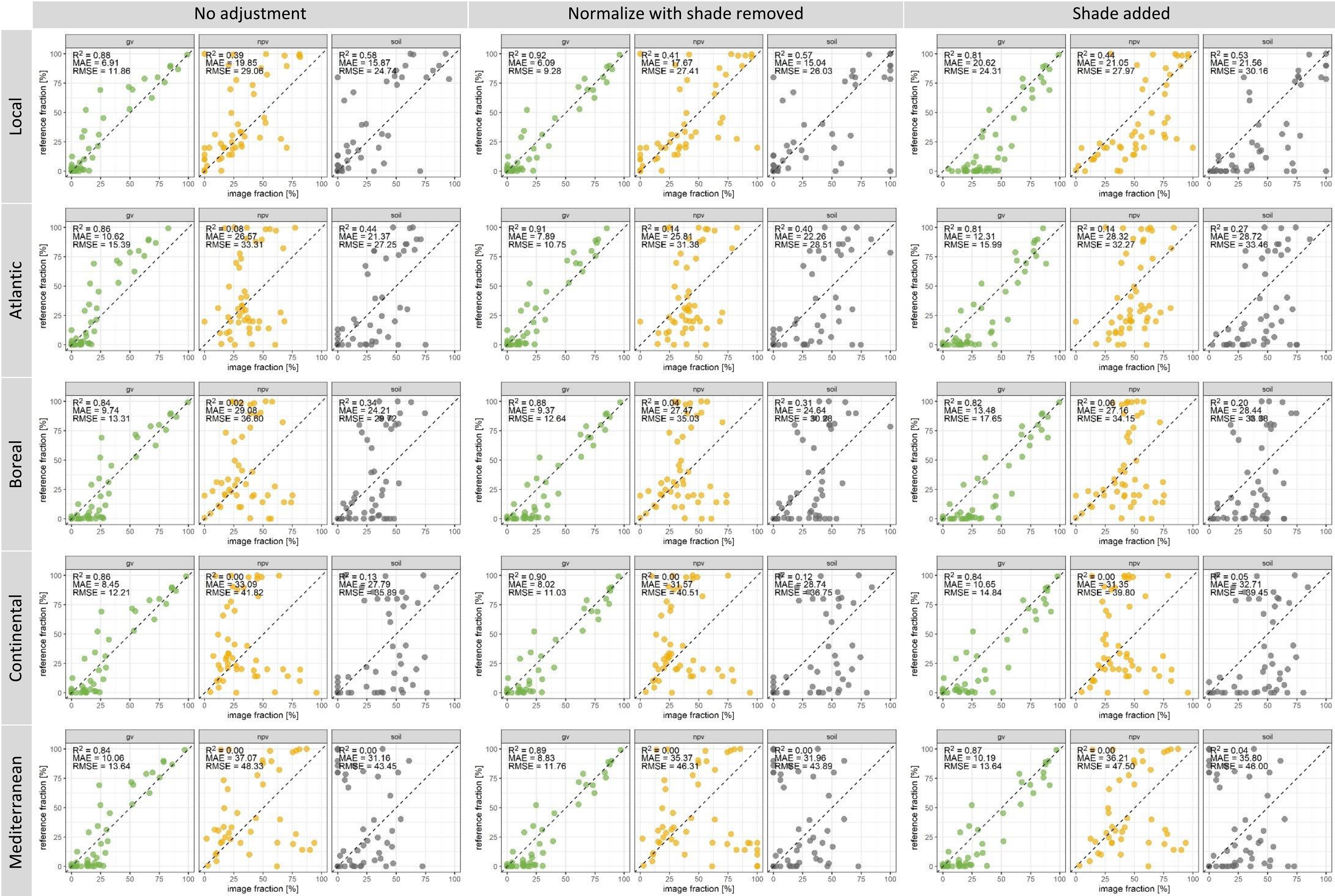

Figure SA7 Validation of the SMA results for the FR site. Results for five different endmember sets and under three different variants of accounting for the shade ground cover fraction.

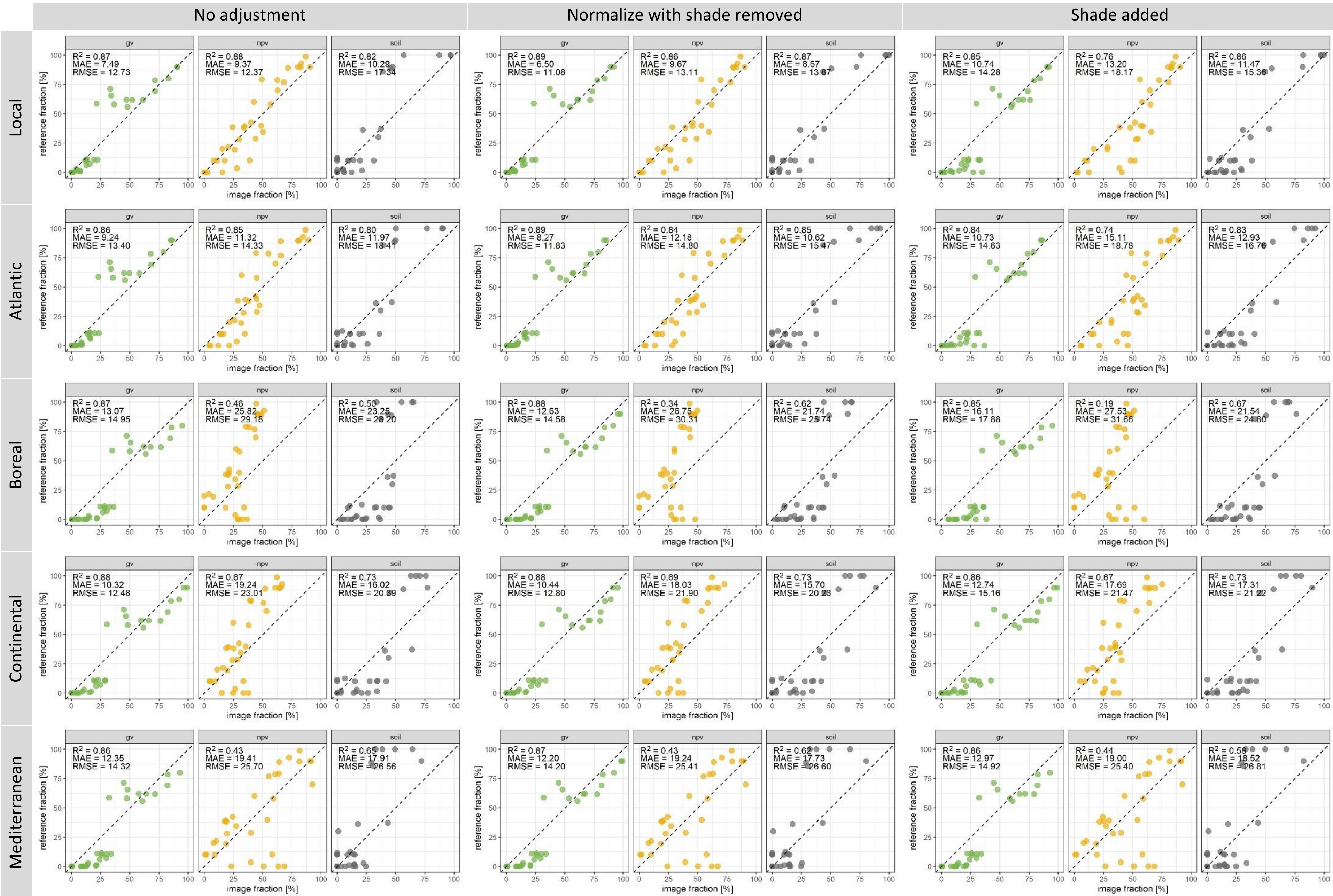

Figure SA8 Validation of the SMA results for the IE site. Results for five different endmember sets and under three different variants of accounting for the shade ground cover fraction.

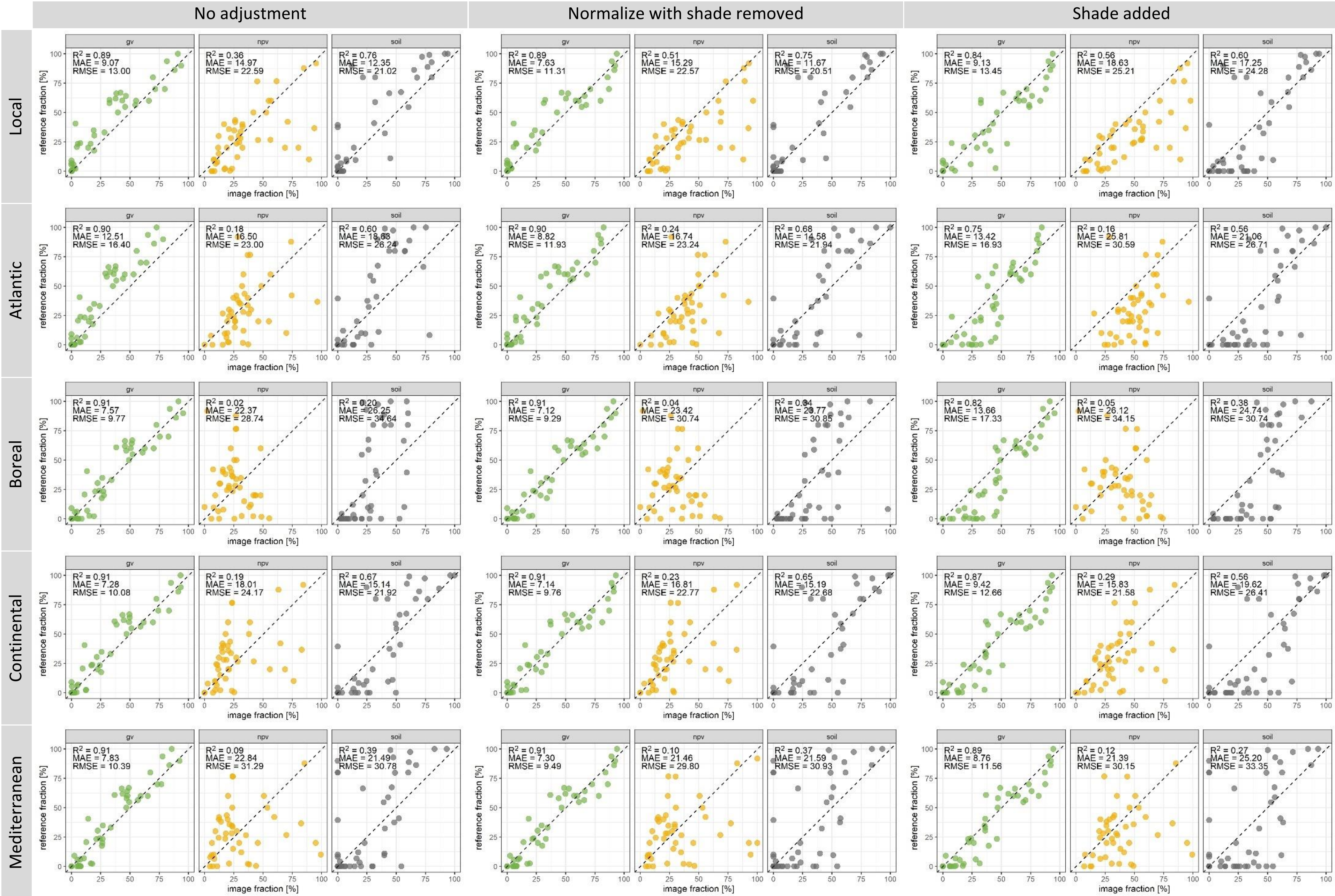

Figure SA9 Validation of the SMA results for the LX site. Results for five different endmember sets and under three different variants of accounting for the shade ground cover fraction.

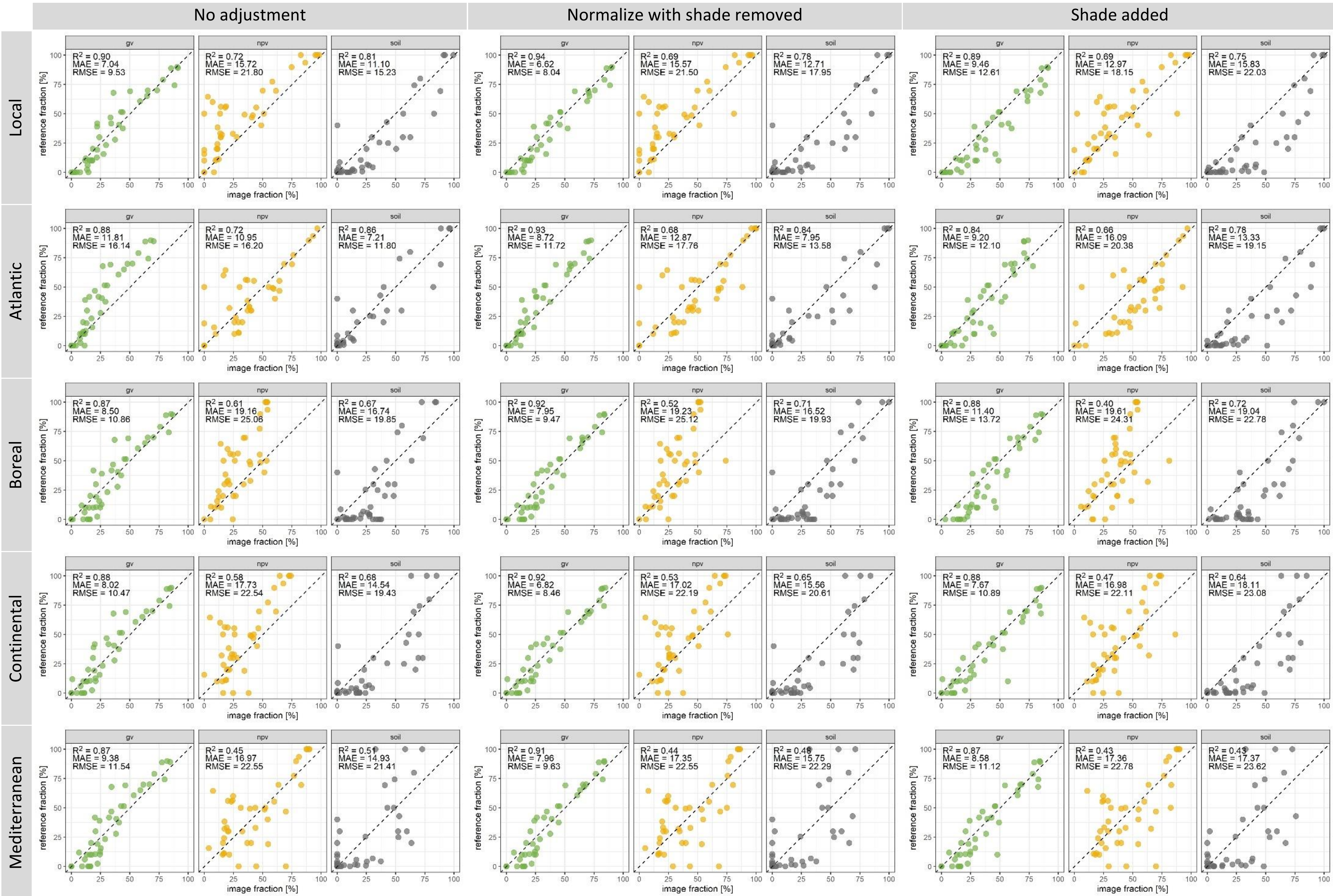

Figure SA10 Validation of the SMA results for the PL site. Results for five different endmember sets and under three different variants of accounting for the shade ground cover fraction.

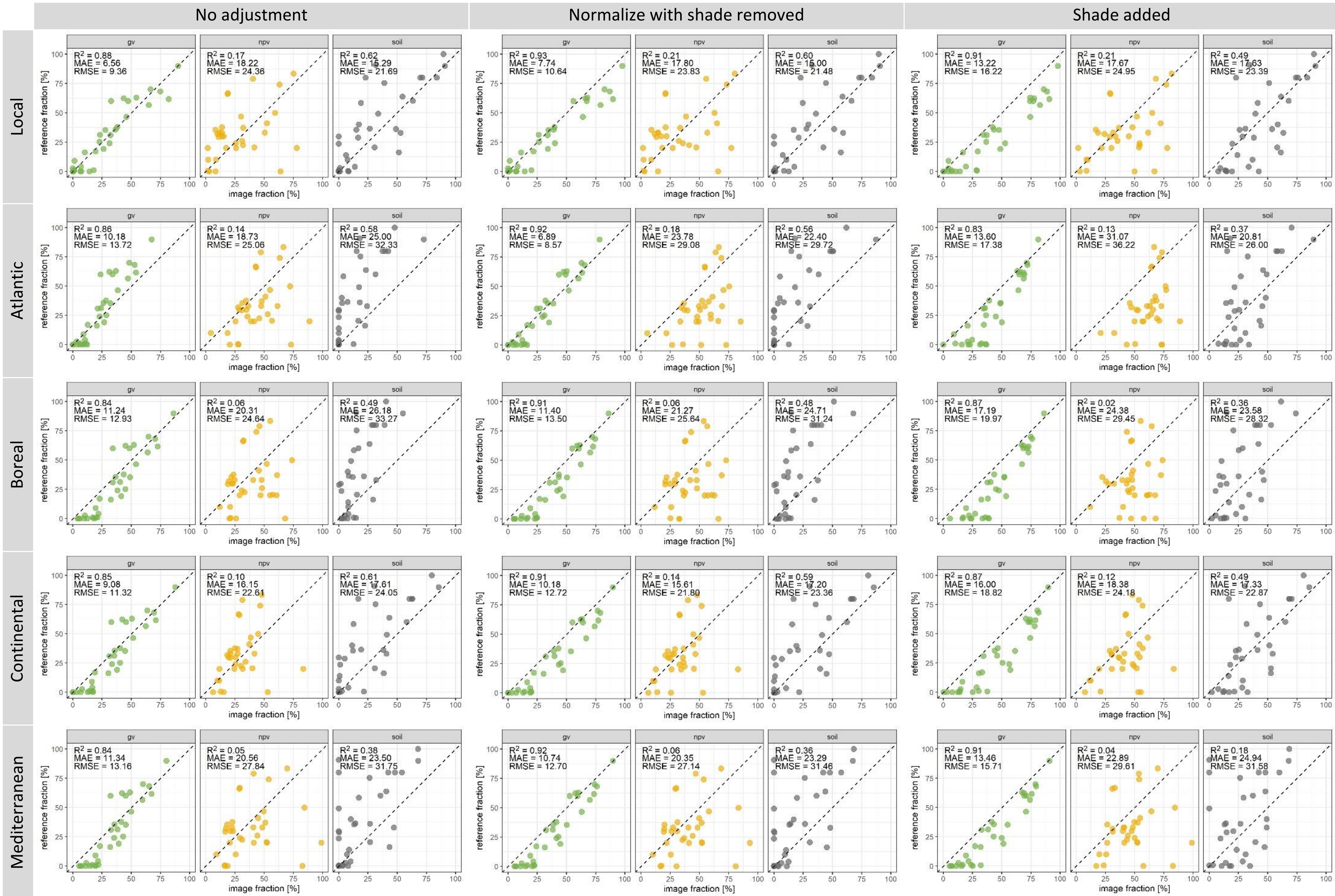

Figure SA11 Validation of the SMA results for the RO site. Results for five different endmember sets and under three different variants of accounting for the shade ground cover fraction.

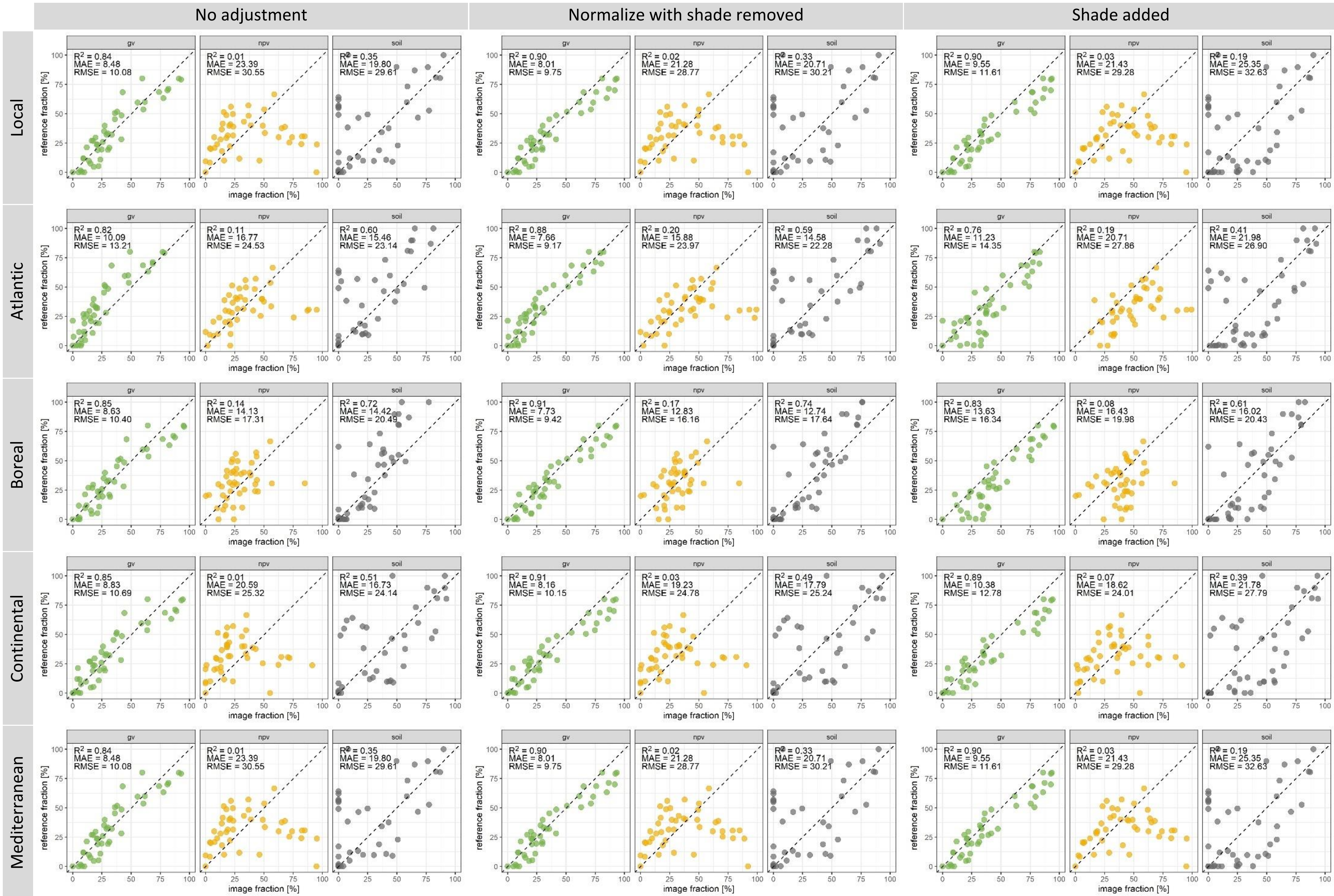

Figure SA12 Validation of the SMA results for the SA site. Results for five different endmember sets and under three different variants of accounting for the shade ground cover fraction.

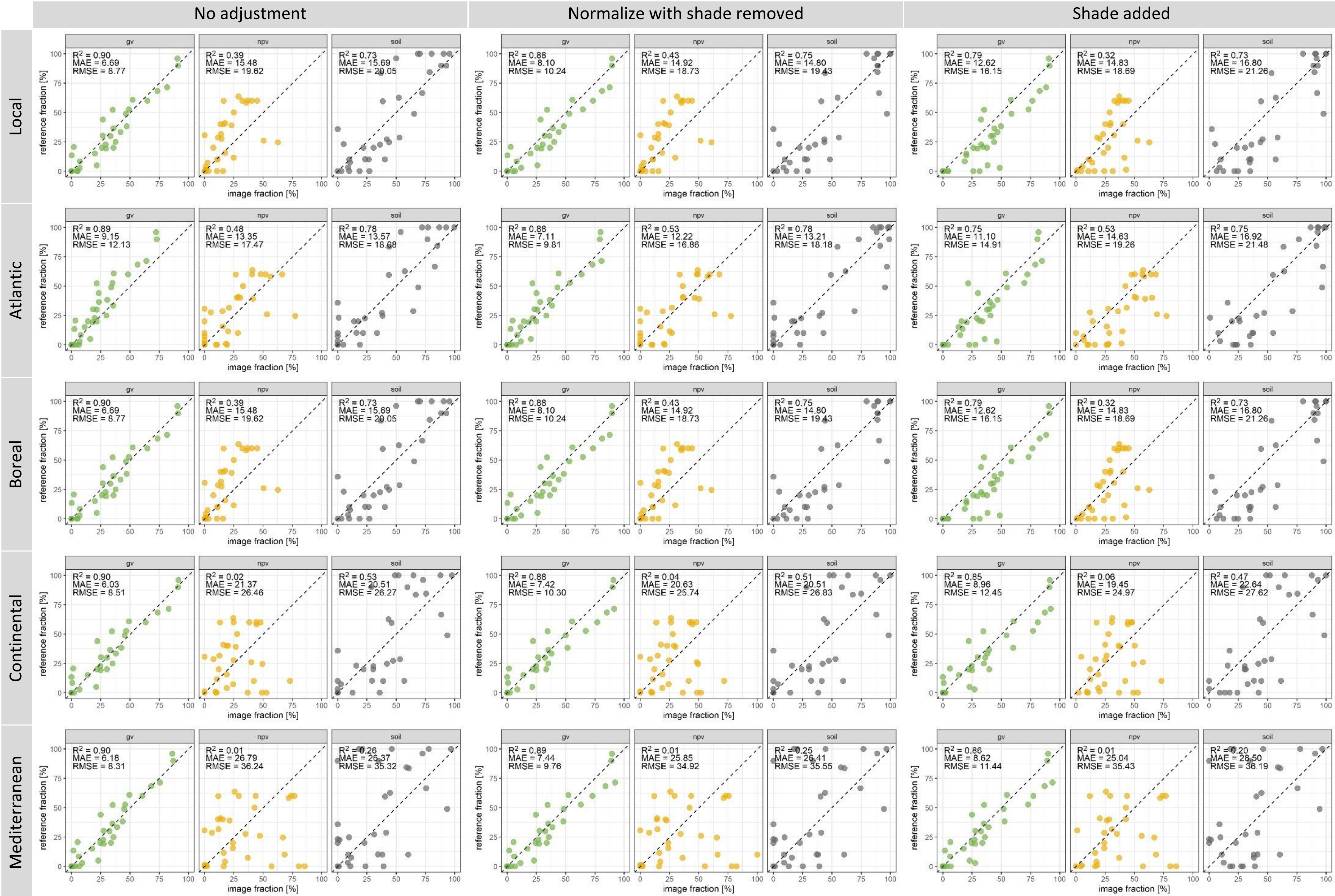

Figure SA13 Validation of the SMA results for the SE site. Results for five different endmember sets and under three different variants of accounting for the shade ground cover fraction.

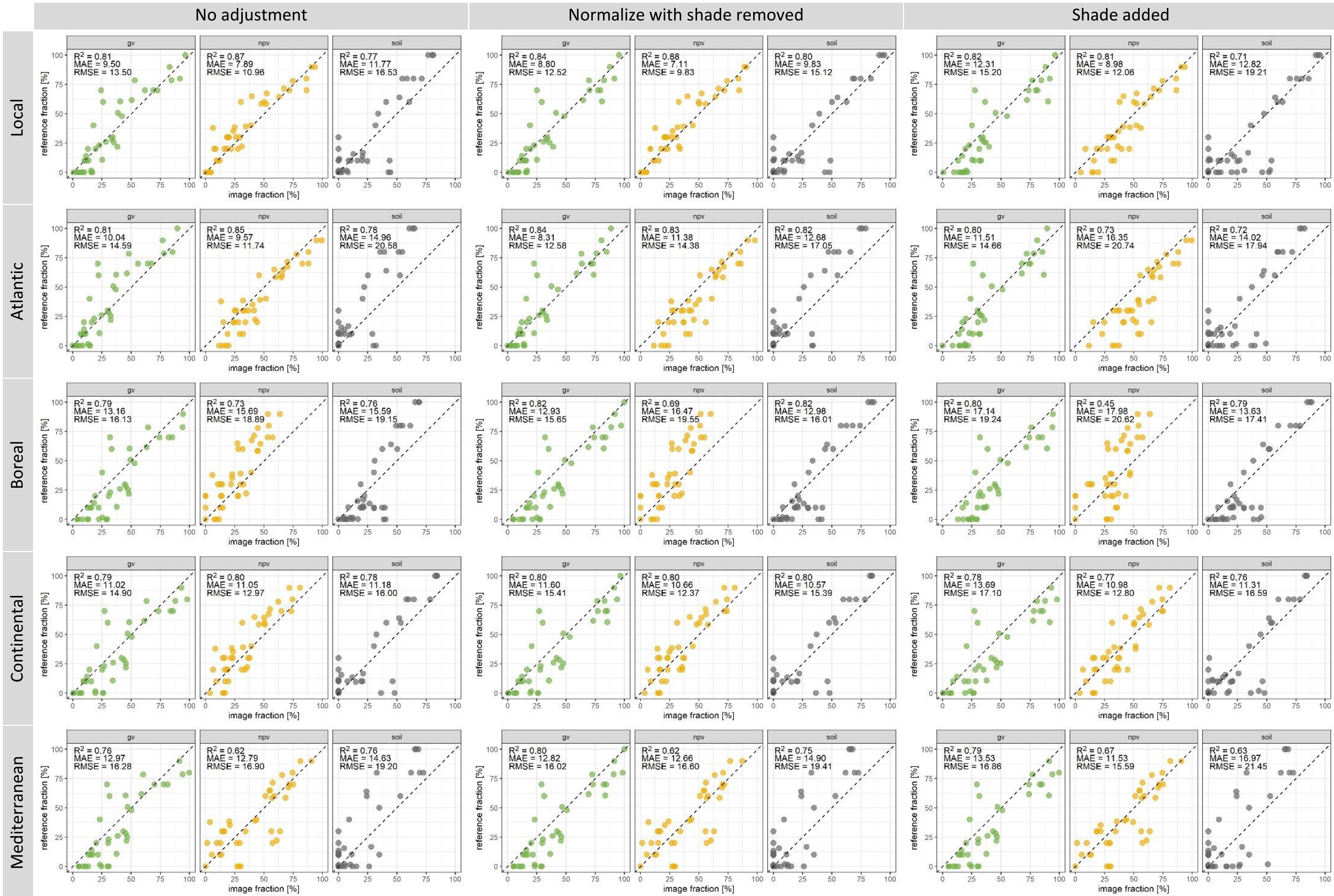

Figure SA14 Validation of the SMA results for the UK site. Results for five different endmember sets and under three different variants of accounting for the shade ground cover fraction.

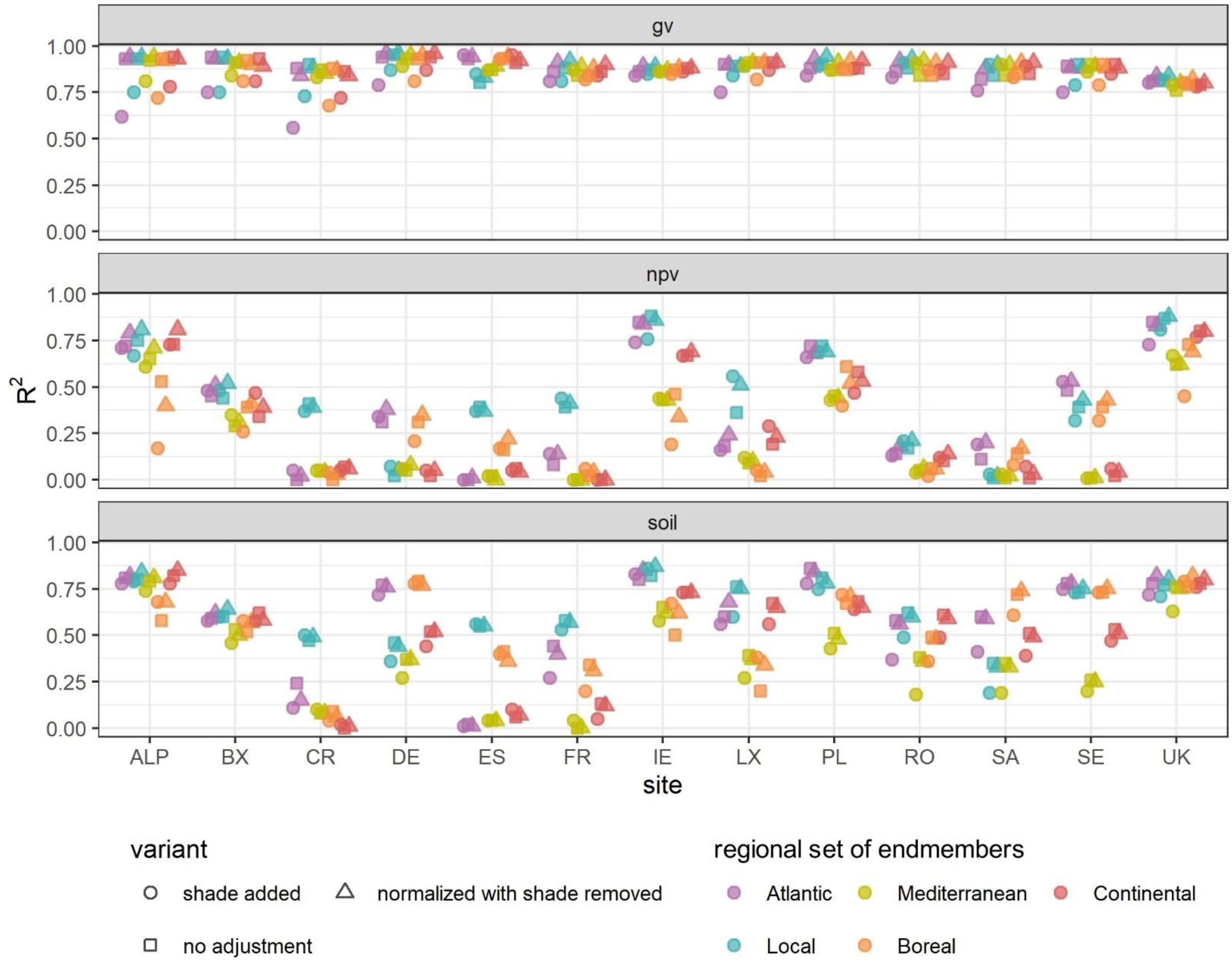

Figure SA15 The comparison of linear regression (R^2) obtained at each site, each regional set of endmembers, and under one of three variants for accounting for shade ground cover fraction.

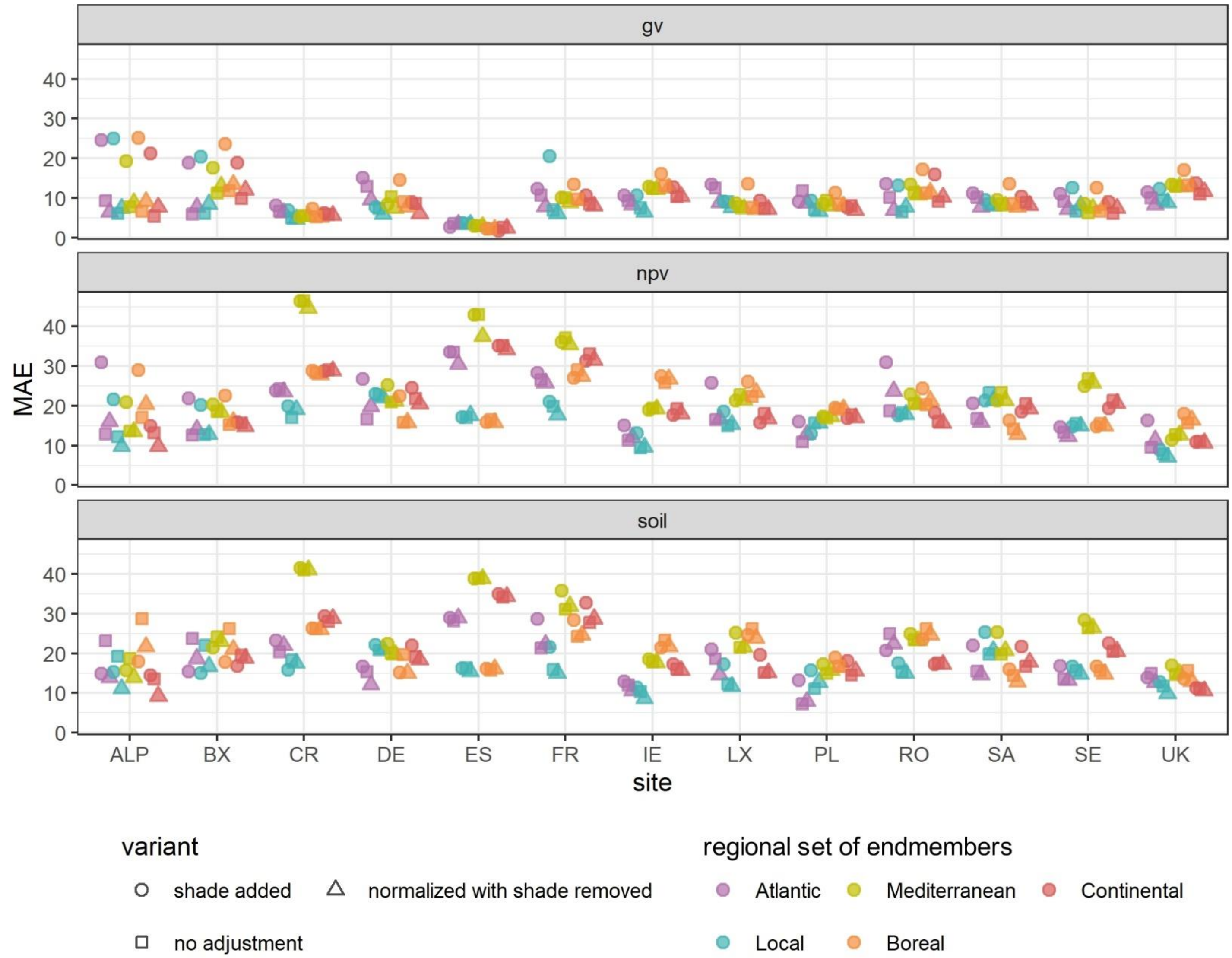

Figure SA16 The comparison Mean Absolute Error (MAE) obtained at each site, each regional set of endmembers, and under one of three variants for accounting for shade ground cover fraction.

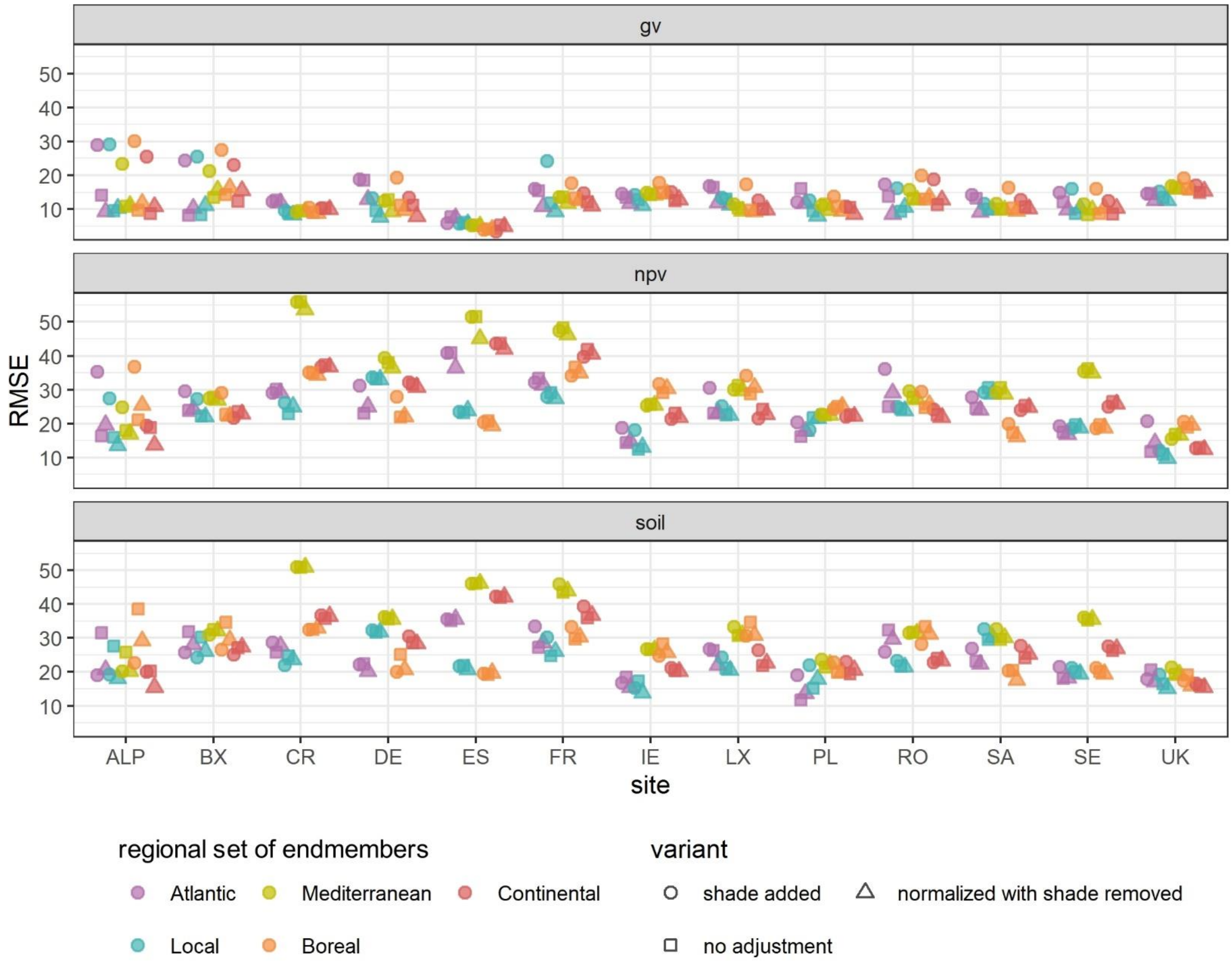

Figure SA17 The comparison of RMSE obtained at each site, each regional set of endmembers, and under one of three variants for accounting for shade ground cover fraction.

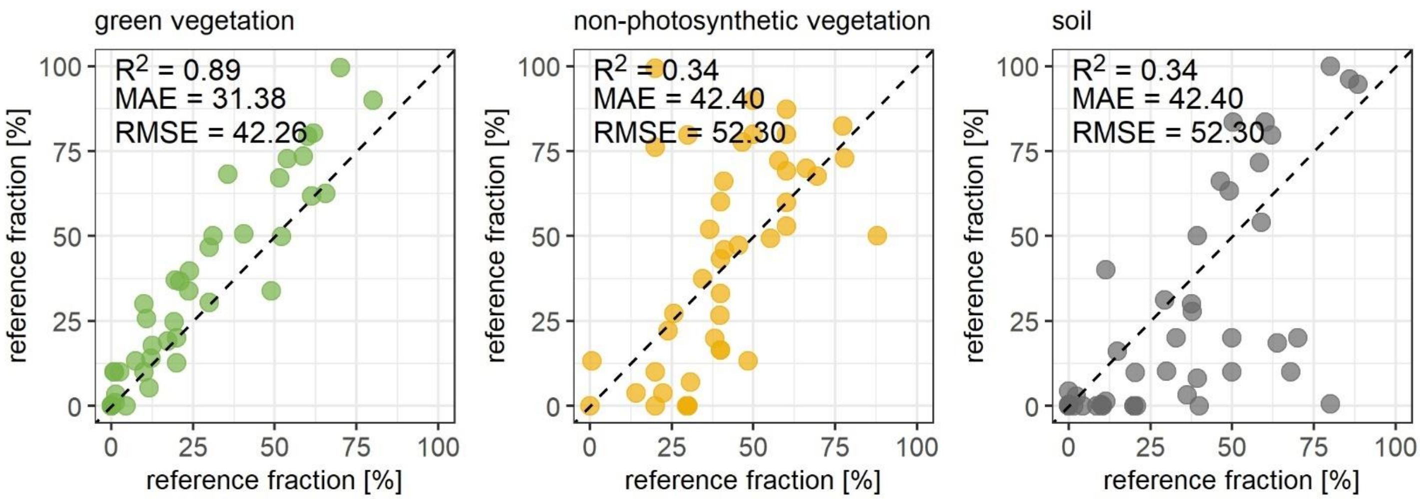

Figure SA18 Cross validation between green vegetation, non-photosynthetic vegetation, and soil ground cover fractions estimated by the main interpreter (x axis) and three independent experts (y axis) across 13 test sites.

Impact of data density and endmember definitions on long-term trends in ground cover fractions across European grasslands

Supplement B

Katarzyna Ewa Lewińska [1,2], Akpona Okujeni [3,1], Katja Kowalski [4,1], Fabian Lehmann [5],

Volker C. Radeloff [2], Ulf Leser [5], Patrick Hostert [1,6]

[1] Geography Department, Humboldt-Universität zu Berlin, Unter den Linden 6, 10099 Berlin, Germany.

[2] SILVIS Lab, Department of Forest and Wildlife Ecology, University of Wisconsin-Madison, 1630 Linden Drive, Madison WI 53706, USA.

[3] Helmholtz Center Potsdam, GFZ German Research Center for Geosciences, Telegrafenberg, 14473 Potsdam, Germany

[4] Earth Observation for Ecosystem Management, School of Life Sciences, Technical University of Munich, 11 Hans-Carl-v.-Carlowitz-Platz 2, 85354 Freising, Germany

[5] Department of Computer Science, Humboldt-Universität zu Berlin, Unter den Linden 6, 10099 Berlin, Germany

[6] Integrative Research Institute on Transformations of Human-Environment Systems (IRI THESys), Humboldt-Universität zu Berlin, Unter den Linden 6, 10099 Berlin, Germany

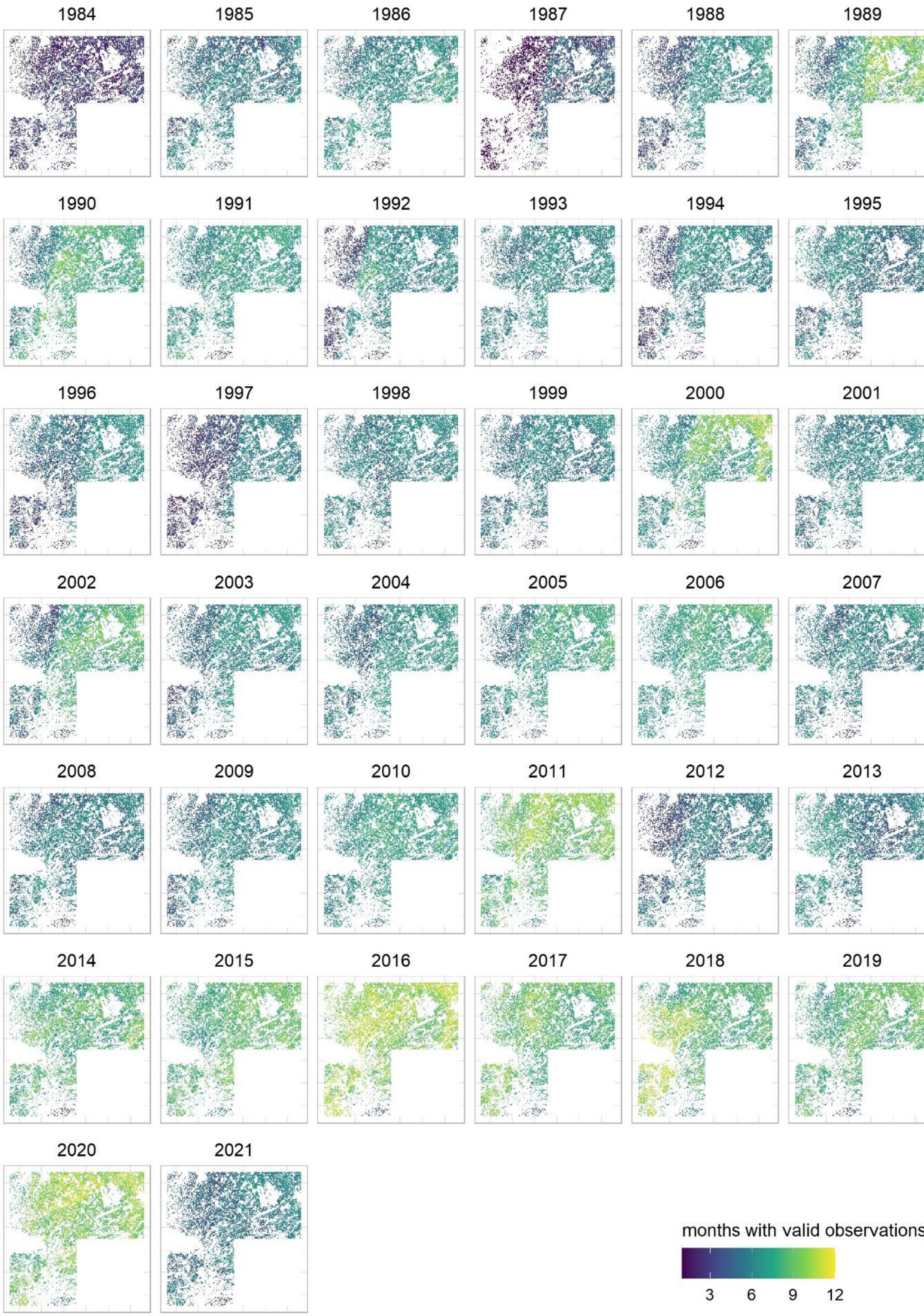

Figure SB1 Availability of monthly composites across 1984-2021 calendar years on the AL site.

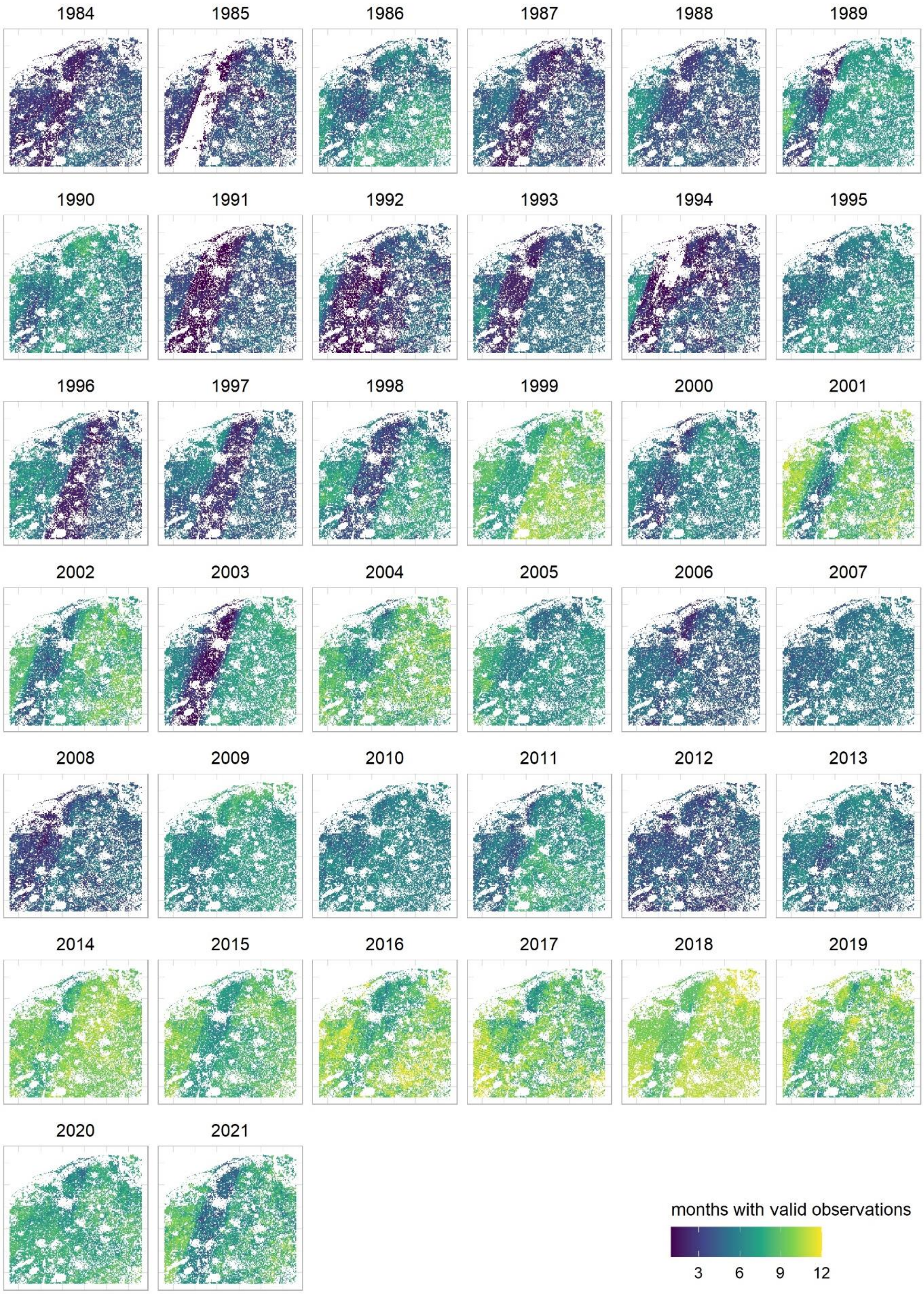

Figure SB2 Availability of monthly composites across 1984-2021 calendar years on the BX site.

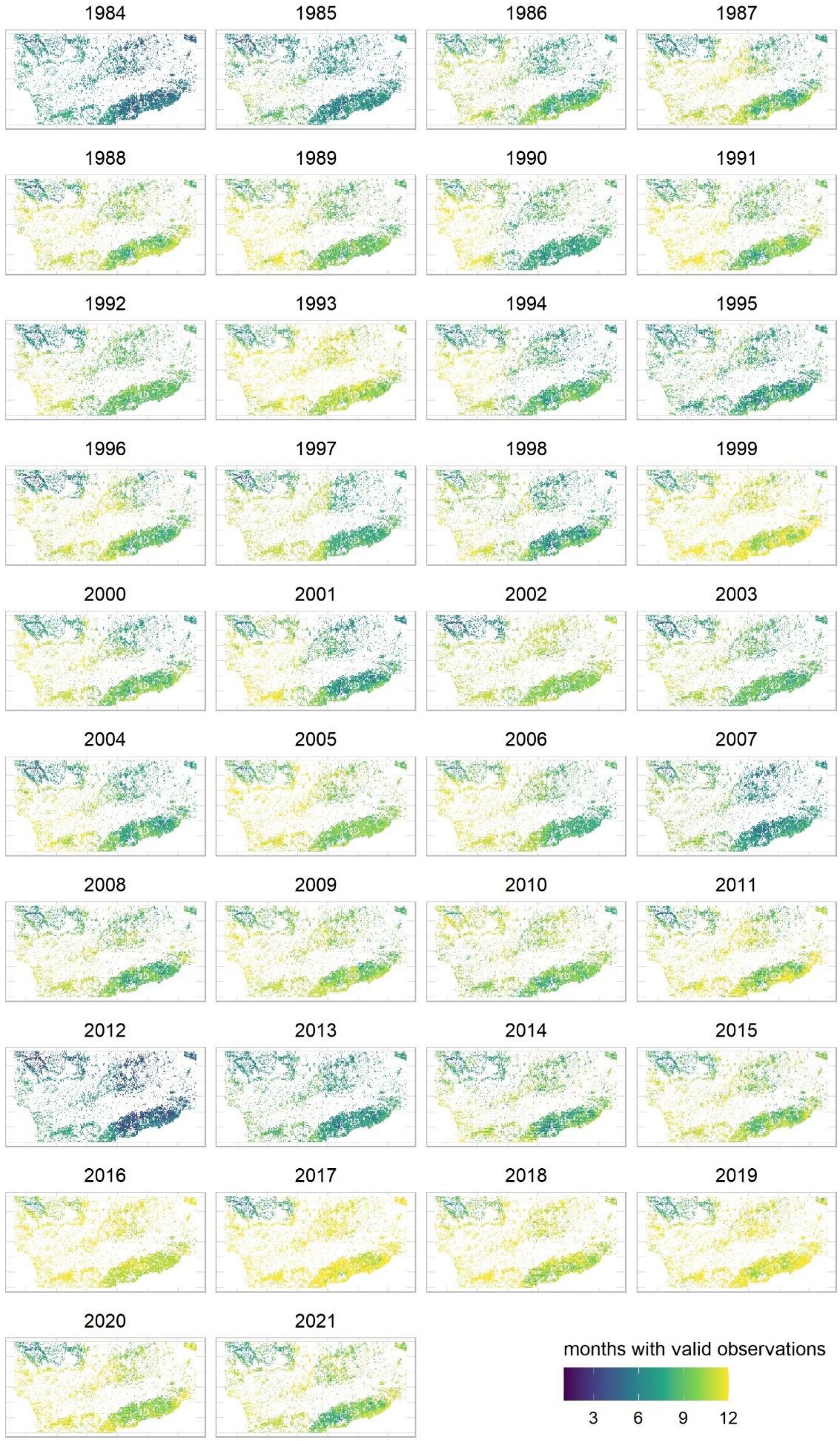

Figure SB3 Availability of monthly composites across 1984-2021 calendar years on the CR site.

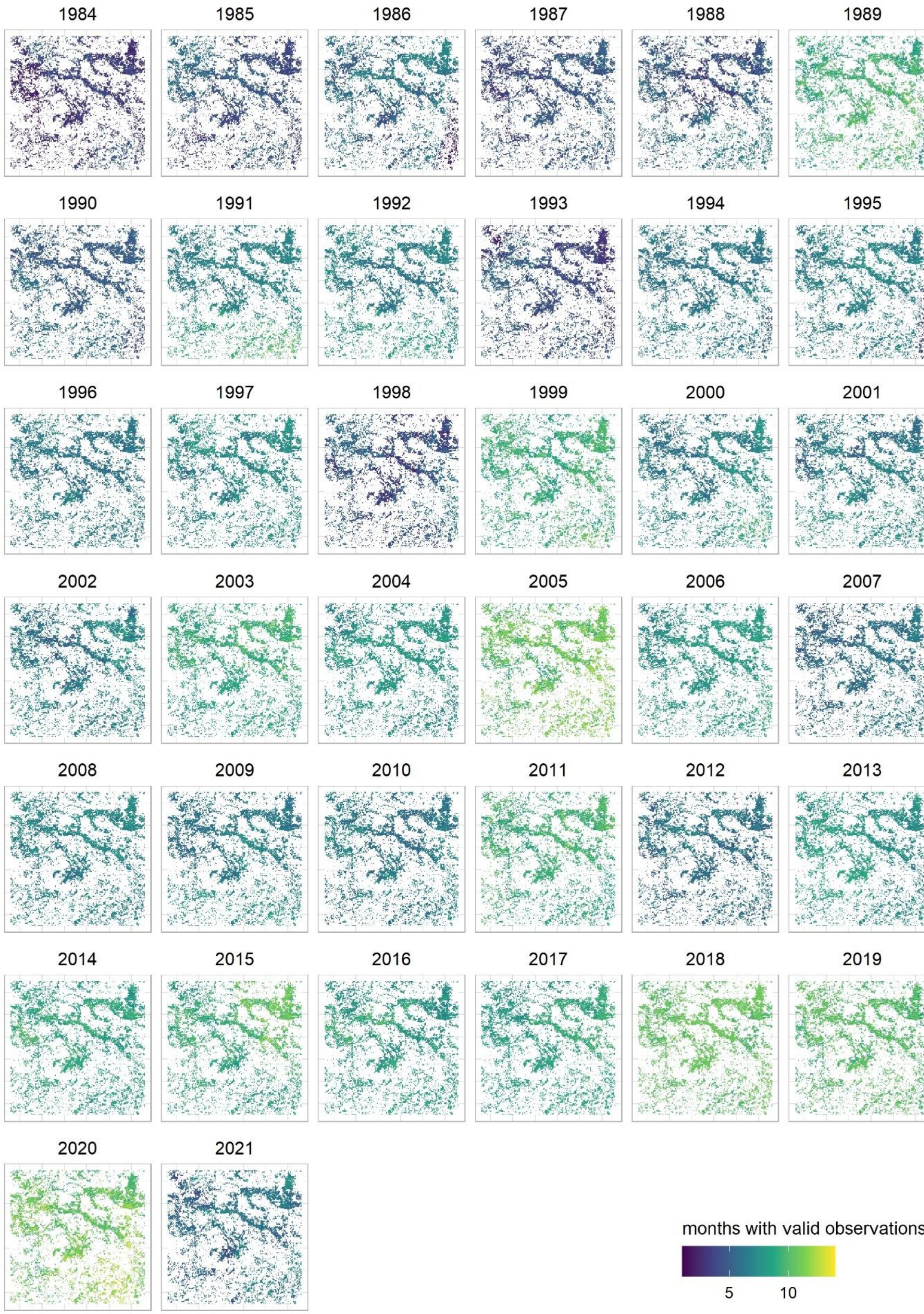

Figure SB4 Availability of monthly composites across 1984-2021 calendar years on the DE site.

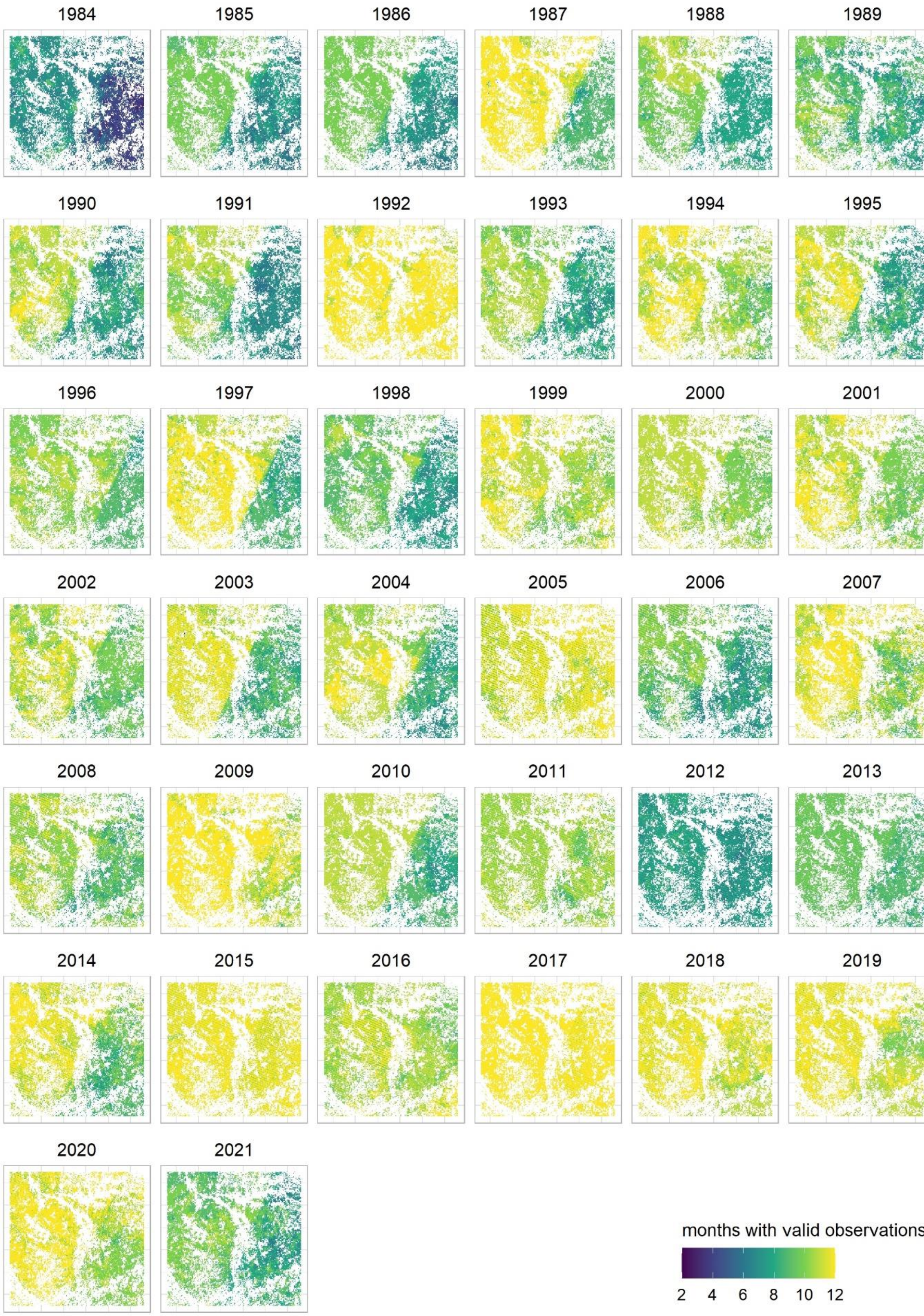

Figure SB5 Availability of monthly composites across 1984-2021 calendar years on the ES site.

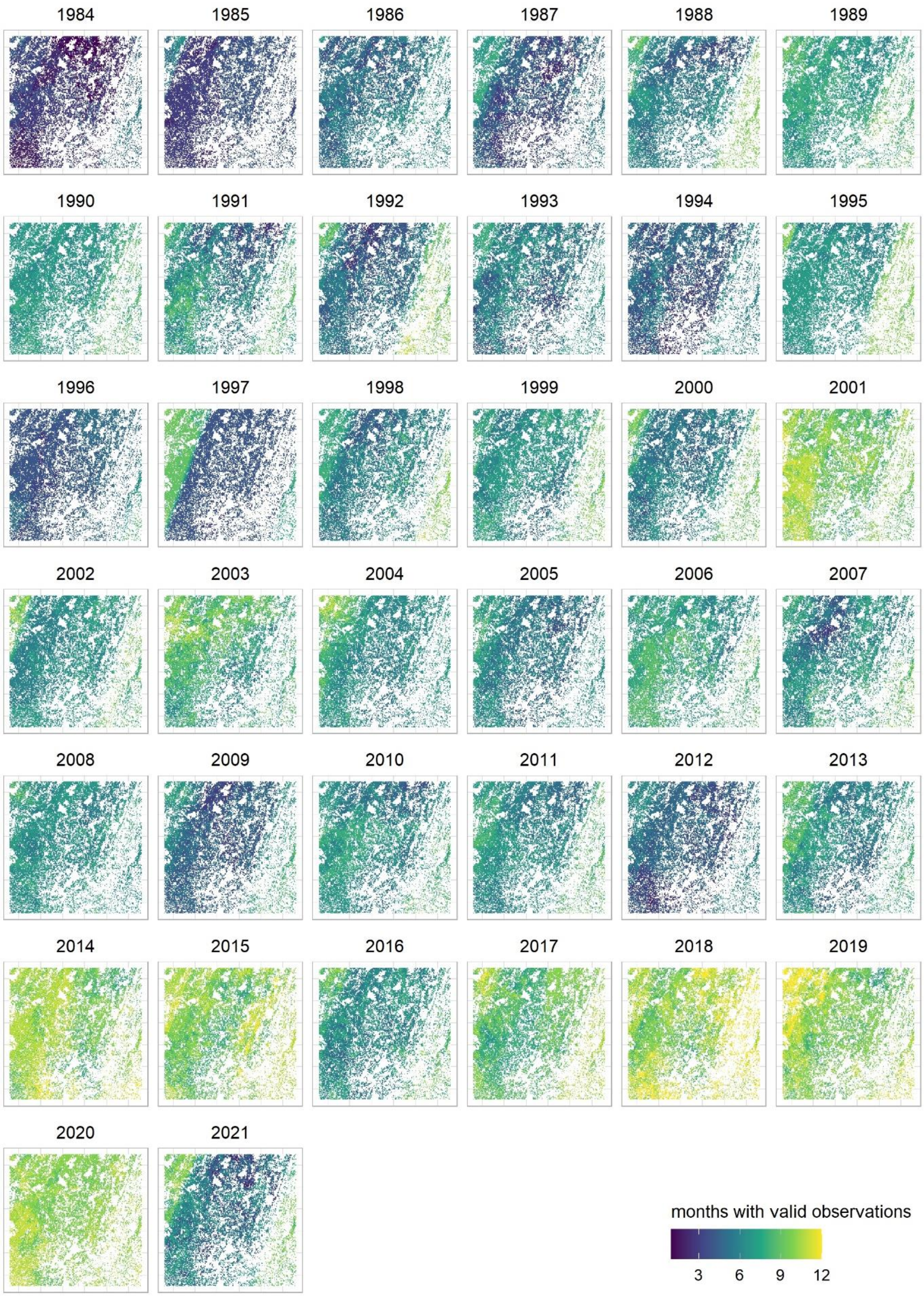

Figure SB6 Availability of monthly composites across 1984-2021 calendar years on the FR site.

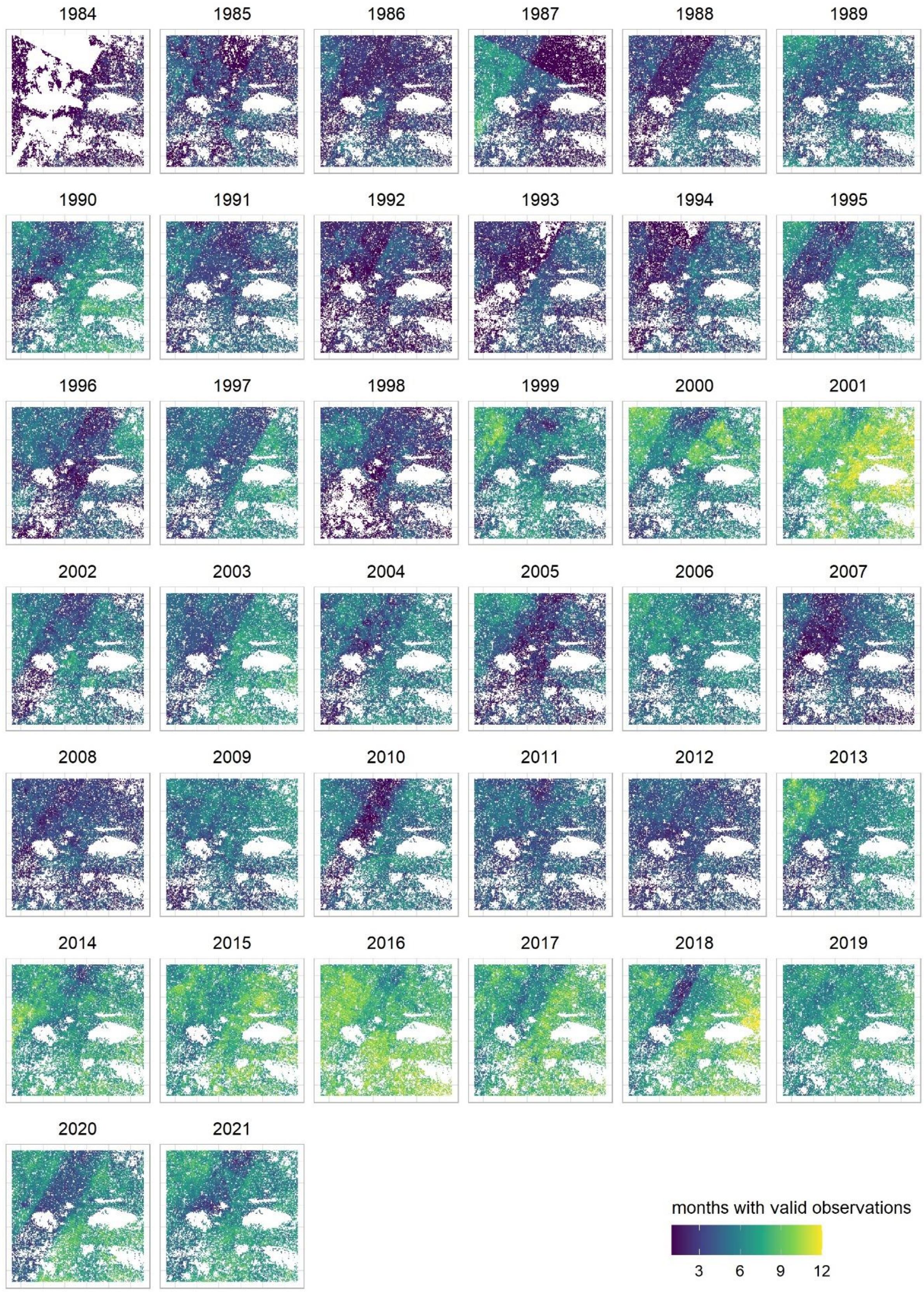

Figure SB7 Availability of monthly composites across 1984-2021 calendar years on the IE site.

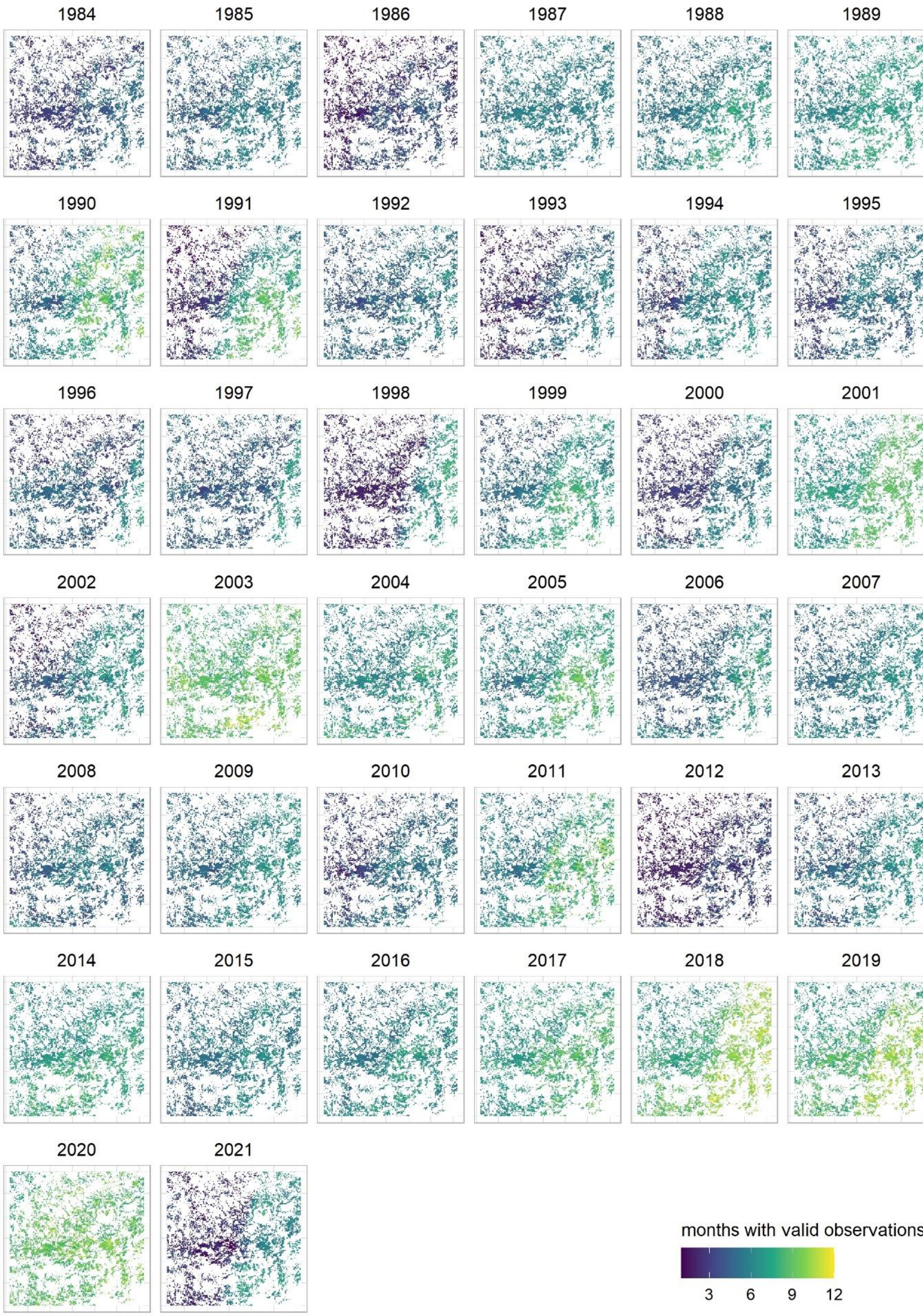

Figure SB8 Availability of monthly composites across 1984-2021 calendar years on the LX site.

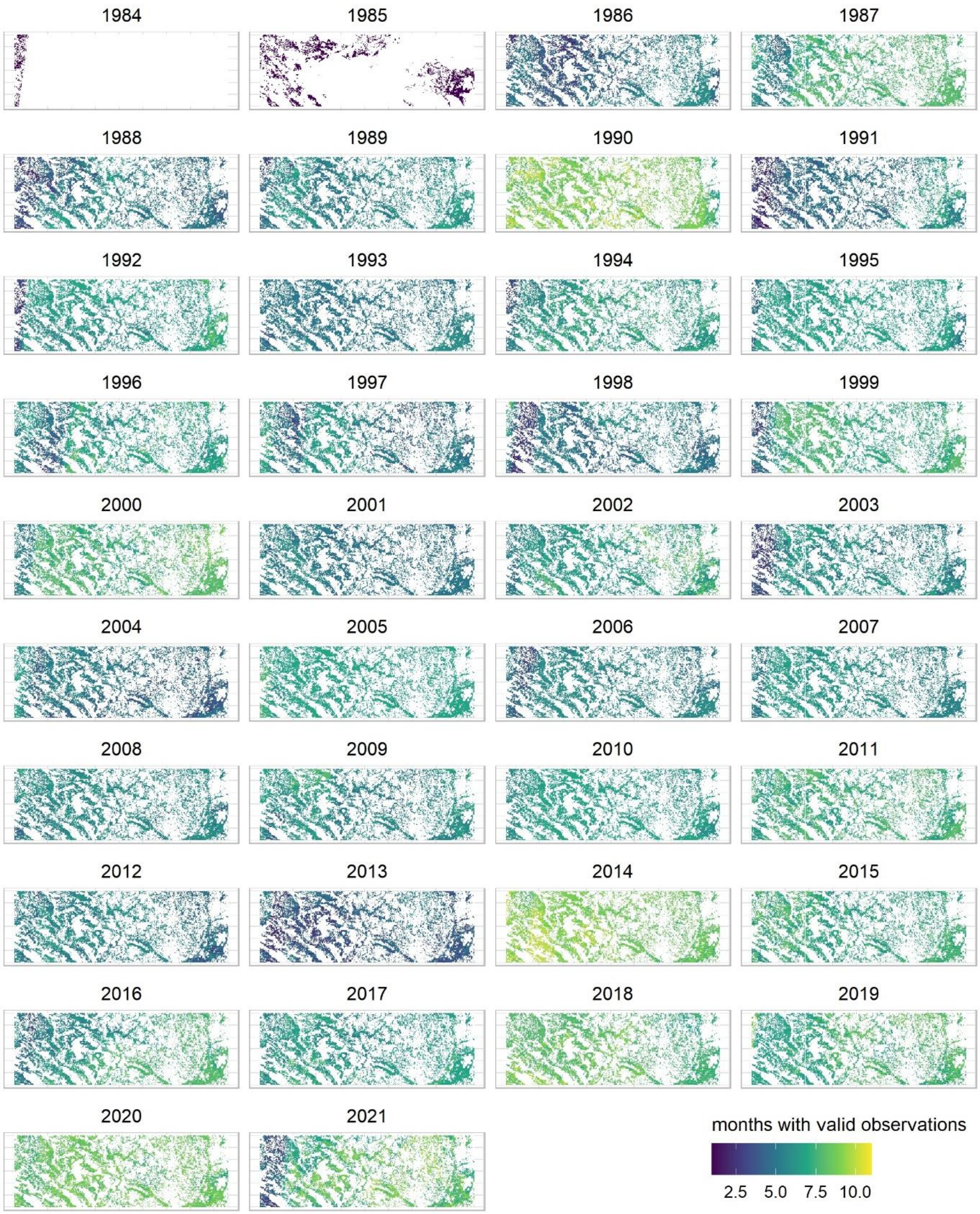

Figure SB9 Availability of monthly composites across 1984-2021 calendar years on the PL site.

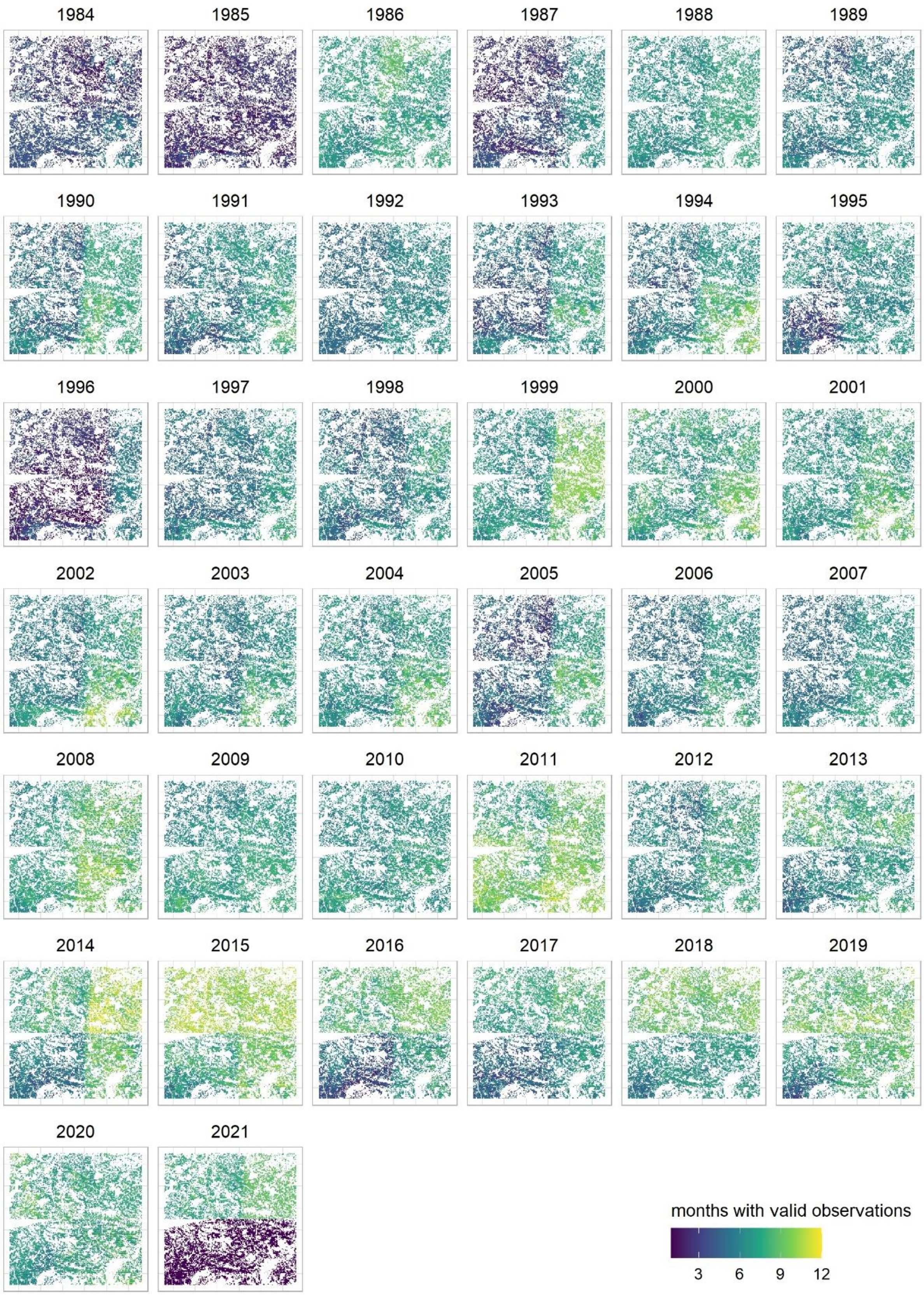

Figure SB10 Availability of monthly composites across 1984-2021 calendar years on the RO site.

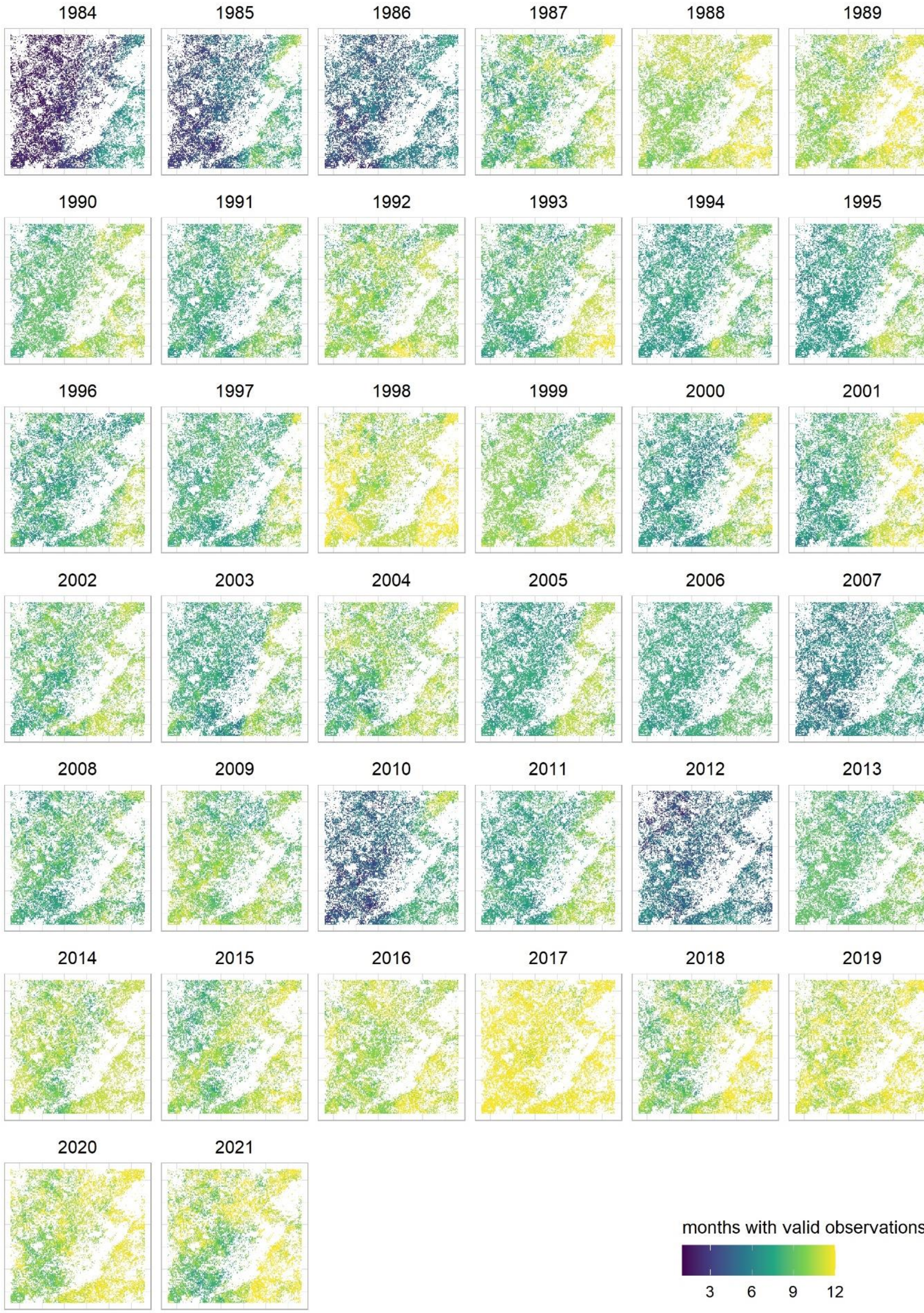

Figure SB11 Availability of monthly composites across 1984-2021 calendar years on the SA site.

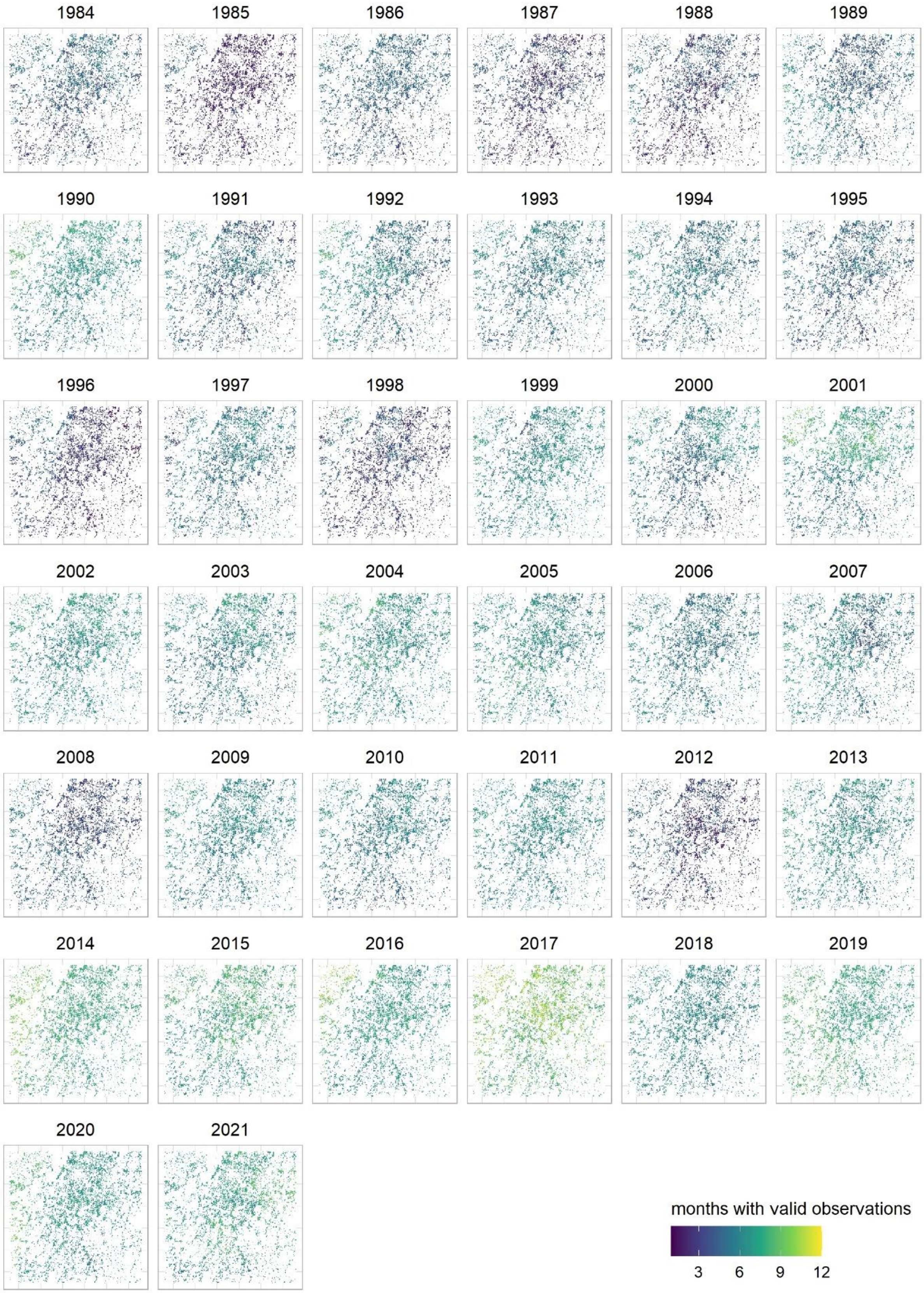

Figure SB12 Availability of monthly composites across 1984-2021 calendar years on the SE site.

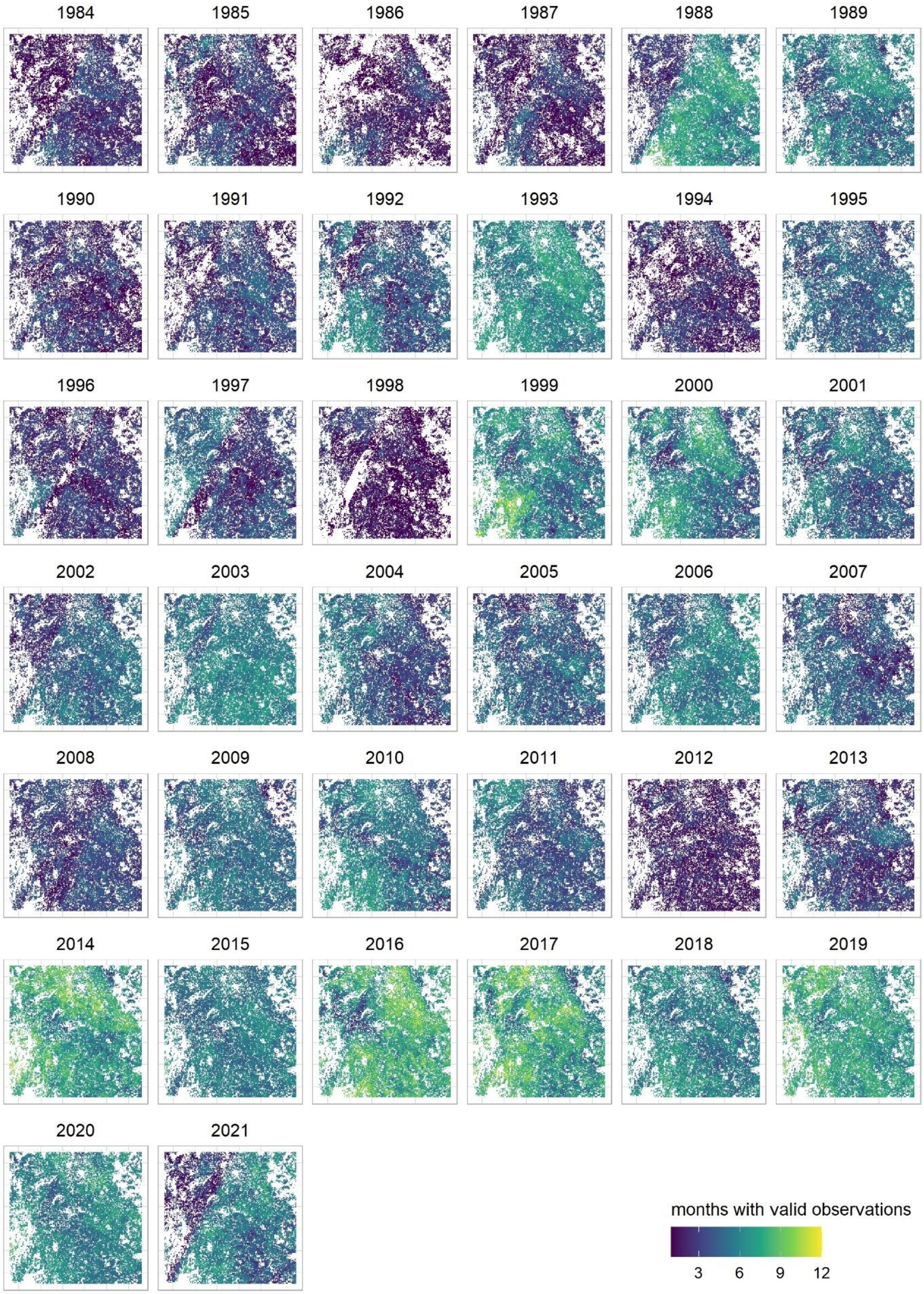

Figure SB13 Availability of monthly composites across 1984-2021 calendar years on the UK site.

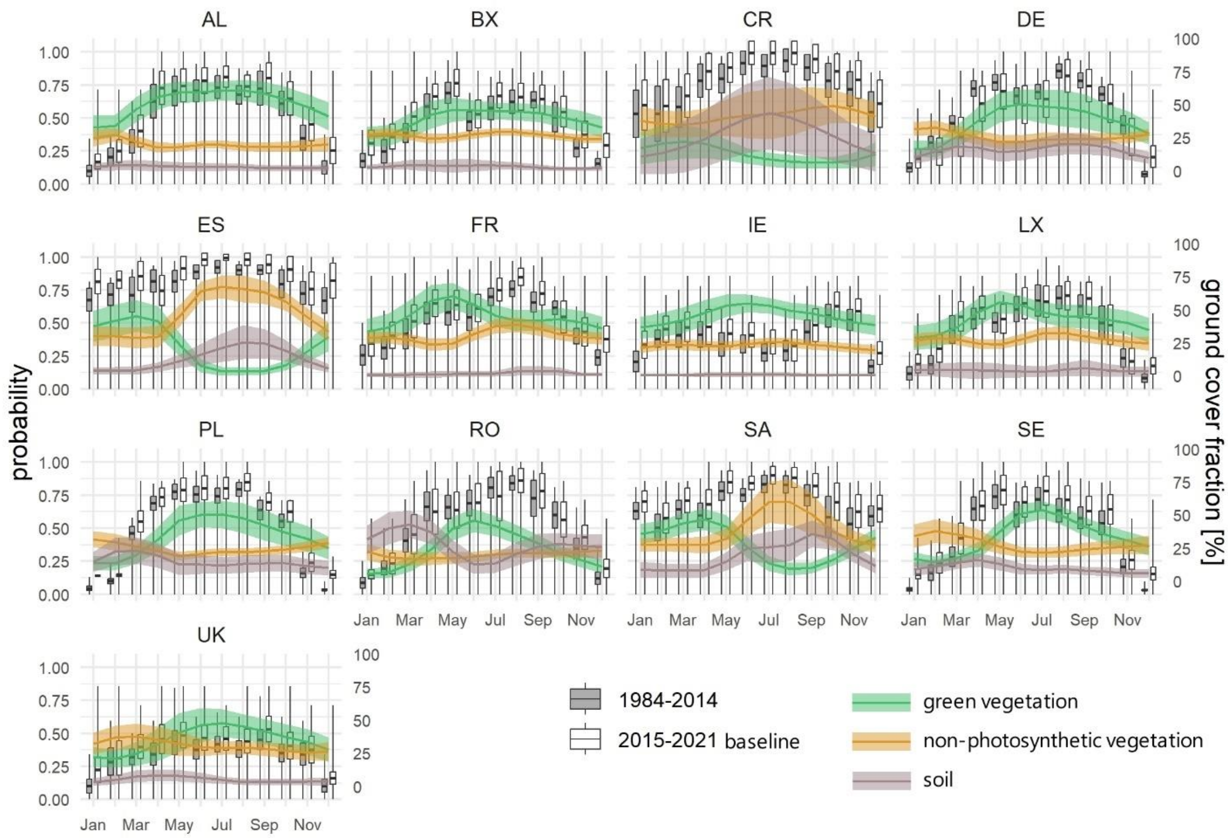

Figure SB14 Monthly mean probabilities (± standard deviation) of usable Landsat observations for 1984-2014 period and Landsat-baseline for 2015-2021 period on a backdrop of mean (± standard deviation) monthly green vegetation, non-photosynthetic vegetation, and soil fractions.

Impact of data density and endmember definitions on long-term trends in ground cover fractions across European grasslands

Supplement C

Katarzyna Ewa Lewińska [1,2], Akpona Okujeni [3,1], Katja Kowalski [4,1], Fabian Lehmann [5], Volker C. Radeloff [2], Ulf Leser [5], Patrick Hostert [1,6]

[1] Geography Department, Humboldt-Universität zu Berlin, Unter den Linden 6, 10099 Berlin, Germany.

[2] SILVIS Lab, Department of Forest and Wildlife Ecology, University of Wisconsin-Madison, 1630 Linden Drive, Madison WI 53706, USA.

[3] Helmholtz Center Potsdam, GFZ German Research Center for Geosciences, Telegrafenberg, 14473 Potsdam, Germany

[4] Earth Observation for Ecosystem Management, School of Life Sciences, Technical University of Munich, 11 Hans-Carl-v.-Carlowitz-Platz 2, 85354 Freising, Germany

[5] Department of Computer Science, Humboldt-Universität zu Berlin, Unter den Linden 6, 10099 Berlin, Germany

[6] Integrative Research Institute on Transformations of Human-Environment Systems (IRI THESys), Humboldt-Universität zu Berlin, Unter den Linden 6, 10099 Berlin, Germany

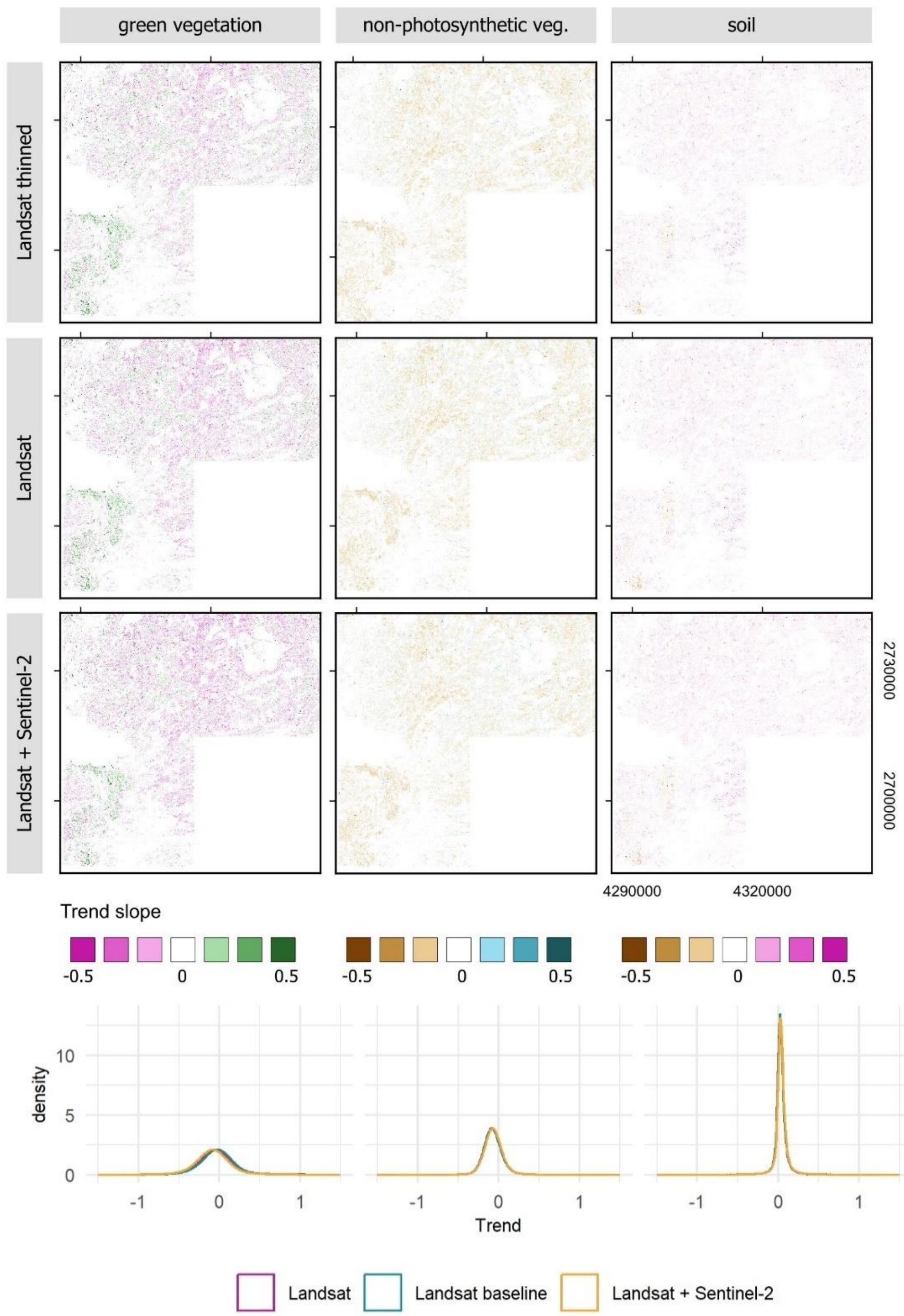

Figure SC1 Slope (in percentage point) of long-term trends in green vegetation, non-photosynthetic vegetation, and soil ground covers derived for the AL test site using 1984-2021 time series of Landsat-baseline, Landsat, and combined Landsat and Sentinel-2. Density distribution of respective trend values below the maps. Comparison among density distribution of slopes based on the Kolmogorov-Smirnov test in Table SC1.

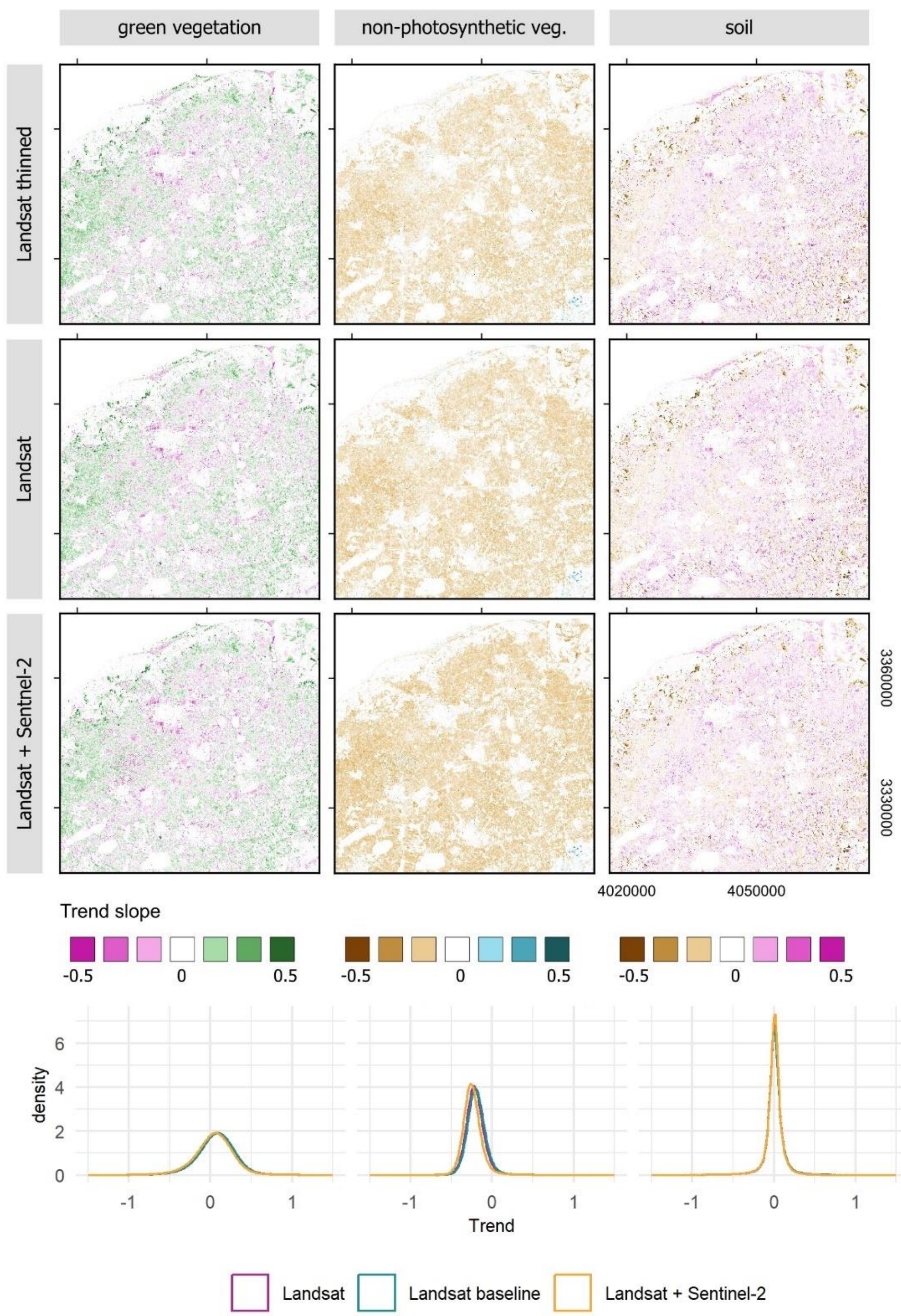

Figure SC2 Slope (in percentage point) of long-term trends in green vegetation, non-photosynthetic vegetation, and soil ground covers derived for the BX test site using 1984-2021 time series of Landsat-baseline, Landsat, and combined Landsat and Sentinel-2. Density distribution of respective trend values below the maps. Comparison among density distribution of slopes based on the Kolmogorov-Smirnov test in Table SC1.

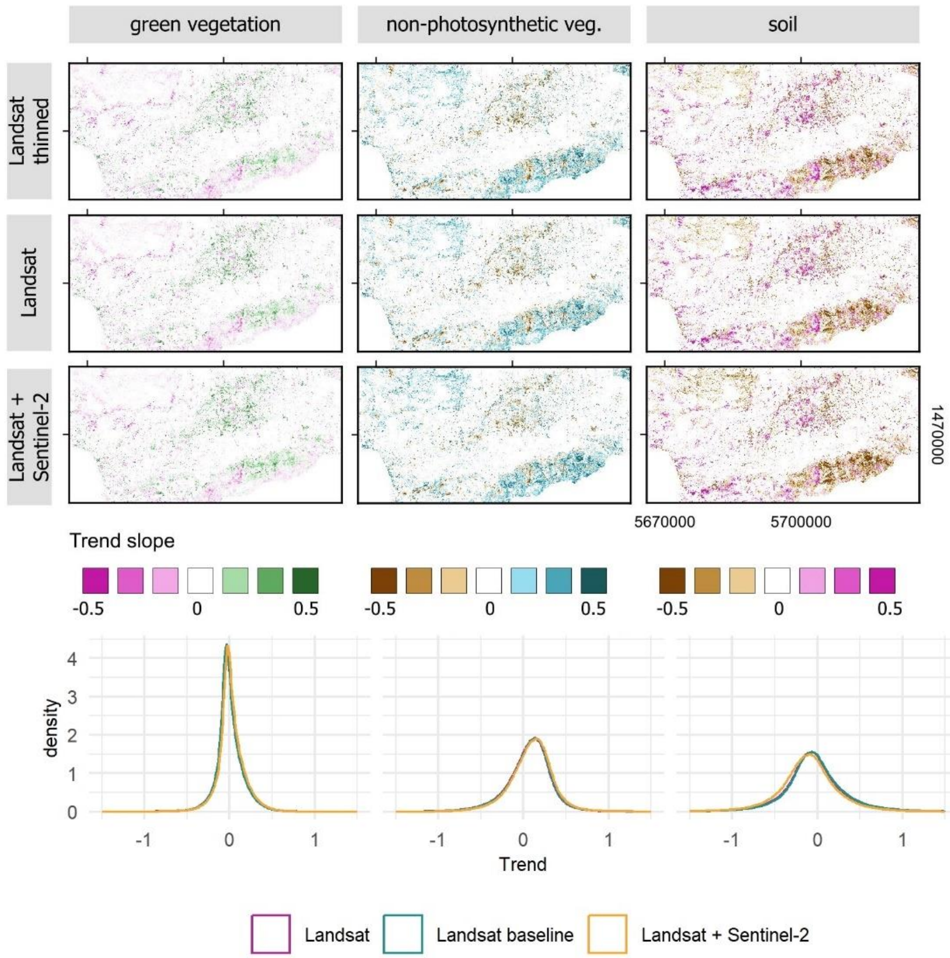

Figure SC3 Slope (in percentage point) of long-term trends in green vegetation, non-photosynthetic vegetation, and soil ground covers derived for the CR test site using 1984-2021 time series of Landsat-baseline, Landsat, and combined Landsat and Sentinel-2. Density distribution of respective trend values below the maps. Comparison among density distribution of slopes based on the Kolmogorov-Smirnov test in Table SC1.

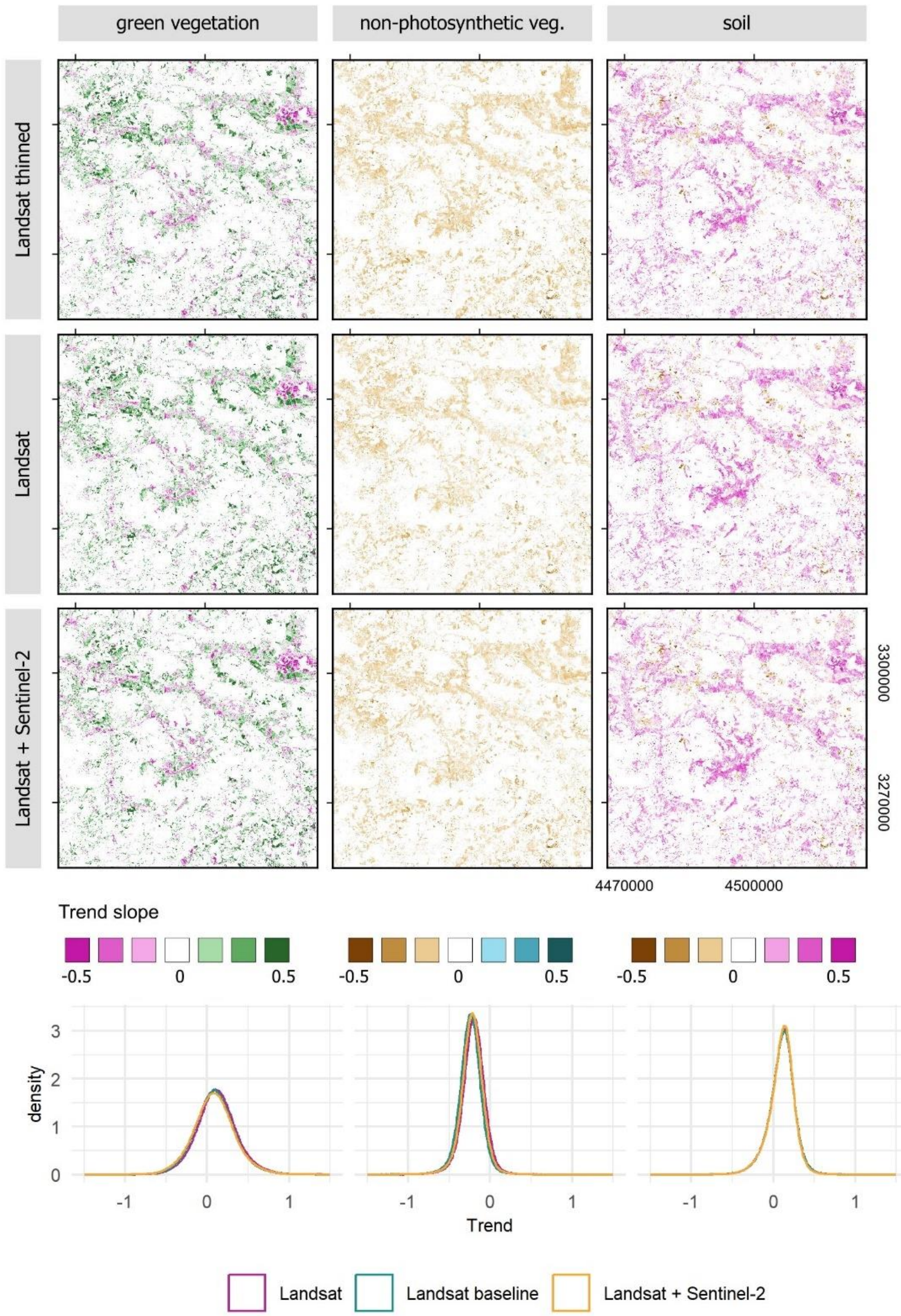

Figure SC4 Slope (in percentage point) of long-term trends in green vegetation, non-photosynthetic vegetation, and soil ground covers derived for the DE test site using 1984-2021 time series of Landsat-baseline, Landsat, and combined Landsat and Sentinel-2. Density distribution of respective trend values below the maps. Comparison among density distribution of slopes based on the Kolmogorov-Smirnov test in Table SC1.

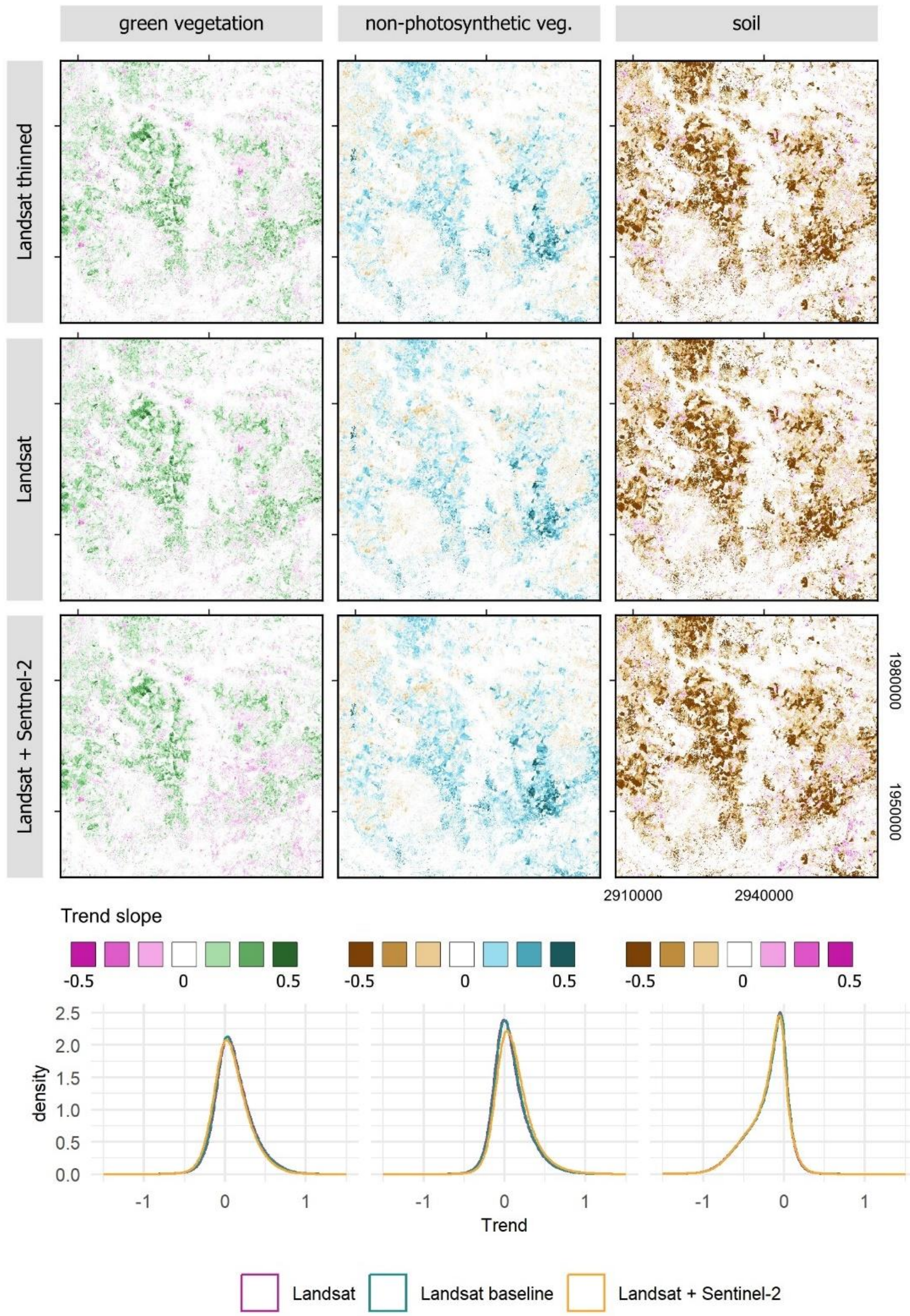

Figure SC5 Slope (in percentage point) of long-term trends in green vegetation, non-photosynthetic vegetation, and soil ground covers derived for the ES test site using 1984-2021 time series of Landsat-baseline, Landsat, and combined Landsat and Sentinel-2. Density distribution of respective trend values below the maps. Comparison among density distribution of slopes based on the Kolmogorov-Smirnov test in Table SC1.

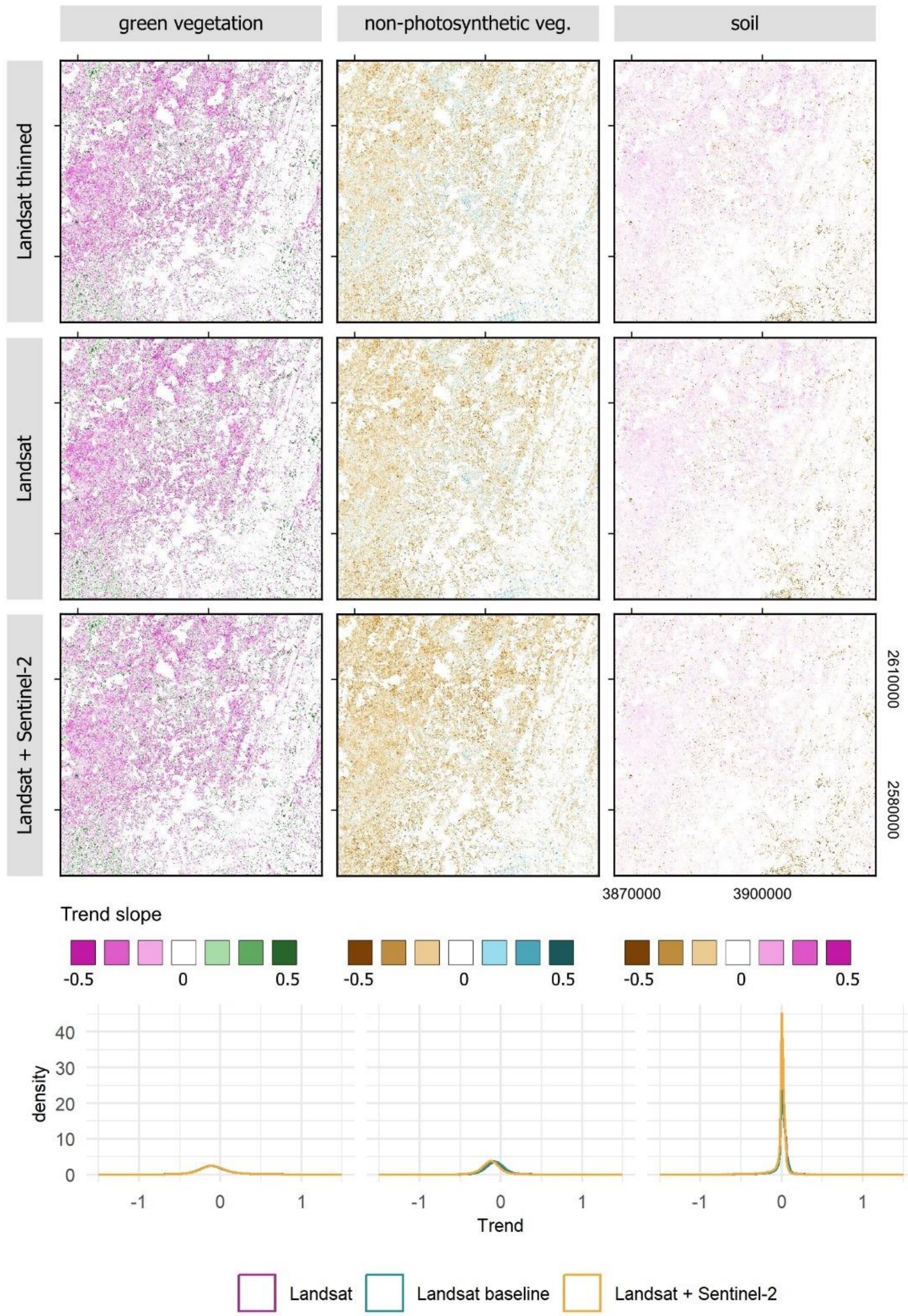

Figure SC6 Slope (in percentage point) of long-term trends in green vegetation, non-photosynthetic vegetation, and soil ground covers derived for the FR test site using 1984-2021 time series of Landsat-baseline, Landsat, and combined Landsat and Sentinel-2. Density distribution of respective trend values below the maps. Comparison among density distribution of slopes based on the Kolmogorov-Smirnov test in Table SC1.

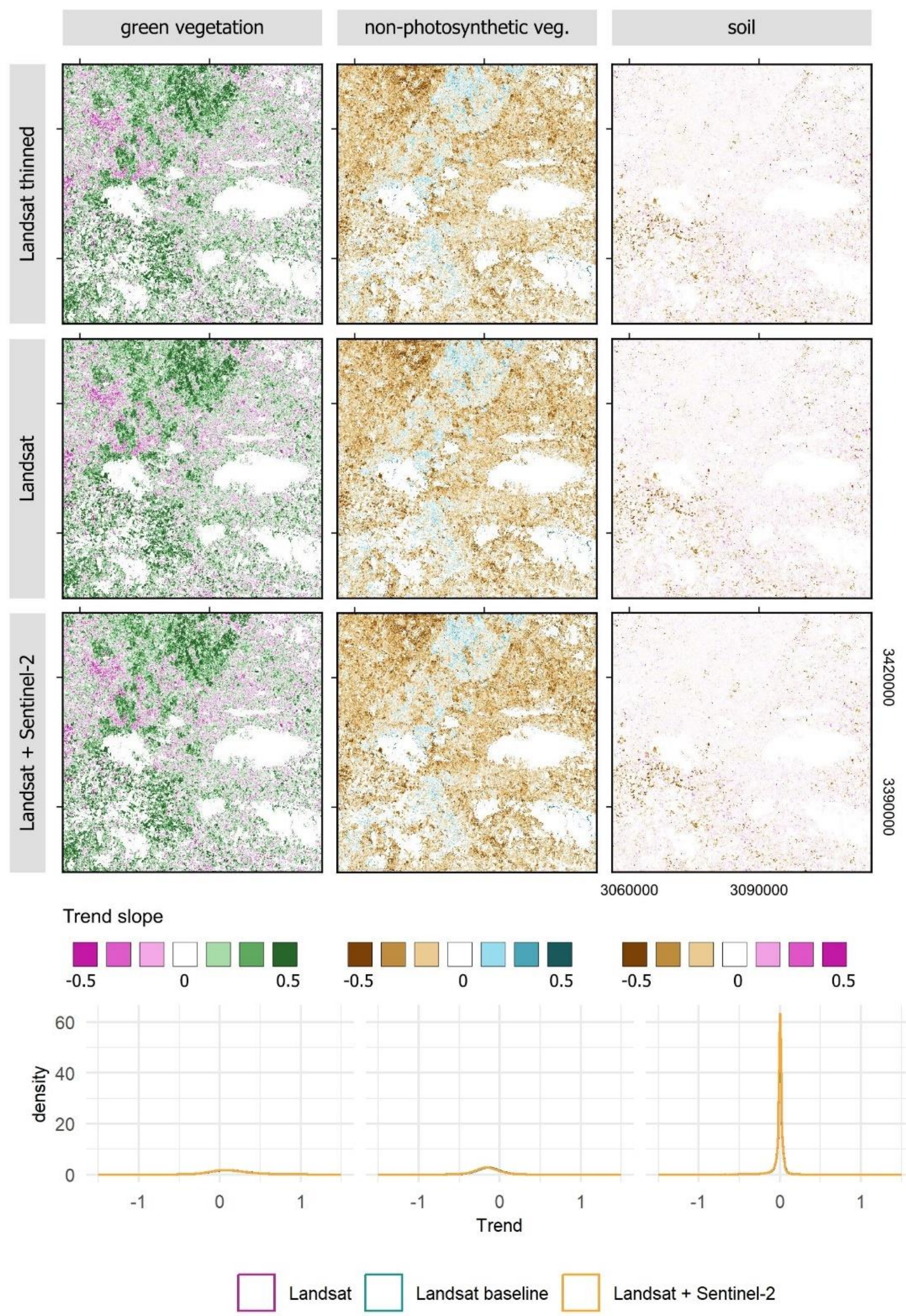

Figure SC7 Slope (in percentage point) of long-term trends in green vegetation, non-photosynthetic vegetation, and soil ground covers derived for the IE test site using 1984-2021 time series of Landsat-baseline, Landsat, and combined Landsat and Sentinel-2. Density distribution of respective trend values below the maps. Comparison among density distribution of slopes based on the Kolmogorov-Smirnov test in Table SC1.

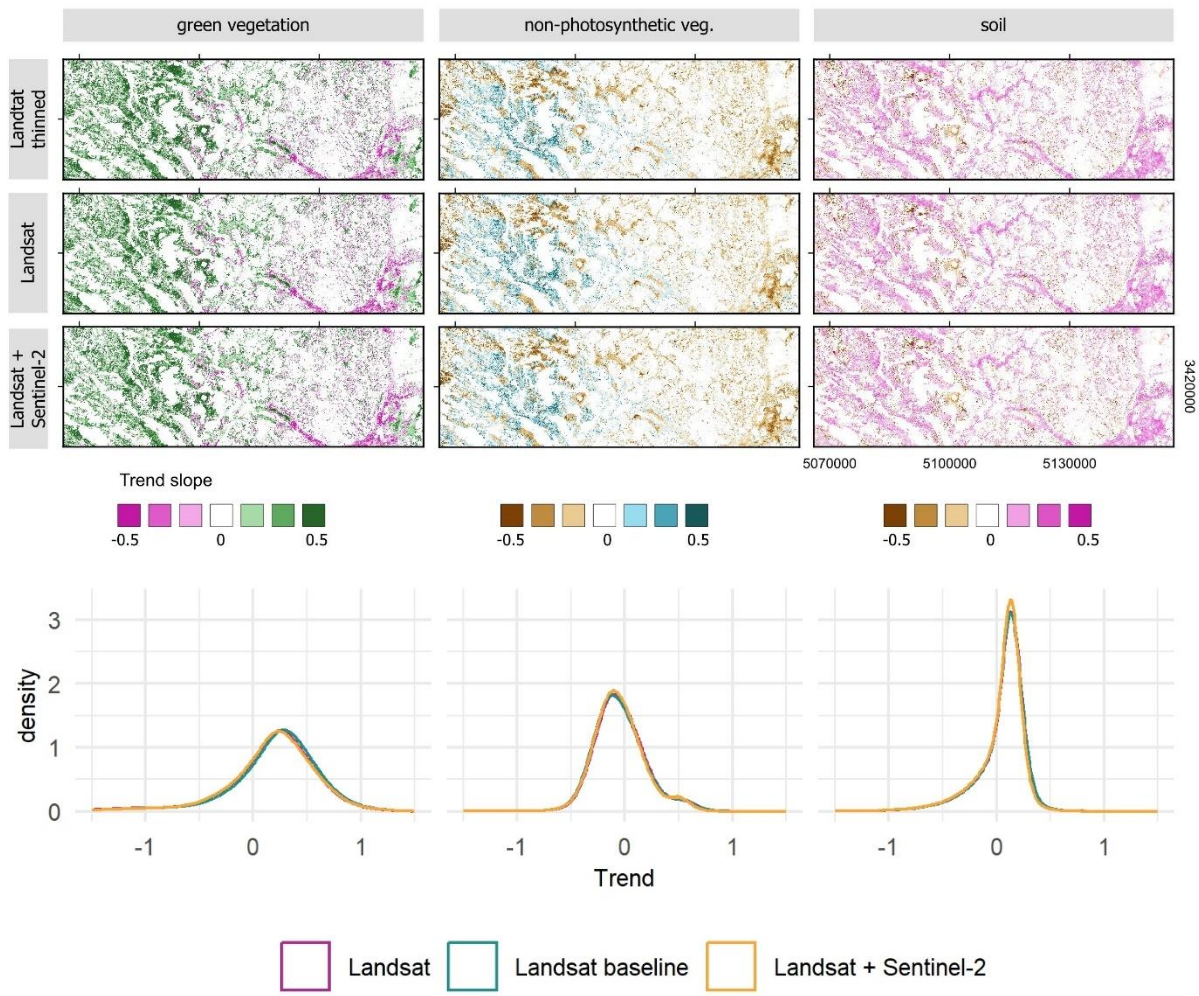

Figure SC8 Slope (in percentage point) of long-term trends in green vegetation, non-photosynthetic vegetation, and soil ground covers derived for the PL test site using 1984-2021 time series of Landsat-baseline, Landsat, and combined Landsat and Sentinel-2. Density distribution of respective trend values below the maps. Comparison among density distribution of slopes based on the Kolmogorov-Smirnov test in Table SC1.

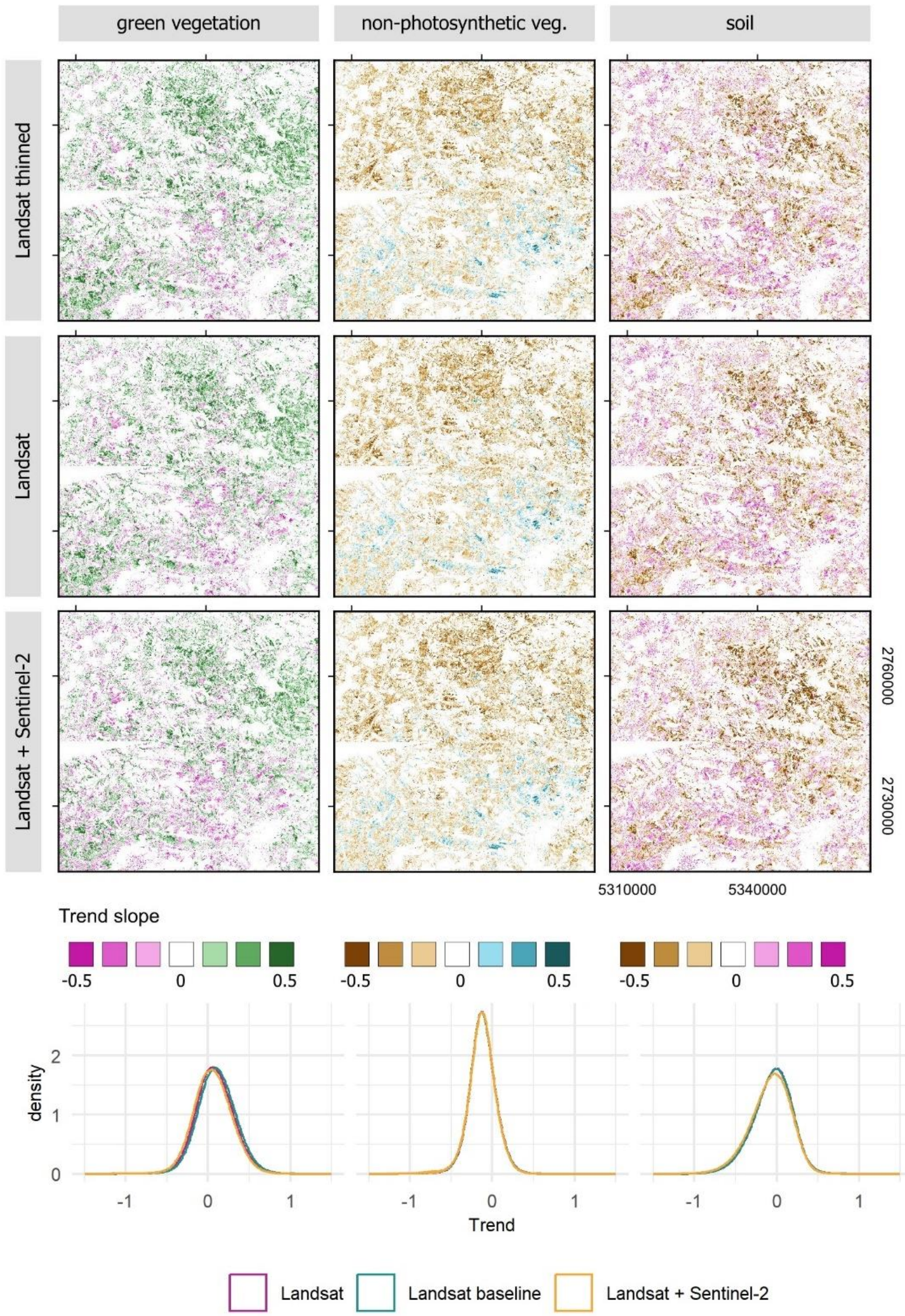

Figure SC9 Slope (in percentage point) of long-term trends in green vegetation, non-photosynthetic vegetation, an dsoil ground covers derived for the RO test site using 1984-2021 time series of Landsat-baseline, Landsat, and combined Landsat and Sentinel-2. Density distribution of respective trend values below the maps. Comparison among density distribution of slopes based on the Kolmogorov-Smirnov test in Table SC1.

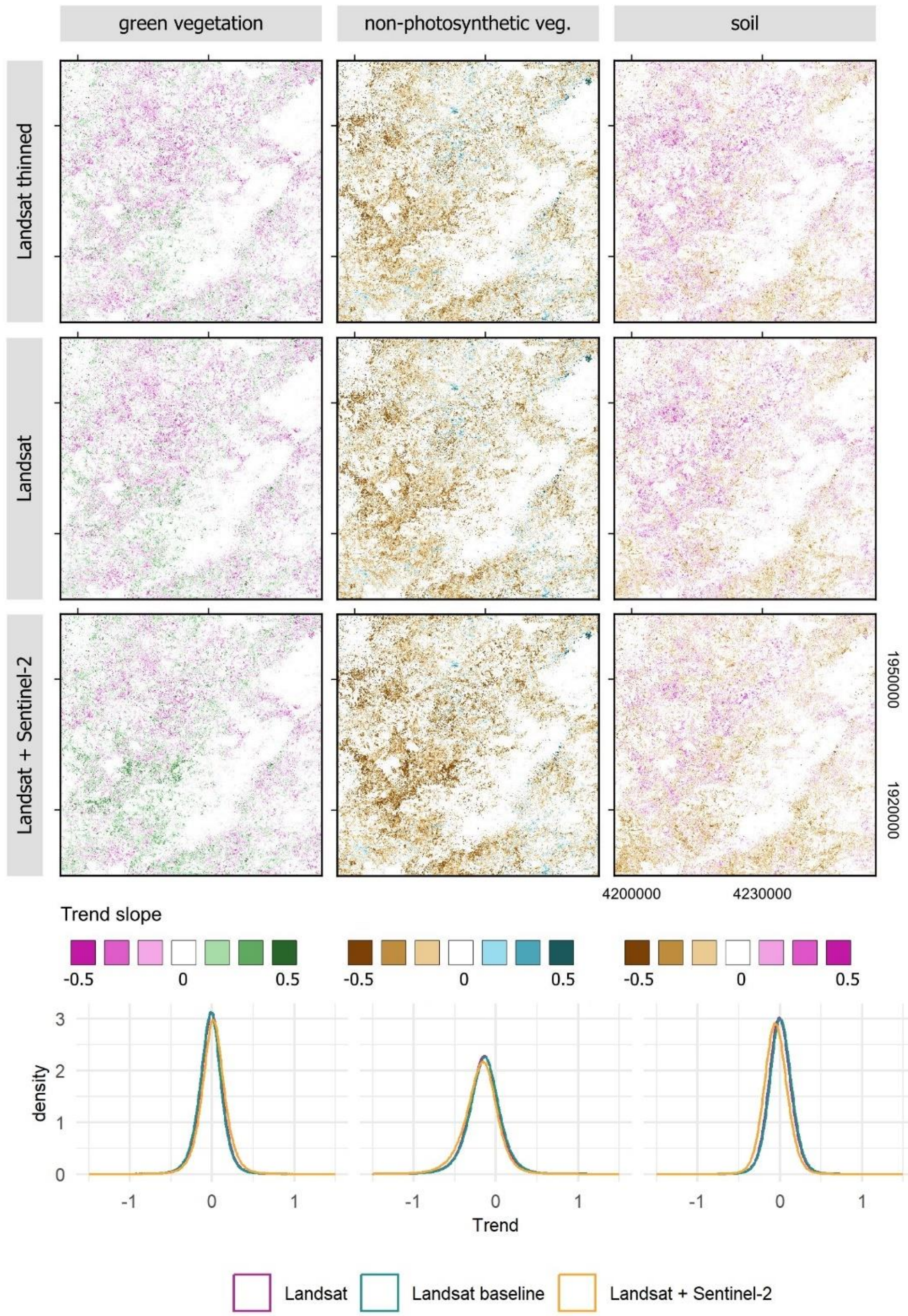

Figure SC10 Slope (in percentage point) of long-term trends in green vegetation, non-photosynthetic vegetation, and soil ground covers derived for the SA test site using 1984-2021 time series of Landsat-baseline, Landsat, and combined Landsat and Sentinel-2. Density distribution of respective trend values below the maps. Comparison among density distribution of slopes based on the Kolmogorov-Smirnov test in Table SC1.

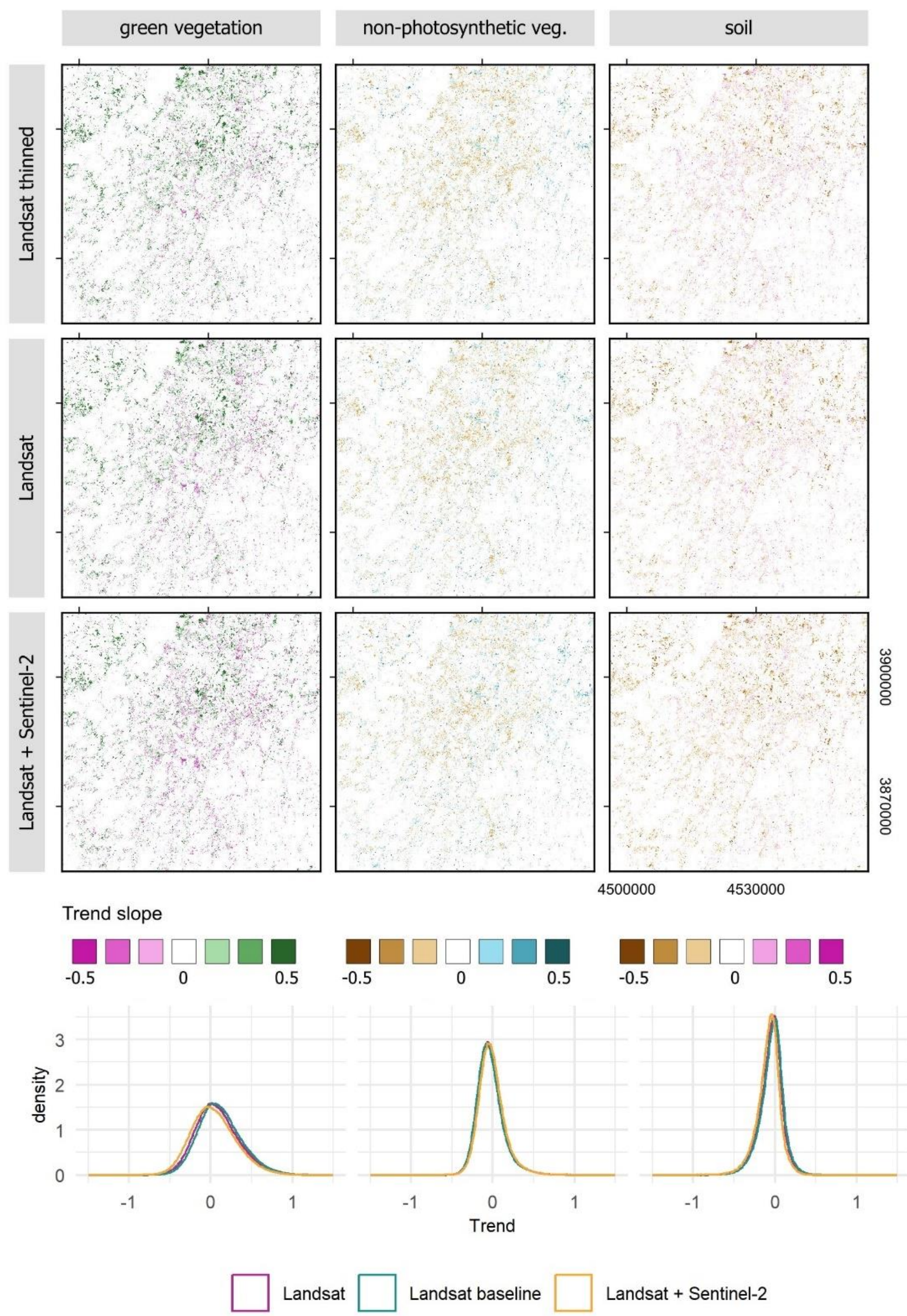

Figure SC11 Slope (in percentage point) of long-term trends in green vegetation, non-photosynthetic vegetation, and soil ground covers derived for the SE test site using 1984-2021 time series of Landsat-baseline, Landsat, and combined Landsat and Sentinel-2. Density distribution of respective trend values below the maps. Comparison among density distribution of slopes based on the Kolmogorov-Smirnov test in Table SC1.

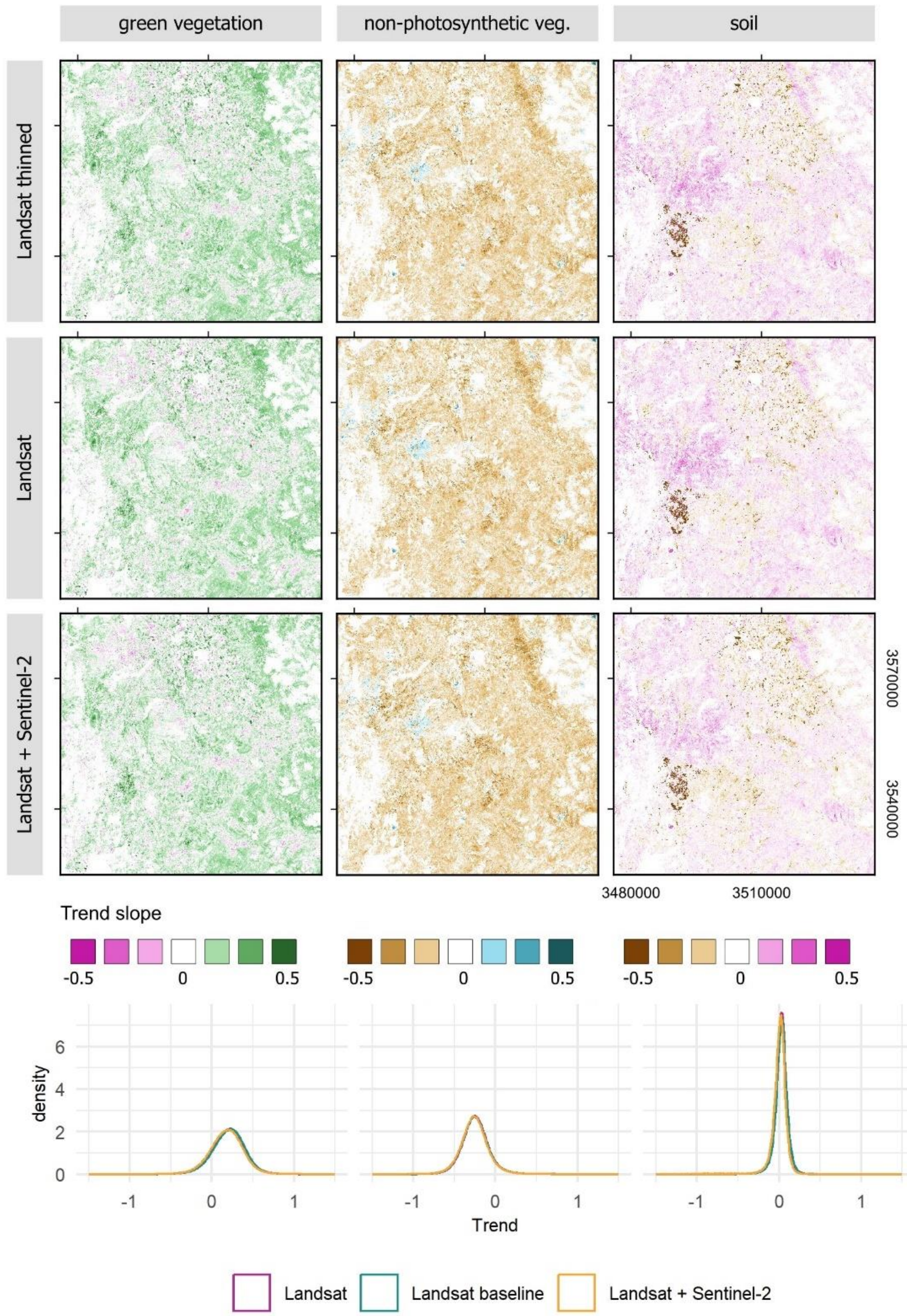

Figure SC12 Slope (in percentage point) of long-term trends in green vegetation, non-photosynthetic vegetation, and soil ground covers derived for the UK test site using 1984-2021 time series of Landsat-baseline, Landsat, and combined Landsat and Sentinel-2. Density distribution of respective trend values below the maps. Comparison among density distribution of slopes based on the Kolmogorov-Smirnov test in Table SC1.

Table SC1 Kolmogorov-Smirnov test results comparing density distribution of pixel-level trend slope values derived for each test site based on 1984-2021 time series of Landsat-baseline, Landsat, and combined Landsat and Sentinel-2. Sample size of 5,000. H_0 – tested distributions are the same.

Test site	Time series	gv		npv		soil	
		D	p-val	D	p-val	D	p-val
AL	Landsat vs. Landsat-baseline	0.044	0.000	0.026	0.061	0.030	0.025
	Landsat vs. Landsat + Sentinel-2	0.070	0.000	0.033	0.008	0.061	0.000
	Landsat-baseline vs. Landsat + Sentinel-2	0.128	0.000	0.032	0.011	0.085	0.000
BX	Landsat vs. Landsat-baseline	0.041	0.001	0.085	0.000	0.017	0.450
	Landsat vs. Landsat + Sentinel-2	0.026	0.072	0.146	0.000	0.019	0.315
	Landsat-baseline vs. Landsat + Sentinel-2	0.088	0.000	0.216	0.000	0.034	0.007
CR	Landsat vs. Landsat-baseline	0.025	0.084	0.017	0.496	0.014	0.711
	Landsat vs. Landsat + Sentinel-2	0.064	0.000	0.054	0.000	0.095	0.000
	Landsat-baseline vs. Landsat + Sentinel-2	0.084	0.000	0.035	0.005	0.097	0.000
DE	Landsat vs. Landsat-baseline	0.053	0.000	0.145	0.000	0.026	0.068
	Landsat vs. Landsat + Sentinel-2	0.043	0.000	0.086	0.000	0.015	0.610
	Landsat-baseline vs. Landsat + Sentinel-2	0.013	0.792	0.082	0.000	0.023	0.142
ES	Landsat vs. Landsat-baseline	0.032	0.012	0.018	0.393	0.019	0.353
	Landsat vs. Landsat + Sentinel-2	0.073	0.000	0.094	0.000	0.014	0.711
	Landsat-baseline vs. Landsat + Sentinel-2	0.048	0.000	0.077	0.000	0.049	0.000
FR	Landsat vs. Landsat-baseline	0.023	0.142	0.072	0.000	0.044	0.000
	Landsat vs. Landsat + Sentinel-2	0.039	0.001	0.114	0.000	0.091	0.000
	Landsat-baseline vs. Landsat + Sentinel-2	0.026	0.072	0.194	0.000	0.107	0.000
IE	Landsat vs. Landsat-baseline	0.021	0.239	0.034	0.007	0.023	0.136
	Landsat vs. Landsat + Sentinel-2	0.029	0.028	0.055	0.000	0.021	0.239
	Landsat-baseline vs. Landsat + Sentinel-2	0.020	0.270	0.049	0.000	0.029	0.028
LX	Landsat vs. Landsat-baseline	0.013	0.776	0.031	0.014	0.028	0.044
	Landsat vs. Landsat + Sentinel-2	0.037	0.002	0.138	0.000	0.056	0.000
	Landsat-baseline vs. Landsat + Sentinel-2	0.033	0.009	0.193	0.000	0.036	0.003
PL	Landsat vs. Landsat-baseline	0.058	0.000	0.026	0.065	0.013	0.776
	Landsat vs. Landsat + Sentinel-2	0.028	0.042	0.041	0.000	0.047	0.000
	Landsat-baseline vs. Landsat + Sentinel-2	0.060	0.000	0.023	0.149	0.045	0.000
RO	Landsat vs. Landsat-baseline	0.054	0.000	0.010	0.970	0.015	0.644
	Landsat vs. Landsat + Sentinel-2	0.046	0.000	0.035	0.005	0.042	0.000
	Landsat-baseline vs. Landsat + Sentinel-2	0.117	0.000	0.026	0.075	0.045	0.000
SA	Landsat vs. Landsat-baseline	0.039	0.001	0.049	0.000	0.022	0.186
	Landsat vs. Landsat + Sentinel-2	0.088	0.000	0.075	0.000	0.161	0.000
	Landsat-baseline vs. Landsat + Sentinel-2	0.126	0.000	0.077	0.000	0.183	0.000

Table SC1 continuation

Test site	Time series	gv		npv		soil	
		D	p-val	D	p-val	D	p-val
SE	Landsat vs. Landsat-baseline	0.048	0.000	0.044	0.000	0.035	0.004
	Landsat vs. Landsat + Sentinel-2	0.066	0.000	0.047	0.000	0.121	0.000
	Landsat-baseline vs. Landsat + Sentinel-2	0.126	0.000	0.063	0.000	0.158	0.000
UK	Landsat vs. Landsat-baseline	0.050	0.000	0.016	0.560	0.026	0.068
	Landsat vs. Landsat + Sentinel-2	0.031	0.016	0.028	0.035	0.122	0.000
	Landsat-baseline vs. Landsat + Sentinel-2	0.075	0.000	0.028	0.040	0.138	0.000

Table SC2 Range of autocorrelation for CEF time series based on Landsat, Landsat-baseline, and combined Landsat and Sentinel-2 time series.

	Landsat baseline			Landsat			Landsat + Sentinel-2		
Test site	gv	npv	soil	gv	npv	soil	gv	npv	soil
AL	5.27	7.82	1.55	5.35	8.11	1.90	5.19	8.51	1.91
BX	5.29	9.15	6.87	5.56	9.38	7.07	5.15	8.68	6.08
CR	19.49	0.84	3.79	19.99	0.78	3.94	19.85	0.98	5.31
DE	19.67	14.54	15.83	18.61	16.98	17.48	18.60	15.35	15.77
ES	49.98	23.15	26.01	53.05	23.82	25.69	42.73	19.55	25.99
FR	31.44	23.12	17.08	33.39	22.41	17.28	32.62	20.46	19.60
IE	2.66	3.66	0.24	2.96	3.80	0.27	3.11	4.62	0.22
LX	9.36	10.58	0.51	9.64	10.47	0.71	9.25	9.88	0.39
PL	15.96	10.93	8.09	16.35	11.25	8.59	16.85	11.83	7.78
RO	27.34	9.74	25.55	27.73	9.77	26.42	24.58	9.30	26.51
SA	27.19	21.86	14.04	27.32	22.22	14.49	23.74	19.62	15.66
SE	7.87	12.96	6.60	8.05	13.74	6.91	6.76	11.68	7.46
UK	6.84	8.32	11.80	7.33	8.56	12.02	7.92	7.66	11.44

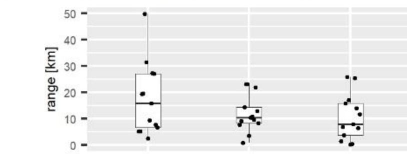

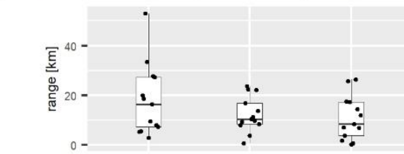

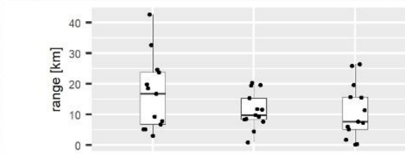

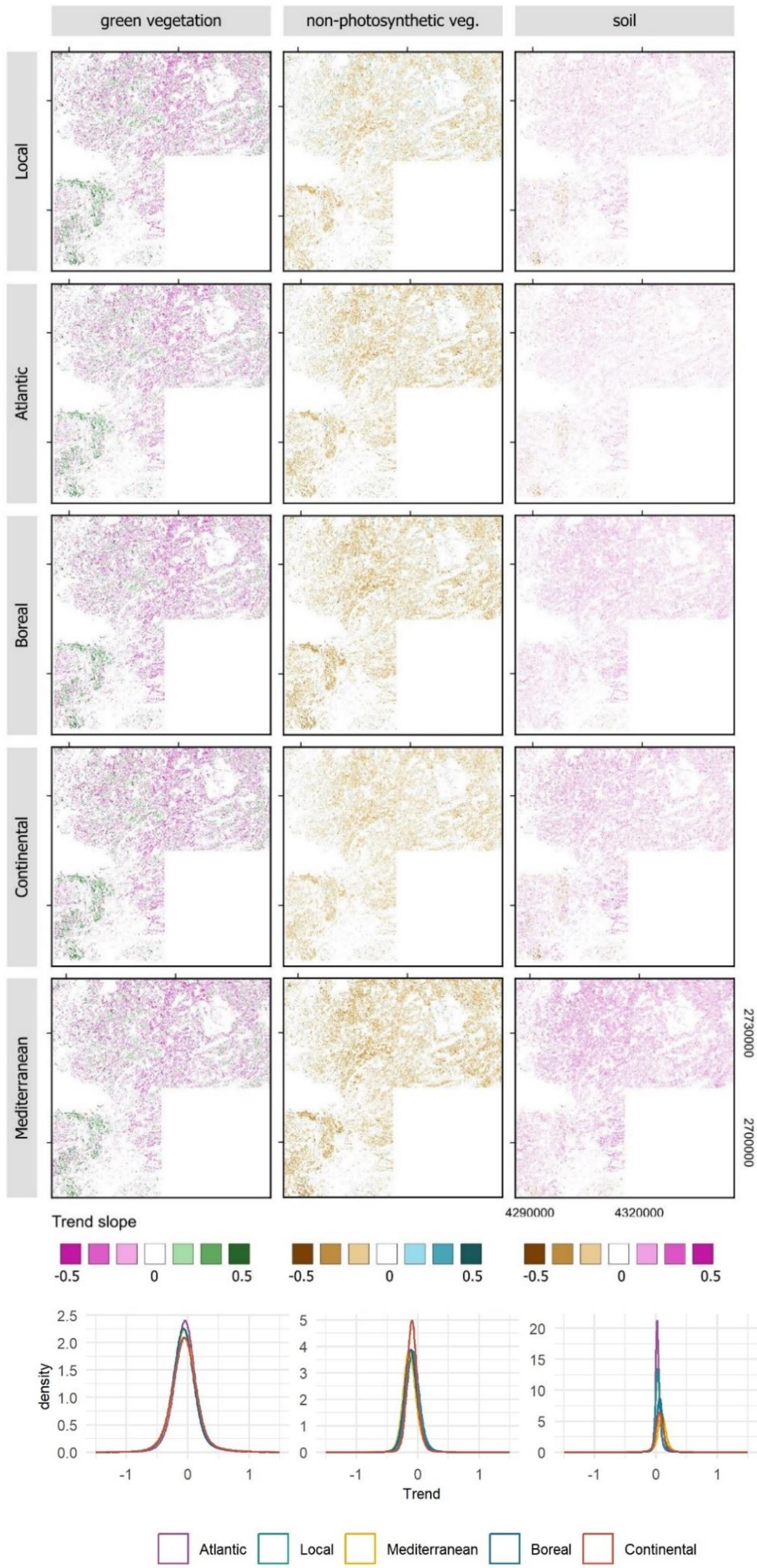

Figure SCF13 Slope (in percentage point) of long-term trends in green vegetation, non-photosynthetic vegetation, and soil ground cover fractions derived for the AL test site using 1984-2021 time series of Landsat data using different sets of endmembers. Comparison among density distribution of slopes based on the Kolmogorov Smirnov test in Table SC3.

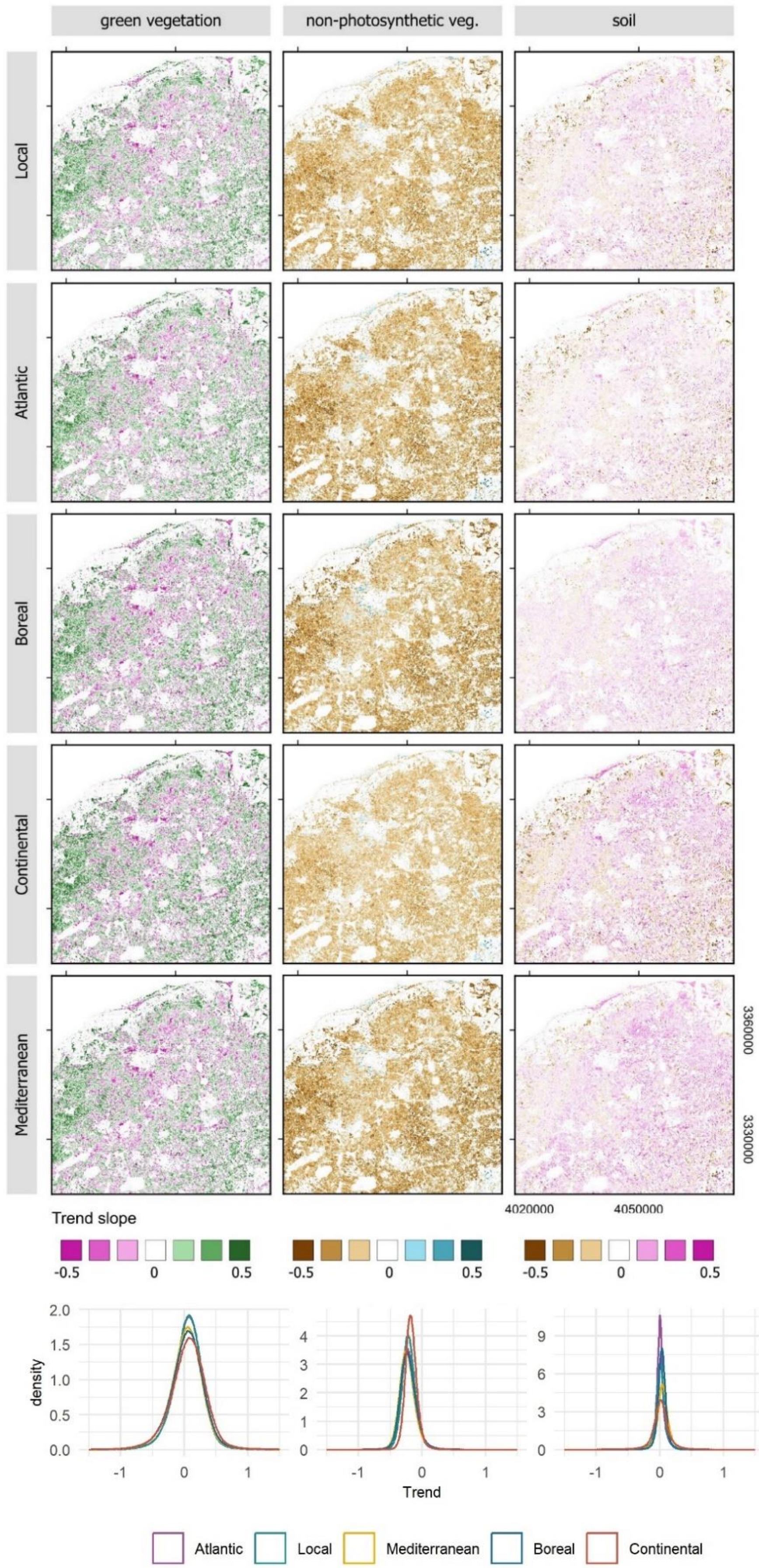

Figure SC14 Slope (in percentage point) of long-term trends in green vegetation, non-photosynthetic vegetation, and soil ground cover fractions derived for the BX test site using 1984-2021 time series of Landsat data using different sets of endmembers. Comparison among density distribution of slopes based on the Kolmogorov Smirnov test in Table SC3.

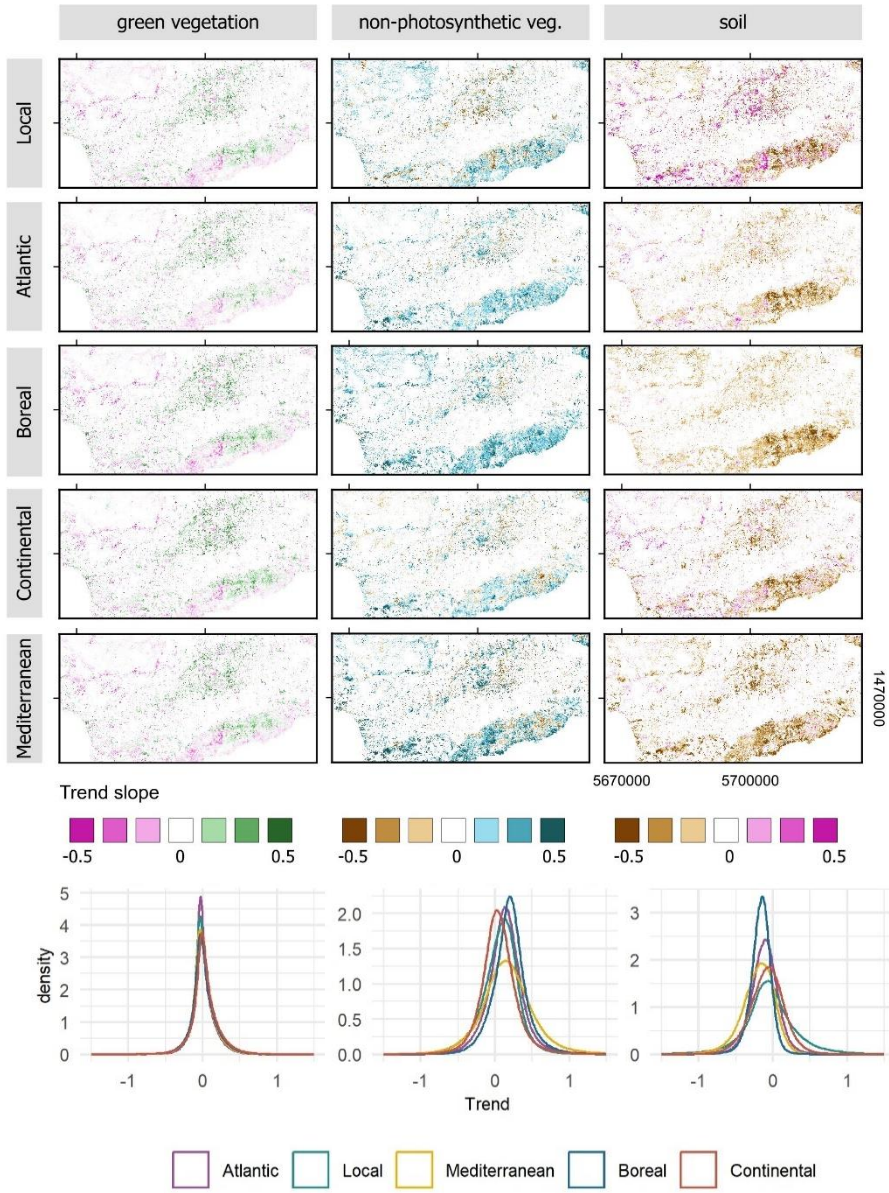

Figure SC15 Slope (in percentage point) of long-term trends in green vegetation, non-photosynthetic vegetation, and soil ground cover fractions derived for the CR test site using 1984-2021 time series of Landsat data using different sets of endmembers. Comparison among density distribution of slopes based on the Kolmogorov Smirnov test in Table SC3.

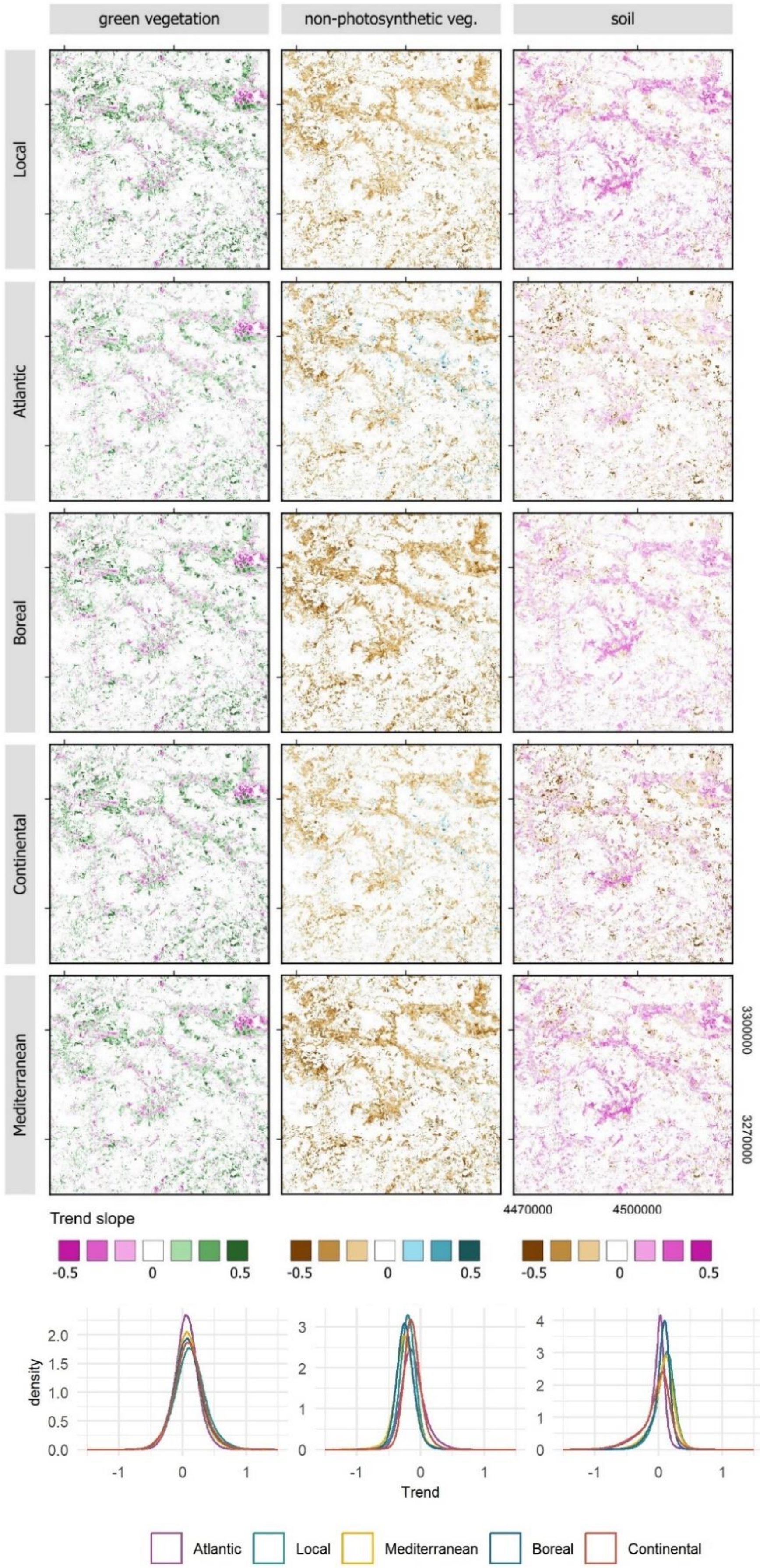

Figure SC16 Slope (in percentage point) of long-term trends in green vegetation, non-photosynthetic vegetation, and soil ground cover fractions derived for the DE test site using 1984-2021 time series of Landsat data using different sets of endmembers. Comparison among density distribution of slopes based on the Kolmogorov Smirnov test in Table SC3.

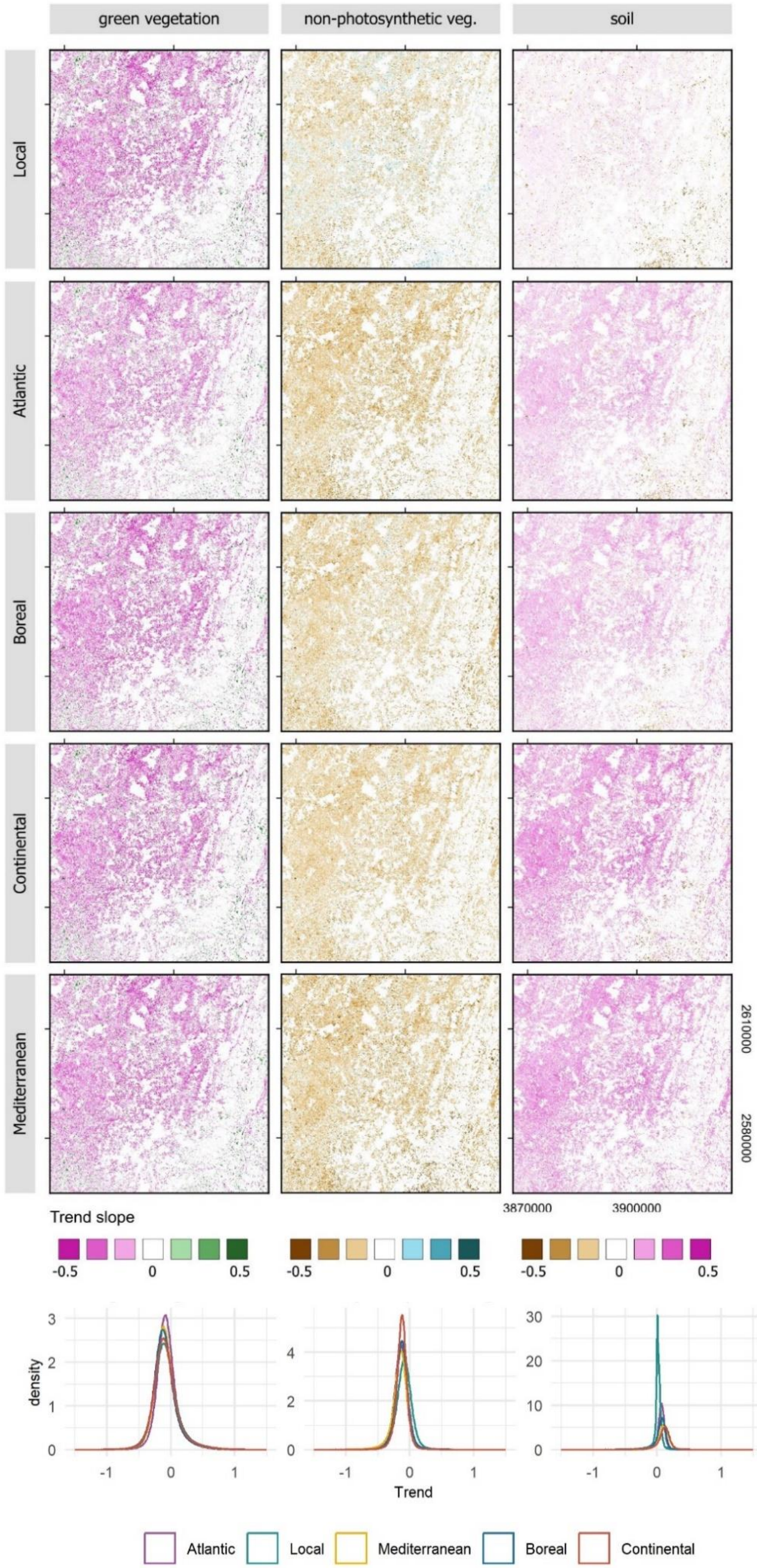

Figure SC17 Slope (in percentage point) of long-term trends in green vegetation, non-photosynthetic vegetation, and soil ground cover fractions derived for the FR test site using 1984-2021 time series of Landsat data using different sets of endmembers. Comparison among density distribution of slopes based on the Kolmogorov Smirnov test in Table SC3.

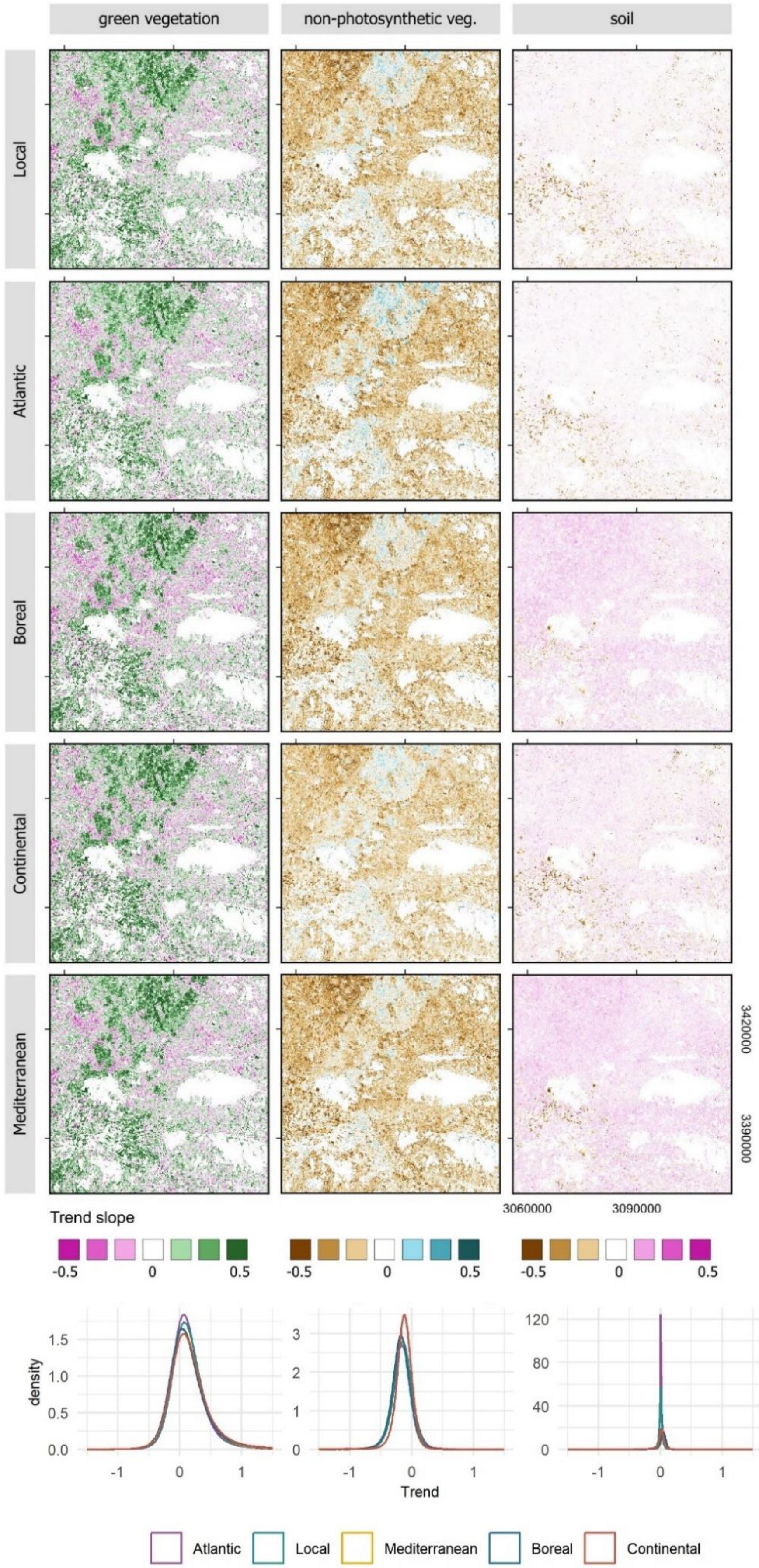

Figure SC18 Slope (in percentage point) of long-term trends in green vegetation, non-photosynthetic vegetation, and soil ground cover fractions derived for the IE test site using 1984-2021 time series of Landsat data using different sets of endmembers. Comparison among density distribution of slopes based on the Kolmogorov Smirnov test in Table SC3.

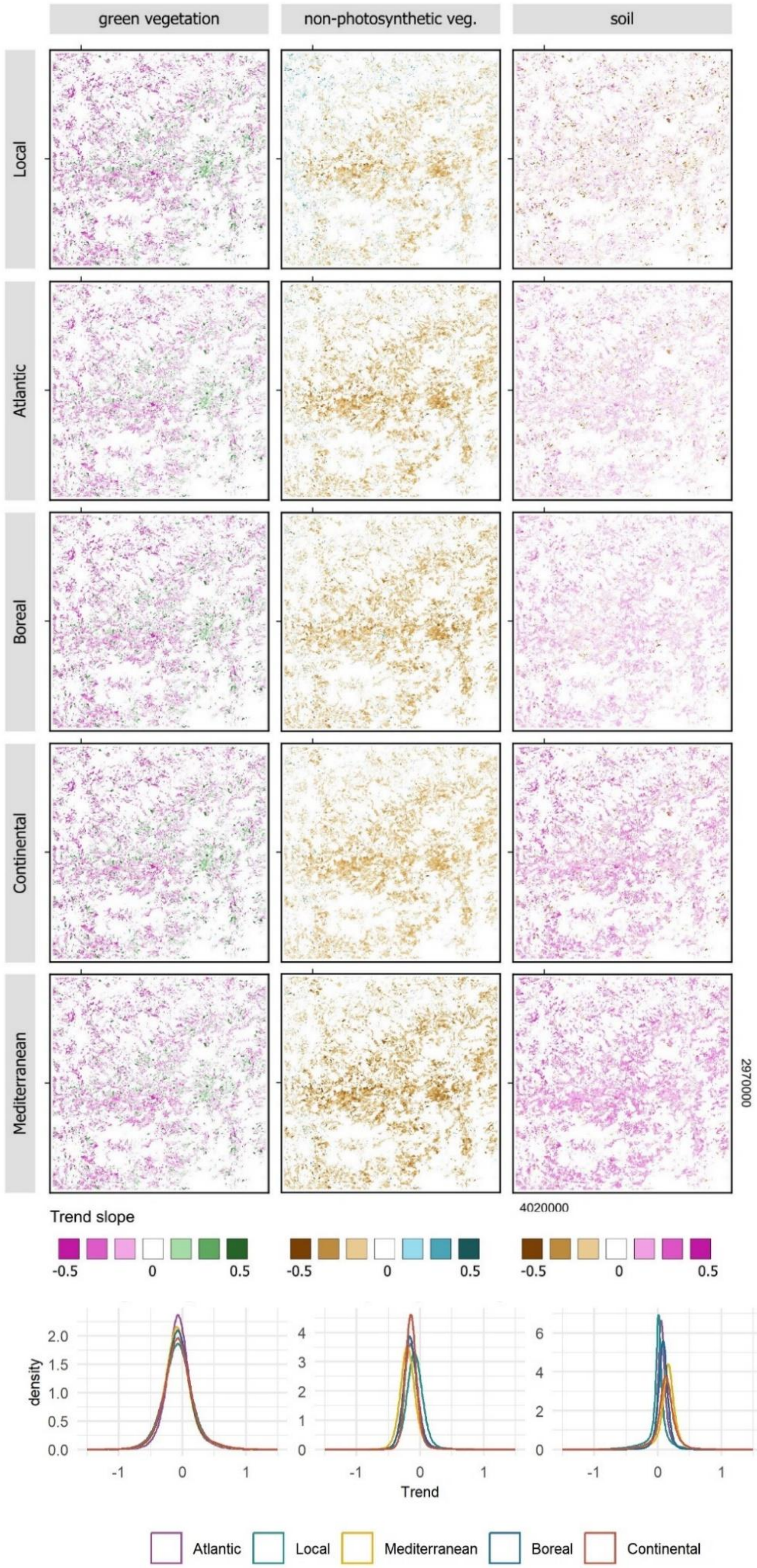

Figure SC19 Slope (in percentage point) of long-term trends in green vegetation, non-photosynthetic vegetation, and soil ground cover fractions derived for the LX test site using 1984-2021 time series of Landsat data using different sets of endmembers. Comparison among density distribution of slopes based on the Kolmogorov Smirnov test in Table SC3.

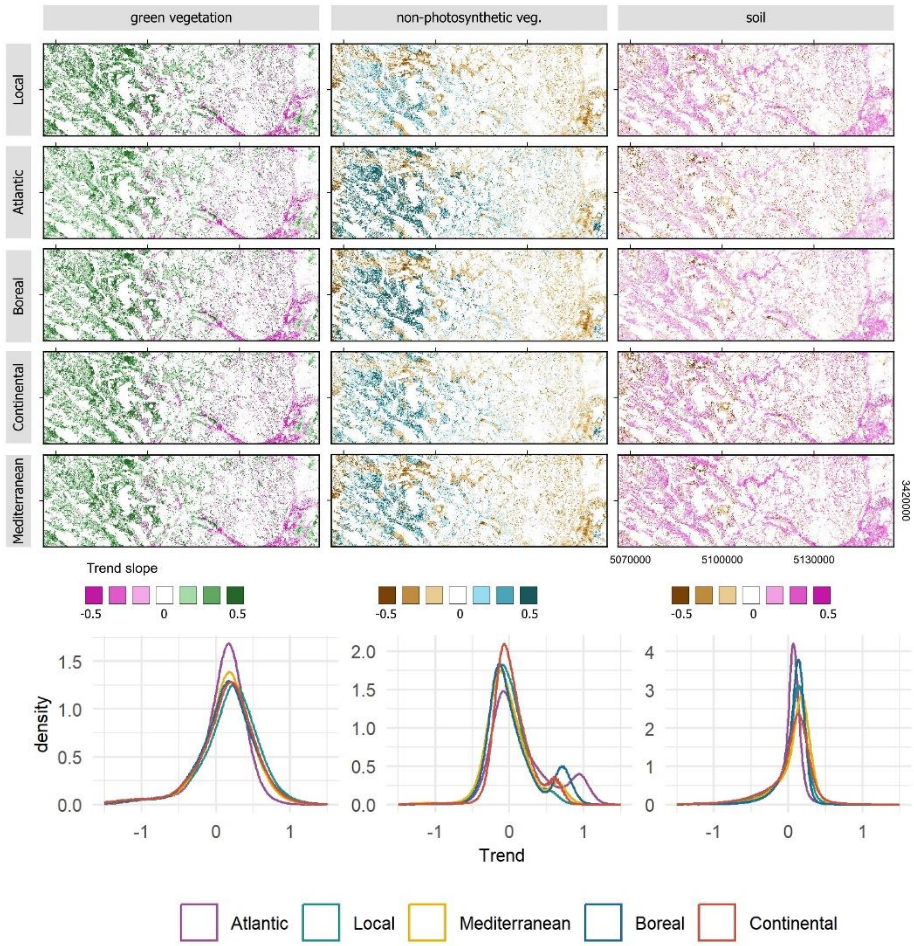

Figure SC20 Slope (in percentage point) of long-term trends in green vegetation, non-photosynthetic vegetation, and soil ground cover fractions derived for the PL test site using 1984-2021 time series of Landsat data using different sets of endmembers. Comparison among density distribution of slopes based on the Kolmogorov Smirnov test in Table SC3.

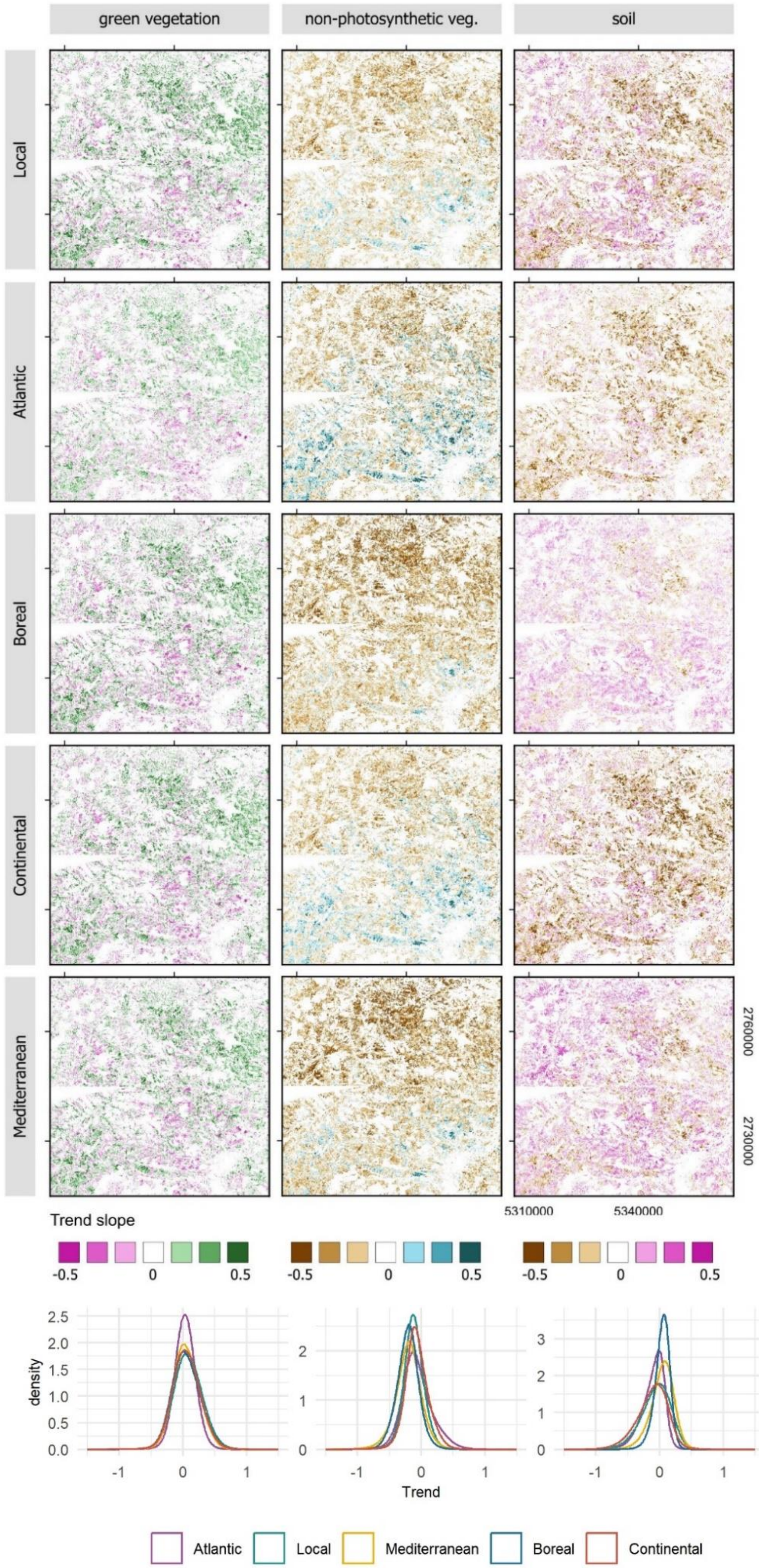

Figure SC21 Slope (in percentage point) of long-term trends in green vegetation, non-photosynthetic vegetation, and soil ground cover fractions derived for the RO test site using 1984-2021 time series of Landsat data using different sets of endmembers. Comparison among density distribution of slopes based on the Kolmogorov Smirnov test in Table SC3.

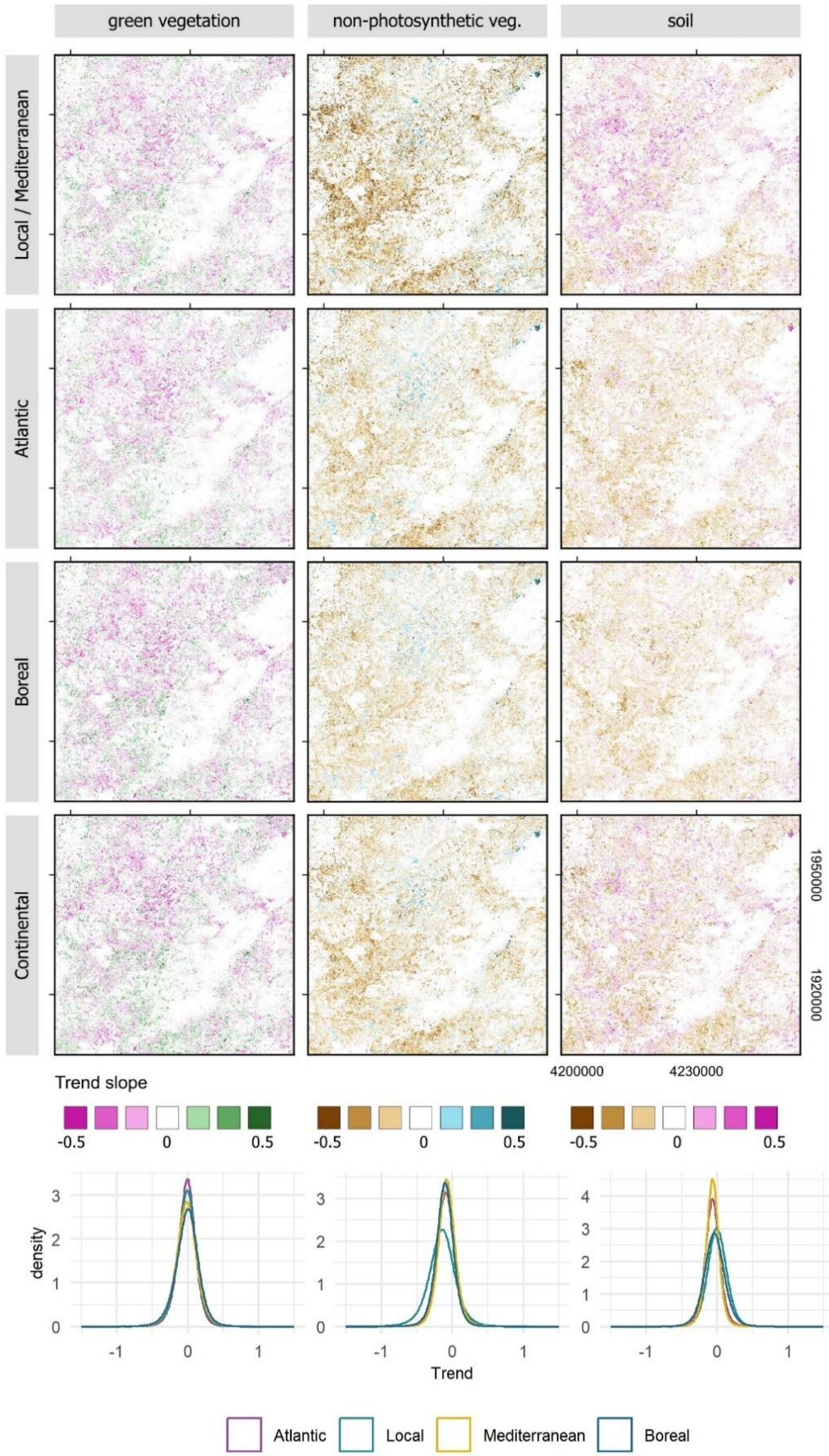

Figure SC22 Slope (in percentage point) of long-term trends in green vegetation, non-photosynthetic vegetation, and soil ground cover fractions derived for the SA test site using 1984-2021 time series of Landsat data using different sets of endmembers. Comparison among density distribution of slopes based on the Kolmogorov Smirnov test in Table SC3.

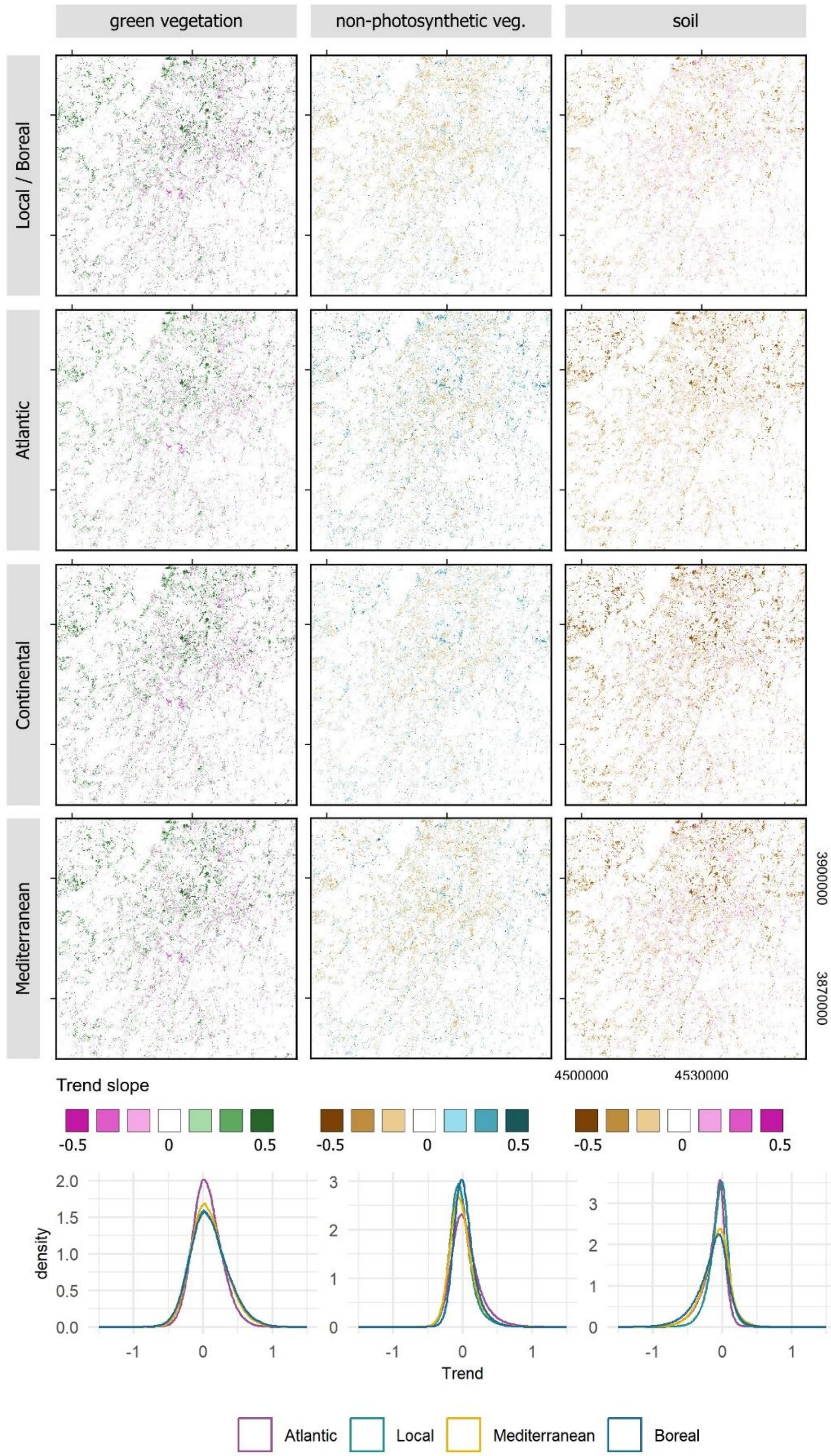

Figure SC23 Slope (in percentage point) of long-term trends in green vegetation, non-photosynthetic vegetation, and soil ground cover fractions derived for the SE test site using 1984-2021 time series of Landsat data using different sets of endmembers. Comparison among density distribution of slopes based on the Kolmogorov Smirnov test in Table SC3.

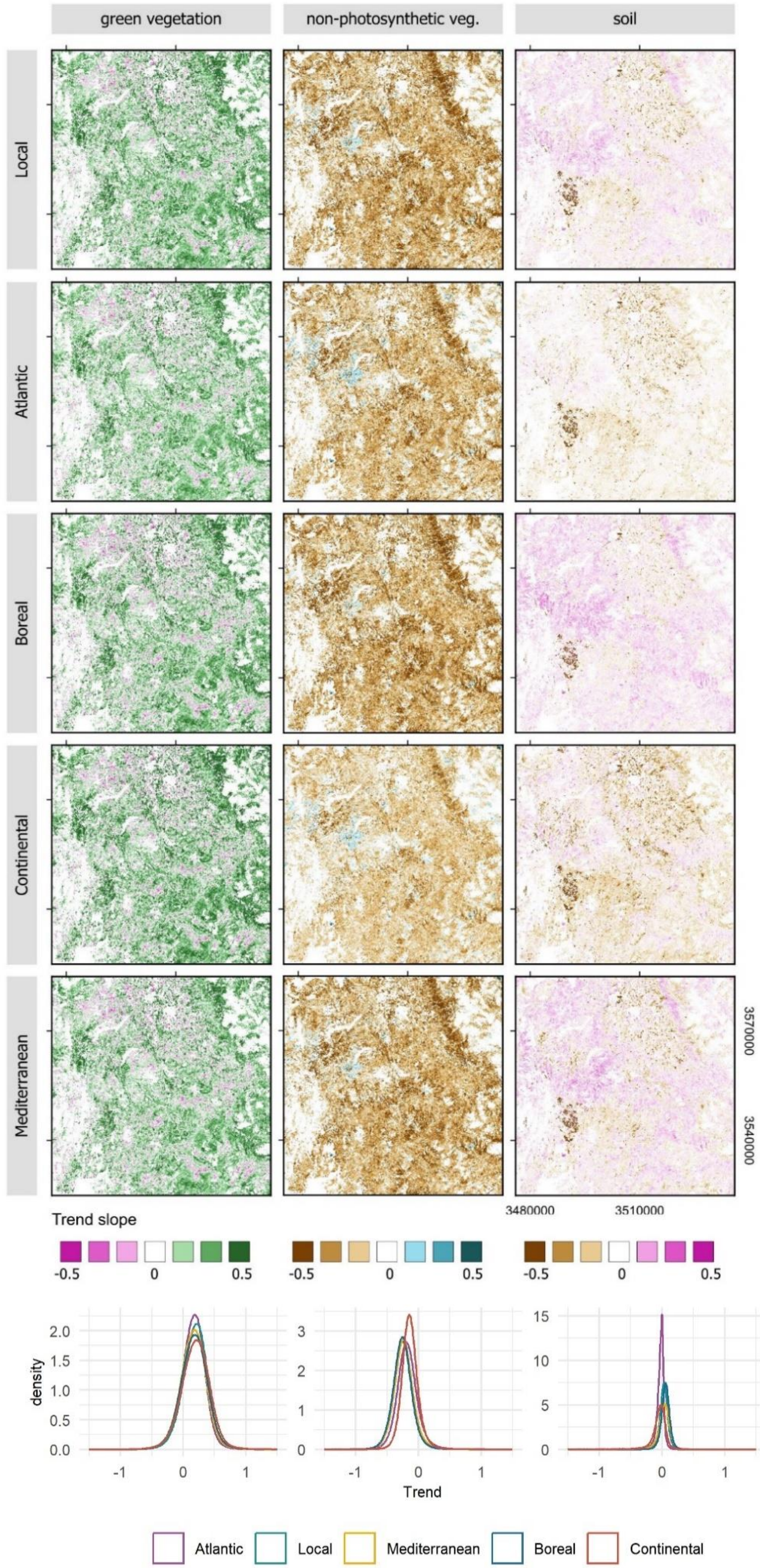

Figure SC24 Slope (in percentage point) of long-term trends in green vegetation, non-photosynthetic vegetation, and soil ground cover fractions derived for the UK test site using 1984-2021 time series of Landsat data using different sets of endmembers. Comparison among density distribution of slopes based on the Kolmogorov Smirnov test in Table SC3.

Table SC3 Kolmogorov-Smirnov test results comparing density distribution of pixel-level trend slope values derived for each test site using 1984-2021 time series of Landsat data and different sets of endmembers. Sample size of 5,000. H0 – tested distributions are the same.

Test site	Endmember sets	gv		npv		soil	
		D	p-val	D	p-val	D	p-val
AL	Local vs. Atlantic	0.045	0.000	0.114	0.000	0.100	0.000
	Local vs. Mediterranean	0.034	0.006	0.200	0.000	0.479	0.000
	Local vs. Boreal	0.058	0.000	0.153	0.000	0.290	0.000
	Local vs. Continental	0.012	0.877	0.109	0.000	0.281	0.000
	Atlantic vs. Mediterranean	0.048	0.000	0.126	0.000	0.558	0.000
	Atlantic vs. Boreal	0.084	0.000	0.033	0.009	0.371	0.000
	Atlantic vs. Continental	0.047	0.000	0.109	0.000	0.349	0.000
	Mediterranean vs. Boreal	0.016	0.528	0.016	0.577	0.019	0.353
	Mediterranean vs. Continental	0.026	0.068	0.209	0.000	0.215	0.000
	Boreal vs. Continental	0.036	0.003	0.147	0.000	0.086	0.000
BX	Local vs. Atlantic	0.013	0.822	0.061	0.000	0.099	0.000
	Local vs. Mediterranean	0.057	0.000	0.118	0.000	0.213	0.000
	Local vs. Boreal	0.046	0.000	0.078	0.000	0.150	0.000
	Local vs. Continental	0.060	0.000	0.175	0.000	0.126	0.000
	Atlantic vs. Mediterranean	0.052	0.000	0.070	0.000	0.279	0.000
	Atlantic vs. Boreal	0.046	0.000	0.030	0.022	0.235	0.000
	Atlantic vs. Continental	0.064	0.000	0.206	0.000	0.177	0.000
	Mediterranean vs. Boreal	0.025	0.092	0.013	0.822	0.019	0.327
	Mediterranean vs. Continental	0.069	0.000	0.275	0.000	0.172	0.000
	Boreal vs. Continental	0.058	0.000	0.231	0.000	0.170	0.000
CR	Local vs. Atlantic	0.033	0.009	0.114	0.000	0.192	0.000
	Local vs. Mediterranean	0.019	0.340	0.176	0.000	0.240	0.000
	Local vs. Boreal	0.029	0.028	0.227	0.000	0.317	0.000
	Local vs. Continental	0.085	0.000	0.101	0.000	0.094	0.000
	Atlantic vs. Mediterranean	0.042	0.000	0.129	0.000	0.164	0.000
	Atlantic vs. Boreal	0.047	0.000	0.146	0.000	0.181	0.000
	Atlantic vs. Continental	0.110	0.000	0.197	0.000	0.119	0.000
	Mediterranean vs. Boreal	0.020	0.259	0.013	0.822	0.017	0.435
	Mediterranean vs. Continental	0.096	0.000	0.227	0.000	0.209	0.000
	Boreal vs. Continental	0.066	0.000	0.317	0.000	0.280	0.000
DE	Local vs. Atlantic	0.172	0.000	0.210	0.000	0.441	0.000
	Local vs. Mediterranean	0.094	0.000	0.138	0.000	0.057	0.000
	Local vs. Boreal	0.092	0.000	0.125	0.000	0.187	0.000
	Local vs. Continental	0.050	0.000	0.212	0.000	0.282	0.000
	Atlantic vs. Mediterranean	0.044	0.000	0.289	0.000	0.385	0.000
	Atlantic vs. Boreal	0.067	0.000	0.281	0.000	0.337	0.000
	Atlantic vs. Continental	0.104	0.000	0.074	0.000	0.184	0.000
	Mediterranean vs. Boreal	0.012	0.864	0.024	0.107	0.013	0.776
	Mediterranean vs. Continental	0.051	0.000	0.330	0.000	0.197	0.000
	Boreal vs. Continental	0.042	0.000	0.345	0.000	0.213	0.000

Table SC3 continuation

Test site	Endmember sets	gv		npv		soil	
		D	p-val	D	p-val	D	p-val
ES	Local vs. Atlantic	0.067	0.000	0.308	0.000	0.170	0.000
	Local vs. Mediterranean	0.052	0.000	0.455	0.000	0.340	0.000
	Local vs. Boreal	0.022	0.170	0.361	0.000	0.213	0.000
	Local vs. Continental	0.059	0.000	0.367	0.000	0.200	0.000
	Atlantic vs. Mediterranean	0.045	0.000	0.355	0.000	0.338	0.000
	Atlantic vs. Boreal	0.064	0.000	0.121	0.000	0.116	0.000
	Atlantic vs. Continental	0.102	0.000	0.188	0.000	0.196	0.000
	Mediterranean vs. Boreal	0.013	0.807	0.015	0.594	0.015	0.661
	Mediterranean vs. Continental	0.061	0.000	0.184	0.000	0.175	0.000
	Boreal vs. Continental	0.048	0.000	0.082	0.000	0.134	0.000
FR	Local vs. Atlantic	0.086	0.000	0.239	0.000	0.468	0.000
	Local vs. Mediterranean	0.056	0.000	0.211	0.000	0.611	0.000
	Local vs. Boreal	0.052	0.000	0.161	0.000	0.471	0.000
	Local vs. Continental	0.030	0.025	0.212	0.000	0.618	0.000
	Atlantic vs. Mediterranean	0.087	0.000	0.038	0.002	0.288	0.000
	Atlantic vs. Boreal	0.102	0.000	0.075	0.000	0.077	0.000
	Atlantic vs. Continental	0.094	0.000	0.114	0.000	0.367	0.000
	Mediterranean vs. Boreal	0.015	0.661	0.013	0.776	0.021	0.239
	Mediterranean vs. Continental	0.036	0.003	0.118	0.000	0.063	0.000
	Boreal vs. Continental	0.030	0.025	0.052	0.000	0.274	0.000
IE	Local vs. Atlantic	0.031	0.014	0.021	0.211	0.128	0.000
	Local vs. Mediterranean	0.044	0.000	0.096	0.000	0.547	0.000
	Local vs. Boreal	0.036	0.003	0.085	0.000	0.500	0.000
	Local vs. Continental	0.038	0.001	0.108	0.000	0.223	0.000
	Atlantic vs. Mediterranean	0.040	0.001	0.084	0.000	0.560	0.000
	Atlantic vs. Boreal	0.051	0.000	0.087	0.000	0.516	0.000
	Atlantic vs. Continental	0.067	0.000	0.118	0.000	0.214	0.000
	Mediterranean vs. Boreal	0.028	0.042	0.030	0.025	0.026	0.061
	Mediterranean vs. Continental	0.045	0.000	0.187	0.000	0.341	0.000
	Boreal vs. Continental	0.043	0.000	0.170	0.000	0.298	0.000
LX	Local vs. Atlantic	0.072	0.000	0.230	0.000	0.313	0.000
	Local vs. Mediterranean	0.043	0.000	0.359	0.000	0.625	0.000
	Local vs. Boreal	0.032	0.011	0.276	0.000	0.407	0.000
	Local vs. Continental	0.025	0.092	0.264	0.000	0.508	0.000
	Atlantic vs. Mediterranean	0.052	0.000	0.186	0.000	0.487	0.000
	Atlantic vs. Boreal	0.051	0.000	0.037	0.002	0.161	0.000
	Atlantic vs. Continental	0.053	0.000	0.068	0.000	0.335	0.000
	Mediterranean vs. Boreal	0.011	0.912	0.015	0.610	0.017	0.450
	Mediterranean vs. Continental	0.030	0.025	0.224	0.000	0.144	0.000
	Boreal vs. Continental	0.025	0.088	0.083	0.000	0.227	0.000

Table SC3 continuation

Test site	Endmember sets	gv		npv		soil	
		D	p-val	D	p-val	D	p-val
PL	Local vs. Atlantic	0.157	0.000	0.205	0.000	0.249	0.000
	Local vs. Mediterranean	0.084	0.000	0.047	0.000	0.123	0.000
	Local vs. Boreal	0.088	0.000	0.121	0.000	0.064	0.000
	Local vs. Continental	0.063	0.000	0.134	0.000	0.069	0.000
	Atlantic vs. Mediterranean	0.083	0.000	0.166	0.000	0.348	0.000
	Atlantic vs. Boreal	0.085	0.000	0.124	0.000	0.230	0.000
	Atlantic vs. Continental	0.107	0.000	0.149	0.000	0.239	0.000
	Mediterranean vs. Boreal	0.013	0.822	0.019	0.327	0.015	0.627
	Mediterranean vs. Continental	0.045	0.000	0.134	0.000	0.135	0.000
	Boreal vs. Continental	0.034	0.005	0.126	0.000	0.115	0.000
RO	Local vs. Atlantic	0.155	0.000	0.129	0.000	0.191	0.000
	Local vs. Mediterranean	0.074	0.000	0.224	0.000	0.222	0.000
	Local vs. Boreal	0.068	0.000	0.237	0.000	0.279	0.000
	Local vs. Continental	0.066	0.000	0.126	0.000	0.092	0.000
	Atlantic vs. Mediterranean	0.089	0.000	0.232	0.000	0.331	0.000
	Atlantic vs. Boreal	0.100	0.000	0.279	0.000	0.368	0.000
	Atlantic vs. Continental	0.111	0.000	0.067	0.000	0.095	0.000
	Mediterranean vs. Boreal	0.027	0.047	0.014	0.678	0.026	0.061
	Mediterranean vs. Continental	0.031	0.016	0.280	0.000	0.289	0.000
	Boreal vs. Continental	0.016	0.544	0.323	0.000	0.362	0.000
SA	Local vs. Atlantic	0.034	0.006	0.179	0.000	0.243	0.000
	Local vs. Boreal	0.035	0.005	0.235	0.000	0.273	0.000
	Local vs. Continental	0.047	0.000	0.178	0.000	0.114	0.000
	Atlantic vs. Boreal	0.051	0.000	0.057	0.000	0.029	0.030
	Atlantic vs. Continental	0.069	0.000	0.073	0.000	0.121	0.000
	Boreal vs. Continental	0.057	0.000	0.096	0.000	0.170	0.000
SE	Local vs. Atlantic	0.070	0.000	0.155	0.000	0.161	0.000
	Local vs. Mediterranean	0.022	0.178	0.039	0.001	0.140	0.000
	Local vs. Continental	0.023	0.129	0.138	0.000	0.202	0.000
	Atlantic vs. Mediterranean	0.067	0.000	0.135	0.000	0.114	0.000
	Atlantic vs. Continental	0.088	0.000	0.076	0.000	0.088	0.000
	Boreal vs. Continental	0.022	0.170	0.128	0.000	0.087	0.000
UK	Local vs. Atlantic	0.087	0.000	0.179	0.000	0.409	0.000
	Local vs. Mediterranean	0.039	0.001	0.325	0.000	0.347	0.000
	Local vs. Boreal	0.077	0.000	0.032	0.014	0.099	0.000
	Local vs. Continental	0.049	0.000	0.046	0.000	0.177	0.000
	Atlantic vs. Mediterranean	0.109	0.000	0.138	0.000	0.169	0.000
	Atlantic vs. Boreal	0.033	0.009	0.142	0.000	0.435	0.000
	Atlantic vs. Continental	0.062	0.000	0.193	0.000	0.566	0.000
	Mediterranean vs. Boreal	0.070	0.000	0.306	0.000	0.338	0.000
	Mediterranean vs. Continental	0.064	0.000	0.376	0.000	0.469	0.000
	Boreal vs. Continental	0.023	0.129	0.014	0.744	0.024	0.118

Table SC4 Range of autocorrelation for CEFs based on Landsat time series unmixed using a variety of local and regional endmembers.

green vegetation

Test site	Local	Atlantic	Boreal	Continental	Mediterranean
AL	5.35	6.09	4.74	5.11	6.09
BX	5.56	6.23	4.98	5.96	6.23
CR	19.99	16.83	19.30	18.43	16.83
DE	18.61	19.09	18.78	18.93	19.09
ES	53.05	45.69	52.48	46.08	45.69
FR	33.39	30.51	31.71	31.74	30.51
IE	2.96	2.94	2.35	2.71	2.94
LX	9.64	9.18	8.72	9.39	9.18
PL	16.35	16.18	16.35	15.97	16.18
RO	27.73	27.45	28.59	28.44	27.45
SA	27.22	28.48	27.43	28.48	28.48
SE	7.70	9.12	8.13	9.12	9.12
UK	7.33	7.27	6.09	6.84	7.27

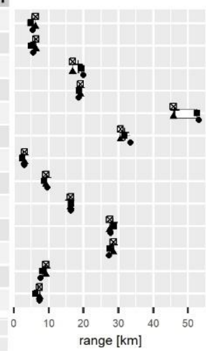

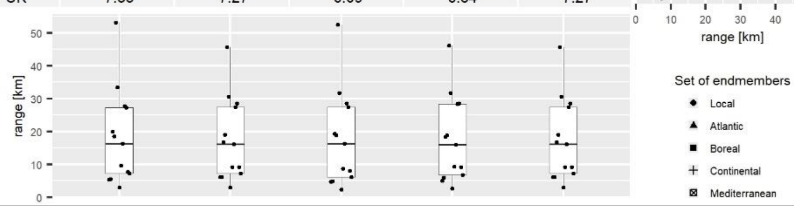

non-photosynthetic vegetation

Test site	Local	Atlantic	Boreal	Continental	Mediterranean
AL	8.11	8.32	9.59	7.69	8.32
BX	9.38	9.76	11.12	9.06	9.76
CR	0.78	3.45	4.64	4.46	3.45
DE	16.98	7.91	18.13	7.04	7.91
ES	23.82	32.54	18.90	26.74	32.54
FR	22.41	10.00	22.18	9.94	10.00
IE	3.80	3.68	5.80	3.17	3.68
LX	10.47	8.39	8.20	7.69	8.39
PL	11.25	10.14	12.86	9.94	10.14
RO	9.77	9.99	13.91	9.70	9.99
SA	21.90	20.12	18.54	23.34	20.12
SE	11.74	6.49	13.63	7.10	6.49
UK	8.56	7.10	9.87	7.12	7.10

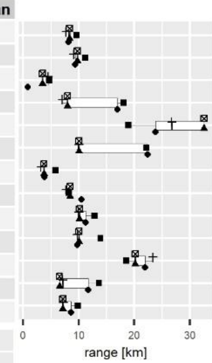

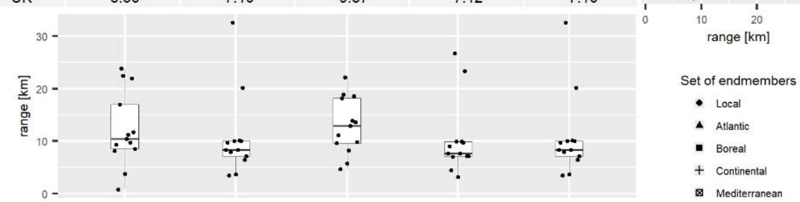

soil

Test site	Local	Atlantic	Boreal	Continental	Mediterranean
AL	1.90	2.97	9.83	4.63	2.97
BX	7.07	7.13	13.65	8.16	7.13
CR	3.94	13.50	11.62	8.41	13.50
DE	17.48	10.99	13.89	14.74	10.99
ES	25.69	73.09	67.84	60.08	73.09
FR	17.28	37.41	41.93	39.25	37.41
IE	0.27	0.52	13.85	3.97	0.52
LX	0.71	5.92	8.90	6.92	5.92
PL	8.59	5.66	9.58	7.14	5.66
RO	26.42	25.95	22.60	27.22	25.95
SA	14.30	24.62	26.04	21.37	24.62
SE	6.18	7.97	6.65	6.63	7.97
UK	12.02	8.56	12.10	9.12	8.56

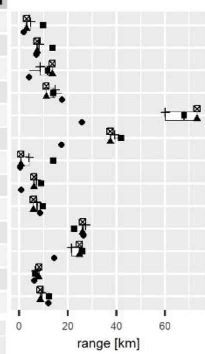

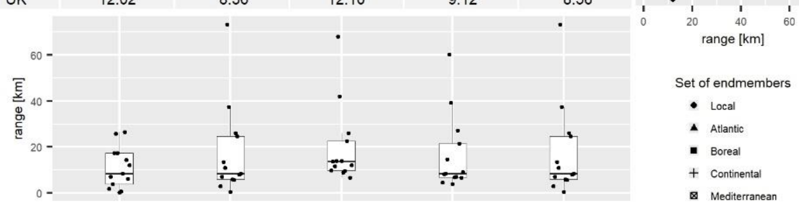

Table SC5 Generalized Least Square (GLS) regression results for trends for regions of different soil types (H0: there is no temporal trend on soil type i) and the overall effect of soil type on the long-term trends (H0: soil type has no overall effect on trends) for each *gv* Cumulative Endmember Fraction calculated using five different endmember sets: Local, Atlantic, Mediterranean, Boreal and Temperate. Est gives the overall trend, SE its standard deviation, t.stat and pval.t report t-test value and its significance, respectively. Endmember sets in Figure 2.

Local

Soil Type	Est	SE	t.stat	pval.t
Andosols	0.036	0.030	1.223	0.222
Arenosls	0.044	0.049	0.908	0.364
Cambisols	0.059	0.015	3.887	<0.001
Fluvisols	0.081	0.026	3.102	0.002
Gleysols	0.151	0.025	5.960	<0.001
Histosols	0.110	0.023	4.901	<0.001
Lithosols	-0.008	0.051	-0.161	0.872
Luvisols	0.054	0.018	3.054	0.002
Phaeozems	0.064	0.038	1.674	0.094
Planosols	0.132	0.038	3.499	<0.001
Podzols	0.136	0.022	6.129	<0.001
Rankers	0.159	0.047	3.394	0.001
Regosols	0.003	0.051	0.063	0.95

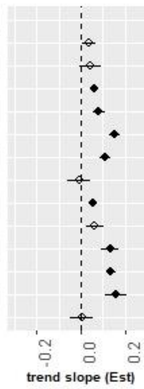

Chi-squared test p-value 0

Atlantic

Soil Type	Est	SE	t.stat	pval.t
Andosols	0.027	0.025	1.092	0.275
Arenosls	0.031	0.040	0.785	0.432
Cambisols	0.045	0.013	3.504	<0.001
Fluvisols	0.061	0.023	2.697	0.007
Gleysols	0.128	0.021	5.951	<0.001
Histosols	0.078	0.019	4.098	<0.001
Lithosols	-0.011	0.043	-0.267	0.789
Luvisols	0.039	0.015	2.590	0.01
Phaeozems	0.035	0.033	1.069	0.285
Planosols	0.115	0.033	3.473	0.001
Podzols	0.109	0.019	5.759	<0.001
Rankers	0.130	0.043	3.048	0.002
Regosols	0.001	0.044	0.032	0.975

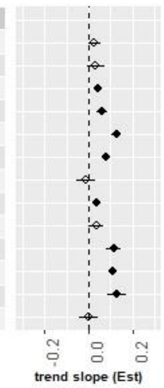

Chi-squared test p-value 0.001

Mediterranean

Soil Type	Est	SE	t.stat	pval.t
Andosols	0.024	0.029	0.850	0.395
Arenosls	0.018	0.047	0.388	0.698
Cambisols	0.046	0.014	3.226	0.001
Fluvisols	0.052	0.026	2.021	0.043
Gleysols	0.142	0.025	5.733	<0.001
Histosols	0.083	0.022	3.851	<0.001
Lithosols	-0.014	0.048	-0.295	0.768
Luvisols	0.038	0.017	2.221	0.026
Phaeozems	0.049	0.038	1.292	0.196
Planosols	0.102	0.037	2.756	0.006
Podzols	0.124	0.022	5.741	<0.001
Rankers	0.147	0.050	2.938	0.003
Regosols	-0.012	0.054	-0.218	0.828

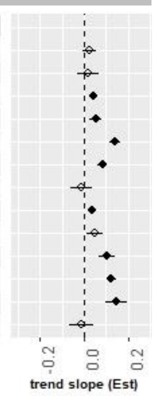

Chi-squared test p-value 0

Boreal

Soil Type	Est	SE	t.stat	pval.t
Andosols	0.026	0.030	0.871	0.384
Arenosls	0.028	0.050	0.566	0.572
Cambisols	0.051	0.015	3.365	0.001
Fluvisols	0.063	0.027	2.343	0.019
Gleysols	0.150	0.026	5.777	<0.001
Histosols	0.091	0.023	3.958	<0.001
Lithosols	-0.013	0.051	-0.256	0.798
Luvisols	0.042	0.018	2.372	0.018
Phaeozems	0.053	0.040	1.330	0.183
Planosols	0.114	0.040	2.849	0.004
Podzols	0.136	0.023	5.932	<0.001
Rankers	0.158	0.052	3.047	0.002
Regosols	-0.009	0.048	-0.180	0.857

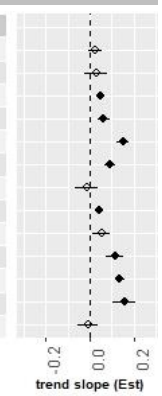

Chi-squared test p-value 0

Temperate

Soil Type	Est	SE	t.stat	pval.t
Andosols	0.038	0.031	1.226	0.22
Arenosls	0.042	0.051	0.819	0.413
Cambisols	0.060	0.016	3.749	<0.001
Fluvisols	0.078	0.028	2.822	0.005
Gleysols	0.158	0.027	5.905	<0.001
Histosols	0.101	0.024	4.255	<0.001
Lithosols	0.002	0.055	0.030	0.976
Luvisols	0.053	0.019	2.830	0.005
Phaeozems	0.057	0.041	1.391	0.164
Planosols	0.144	0.042	3.473	0.001
Podzols	0.140	0.024	5.920	<0.001
Rankers	0.164	0.053	3.076	0.002
Regosols	0.008	0.050	0.161	0.872

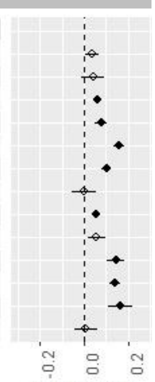

Chi-squared test p-value 0.001

Table SC6 Generalized Least Square (GLS) regression results for trends for regions of different soil types (H0: there is no temporal trend on soil type i) and the overall effect of soil type on the long-term trends (H0: soil type has no overall effect on trends) for each *npv* Cumulative Endmember Fraction calculated using five different endmember sets: Local, Atlantic, Mediterranean, Boreal and Temperate. Est gives the overall trend, SE its standard deviation, t.stat and pval.t report t-test value and its significance, respectively. Endmember sets in Figure 2.

Local

Soil Type	Est	SE	t.stat	pval.t
Andosols	-0.103	0.024	-4.294	<0.001
Arenosls	-0.107	0.042	-2.530	0.011
Cambisols	-0.084	0.012	-7.207	<0.001
Fluvisols	-0.149	0.021	-7.004	<0.001
Gleysols	-0.139	0.021	-6.700	<0.001
Histosols	-0.133	0.018	-7.251	<0.001
Lithosols	0.021	0.041	0.506	0.613
Luvisols	-0.104	0.014	-7.449	<0.001
Phaeozems	-0.086	0.031	-2.733	0.006
Planosols	-0.228	0.031	-7.243	<0.001
Podzols	-0.102	0.018	-5.611	<0.001
Rankers	-0.148	0.041	-3.578	<0.001
Regosols	-0.017	0.041	-0.408	0.683

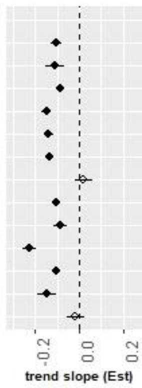

Chi-squared test p-value <0.001

Atlantic

Soil Type	Est	SE	t.stat	pval.t
Andosols	-0.085	0.025	-3.340	0.001
Arenosls	-0.120	0.043	-2.817	0.005
Cambisols	-0.082	0.012	-6.854	<0.001
Fluvisols	-0.137	0.022	-6.205	<0.001
Gleysols	-0.097	0.022	-4.477	<0.001
Histosols	-0.091	0.019	-4.786	<0.001
Lithosols	0.018	0.045	0.397	0.692
Luvisols	-0.094	0.014	-6.564	<0.001
Phaeozems	-0.048	0.033	-1.483	0.138
Planosols	-0.222	0.035	-6.428	<0.001
Podzols	-0.050	0.019	-2.659	0.008
Rankers	-0.079	0.043	-1.838	0.066
Regosols	0.002	0.049	0.032	0.974

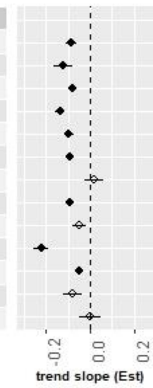

Chi-squared test p-value 0

Mediterranean

Soil Type	Est	SE	t.stat	pval.t
Andosols	-0.141	0.025	-5.528	<0.001
Arenosls	-0.184	0.043	-4.257	<0.001
Cambisols	-0.145	0.012	-11.644	<0.001
Fluvisols	-0.201	0.023	-8.851	<0.001
Gleysols	-0.168	0.022	-7.638	<0.001
Histosols	-0.176	0.019	-9.126	<0.001
Lithosols	0.025	0.044	0.573	0.566
Luvisols	-0.158	0.015	-10.584	<0.001
Phaeozems	-0.129	0.033	-3.892	<0.001
Planosols	-0.295	0.034	-8.628	<0.001
Podzols	-0.132	0.019	-6.967	<0.001
Rankers	-0.148	0.043	-3.471	0.001
Regosols	0.017	0.043	0.404	0.686

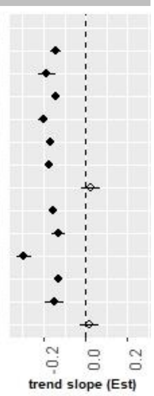

Chi-squared test p-value <0.001

Boreal

Soil Type	Est	SE	t.stat	pval.t
Andosols	-0.122	0.024	-5.198	<0.001
Arenosls	-0.160	0.039	-4.074	<0.001
Cambisols	-0.136	0.012	-10.990	<0.001
Fluvisols	-0.187	0.021	-9.119	<0.001
Gleysols	-0.166	0.021	-8.050	<0.001
Histosols	-0.170	0.018	-9.420	<0.001
Lithosols	0.037	0.040	0.911	0.362
Luvisols	-0.147	0.014	-10.280	<0.001
Phaeozems	-0.141	0.030	-4.729	<0.001
Planosols	-0.289	0.031	-9.324	<0.001
Podzols	-0.120	0.018	-6.677	<0.001
Rankers	-0.177	0.039	-4.498	<0.001
Regosols	0.006	0.045	0.135	0.893

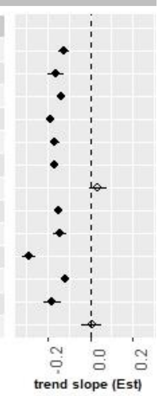

Chi-squared test p-value <0.001

Temperate

Soil Type	Est	SE	t.stat	pval.t
Andosols	-0.092	0.019	-4.843	<0.001
Arenosls	-0.137	0.032	-4.237	<0.001
Cambisols	-0.085	0.008	-10.293	<0.001
Fluvisols	-0.134	0.017	-7.982	<0.001
Gleysols	-0.092	0.016	-5.639	<0.001
Histosols	-0.092	0.014	-6.492	<0.001
Lithosols	-0.010	0.031	-0.324	0.746
Luvisols	-0.098	0.010	-9.520	<0.001
Phaeozems	-0.052	0.025	-2.088	0.037
Planosols	-0.201	0.025	-7.910	<0.001
Podzols	-0.061	0.014	-4.384	<0.001
Rankers	-0.073	0.033	-2.208	0.027
Regosols	-0.031	0.039	-0.794	0.427

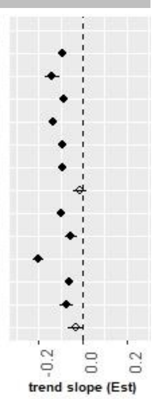

Chi-squared test p-value <0.001

Table SC7 Generalized Least Square (GLS) regression results for trends for regions of different soil types (H0: there is no temporal trend on soil type i) and the overall effect of soil type on the long-term trends (H0: soil type has no overall effect on trends) for each *soil* Cumulative Endmember Fraction calculated using five different endmember sets: Local, Atlantic, Mediterranean, Boreal and Temperate. Est gives the overall trend, SE its standard deviation, t.stat and pval.t report t-test value and its significance, respectively. Endmember sets in Figure 2.

Local

Soil Type	Est	SE	t.stat	pval.t
Andosols	0.005	0.022	0.217	0.828
Arenosls	-0.001	0.034	-0.044	0.965
Cambisols	-0.009	0.011	-0.896	0.37
Fluvisols	0.008	0.019	0.416	0.677
Gleysols	0.025	0.019	1.352	0.176
Histosols	0.025	0.016	1.526	0.127
Lithosols	-0.036	0.037	-0.967	0.334
Luvisols	0.000	0.013	-0.032	0.974
Phaeozems	0.002	0.029	0.081	0.936
Planosols	-0.034	0.026	-1.282	0.2
Podzols	0.008	0.016	0.484	0.629
Rankers	0.085	0.038	2.210	0.027
Regosols	0.011	0.040	0.283	0.778

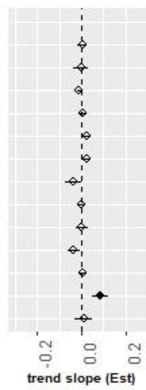

Chi-squared test p-value 0.003

Atlantic

Soil Type	Est	SE	t.stat	pval.t
Andosols	-0.032	0.017	-1.833	0.067
Arenosls	0.000	0.028	-0.003	0.998
Cambisols	-0.024	0.009	-2.543	0.011
Fluvisols	-0.025	0.016	-1.567	0.117
Gleysols	-0.010	0.015	-0.648	0.517
Histosols	-0.020	0.013	-1.477	0.14
Lithosols	-0.034	0.029	-1.152	0.249
Luvisols	-0.022	0.011	-1.992	0.046
Phaeozems	-0.030	0.022	-1.346	0.178
Planosols	-0.054	0.021	-2.559	0.01
Podzols	-0.030	0.013	-2.204	0.028
Rankers	0.029	0.028	1.039	0.299
Regosols	-0.010	0.030	-0.350	0.727

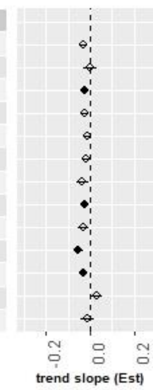

Chi-squared test p-value 0.572

Mediterranean

Soil Type	Est	SE	t.stat	pval.t
Andosols	0.037	0.019	1.948	0.051
Arenosls	0.083	0.029	2.852	0.004
Cambisols	0.050	0.011	4.616	<0.001
Fluvisols	0.055	0.017	3.172	0.002
Gleysols	0.071	0.016	4.319	<0.001
Histosols	0.063	0.015	4.210	<0.001
Lithosols	-0.024	0.033	-0.731	0.465
Luvisols	0.057	0.012	4.615	<0.001
Phaeozems	0.061	0.025	2.477	0.013
Planosols	0.035	0.024	1.466	0.143
Podzols	0.047	0.015	3.155	0.002
Rankers	0.112	0.030	3.675	<0.001
Regosols	-0.022	0.033	-0.669	0.503

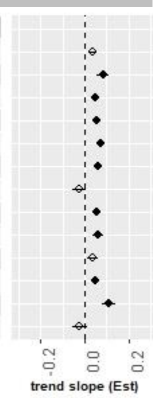

Chi-squared test p-value 0.007

Boreal

Soil Type	Est	SE	t.stat	pval.t
Andosols	0.020	0.014	1.417	0.157
Arenosls	0.043	0.022	1.942	0.052
Cambisols	0.035	0.008	4.183	<0.001
Fluvisols	0.041	0.013	3.183	0.001
Gleysols	0.062	0.012	5.093	<0.001
Histosols	0.051	0.011	4.604	<0.001
Lithosols	-0.052	0.025	-2.100	0.036
Luvisols	0.037	0.009	3.962	<0.001
Phaeozems	0.064	0.018	3.471	0.001
Planosols	0.034	0.018	1.870	0.062
Podzols	0.044	0.011	3.996	<0.001
Rankers	0.123	0.022	5.696	<0.001
Regosols	-0.022	0.024	-0.931	0.352

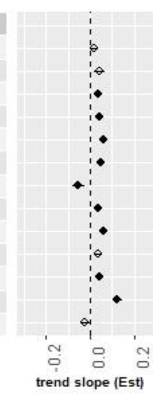

Chi-squared test p-value 0

Temperate

Soil Type	Est	SE	t.stat	pval.t
Andosols	-0.016	0.023	-0.689	0.491
Arenosls	0.036	0.037	0.974	0.33
Cambisols	-0.007	0.013	-0.558	0.577
Fluvisols	-0.010	0.021	-0.487	0.626
Gleysols	0.000	0.020	0.013	0.99
Histosols	-0.009	0.018	-0.469	0.639
Lithosols	0.008	0.040	0.194	0.846
Luvisols	-0.003	0.015	-0.190	0.85
Phaeozems	-0.019	0.030	-0.647	0.517
Planosols	-0.049	0.031	-1.560	0.119
Podzols	-0.021	0.018	-1.163	0.245
Rankers	0.050	0.038	1.319	0.187
Regosols	0.033	0.042	0.795	0.427

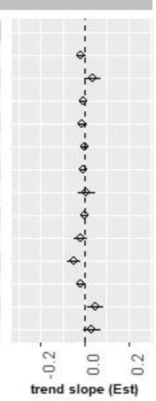

Chi-squared test p-value 0.133

Impact of data density and endmember definitions on long-term trends in ground cover fractions across European grasslands

Supplement D

Katarzyna Ewa Lewińska [1,2], Akpona Okujeni [3,1], Katja Kowalski [4,1], Fabian Lehmann [5], Volker C. Radeloff [2], Ulf Leser [5], Patrick Hostert [1,6]

[1] Geography Department, Humboldt-Universität zu Berlin, Unter den Linden 6, 10099 Berlin, Germany.

[2] SILVIS Lab, Department of Forest and Wildlife Ecology, University of Wisconsin-Madison, 1630 Linden Drive, Madison WI 53706, USA.

[3] Helmholtz Center Potsdam, GFZ German Research Center for Geosciences, Telegrafenberg, 14473 Potsdam, Germany

[4] Earth Observation for Ecosystem Management, School of Life Sciences, Technical University of Munich, 11 Hans-Carl-v.-Carlowitz-Platz 2, 85354 Freising, Germany

[5] Department of Computer Science, Humboldt-Universität zu Berlin, Unter den Linden 6, 10099 Berlin, Germany

[6] Integrative Research Institute on Transformations of Human-Environment Systems (IRI THESys), Humboldt-Universität zu Berlin, Unter den Linden 6, 10099 Berlin, Germany

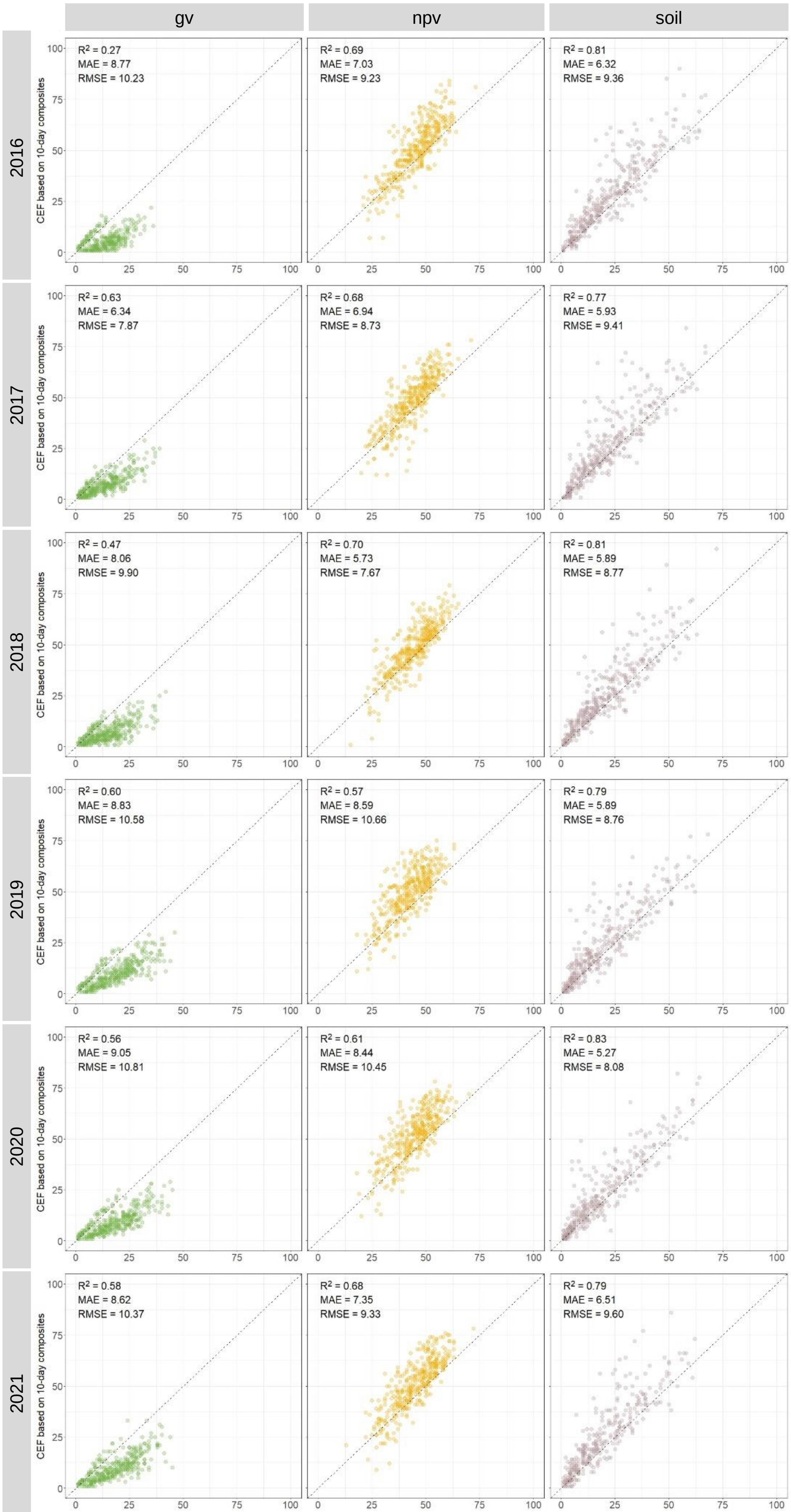

Figure SD1 Comparison between CEFs calculated based on monthly composites (x-axis) and 10-day composites (y-axis) for CR test site. Unmixing done using the local set of endmembers.

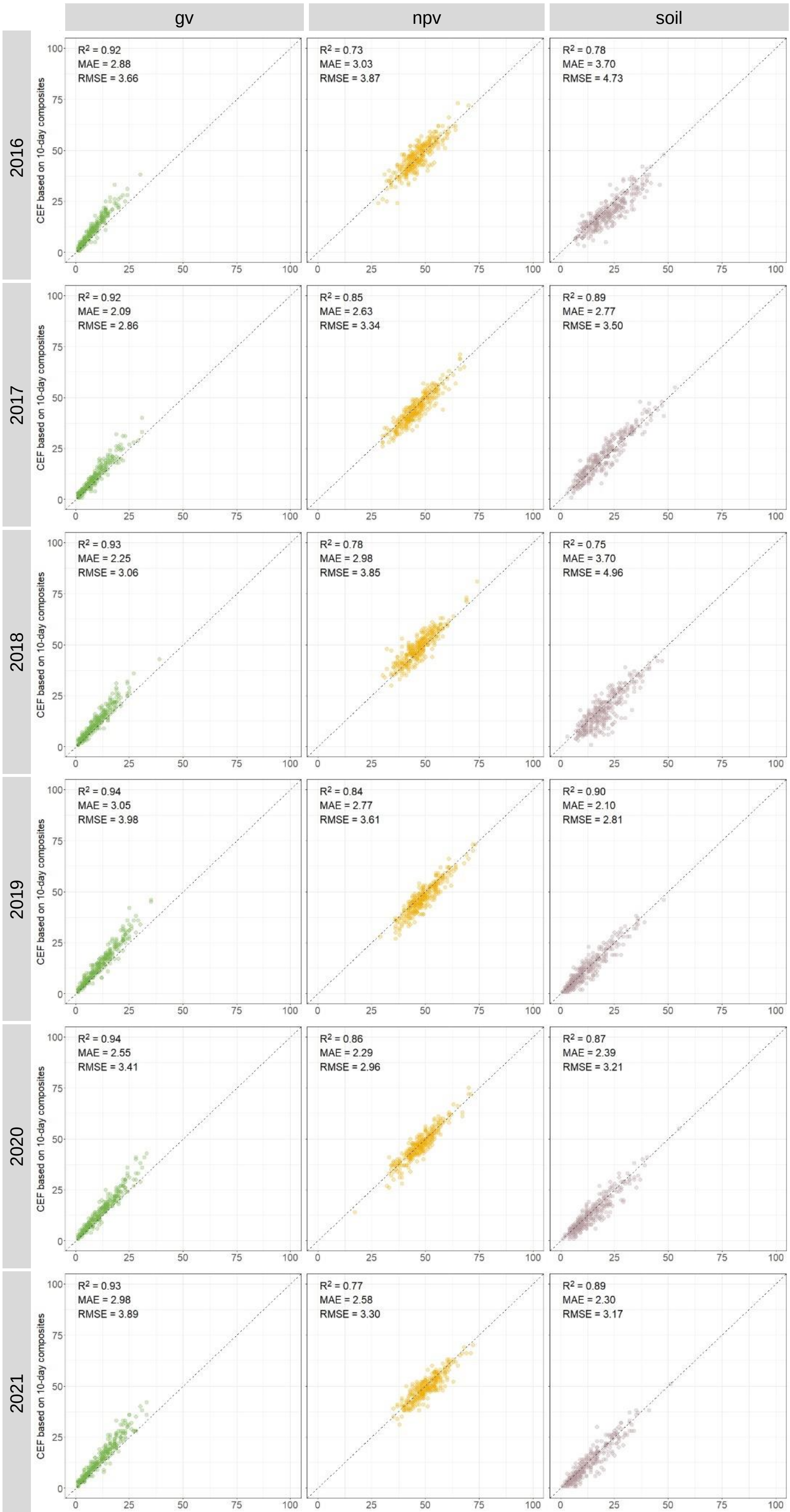

Figure SD2 Comparison between CEFs calculated based on monthly composites (x-axis) and 10-day composites (y-axis) for CR test site. Unmixing done using the Atlantic set of endmembers.

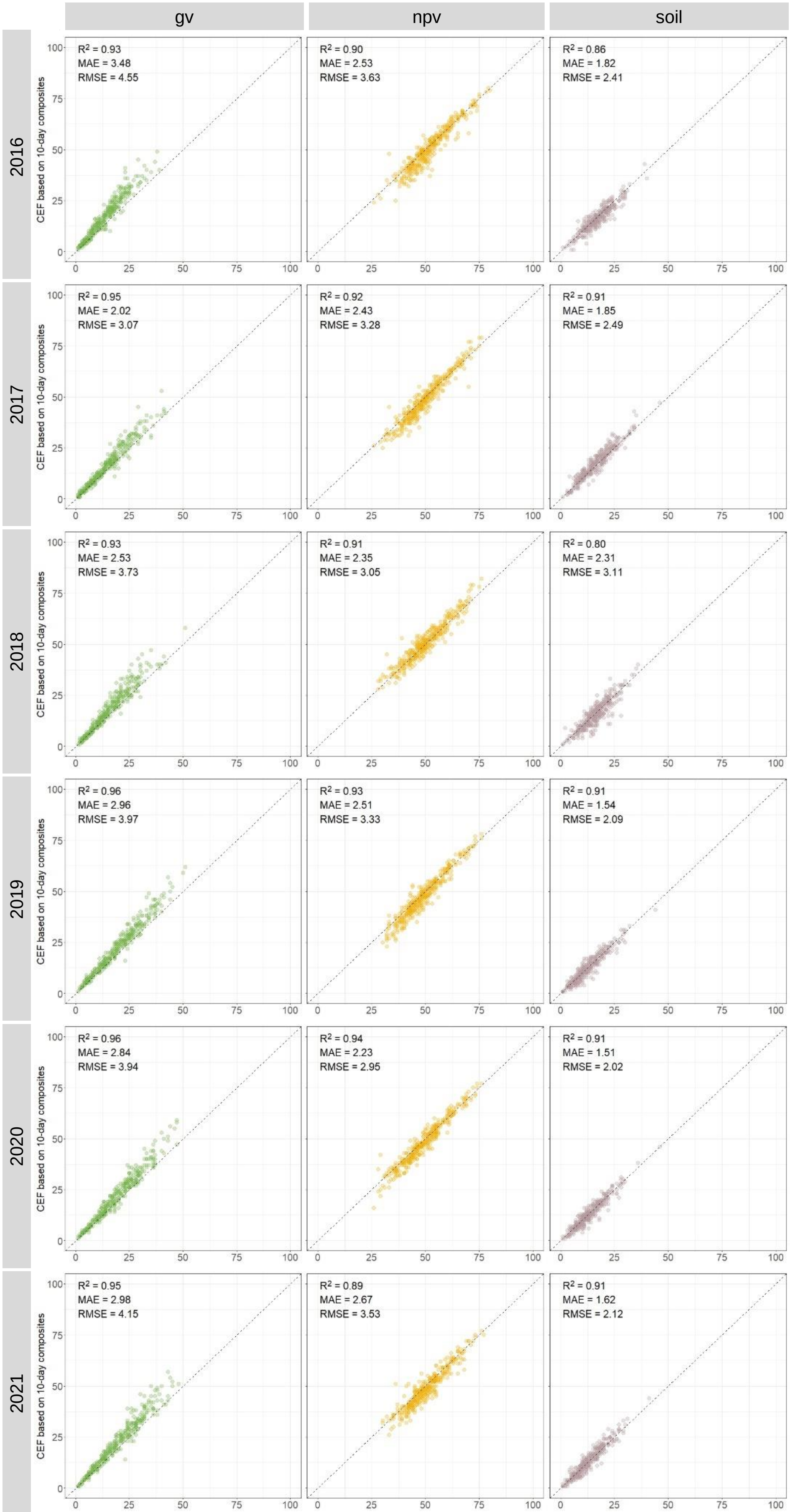

Figure SD3 Comparison between CEFs calculated based on monthly composites (x-axis) and 10-day composites (y-axis) for CR test site. Unmixing done using the Boreal set of endmembers.

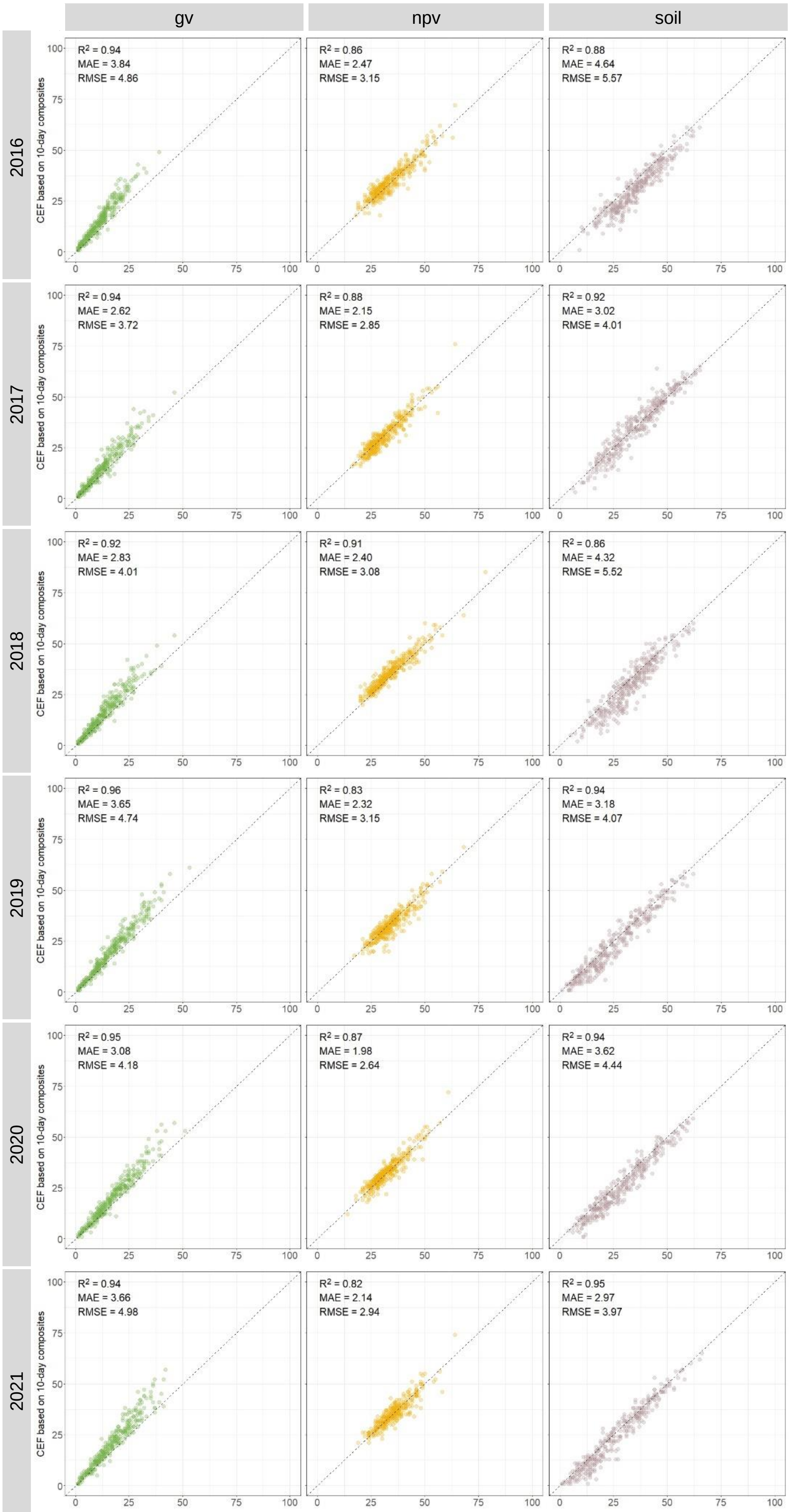

Figure SD4 Comparison between CEFs calculated based on monthly composites (x-axis) and 10-day composites (y-axis) for CR test site. Unmixing done using the Continental set of endmembers.

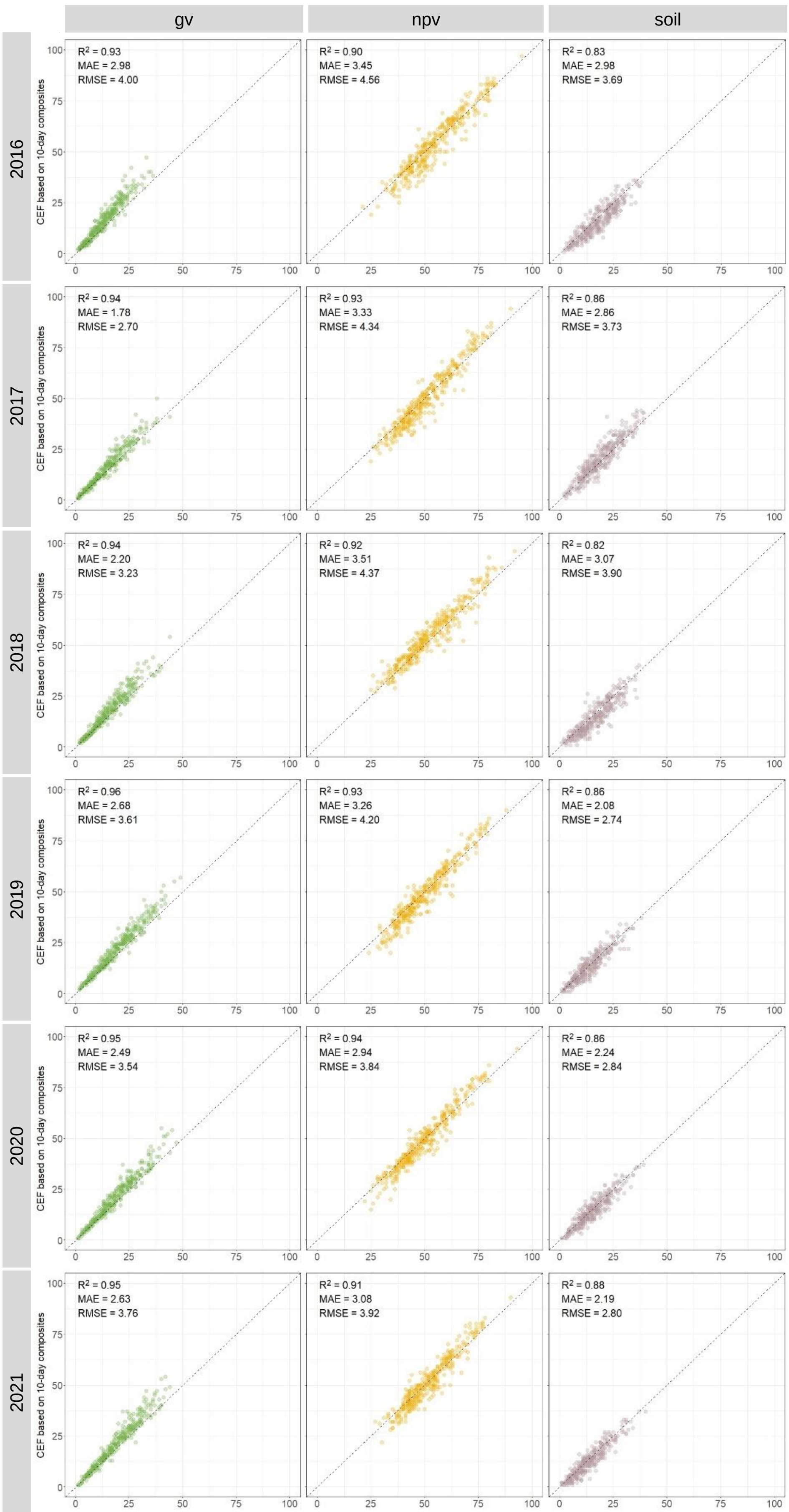

Figure SD5 Comparison between CEFs calculated based on monthly composites (x-axis) and 10-day composites (y-axis) for CR test site. Unmixing done using the Mediterranean set of endmembers.

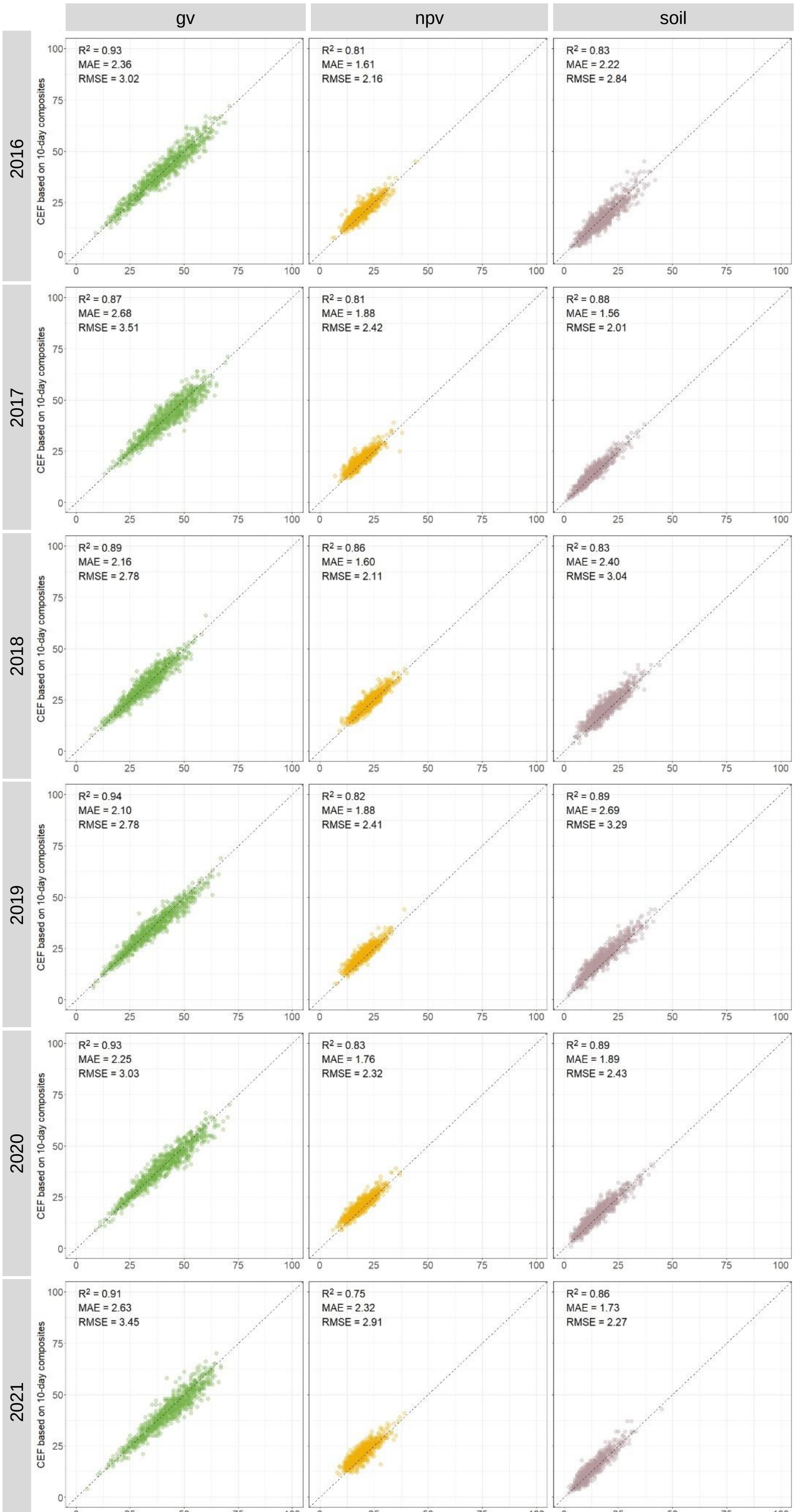

Figure SD6 Comparison between CEFs calculated based on monthly composites (x-axis) and 10-day composites (y-axis) for DE test site. Unmixing done using the local set of endmembers.

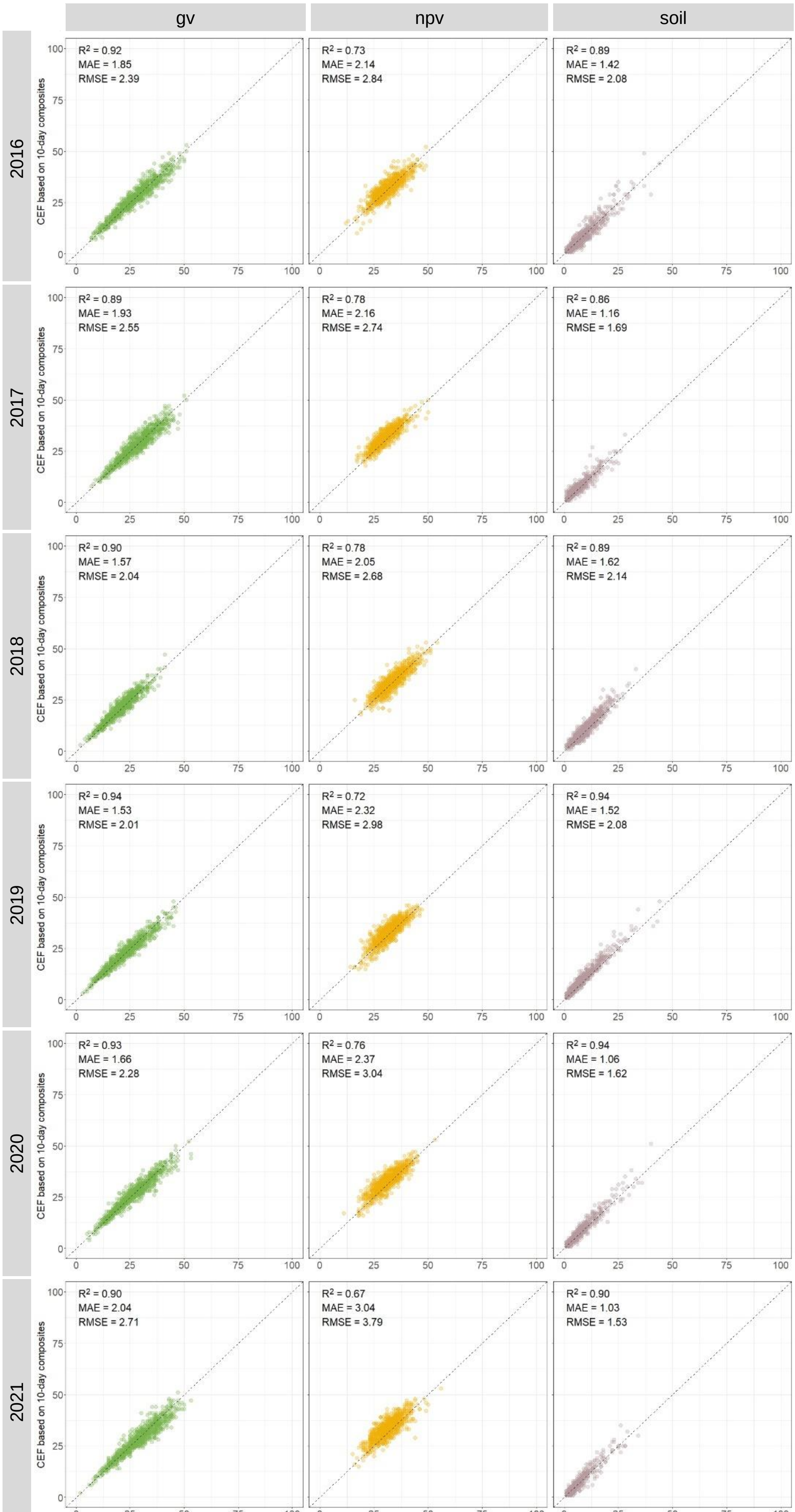

Figure SD7 Comparison between CEFs calculated based on monthly composites (x-axis) and 10-day composites (y-axis) for DE test site. Unmixing done using the Atlantic set of endmembers.

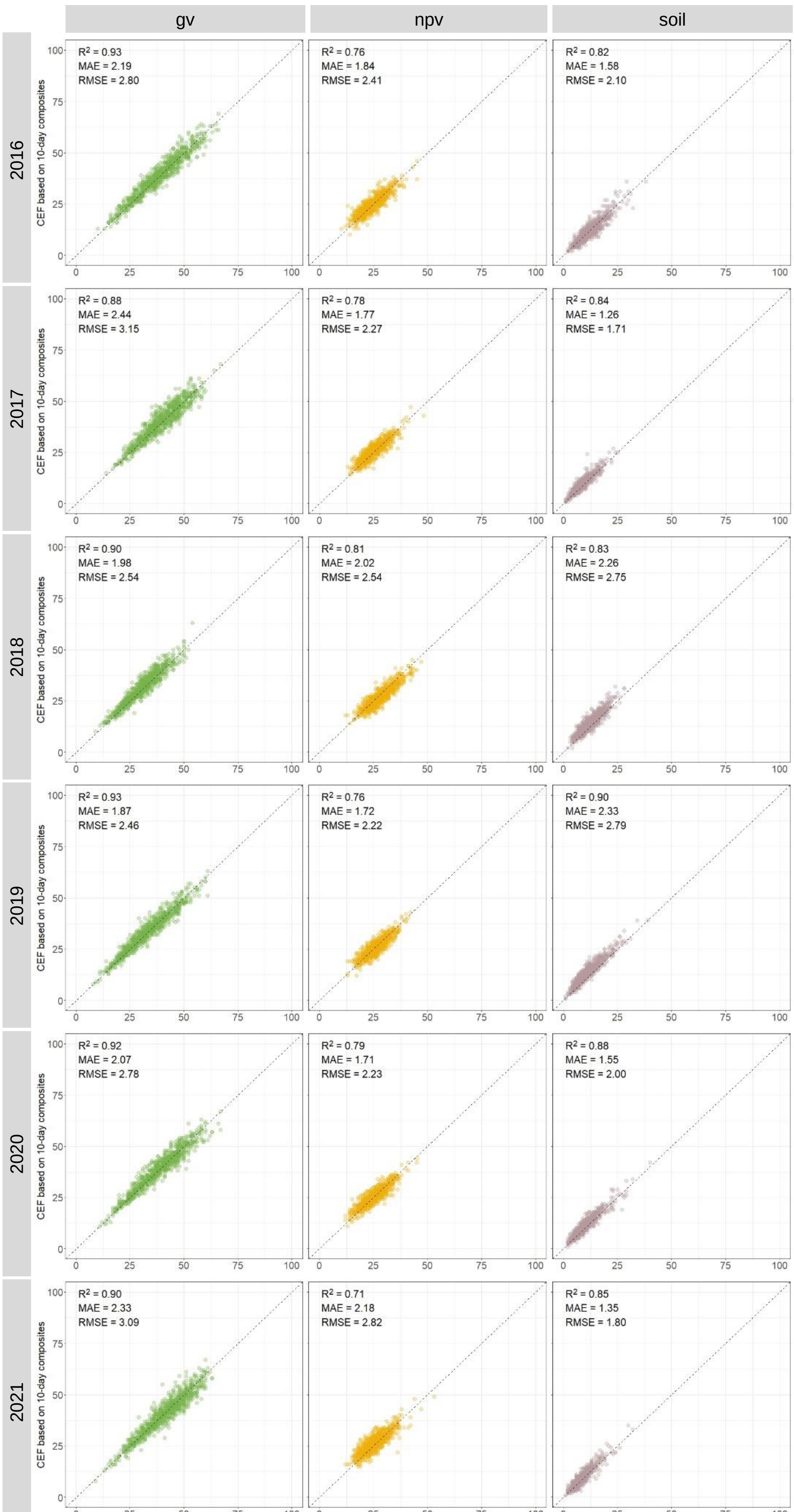

Figure SD8 Comparison between CEFs calculated based on monthly composites (x-axis) and 10-day composites (y-axis) for DE test site. Unmixing done using the Boreal set of endmembers.

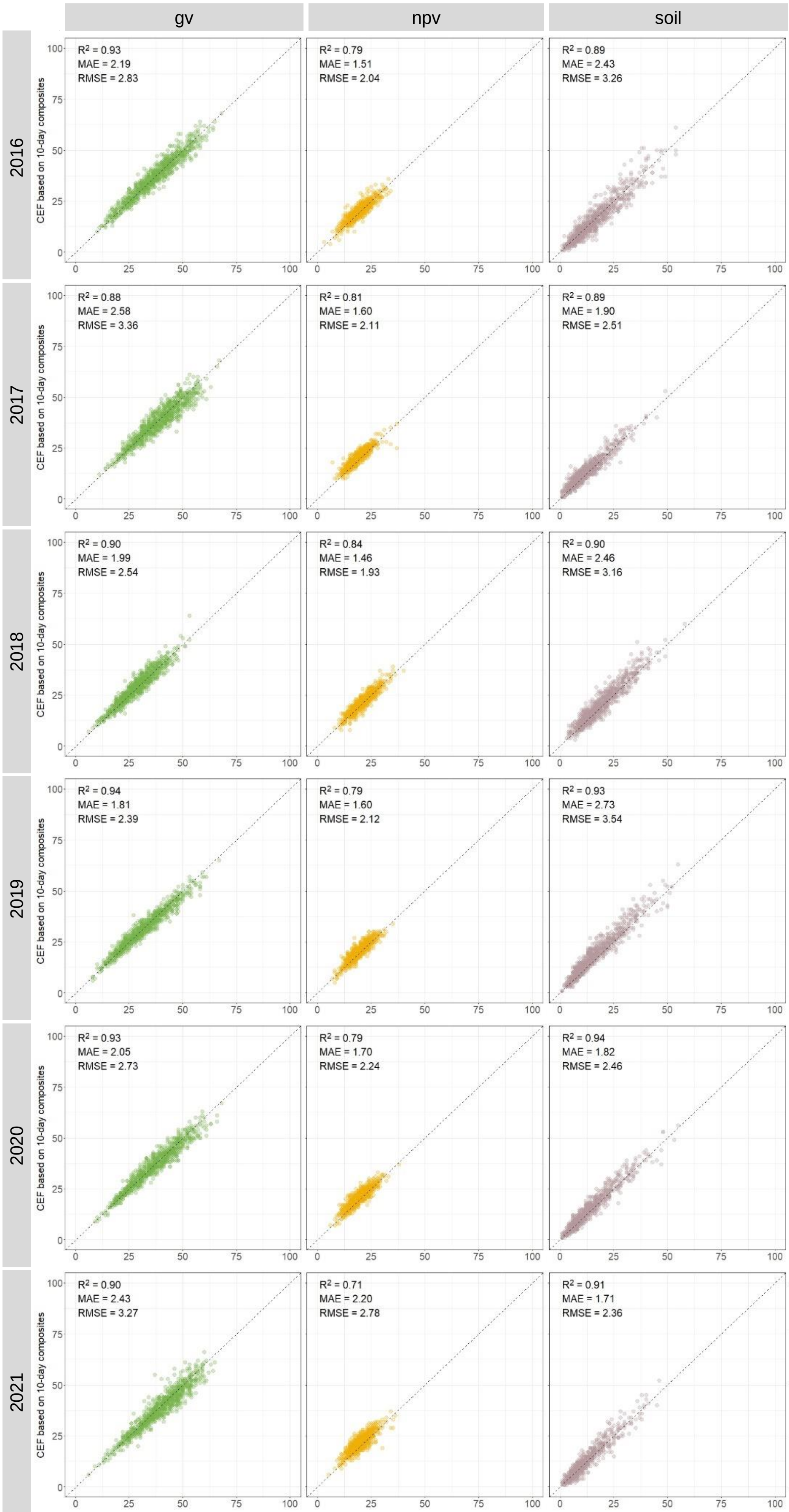

Figure SD9 Comparison between CEFs calculated based on monthly composites (x-axis) and 10-day composites (y-axis) for DE test site. Unmixing done using the Continental set of endmembers.

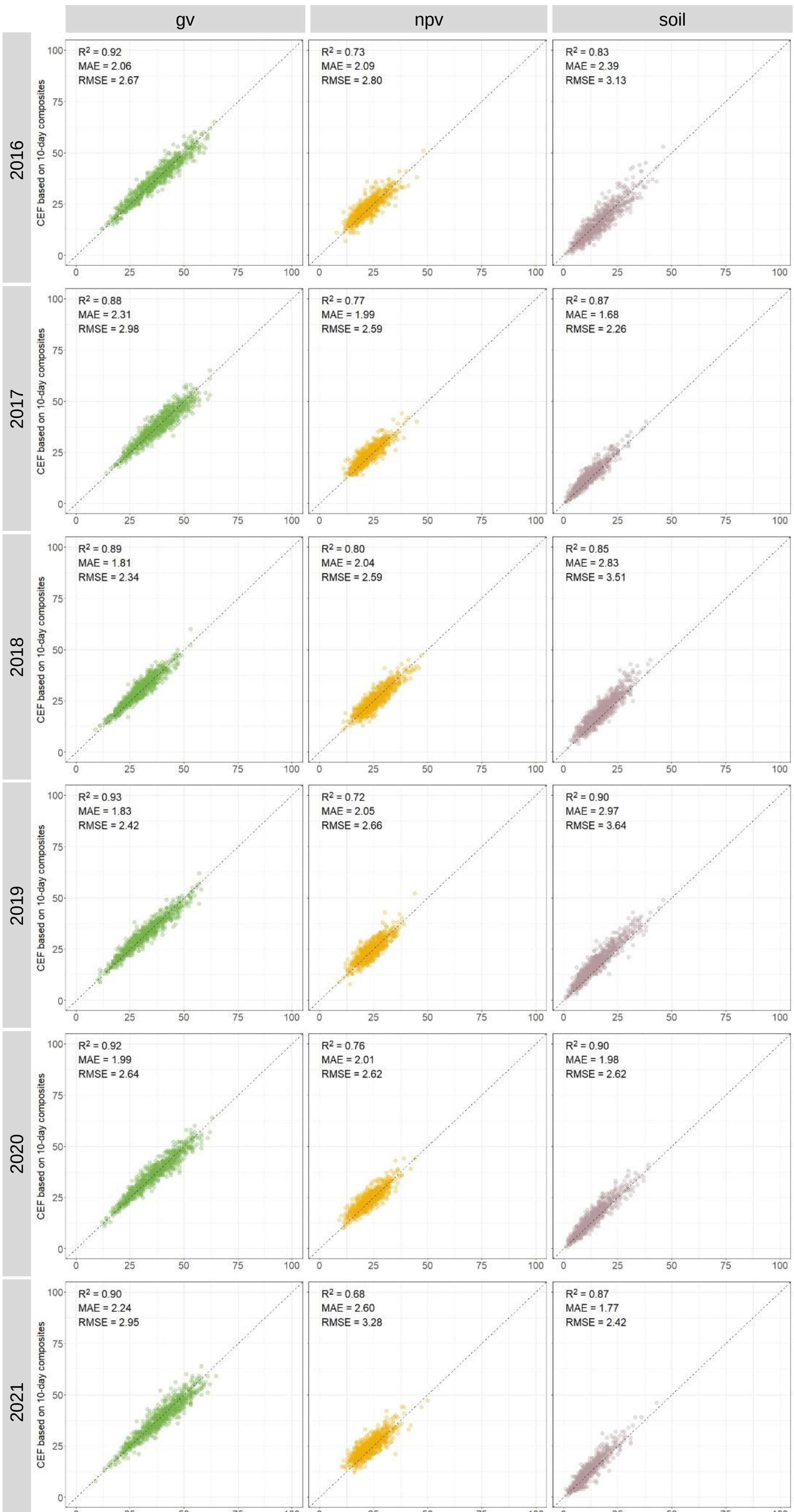

Figure SD10 Comparison between CEFs calculated based on monthly composites (x-axis) and 10-day composites (y-axis) for DE test site. Unmixing done using the Mediterranean set of endmembers.